Low Temperature Physics/Fizika Nizkikh Temperatur, 2012, v. 38, No. 2, pp. 119–190

de Haas–van Alphen effect and Fermi surface properties in rare earth and actinide compounds

(Review Article)

Yoshichika Ōnuki and Rikio Settai

Graduate School of Science, Osaka University, Toyonaka, Osaka 560-0043, Japan
E-mail: onuki@phys.sci.osaka-u.ac.jp
settai@phys.sci.osaka-u.ac.jp

Received May 17, 2011

Fermi surface properties in rare earth (R) and actinide (An) compounds of RX_3 (X: Al, Ga, In, Si, Ge, Sn, Pb), AnX_3 , $RTIn_5$ (T: transition metal), and $AnTGa_5$ are clarified as a function of the number of valence electrons. The electronic state can be changed by applying pressure and magnetic field. A change of Fermi surface properties associated with the metamagnetic behavior and the quantum critical point is also clarified precisely, together with the split Fermi surfaces in the non-centrosymmetric crystal structure, and the de Haas–van Alphen oscillations in the superconducting mixed state. In the quantum critical point region, the conduction electrons, or quasi-particles, are of an *f*-electron character, with heavy effective masses of 10–100 m_0 (m_0 is the rest mass of an electron) and condense into the unconventional (anisotropic) superconducting state.

PACS: **71.18.+y** Fermi surface: calculations and measurements; effective mass, *g*-factor;
71.20.–b Electron density of states and band structure of crystalline solids;
81.05.U– Carbon/carbon-based materials.

Keywords: de Haas–van Alphen effect, rare earth, actinide compounds, Fermi surface.

Contents

Dedicated to the memory of Prof. David Shoenberg

1. Introduction

The *f*-electron compounds of lanthanide and actinide compounds, especially lanthanide compounds, are usually treated in magnetism by an *f*-localized model, whereas they indicate various interesting phenomena such as heavy fermions and anisotropic superconductivity. These originate from the *f* electrons in the lanthanide and actinide compounds. Here, the 4*f* (5*f*) electrons in the lanthanide (actinide) atoms are pushed deep into the interior of the closed $5s^2 5p^6$ ($6s^2 6p^6$) shells because of the strong centrifugal potential $\ell(\ell+1)/r^2$, where $\ell = 3$ holds for the *f* electrons. This is the reason why the *f* electrons possess an atomic-like character even in a compound. The localized *f*-electron picture is thus a good starting point in magnetism, especially in the lanthanide compounds. On the other hand, the tail of their wave function in the *f*-electron compounds spreads to the outside of the closed $5s^2 5p^6$ ($6s^2 6p^6$) shells because it is highly influenced by the potential energy, the relativistic effect, the distance between the lanthanide (actinide) atoms, and hybridization of the *f* electrons with the conduction electrons.

The *f* electrons of cerium and uranium compounds are typical in exhibiting a variety of characteristic features including spin and charge orderings, spin and valence fluctuations, heavy fermions and anisotropic superconductivity [1–3]. In these compounds, the Ruderman–Kittel–Kasuya–Yosida (RKKY) interaction and the Kondo effect compete with each other. The RKKY interaction enhances the long-range magnetic order, where the *f* electrons with magnetic moments are treated as localized electrons, and the indirect *f*–*f* interaction is mediated by the spin polarization of the conduction electrons. The intensity of the RKKY interaction is proportional to the square of the magnetic exchange interaction J_{cf} between the *f* electrons and conduction electrons, and the corresponding characteristic temperature T_{RKKY} is expressed by

$$T_{RKKY} \propto D(\varepsilon_F)\,|\,J_{cf}\,|^2, \qquad (1)$$

where $D(\varepsilon_F)$ is the electronic density of states at the Fermi energy ε_F.

On the other hand, the Kondo effect quenches the magnetic moments of the localized *f* electrons by the spin polarization of the conduction electrons, producing a spin singlet state with a binding energy $k_B T_K$ at the cerium and uranium sites, which leads to a heavy fermion state with an extremely large effective mass at temperatures lower than the Kondo temperature T_K. The Kondo effect is characterized by the Kondo temperature T_K, which depends exponentially on $|J_{cf}|$ as follows:

$$T_K \propto \exp\{-1/(D(\varepsilon_F)\,|J_{cf}|)\}. \qquad (2)$$

The competition between the RKKY interaction and the Kondo effect was discussed by Doniach [4] as a function of $|J_{cf}|D(\varepsilon_F)$, as shown schematically in Fig. 1,*a*. The Doniach phase diagram is a good guiding principle to reach the quantum critical point, which is defined as the magnetic ordering temperature $T_{\rm ord} \to 0$. This is expressed experimentally by the chemical pressure as in UX_3 (X: Si, Ge, Sn, Pb) shown in Fig. 1,*b* and by applying external pressure, as shown later.

The magnetic susceptibility of $CeCu_6$ and $CeRu_2Si_2$ as well as that of UPt_3 and UPd_2Al_3, shown in Fig. 2, increases with decreasing temperature, following the Curie–

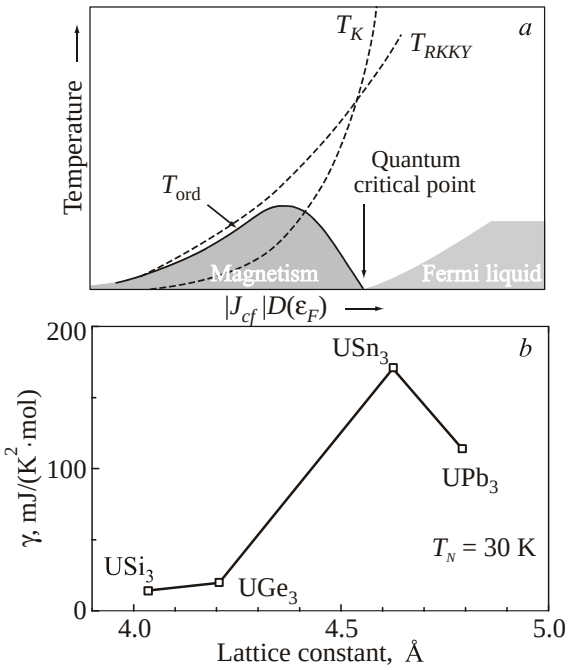

Fig. 1. Doniach phase diagram (*a*) and the γ vs lattice constant in UX_3, cited from Ref. 3 (*b*).

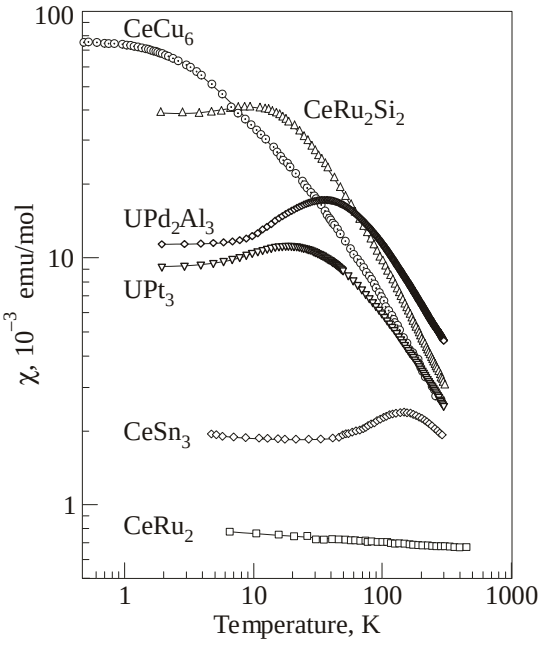

Fig. 2. Temperature dependence of the magnetic susceptibility in the typical cerium and uranium compounds, cited from Ref. 3.

Weiss law at high temperatures, and has a maximum at a characteristic temperature $T_{\chi\max}$ [3]. Below $T_{\chi\max}$, the susceptibility becomes almost temperature-independent, and the *f*-electron system is changed into a new electronic state, called the heavy fermion state. Here $T_{\chi\max}$ approximately corresponds to the Kondo temperature T_K.

The heavy fermion state in the cerium compounds is roughly understood as follows [5]. The 4*f* levels of the cerium ions are split into *J*-multiplets (J = 7/2 and 5/2) due to the spin-orbit interaction, where the 4*f* electrons in the cerium compounds are almost localized in nature, as mentioned above. The corresponding sixfold J = 5/2 multiplet is furthermore split into three doublets in the non-cubic crystalline electric field (CEF) scheme. The magnetic susceptibility at high temperatures follows the Curie–Weiss law with the effective magnetic moment of Ce^{3+}, namely, 2.5 μ_B/Ce. The electronic state is, however, changed with decreasing temperature. At low temperatures, the magnetic entropy of the ground-state doublet in the 4*f* levels, $R \log 2$, is obtained by integrating the magnetic specific heat C_m in the form of C_m/T over the temperature. When C_m is changed into the electronic specific heat γT via the many-body Kondo effect, the following relations are obtained:

$$\mathrm{R} \log 2 = \int_0^{T_K} \frac{C_m}{T}\, dT, \tag{3}$$

$$C_m = \gamma T\ . \tag{4}$$

The γ value can be obtained as

$$\gamma = \frac{R \log 2}{T_K} \simeq \frac{10^4}{T_K}\ (\mathrm{mJ/K^2 \cdot mol}). \tag{5}$$

For example, the γ value and the Kondo temperature are 1600 mJ/(K^2·mol) and 5 K in $CeCu_6$, and 350 mJ/(K^2·mol) and 20 K in $CeRu_2Si_2$, respectively. The 4*f*-localized electronic state is thus changed into a 4*f*-derived band with a flat energy vs momentum dispersion, possessing an extremely large effective mass. The 4*f*-itinerant band model is highly applicable to the Fermi surfaces in $CeRu_2$, $CeSn_3$ and $CeRu_2Si_2$, which are determined from the de Haas–van Alphen (dHvA) experiment, although the detected cyclotron mass m_c^* is larger than the corresponding band mass m_b. This is because the many-body Kondo effect is not included in the conventional band calculation. A similar feature is found in uranium compounds such as UPt_3 and UPd_2Al_3.

These strongly correlated electrons follow the Fermi liquid nature at low temperatures. The electrical resistivity ρ varies as $\rho = \rho_0 + AT^2$, where ρ_0 is the residual resistivity. The coefficient $\sqrt{A}$ is two to three orders of magnitude larger than that in the usual *s* and *p* electron systems. $\sqrt{A}$ correlates with an enhanced Pauli susceptibility $\chi(T \to 0) \simeq \chi_0$ and with a large electronic specific heat coefficient $C/T(T \to 0) \simeq \gamma$.

Interestingly, some heavy fermion systems show unconventional (anisotropic) superconductivity [6]. The most important observation for the well-known heavy fermion superconductors such as $CeCu_2Si_2$, UPt_3, and UPd_2Al_3 is that superconductivity is realized in the magnetically ordered state or the antiferromagnetic (ferromagnetic) fluctuations. The physical quantities such as the specific heat and the spin-lattice relaxation rate do not follow the exponential dependence of $\exp(-\Delta/k_BT)$ in the superconducting state, which is expected from Bardeen–Cooper–Schrieffer (BCS) theory, but obey a power law of T^n. Here, Δ is the superconducting energy gap, and n is an integer. This means that the superconducting gap is not completely opened in k space but possesses line and/or point nodes. For example, $n = 2$ corresponds to the line node. These results are based on the fact that quasi-particles with heavy masses of 10–100 m_0 (m_0 is the rest mass of an electron) are of an *f*-electron character, which originates from the strong Coulomb repulsion between the *f* electrons. These quasi-particles condense into Cooper pairs.

When the phonon-mediated attractive interaction is compared with the strong repulsive interaction among the *f* electrons, it is theoretically difficult for the former interaction to overcome the latter. To avoid a large overlap of the wave functions of the paired particles, the heavy fermion system preferentially chooses an anisotropic channel, such as a *p*-wave spin triplet state or a *d*-wave spin singlet state to form Cooper pairs [6]. The neutron-scattering experiments clearly indicated evidence of a close relationship between superconductivity and magnetic excitation in UPd_2Al_3 [7–9]. The magnetic excitation gap of UPd_2Al_3, which appears in the inelastic neutron profile below the superconducting transition temperature T_{sc}, corresponds to the superconducting order parameter.

Figure 3 shows a schematic view of the superconducting order parameter with *s*-, *d*-, and *p*-wave pairing. The order parameter $\Psi(r)$ with even parity (*s*- and *d*-waves) is symmetric with respect to r, where one electron with the up-spin state, $\uparrow$ of the Cooper pair is simply considered to be located at the center of $\Psi(r)$, where r = 0, and the other electron with the down-spin state, $\downarrow$ is located at r. The width of $\Psi(r)$ with respect to r is called the coherence length ξ, as shown in Fig. 3,*a*.

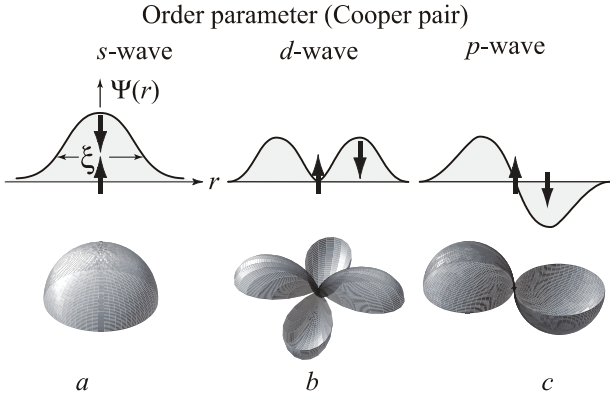

Fig. 3. Schematic view of the superconducting order parameter with *s*-wave, *d*-wave and *p*-wave pairing, cited from Ref. 3.

The technique of nuclear magnetic resonance (NMR) and nuclear quadrupole resonance (NQR) has proved to be a useful tool for determining the symmetry of the superconducting condensate. UPd_2Al_3 is considered to be a *d*-wave superconductor from NMR experiments [10], which corresponds to the case in Fig. 3,*b*. The origin of pairing has also been clarified by neutron-scattering experiments on UPd_2Al_3 [7–9], as mentioned above. On the other hand, $\Psi(r)$ with odd parity (*p*-wave) is not symmetric with respect to *r*, where the parallel spin state is shown in Fig. 3,*c*. From NMR and magnetization experiments [11,12], UPt_3 is considered to possess odd parity in symmetry.

Recently, a new aspect of cerium and uranium compounds with magnetic ordering has been discovered. When pressure *P* is applied to compounds with antiferromagnetic ordering such as $CeCu_2Ge_2$ [13], $CeIn_3$, $CePd_2Si_2$ [14] and $CeRhIn_5$ [15], the Néel temperature T_N reaches zero at the quantum critical pressure P_c: $T_N \to 0$ for $P \to P_c$, and superconductivity is observed at around P_c. Superconductivity is surprisingly found even in the ferromagnetic states of UGe_2 [16], URhGe [17], UIr [18] and UCoGe [19]. The crossover from the magnetically ordered state to the nonmagnetic state under pressure, crossing the quantum critical point, is the most interesting issue in strongly correlated *f*-electron systems. The electronic states can be tuned by pressure. Experimentally, the quantity $|J_{cf}|D(\varepsilon_F)$ in Fig. 1,*a* corresponds to pressure *P*.

It is also noted that the wave function of *f* electrons in the lanthanide and actinide metals shrinks with increasing the number of *f* electrons. In the lanthanide metals, this is well known as the lanthanide contraction. There exists the similar trend for the actinide metals such as Am, Cm, Bk, and Cf, revealing the localized nature of 5*f* electrons. On the other hand, the Wigner–Seitz radius R_{WS}, which is related to the atomic volume $V_{WS}\,(=(4\pi/3)R_{WS}^3)$, steeply decreases from Th to Np, as in transition metals, but increases as a function of the number of 5*f* electrons, as shown in Fig. 4 [20]. The Wigner–Seitz radius of Am is close to the localized 4*f*-electron radius of lanthanide metals, and thus the radius of Pu has an intermediate value between Np and Am. This is an important feature to understand the electronic states of actinide compounds, which is also related to the crystal structure. The 5*f*-itinerant band model is applicable to the electronic state of a heavy fermion superconductor UPt_3, as shown later. On the other hand, the 5*f*-localized electronic state is also well established experimentally in UPd_3. Our attention is similarly concentrated on the electronic states in transuranium compounds including Np and Pu [21].

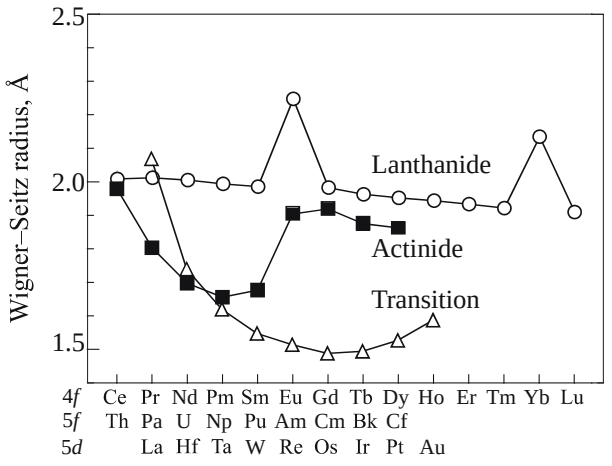

Fig. 4. Wigner–Seitz radius of the actinide, lanthanide and transition metals, cited from Ref. 20.

In this paper, we discuss the Fermi surface properties of lanthanide and actinide compounds including the corresponding Sc and Y compounds, and here after the rare earth is used instead of the lanthanide.

In the next chapter, we present several kinds of techniques for growing high-quality single crystals of rare earth and actinide compounds, and describe the dHvA effect. We present in Chaps. 3–9 the Fermi surface properties based on the results of dHvA experiment and energy band calculation in RX_3 (AnX_3), $RTIn_5$ (R: rare earth, T: transition metal) and $AnTGa_5$ (An: actinide), a change of Fermi surface properties in metamagnetism and quantum critical point, split Fermi surfaces in the non-centrosymmetric crystal structure, and dHvA oscillations in the superconducting mixed states. In the final chapter, the characteristic features in these compounds are summarized.

2. Single crystal growth and dHvA experiment

In the dHvA experiment, we need high-quality single crystals as well as low temperatures down to 30 mK and strong magnetic fields up to 170 kOe, for example. Various techniques for the single crystal growth were applied to rare earth and actinide compounds, depending on the melting point and the degree of the vapor pressure of the melt, as shown in Tables 1–4, for cerium, thorium, uranium and transuranium compounds, respectively [22]. These compounds were used for the dHvA experiment.

Table 1. Single crystal growth and Fermi surface studies in cerium compounds, which indicate a wide variety of electronic states such as paramagnetism including Pauli paramagnetism, denoted as (P), quadrupolar ordering (Q) including multipolar ordering, ferromagnetism (F), antiferromagnetism (AF), and superconductivity (S)

Cz	$CeRu_2$ (P,S)	$CeRh_2$ (P)	$CeSn_3$ (P)	CeNi (P)
	$CeRu_2Si_2$ (P)	CeAg (Q, F)	$CeGa_2$ (F)	$CeRh_3B_2$ (F)
	$CeRu_2Ge_2$ (F)		$CeIn_3$ (AF)	Ce_3Sn_7 (AF)
	$CeRh_2Si_2$ (AF)			
Flux	$CeIrIn_5$ (P,S)	$CeCoIn_5$ (P, S)		$CeAgSb_2$ (F)
	$CeRhIn_5$ (AF)	$CeCoGe_3$ (AF)		
	Ce_2RhIn_8 (AF)			
Br	CeSb (AF)	$CePt_3Si$ (AF, S)	CePtP (AF)	CePtAs (AF)
	$CePd_5Al_2$ (AF)			
FZ	CeB_6 (Q, AF)			

Table 2. Single crystal growth and Fermi surface studies in thorium compounds

Flux	$ThIn_3$ (P)	$ThRhIn_5$ (P)

Table 3. Single crystal growth and Fermi surface studies in uranium compounds

Cz	UC (P) USi_3 (P) UB_2 (P) UB_4 (P) UPt_3 (P, S)
	URu_2Si_2 (S) UGe_2 (F) UIr (F) UPd_2Al_3 (AF, S)
Flux	UAl_3 (P) $UFeGa_5$ (P) $UCoGa_5$ (P) $URhGa_5$ (P)
	UGa2 (F) UGa_3 (AF) UIn_3 (AF) USb_2 (AF) UBi_2 (AF)
	$UNiGa_5$ (AF) $UPdGa_5$ (AF) $UPtGa_5$ (AF)
CT	U_3P_4 (F) U_3As_4 (F) UP_2 (AF) UAs_2 (AF)

Table 4. Single crystal growth and Fermi surface studies in transuranium compounds

Flux	$NpGe_3$ (P)	$NpNiGa_5$ (AF)	$NpCoGa_5$ (AF)
	$NpRhGa_5$ (Q, AF)	$NpPtGa_5$ (AF)	$PuIn_3$ (P)

If the vapor pressure is low, the Czochralski pulling method denoted as Cz is a powerful method to obtain a large size of a single crystal ingot. The rf furnace was used for the Cz method when the melting point is less than 1500 °C and the tungsten crucible is available for $CeCu_6$, for example, as shown in Fig. 5,*a*. In this case, the tungsten crucible, which is surrounded by an rf-working coil, becomes a heater for the $CeCu_6$ melt. A large ingot with 10 mm in diameter and 80 mm in length is obtained in $CeCu_6$, where a necking procedure with a small size less than 1 mm in diameter in the pulling process is available in this temperature-stable rf furnace. In the next chapter, we discuss the Fermi surface properties of RIn_3. Single crystals of light rare earth RIn_3 (R: La–Gd) compounds, except $SmIn_3$, were grown by the Cz method in the rf furnace. The heavy rare earth RIn_3 (R: Tb–Lu) single crystals, including $SmIn_3$, were grown by the In-self flux method because of high vapor pressure of heavy rare earth metals.

The Cz method was also applied to the compounds with high-melting points, for example about 2500 °C, in the tetra-arc furnace. In this case, as shown in Fig. 5,*b*, the crucible is unnecessary. The starting materials are set on the Cu-heath plate, and grown by the Czochralski method in a tetra-arc furnace. The typical compounds with high-melting points are $CeRh_3B_2$, UB_2 and UC. Figure 5,*c* shows single crystal ingots of UPt_3, $CeRu_2$ and $CeIrSi_3$ grown by the Cz method in the tetra-arc furnace. $CeIrSi_3$ is known to be a pressure-induced superconductor without inversion symmetry in the tetragonal crystal structure [23].

The Cz method was also applied to the incongruent compounds such as $CeRu_2$ and USi_3. Figure 6 is the binary phase diagram of $CeRu_2$ and USi_3. For these compounds, we prepared the off-stoichiometric starting materials of $CeRu_{1.8}$ and $USi_{4.6}$, respectively in the tetra-arc furnace. Large single crystal ingots with 3–4 mm in diameter and 60 mm in length for $CeRu_2$ and USi_3 were grown, as shown in Fig. 5,*c*. Annealing of the electrotransport me-

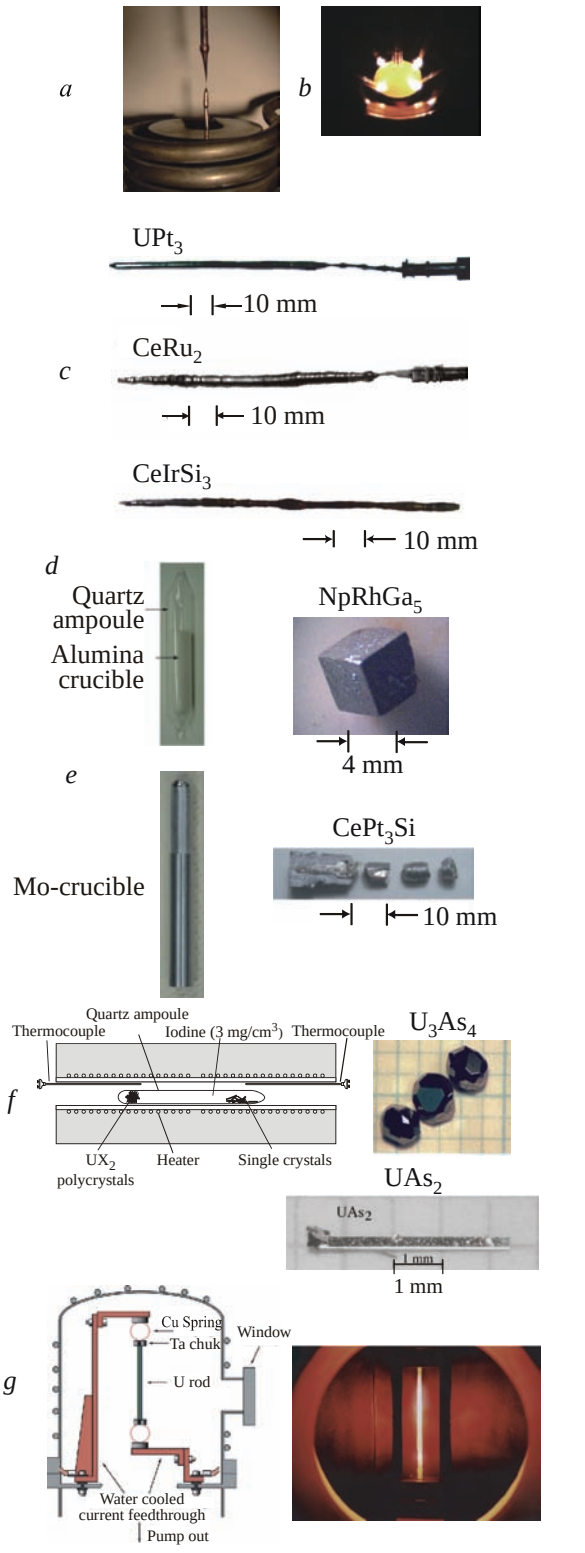

Fig. 5. Photograph of $CeCu_6$ ingot grown by the Czochralski method in the rf furnace with a working coil (*a*), $CeRu_2$ ingot grown in a tetra-arc furnace (*b*), single crystal ingots of UPt_3, $CeRu_2$ and $CeIrSi_3$ obtained by the Czochralski method (*c*), $NpRhGa_5$ grown by the flux method in the alumina crucible (*d*), $CePt_3Si$ grown by the Bridgman method in the Mo-crucible (*e*), U_3As_4 and UAs_2 grown by the chemical transport method (*f*), and a UPt_3 ingot which was annealed under high vacuum of 10^{-10} Torr via the solid state electrotransport method (*g*).

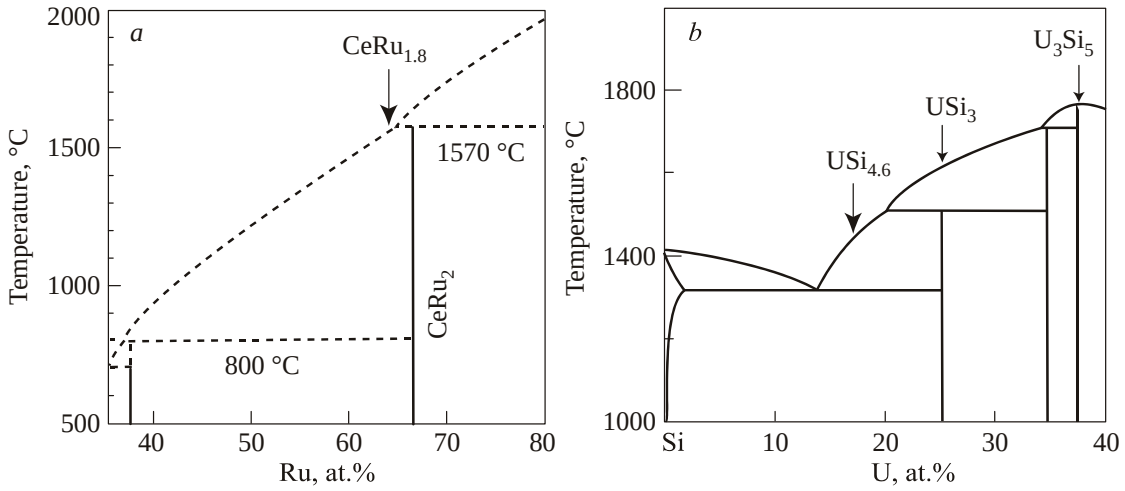

Fig. 6. Binary phase diagrams of $CeRu_2$ (*a*) and USi_3 (*b*), cited from Ref. 22.

thod, which is described below, was also applied to the ingot, reaching the residual resistivity $\rho_0 = 0.6$ μΩ·cm and the residual resistivity ratio 270 in $CeRu_2$.

On the other hand, the flux method (Flux), the chemical transport method (CT) and the Bridgman method (Br) are useful for the compounds with the high vapor pressure, and also for the incongruent compounds. The floating zone method (FZ) was also applied to CeB_6. Figure 5,*d* indicates a single crystal of $NpRhGa_5$ grown by the Ga-flux method, where the starting materials and flux were inserted in an alumina crucible, sealed in a quartz tube, heated up to 900–1000 °C in an electric furnace, and cooled down to lower temperatures, taking about 20 days. Usually, metals with low-temperature melting points such as Al, Ga, In, Sn, Pb, Sb and Bi are available. In the case of $NpRhGa_5$, excess Ga itself becomes flux. A single crystal of $CePt_3Si$ was grown by the Br method in a Mo crucible, as shown in Fig. 5,*e*. Single crystals of U_3P_4 and UAs_2 were grown by the chemical transport method with iodine in an electric furnace with a distinct temperature gradient, as shown in Fig. 5,*f*.

It is noted that the starting material of a uranium ingot was annealed under high vacuum of 10^{-10} Torr via the solid state electrotransport method, as shown in Fig. 5,*g*. For example, an Fe impurity of 40 ppm in the uranium ingot was reduced to less than 2 ppm, and the Cu impurity was completely removed [24]. Subsequent annealing under high vacuum using the electrotransport method drastically improved the quality of the single crystal, which was applied to $CeRu_2$, UPt_3 and URu_2Si_2, as shown in Fig. 5,*g* for UPt_3. For example, we recently obtained an extremely high-quality single crystal sample of URu_2Si_2, where the residual resistivity ratio (RRR) reaches more than 500 [21].

The dHvA experiment was performed by the standard field-modulation method with a modulation frequency of 7 Hz and a modulation field of 100 Oe [1,2]. Pressure was applied up to 3 GPa using an MP35N piston-cylinder cell with a 1:2 mixture of commercial Daphne oil (7373) and petroleum ether as a pressure-transmitting medium. The pressure was calibrated by the superconducting transition temperature T_{sc} of Sn, which is accurate within 0.05 GPa of the absolute value. It is also noted that the cantilever type dHvA method is applicable and useful to an extremely small sample with 0.1×0.1×0.05 mm, for example [25–27].

The detected dHvA signal $V_{\rm osc}$ in the 2ω technique is written as follows [28]:

$$V_{\rm osc} = \sum_p A_p \sin\left(\frac{2\pi pF}{H} + \phi_p\right), \tag{6}$$

$$A_p \propto J_2\left(\frac{2\pi Fh}{H^2}\right) H^{1/2} p^{-3/2} \left|\frac{\partial^2 S_F(k_z)}{\partial k_z^2}\right|^{-1/2} R_T R_D R_S, \tag{7}$$

$$R_T = \frac{2\alpha m_c^* T/H}{\sinh(2\alpha m_c^* T/H)}, \tag{8}$$

$$R_D = \exp(-\alpha m_c^* T_D/H), \tag{9}$$

$$R_S = \cos(p\pi m_c^* g/2m_0), \tag{10}$$

$$\alpha = 2\pi^2 pck_B/e\hbar. \tag{11}$$

Index p = 1, 2, 3, ... represents the fundamental (p = 1) and the higher-harmonic (p = 2, 3, ...) dHvA frequencies, and J_2 is the Bessel function. The dHvA amplitude A_p is related to the so-called curvature factor $\partial^2 S_F(k_z)/\partial k_z^2$, the thermal reduction factor R_T ($R_T \to 1$ for $T \to 0$), the Dingle reduction factor R_D ($R_D \to 1$ for the Dingle temperature $T_D \to 0$), which is caused by the finite scattering lifetime of the conduction electrons, and the spin reduction factor R_S (R_S = 1 for the cyclotron mass $m_c^* = m_0$ and g = 2), which is the interference between the oscillations of spin-up and spin-down electrons. Here m_0 is the rest mass of an electron. The dHvA frequency $F = c\hbar S_F/2\pi e$, which obtained in the fast Fourier transformation (FFT) spectrum of the oscillation, is proportional to the extremal (maximum or minimum) cross-sectional area S_F of the Fermi surface. From the temperature and field dependences of the dHvA amplitude, we can determine the cyclotron effective mass m_c^* and the Dingle temperature T_D, respectively.

$T_D = \hbar/2\pi k_B\tau$ is inversely proportional to the scattering lifetime τ of an conduction electron. We also estimate the mean free path ℓ from the simple relations: $S_F = \pi k_F^2$, $\hbar k_F = m_c^* v_F$, and $\ell = v_F\tau$, where k_F is half of the caliper dimension of a circular S_F and v_F is the Fermi velocity.

The dHvA experiments were also performed using the micro-cantilever (MouldLessCantilever, SSI-SS-ML-PRC120, Seiko Instruments Inc.) with the same modulation field of $h \simeq 100$ Oe (a modulation frequency of $\omega/2\pi$ = 11 Hz), and without the modulation field. The DC-current ($I_{DC} \sim$ ~ 0.05 mA) was used with the modulation field, and the AC-current ($I_{AC} \sim 0.05$ mA) was used without the modulation field. The amplitude A for the torque method using the cantilever is written as

$$A \propto I_{AC}\,\frac{1}{F}\,\frac{dF}{d\theta} \quad \text{(without the modulation field)} \quad (12)$$

and

$$A \propto I_{DC}\omega J_1(x)\,\frac{1}{F}\,\frac{dF}{d\theta} \quad (13)$$

(with the modulation field and ω detecting technique), where I_{AC} and I_{DC} are the AC and DC excitation current for the cantilever. $J_1(x)$ is the first Bessel function due to the modulation field.

The experimentally obtained dHvA results of cerium, thorium, uranium and transuranium compounds, which are shown in Tables 1–4, respectively, were compared with the results of energy band calculation [1–3,5,21–23,29–31]. These compounds include a wide variety of electronic states such as paramagnetism including Pauli paramagnetism, denoted as (P) in Tables 1–4, quadrupolar ordering (Q) including the multi-polar ordering, ferromagnetism (F), antiferromagnetism (AF), and superconductivity (S).

3. Fermi surface properties in RIn_3 (R: La–Lu)

The RIn_3 and RGa_3 (R: Sc, Y, and La–Lu) compounds crystallize in the $AuCu_3$-type cubic crystal structure, as shown in Fig. 7,*a*, where the corner-sites are occupied by the R atoms and the face-centered sites are occupied by the In and Ga atoms. The characteristic properties of RIn_3 is summarized in Table 5 and in Fig. 7. Most of RIn_3 compounds order antiferromagnetically, except a paramagnet of $PrIn_3$ with the singlet ground state in the CEF scheme and a divalent Pauli paramagnet of $YbIn_3$. The divalent property of $YbIn_3$ is clear from the lattice constant of RIn_3, as shown in Fig. 7,*b*, because the lattice constant of $YbIn_3$ deviates from the lanthanide contraction [32]. The Néel temperature T_N of RIn_3 is shown in Fig. 7,*c*, which approximately follows the de Gennes scaling: $T_N \sim (g_J - 1)^2 J(J+1)$, where g_J is the Landé *g*-factor and *J* is the total angular momentum [33,34]. Among RIn_3 antiferromagnets, $CeIn_3$ is a well known Kondo-lattice compound showing antiferromagnetic ordering at a Néel temperature T_N = 10 K [35–38]. The ordered moment 0.65 μ_B/Ce is comparable to the value 0.71 μ_B/Ce expected from the Γ_7 ground state in the CEF scheme. Nevertheless,

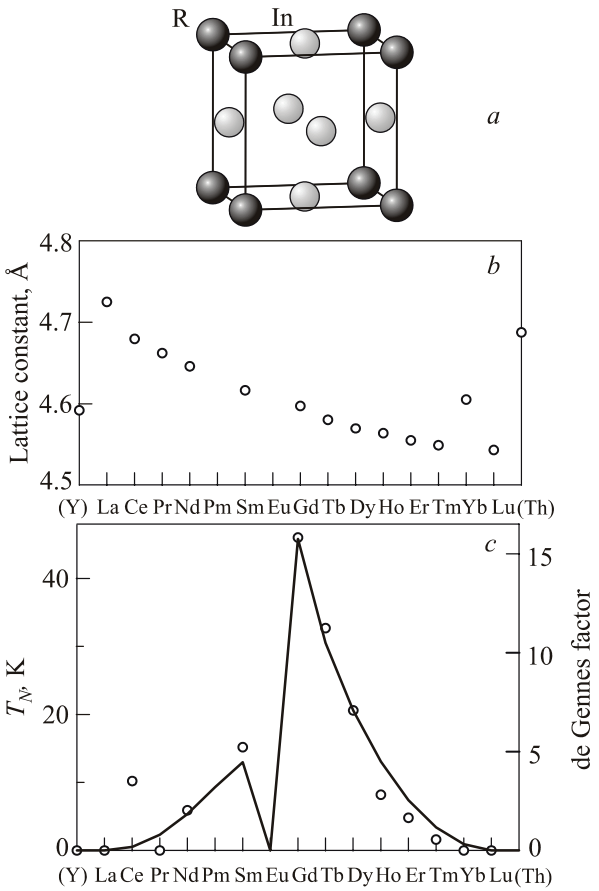

Fig. 7. Cubic crystal structure (*a*), lattice constant (*b*), cited from Ref. 32, and the Néel temperature T_N in RIn_3, where a solid line indicates the de Gennes scaling (*c*).

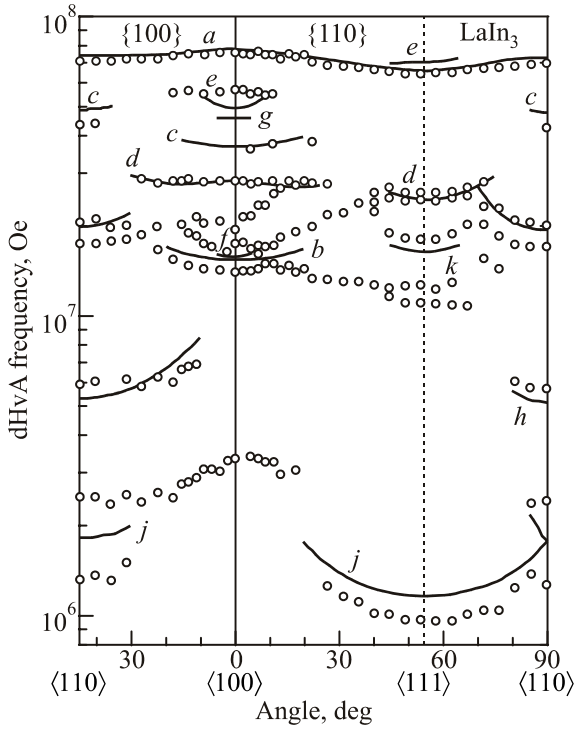

Fig. 8. Angular dependence of the dHvA frequency in $LaIn_3$, cited from Ref. 39. The solid lines are the results of band calculations [40].

Table 5. Magnetic properties, dHvA frequency and the corresponding cyclotron mass for $H \parallel \langle 100 \rangle$ (only branch j for $H \parallel \langle 111 \rangle$) in RIn_3 [39–42,45–50], $ScGa_3$ and $LuGa_3$ [55]

RIn_3	T_N, K	μ_s, μ_B/R	Electronic states at dHvA experiments	a, 10^7 Oe (m_c^*, m_0)	d, 10^7 Oe (m_c^*, m_0)	b, 10^7 Oe (m_c^*, m_0)	j, 10^7 Oe (m_c^*, m_0)
YIn_3	0	0	Pauli Para	8.13 (0.64)	3.34	1.05 (0.27)	
$LaIn_3$	0	0	Pauli Para $\gamma = 7.7$ mJ/(K^2·mol)	7.47 (0.57)	2.78 (0.40)	1.38 (0.26)	0.096 (0.17)
$CeIn_3$	10	0.65	AF [H_c = 610 kOe]		3.0 (2.0)		
$PrIn_3$	0	singlet CEF	Para $\gamma = 11.4$ mJ/(K^2·mol)	7.57 (0.99)	3.02 (0.60)	1.28 (0.36)	0.128 (0.28)
$NdIn_3$	5.9	2.3 (at 2 K)	AF ($H < H_{c3}$) Para ($H > H_{c3}$) [H_{c1} = 78, H_{c2} = 89, H_{c3} = 111 kOe]	8.09 (1.05) 7.75 (1.14)	3.17 (0.80) 3.0		0.12 (0.31) 0.12
$SmIn_3$	T_{N1} = 15.9 T_{N2} = 15.2 T_{N3} = 14.7		AF (H < 130 kOe)	$H \parallel \langle 110 \rangle$ 7.81 (1.30)	3.08 (0.80)		
$GdIn_3$	46		AF (H < 150 kOe)		3.07 (0.49)		0.096 (0.29)
$TbIn_3$	T_{N1} = 32 T_{N2} = 25	8.9 (at 3 K)	AF (H < 130 kOe) [H_{c1} = 102, H_{c2} = 102, H_{c3} = 157, H_{c4} = 311, H_{c5} = 235, H_{c6} = 398 kOe]	7.83 (1.60)	3.13 (0.34)	0.93 (0.19)	
$DyIn_3$	20	8.8 (at 3 K)	AF (H < 130 kOe) [H_{c1} = 50, H_{c2} = 115 kOe]	8.16 (0.88)	3.43 (0.57)	1.41 (0.57)	0.065 (0.20)
$HoIn_3$	T_{n1} = 8.2 T_{N2} = 7.7	9.2 (at 1.5 K)	Para ($H > H_{c4}$) [H_{c1} = 17, H_{c2} = 87, H_{c3} = 40, H_{c4} = 101 kOe]	8.26 (0.92)	3.46 (0.85)	1.02 (0.22)	
$ErIn_3$	4.6	8.2 (at 3 K)	Para ($H > H_{c3}$) [H_{c1} = 27, H_{c2} = 53, H_{c3} = 58 kOe]	8.15 (0.80)	3.49 (0.88)	0.92 (0.38)	
$TmIn_3$	1.5	3.5 (at 1.3 K)	Para ($H > H_c$) [H_c = 9 kOe]	7.23 (0.93)	3.05 (1.12)	0.82 (0.24)	
$LuIn_3$	0	0	Pauli Para $\gamma = 7.5$ mJ/(K^2·mol)	8.18 (0.61)	3.57 (0.77)	0.89 (0.24)	
$ScGa_3$	0	0	Pauli Para	10.55 (0.75)	4.41 (0.67)	0.94 (0.31)	
$LuGa_3$	0	0	Pauli Para	9.81 (0.74)	4.13 (0.63)	1.19 (0.30)	

$CeIn_3$ possesses a large electronic specific heat coefficient $\gamma = 130$ mJ/(K^2·mol) at low temperatures, which is twenty times larger than $\gamma = 7.7$ mJ/(K^2·mol) in $LaIn_3$.

We will start to explain the Fermi surface properties in RIn_3. Figure 8 shows the angular dependence of the dHvA frequency in $LaIn_3$ [39]. The solid lines represent the results of energy band calculation [40]. Branch *a* originates from the band 7-electron Fermi surface with the nearly spherical topology, while the others originate from the band 6-hole Fermi surface, as shown in Fig. 9. Here, the electronic configuration of the La atom is $[Xe]4f^0 5d^1 6s^2$, while the valence electrons of the In atom are $5s^2 5p^1$. The total number of valence electrons are 12 in $LaIn_3$. $LaIn_3$ is, therefore, a compensated metal with equal number of electrons and holes, or equal volume of the band 7-electron Fermi surface and the band 6-hole Fermi surface. The latter Fermi surface consists of three kinds of major parts. Among them, a Fermi surface centered at Γ, denoted by *d*, is electron in dispersion and is spherical in topology, bulges slightly along the ⟨100⟩ direction and connects with another part of the Fermi surface centered at R by a slender arm elongated along the ⟨111⟩ direction. The arm is denoted by *j*. The topology of the Fermi surface for branch *d* is similar to that of Cu, although the volume is small compared to that of Cu. Here we note that the Γ point is a central position in the cubic Brillouin zone, and the nearly spherical band 7-electron Fermi surface is centered at the corner R point.

Conduction electrons are mainly due to La 5*d* and In 5*p* electrons. The cyclotron masses for branches *a* and *d* for $H \parallel \langle 100 \rangle$ are $0.57\,m_0$ and $0.40\,m_0$, respectively, which are almost the same as the corresponding band masses of $0.58\,m_0$ and $0.53\,m_0$, respectively.

Next we consider a change of the Fermi surface in the antiferromagnetic state of $NdIn_3$ with a Néel temperature $T_N = 5.9$ K [41,42]. The magnetic structure in the antiferromagnetic state with a magnetic wave vector $q = (1/2, 0, 1/2)$, determined by the neutron scattering experiment, is tetragonal, as shown in Fig. 10 [43].

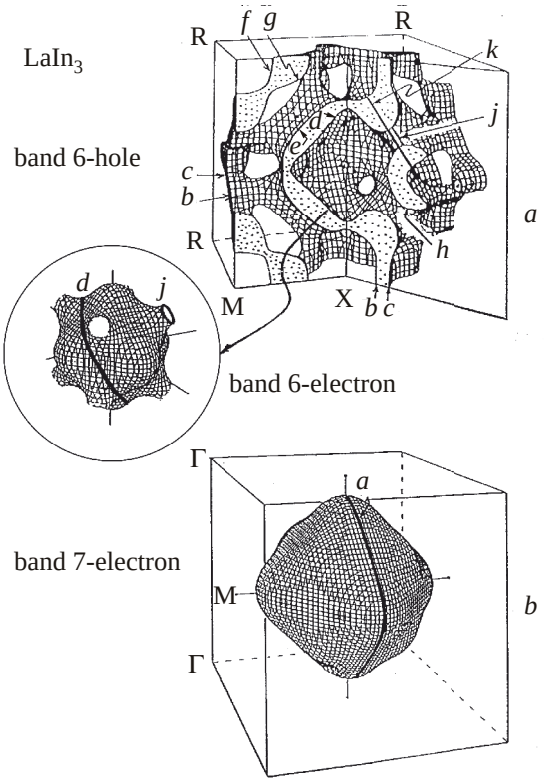

Fig. 9. Band 6-hole (*a*) and band 7-electron Fermi surfaces (*b*) in $LaIn_3$, cited from Refs. 39, 40.

Figure 11 shows the magnetization curve with three metamagnetic transitions at H_{c1} = 78, H_{c2} = 89 and H_{c3} = = 111 kOe, which are indicated by the vertical broken lines [44], and the dHvA oscillation for $H \parallel \langle 100 \rangle$. With increasing magnetic field, the compound changes from the antiferromagnetic state to a field-induced ferromagnetic (or paramagnetic) state at H_c (= H_{c3}) = 111 kOe, passing through the intermediate-magnetic state. The FFT spectrum in $NdIn_3$ is roughly the same as the one in $LaIn_3$ because the 4*f* electrons in $NdIn_3$ are localized and therefore do not contribute

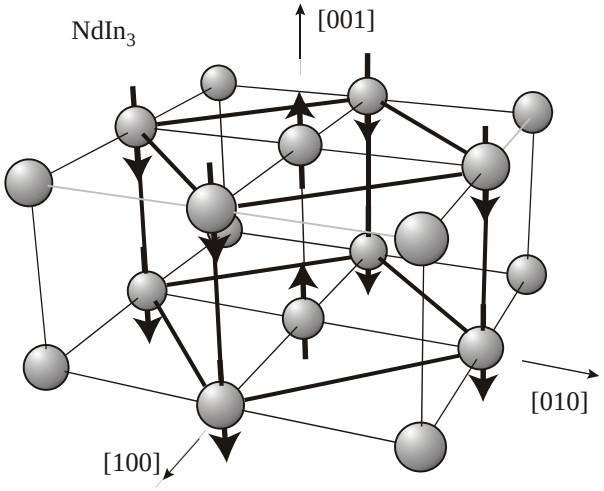

Fig. 10. Antiferromagnetic structure in $NdIn_3$, cited from Ref. 43. Four chemical unit cells are shown, where one magnetic unit cell is represented by thick solid lines with arrows indicating the directions of the magnetic moments.

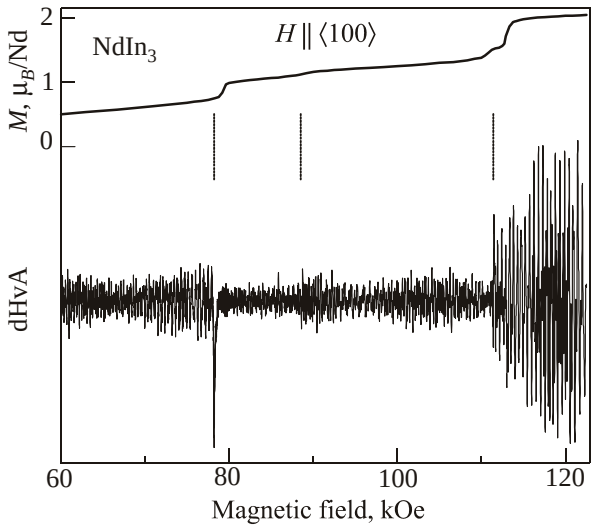

Fig. 11. Magnetization curve and the dHvA oscillation for $H \parallel \langle 100 \rangle$ in $NdIn_3$, cited from Refs. 41, 42, 44.

to the Fermi surface. Among the dHvA branches in the antiferromagnetic state of $NdIn_3$, we remark branch *a* due to the band 7-electron Fermi surface. Figure 12,*a* shows the field dependence of the dHvA frequency of branch *a*. The dHvA frequency corresponding to the up-and down-spin states of the conduction electrons is degenerated in the antiferromagnetic state, and also in the intermediated-magnetic state, but is split into the up-and down-spin states in the field-induced ferromagnetic (paramagnetic) state, as shown schematically in Fig. 12,*b*.

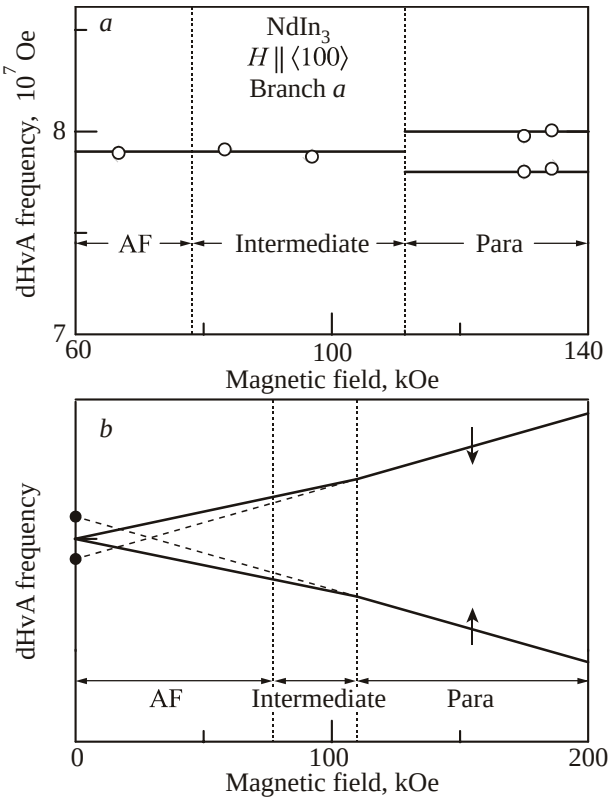

Fig. 12. Field dependence of the dHvA frequency in $NdIn_3$, cited from Refs. 41, 42.

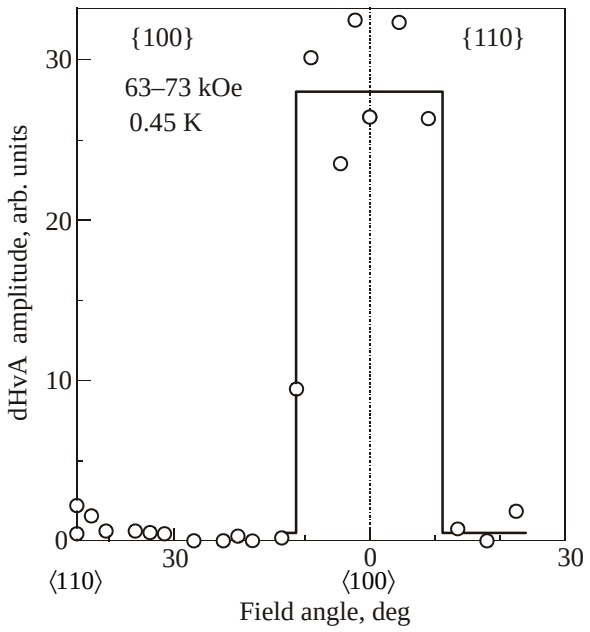

Fig. 13. Angular dependence of the dHvA amplitude for branch *a* in $NdIn_3$, cited from Refs. 41, 42.

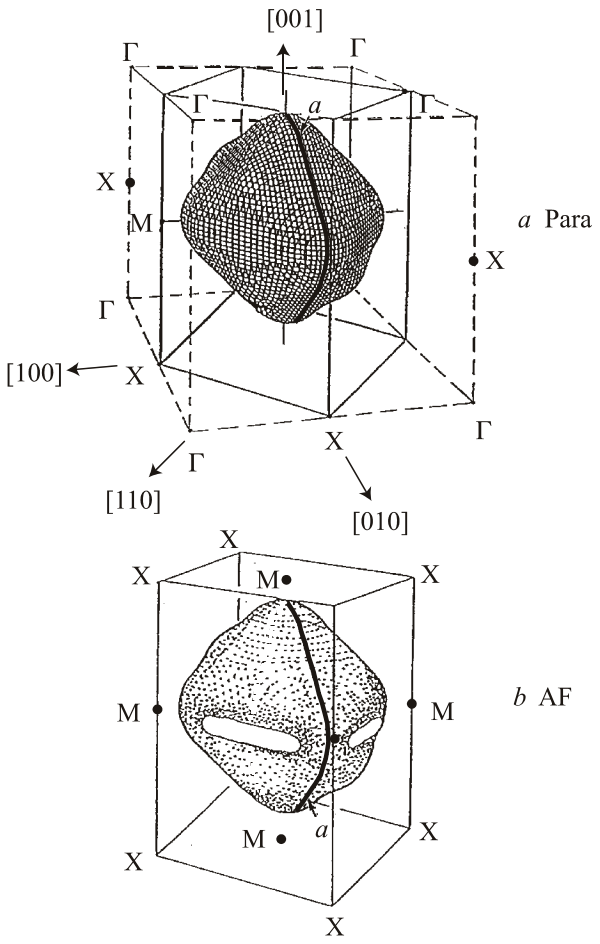

Fig. 14. Fermi surfaces in the paramagnetic state (*a*) and the antiferromagnetic state (*b*) in $NdIn_3$, cited from Refs. 41, 42.

It is noticed that the dHvA amplitude of branch *a* in the antiferromagnetic state strongly depends on the field direction, as shown in Fig. 13. It is usual in the field angle from 0° ($H \parallel \langle 100 \rangle$) to about 10°, but is strongly reduced at angles larger than 10°. This is due to the small magnetic Brillouin zone based on the large tetragonal magnetic structure shown in Fig. 10. From the angular dependence of the dHvA amplitude for branch *a*, the nearly spherical electron-Fermi surface in the paramagnetic state of $NdIn_3$, as shown in Fig. 9,*b* or Fig. 14,*a*, which corresponds to branch *a* in $LaIn_3$, is changed into a multiply-connected Fermi surface with necks along the [110] and [$\bar{1}$10] directions in the antiferromagnetic state, as shown in Fig. 14,*b*. Note that no necks exist along the [100] and [010] directions. A thick solid line in Fig. 14,*b* corresponds to a circulating orbit a for $H \parallel$ [100]. Therefore, the cubic symmetry is broken in the antiferromagnetic state. If we follow the Fermi surface in Fig. 14,*b*, branch *a* is not detectable for $H \parallel \langle 110 \rangle$, but is experimentally detected even in the antiferromagnetic state, although its amplitude is extremely small, as shown in Fig. 13. This is because an electron can circulate along a closed orbit by breaking through the necks of the Fermi surface. The antiferromagnetic Fermi surface in the 4*f*-localized antiferromagnet $NdIn_3$ is thus reconstructed on the basis of the magnetic Brillouin zone. The angular dependence of the dHvA frequency in the antiferromagnetic state and the paramagnetic state is shown later in Figs. 21,*d* and 21,*e*, respectively, where the other Fermi surface properties in RIn_3 are also shown in Fig. 21 [39–42,45–50].

The dHvA experiments of RIn_3 (R: Sm to Tm) were done in the antiferromagnetic state, while some RIn_3 (R: Ho, Er, Tm) compounds were done in the paramagnetic (field-induced ferromagnetic) states, where the corresponding critical field H_c was about 100 kOe or less than 100 kOe, as in $NdIn_3$. $PrIn_3$ was in the paramagnetic state with the singlet state in the 4*f*-CEF scheme [46]. These are summarized in Table 5 [39–42,45–50].

The similar change of the electronic state based on the magnetic structure is also realized in a Kondo-lattice compound $CeIn_3$ with antiferromagnetic ordering at $T_N = 10$ K, where ordered moments of 0.65 μ_B/Ce with the propagation vector $q = (1/2, 1/2, 1/2)$ are aligned along the ⟨111⟩ direction as shown in Fig. 15,*a* [35–37]. The angular dependence of the dHvA frequency in $CeIn_3$ is later shown in Fig. 21,*b* [45,51].

The detected dHvA named *d* in $CeIn_3$ is very close to the one in $LaIn_3$. Branch *d* in $CeIn_3$ is, however, observed in the whole angle region, possessing no arms, indicating that the Fermi surface is a nearly spherical Fermi surface with humps. It is noted that there exist no necks in another non-4*f* ($4f^{14}$) reference compound $LuIn_3$ [49]. The neck in $LaIn_3$ is changed into a hump in $LuIn_3$ and $CeIn_3$, as shown in Fig. 15,*c*.

The cyclotron mass of branch *d* in $CeIn_3$ is strongly field-dependent, ranging from 2.3 to 16 m_0, as shown in Fig. 16,*a*, which brings about a drastic change of the dHvA

amplitude for the magnetic field direction from ⟨100⟩ to ⟨110⟩, as shown in Fig. 16,*b*. This is due to the spin factor in Eq. (10). From the large cyclotron mass of the branch *d* for $H \parallel \langle 110 \rangle$, it is suggested that the electronic state on the hump corresponds to the heavy fermion state. Namely, the heavy electronic state exists locally in the Fermi surface. The orbit for the magnetic field along ⟨110⟩ passes four times on the hump for one cycle of an orbit. On the other hand, the orbit for the magnetic field along ⟨100⟩ does not pass on the hump. The hump is nowadays called "hot spot" [52].

Next we consider the meaning of a heavy fermion state. The conduction electron with a large cyclotron mass is believed to move slowly in the crystal [53]. We confirmed experimentally that the product of the cyclotron mass and the inverse scattering lifetime or the Dingle temperature $m_c^*\tau^{-1}$ or $m_c^* T_D$ is constant by using two orbits of the Fermi surface named *d* in $CeIn_3$. As mentioned in Chap. 2, the following equation is obtained:

$$\frac{m_c^*}{\tau} = \frac{\hbar k_F}{\ell}. \tag{14}$$

Thus, m_c^*/τ is expected to be the same for two similar orbits with the same mean free path. When the effective mass m_c^* is enhanced by a factor of $(1 + \lambda)$ by the many-body Kondo effect, τ should also be enhanced by a factor $(1 + \lambda)$. This occurs because a large cyclotron mass is translated into a small velocity from the equation of $\hbar k_F = m_c^* v_F$ so that the scattering lifetime is enhanced by $(1 + \lambda)$ from the equation of $\ell = v_F \tau$ if the mean free path ℓ is the same between two orbits. In terms of the Dingle temperature, Eq. (12) becomes

$$m_c^* T_D = \frac{\hbar^2 k_F}{2\pi k_B \ell}. \tag{15}$$

The above relation between the cyclotron mass and the Dingle temperature was applied to the nearly spherical Fermi surface *d*. The dHvA frequency *F*, the cyclotron mass m_c^*

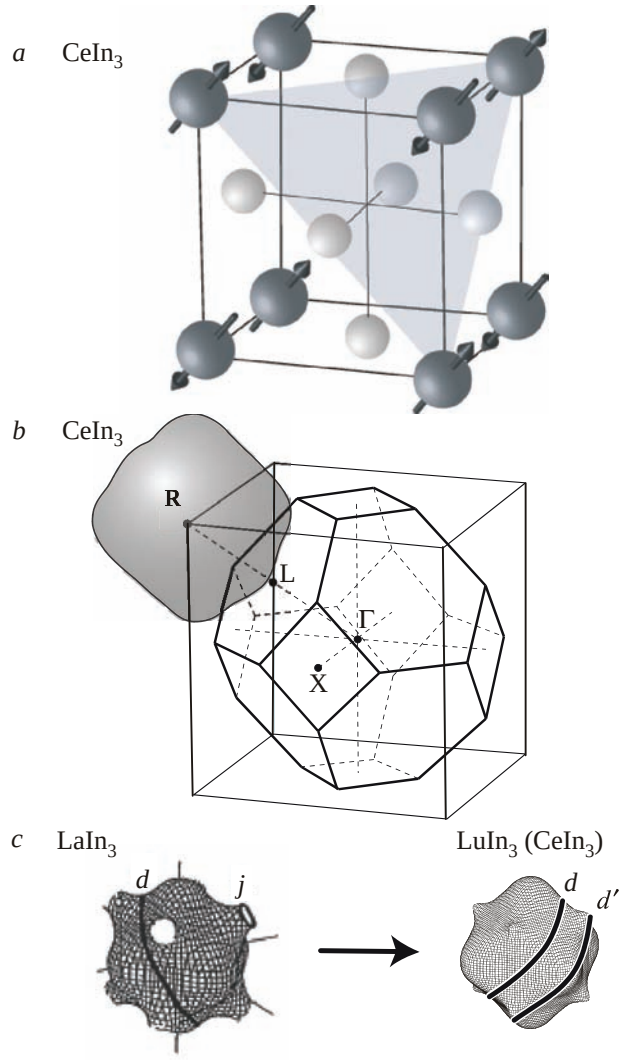

Fig. 15. Crystal and magnetic structure in $CeIn_3$ (*a*), the corresponding magnetic Brillouin zone of $CeIn_3$ and a band 7-electron Fermi surface (*b*), and Fermi surfaces named *d* in $LaIn_3$ and $LuIn_3$ ($CeIn_3$) (*c*), cited from Refs. 38, 49.

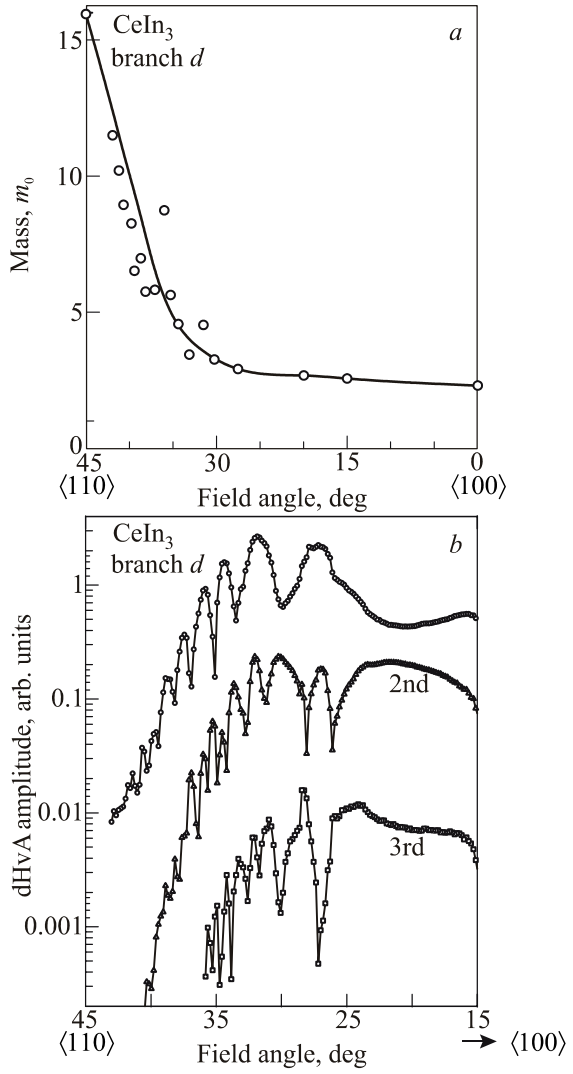

Fig. 16. Angular dependence of the cyclotron mass of the branch *d* (*a*) and the corresponding dHvA amplitude for the fundamental, 2nd and 3rd harmonics in the field range of 70 to 90 kOe at 0.45 K in $CeIn_3$, cited from Ref. 51 (*b*).

and the Dingle temperature T_D are $3.15 \cdot 10^7$ Oe, $2.44\,m_0$ and $T_D = 0.19$ K for $H \parallel \langle 111 \rangle$, and $3.29 \cdot 10^7$ Oe, $12\,m_0$ and $T_D = 0.04$ K for the field direction close the $\langle 110 \rangle$ direction, indicating that the product of $m_c^* T_D$ is constant for the two orbits. We can thus concluded that the larger the cyclotron mass becomes the larger the scattering lifetime is, so that the value of $m_c^* \tau^{-1}$ or $m_c^* T_D$ is constant.

Branch *a* of band 7-electron Fermi surface in Fig. 15,*b* was, however, not detected in $CeIn_3$, which is ascribed to the reconstruction of the Fermi surface on the basis of the antiferromagnetic Brillouin zone. This Brillouin zone is the same as that for the face-centered cubic structure, as shown in Fig. 15,*b*. Most of the band 7-electron Fermi surface centered at the R point is changed into a fully occupied band in this new Brillouin zone, where the original R point is reduced to the Γ point in this Brillouin zone. The antiferromagnetic ordering of $CeIn_3$ is very robust against the magnetic field. The antiferromagnetic phase diagram of T_N vs H_c is obtained as follows: $T_N \sim [1 - (H/H_c)^2]$ and the metamagnetic field from the antiferromagnetic state to the paramagnetic state $H_c \simeq 610$ kOe for $T_N \to 0$ [52]. At high magnetic fields larger than H_c, namely in the paramagnetic state, branch *a* was observed: $F = 7.9 \cdot 10^7$ Oe and $m^* = 6\,m_0$ for $H \parallel \langle 110 \rangle$ [54]. The present dHvA frequency is slightly larger than $7.47 \cdot 10^7$ Oe in $LaIn_3$ [39] and is close to $8.13 \cdot 10^7$ Oe in YIn_3 [55] or $8.18 \cdot 10^7$ Oe in $LuIn_3$ [49].

A drastic change of the Fermi surface in an antiferromagnetic Kondo compound $CeIn_3$ is realized under pressure [38], which will be shown later in Chap. 6.

$YbIn_3$ in Fig. 7,*b* is a Pauli paramagnet with the divalent property of Yb^{2+} [32]. The electronic configuration of the Yb atom is $[Xe]4f^{14}6s^2$, and thus the valence electrons are $6s^2$. Considering the valence electrons of $5s^2 5p^1$ in the In atom, the total number of valence electrons are 11 in $YbIn_3$, revealing an uncompensated metal. Figure 17 shows the angular dependence of the dHvA frequency in $YbIn_3$ [49].

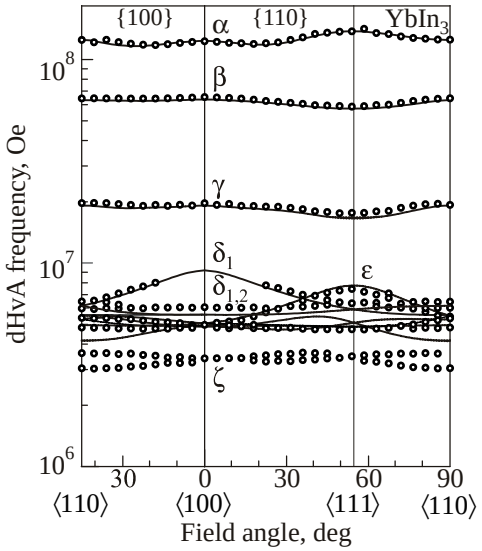

Fig. 17. Angular dependence of the dHvA frequency in a Pauli paramagnet $YbIn_3$. The solid lines are the results of energy band calculation, cited from Ref. 49.

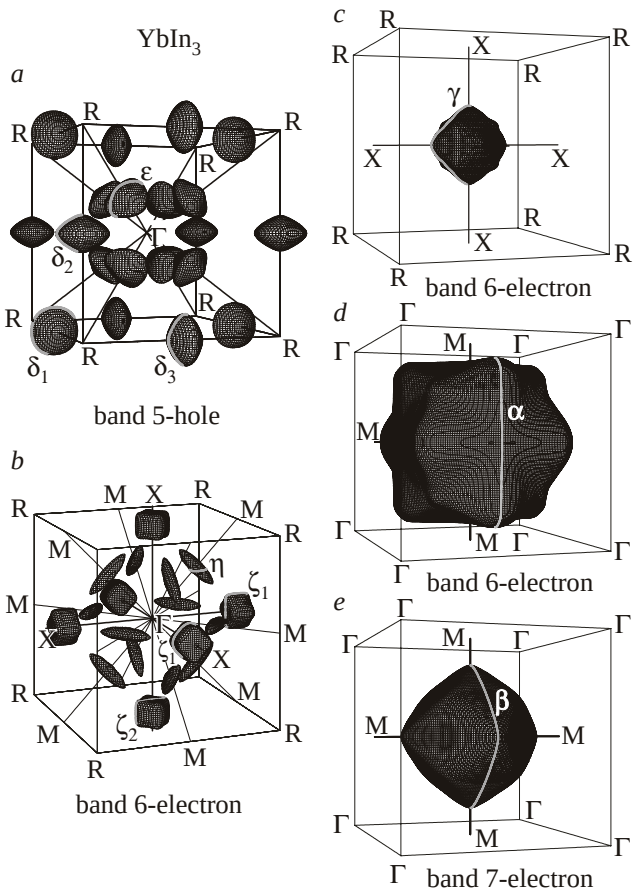

Fig. 18. Theoretical Fermi surfaces in a Pauli paramagnet $YbIn_3$, cited from Ref. 49.

The solid lines in Fig. 17 indicate the results of energy band calculation. The experimental results of dHvA branches named α, β, γ, δ_i and ε are in good agreement with the theoretical ones, as shown in Fig. 18, which are the band 6-electron Fermi surface centered at R, the band 7-electron Fermi surface centered at R, the band 6-electron Fermi surface centered at Γ, the band 5-hole Fermi surface centered at M and band 5-hole located along Λ, respectively.

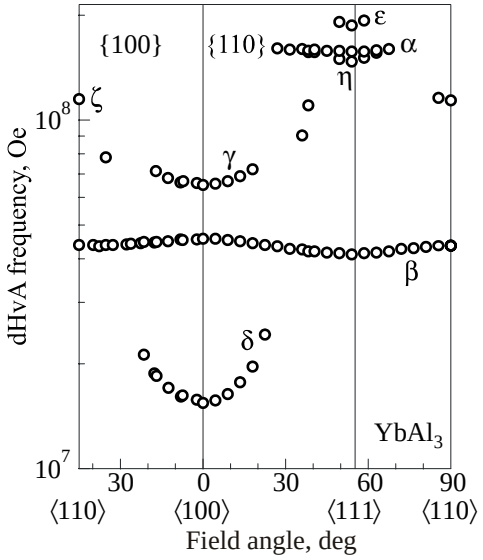

Fig. 19. Angular dependence of the dHvA frequency in $YbAl_3$ [56].

Branch ζ_i also corresponds to the band 6-electron Fermi surface. The cyclotron mass is light and is close to the corresponding band mass m_b, ranging from $1.1\,m_0$ in branch α to $0.22\,m_0$ in branch ζ_i.

Here we note the 4*f*-electron character in Yb compounds. The 4*f* electrons of $YbAl_3$ and $YbCu_2Si_2$, for example, possess the localized moment at high temperatures, with Yb^{3+} with an electron configuration of $[Xe]4f^{13}5d^16s^2$, where the $5d^16s^2$ electrons become the valence electrons. The Fermi surface is thus similar to that of a non-4*f* reference La compound or the corresponding Lu compound with an electron configuration of $[Xe]4f^{14}5d^16s^2$ (Lu^{3+}). The 4*f* electrons, however, become itinerant at low temperatures, via the many-body Kondo effect. The corresponding temperatures are $T_{\chi max}$ = 120 K in $YbAl_3$ and $T_{\chi max}$ = 40 K in $YbCu_2Si_2$, below which the magnetic susceptibility becomes approximately constant. The 4*f* electrons at temperatures lower than $T_{\chi max}$ contribute to the Fermi surface, and therefore the corresponding topology of the Fermi surface is highly different from the Fermi surface with the Yb^{3+} configuration. The 4*f*-itinerant Fermi surfaces of $YbAl_3$ and $YbCu_2Si_2$ are, however, very similar to the corresponding Yb^{2+} compounds, namely $YbIn_3$ and $YbCu_2Ge_2$, respectively. A careful comparison of the dHvA result with the result of energy band calculations is therefore necessary for a better understanding of the Fermi surface in $YbAl_3$ [56] and $YbCu_2Si_2$ [57].

Figure 19 shows the angular dependence of the dHvA frequency in $YbAl_3$ [56]. One of the six dHvA branches, named β with a dHvA frequency of $4.5\cdot10^7$ Oe, is nearly spherical in topology and has a large cyclotron mass of $24\,m_0$. The other branches are in the range $14–17\,m_0$. The topology of the Fermi surface cannot be explained by the conventional band calculations, as shown in Figs. 20,*a*,*b*, because the fully occupied 4*f*-levels in $YbAl_3$ are below the Fermi level in this band calculations. Note that the theoretical Fermi surface of $YbAl_3$ in Fig. 20,*b* is similar to that of $YbIn_3$ in Fig. 18.

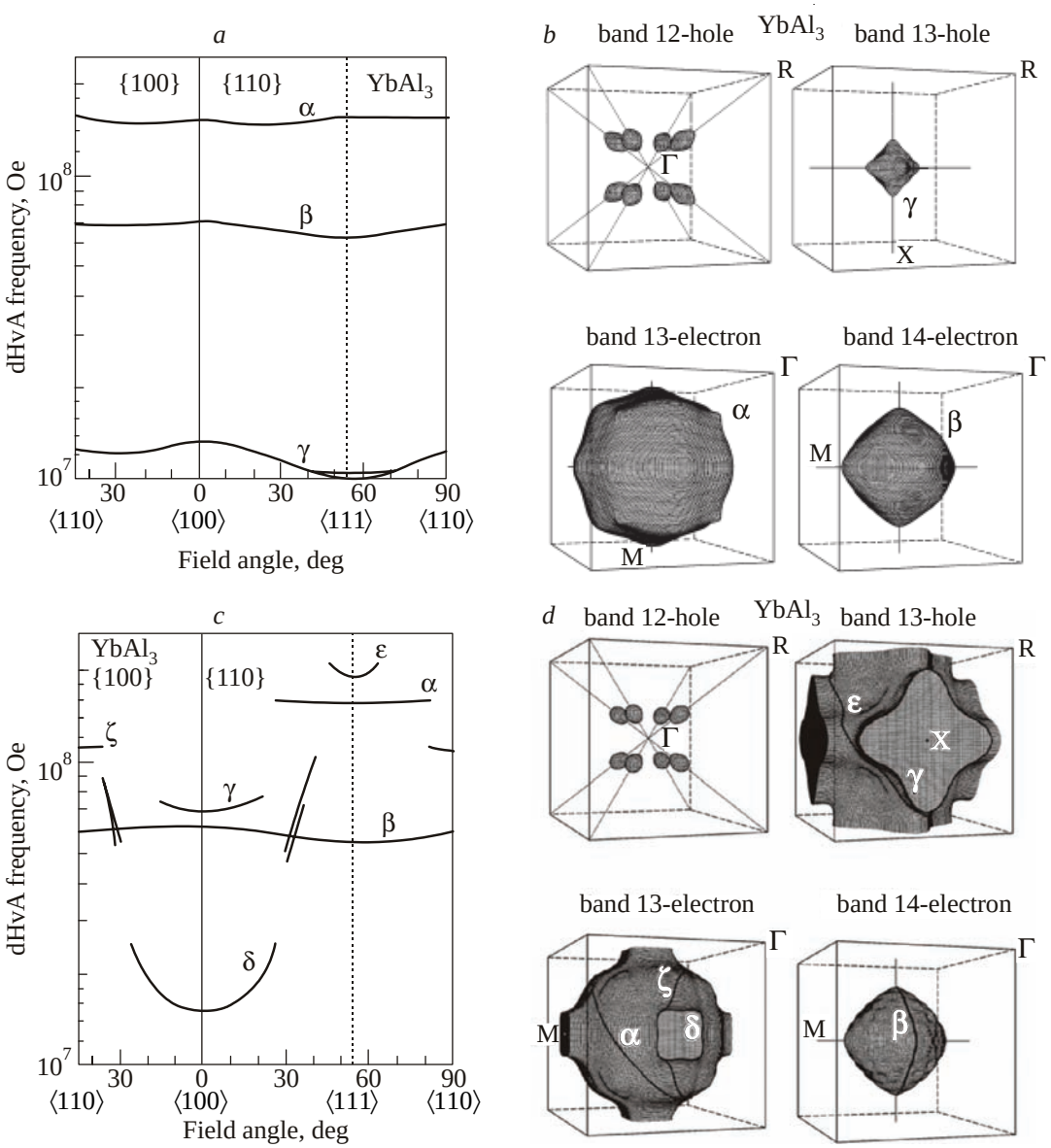

Fig. 20. Angular dependence of the dHvA frequency (*a*) and the corresponding Fermi surfaces based on the conventional band model (*b*); the angular dependence of the dHvA frequency (*c*) and the corresponding modified Fermi surfaces in $YbAl_3$ (*d*), cited from Ref. 56.

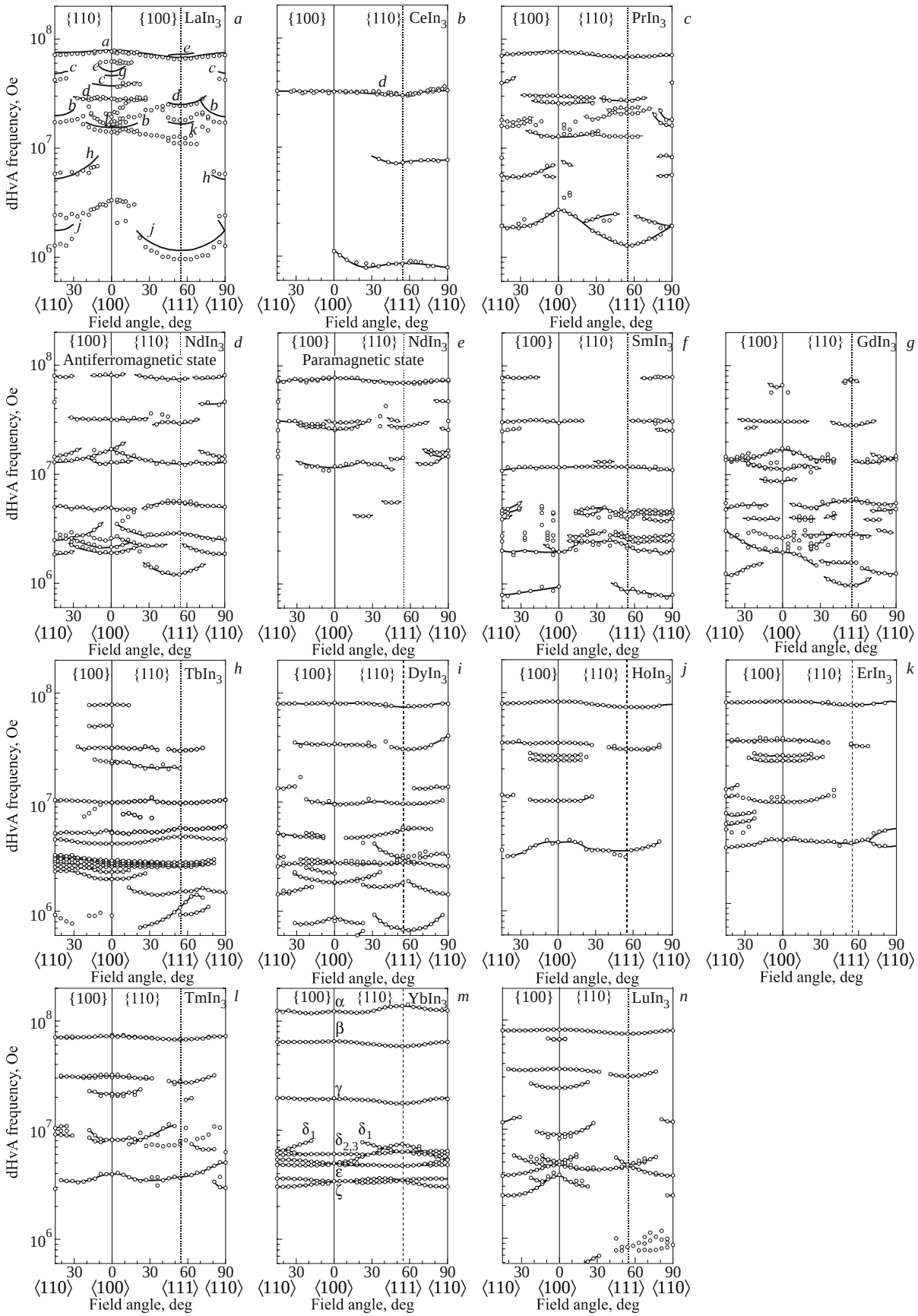

Fig. 21. Angular dependence of the dHvA frequency in RIn_3 (R = La [39], Ce [45], Pr [46], Nd [41], Sm [47], Gd [48], Tb, Dy, Ho, Er, Tm, Yb [49], and Lu [49]). Solid lines in $LaIn_3$ are the results of energy band calculations [40], while the other solid lines connecting the data are guide lines.

A small alteration so as to shift upward the 4*f*-levels by 200 mRy is therefore necessary to fit the experimental dHvA data. Thus obtained angular dependence of the dHvA frequency and Fermi surfaces are shown in Figs. 20,*c* and 20,*d*, respectively. A nearly spherical Fermi surface of branch α is changed into a multiply-connected Fermi surface whose arms are directed along the ⟨100⟩ direction, which is brought about by disappearance of the Fermi surface named γ in Fig. 20,*b*. Branches α, γ, *δ*, ε and ζ in Fig. 19 are well explained by this modified Fermi surface. Such shifting of the 4*f*-levels affects the Fermi surface because the 4*f* electrons directly contribute to the conduction electrons. This effect also plays an important role in the mass enhancement, which is caused by the many-body Kondo effect. The similar modification is necessary for $YbCu_2Si_2$ [57], as well as YbT_2Zn_{20} (T: Co, Rh, Ir) shown in Chap. 6.

We summarize in Fig. 21 and Table 5 the Fermi surface properties of RIn_3 (R: Y, La-Lu), $ScGa_3$ and $LuGa_3$. Main branches *a*, *d*, and *b* are observed in almost all of RIn_3. Almost the same Fermi surface properties are also observed in YIn_3, $ScGa_3$ and $LuGa_3$ [55] in Table 5.

The present results are summarized as follows. The magnetic energy gaps associated with the antiferromagnetic ordering are small enough and thus the electrons undergoing cyclotron motions can break through these energy gaps and circulate on orbits of the paramagnetic Fermi surface. The occurrence of this effect, however, becomes more difficult as the number of *f* electrons increases. In that case, the electrons follow the orbits on the antiferromagnetic Fermi surface, which was constructed in a small Brillouin zone based on the magnetic unit cell larger than the chemical unit cell in volume. The typical example is $NdIn_3$. The paramagnetic (or field-induced ferromagnetic) Fermi surface of $NdIn_3$ is almost the same as that of $LaIn_3$. A nearly spherical Fermi surface in the paramagnetic state, which corresponds to branch *a* of the band 7-electron Fermi surface of $LaIn_3$, is changed into a multiply-connected one with necks in the antiferromagnetic state.

On the other hand, if a Fermi surface is small and is located in the center of the Brillouin zone, it remains in the antiferromagnetic state because it is contained in the magnetic Brillouin zone. Branch *d* in $LaIn_3$ is observed in the magnetic RIn_3 compounds. Moreover, mass enhancement due to the electron–magnon interaction in magnetically ordered compounds is large compared with the one due to the electron–phone interaction. The mass enhancement factor in RIn_3 is in the range of 1–2. An exceptional case is $CeIn_3$. The mass enhancement is extremely large and anisotropic for the field direction in $CeIn_3$.

4. Fermi surface properties in RX_3 and AnX_3

The cubic RX_3 (X: Al, Ga, In, Si, Ge, Sn, Pb) and AnX_3 (An: actinide) compounds are classified in Table 6 according to the number of valence electrons, *n*, from *n* = 11 in a divalent Yb^{2+} compound $YbIn_3$ to *n* = 19 in a 5*f* relevant paramagnet $NpGe_3$, passing through a non-4*f* reference compound $LaIn_3$ ($LuIn_3$), a Kondo-lattice compound with antiferromagnetic ordering $CeIn_3$, $CeIn_3$ under pressure, a non-5*f* reference compound $ThIn_3$, a divalent Yb^{2+} compounds $YbSn_3$ and $YbPb_3$, non-4*f* reference compounds $LaSn_3$ and $LaPb_3$, an antiferroquadrupolar compound $PrPb_3$, a heavy fermion compound UAl_3, antiferromagnets UGa_3 and UIn_3, a 4*f*-itinerant compound $CeSn_3$, an antiferromagnet $NpIn_3$ which is close to $LaIn_3$ in topology of the Fermi surface and is classified in the compounds with *n* = 12, a paramagnet $PuIn_3$, Pauli paramagnets USi_3 and UGe_3, a spin-fluctuation compound USn_3, and a paramagnet $NpGe_3$ [58–71].

Table 6. Numbers of valence electrons and Fermi surface studies in the RX_3 and AnX_3 compounds with the $AuCu_3$-type cubic crystal structure

Number of valence electrons	Compounds	Refs.
11	$YbIn_3$ (P)	[49]
	$YbAl_3$ (P)	[56]
12	$LaIn_3$ (P)	[39]
	$LuIn_3$ (P)	[49]
	$NdIn_3$ (AF)	[41,42]
	$CeIn_3$ (AF)	[45]
	$NpIn_3$ (AF)	[58]
13	$CeIn_3$ under pressure (P, S)	[38]
	$ThIn_3$ (P)	[59]
14	$YbSn_3$ (P)	[60]
	$YbPb_3$ (P)	[61]
15	$LaSn_3$ (P)	[62]
	$LaPb_3$ (P)	[63]
	$PrPb_3$ (Q)	[63]
	UAl_3 (P)	[64]
	UGa_3 (AF)	[65]
	UIn_3 (AF)	[66]
16	$CeSn_3$ (P)	[67]
17	$PuIn_3$ (P)	[68]
18	USi_3 (P)	[69]
	UGe_3 (P)	[70]
	USn_3 (P)	
19	$NpGe_3$ (P)	[71]

The compounds with the number of valence electrons, *n* = 11 and 12 are explained in Chap. 3. The Fermi surface properties of $CeIn_3$ under pressure and $ThIn_3$ will be explained in Chap. 7. We will start from the compounds with the number of valence electrons, *n* = 14, namely Pauli paramagnets $YbSn_3$ and $YbPb_3$ because Yb is divalent and the valence electrons in Sn and Yb are $5s^25p^2$ and $6s^2$, respectively [60,61]. Figure 22 indicates the angular dependence of the dHvA frequency in $YbPb_3$. The detected three branches named α, ε and φ are explained by the result of energy band calculation of which the Fermi surface is shown in Fig. 23. Here, the Fermi surface consists of a band 7-hole Fermi surface named α and band 8-electron Fermi surfaces named ε and φ, indicating a compensated metal as in $LaIn_3$ (*n* = 12) [39]. The similar dHvA data and

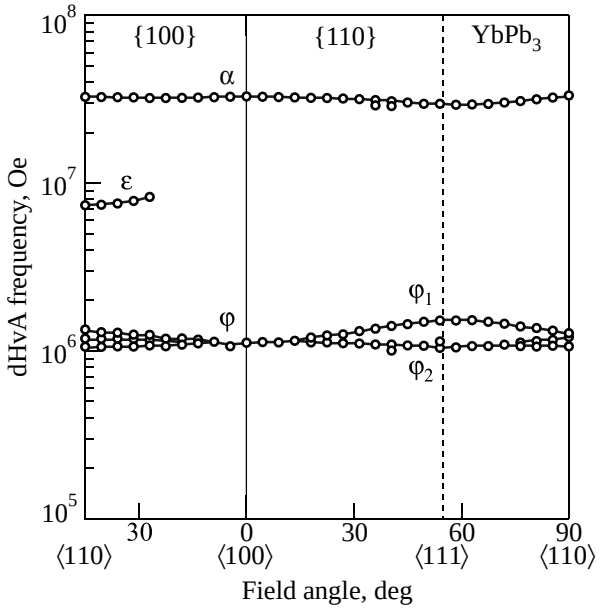

Fig. 22. Angular dependence of the dHvA frequency in a Pauli paramagnet $YbPb_3$, cited from Ref. 61.

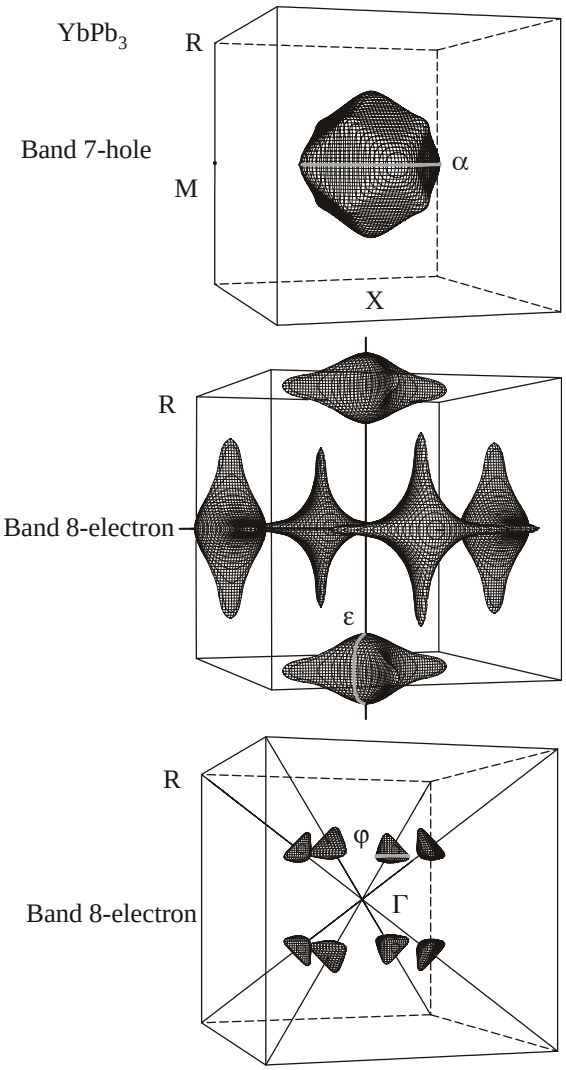

Fig. 23. Fermi surfaces in a Pauli paramagnet $YbPb_3$, cited from Ref. 61.

the corresponding Fermi surfaces are obtained in $YbSn_3$ [60].

Next we show in Fig. 24,*a* the angular dependence of the dHvA frequency in $LaSn_3$ [62]. Main characteristic dHvA branches are as follows. Two branches named α and β exist in the whole range of angles, revealing two nearly spherical Fermi surfaces, three branches named γ_1, γ_2 and γ_3 are centered at ⟨111⟩, and branch δ is centered at ⟨110⟩.

Compared with $LaIn_3$, $LaSn_3$ has three electrons more per primitive cell, and hence the electronic structure of $LaSn_3$ is that of an uncompensated metal. All the sheets of the Fermi surface in $LaIn_3$ disappear in $LaSn_3$. In $LaSn_3$,

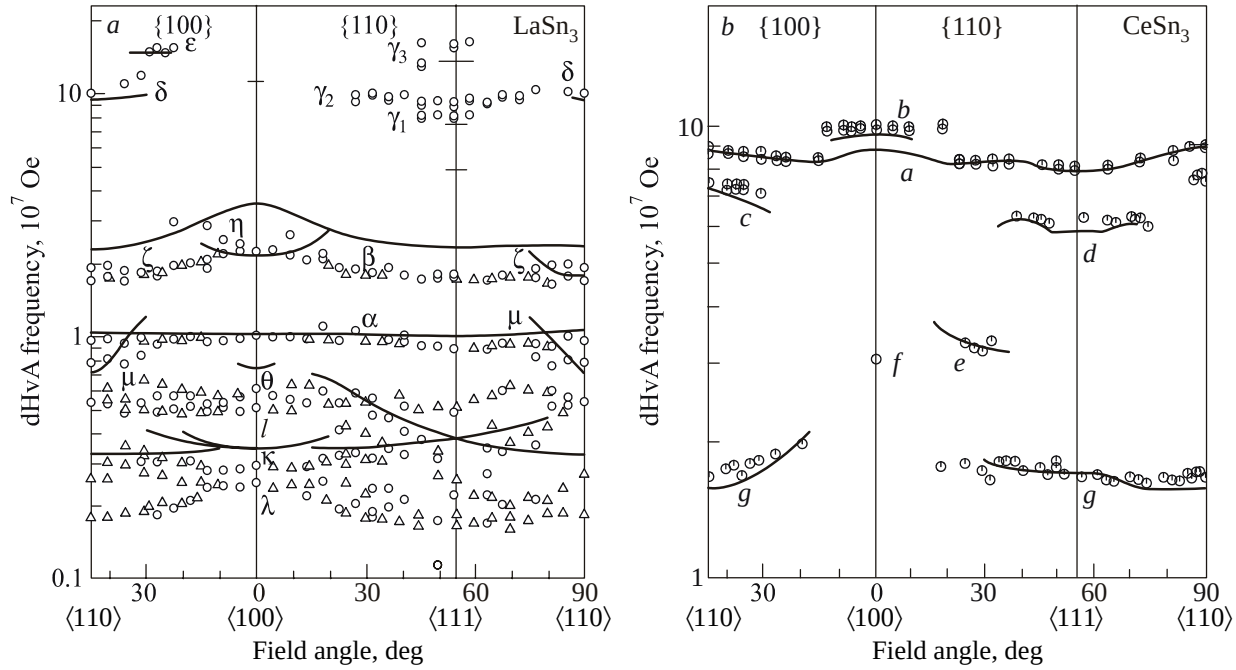

Fig. 24. Angular dependence of the dHvA frequency in a non-4*f* reference compound $LaSn_3$ (*a*) and a 4*f*-itinerant $CeSn_3$ (*b*), cited from Refs. 62, 67, 72, 73. Solid lines are the results of energy band calculation.

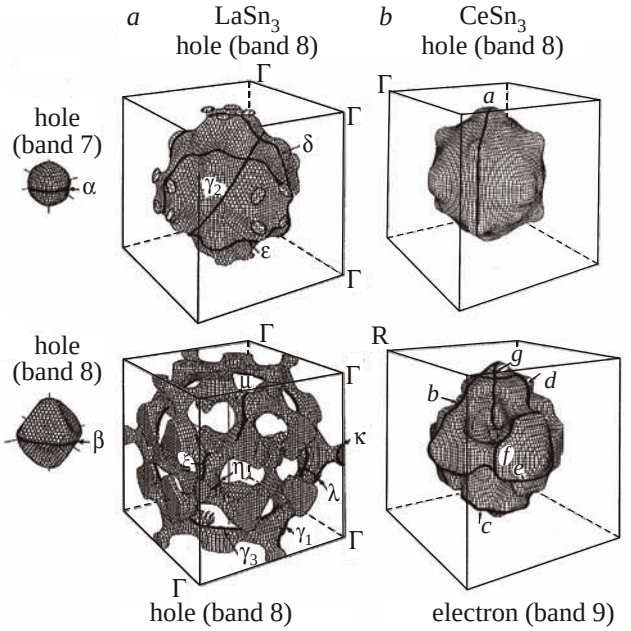

Fig. 25. Fermi surface of $LaSn_3$ (*a*) and $CeSn_3$ (*b*), cited from Refs. 72, 73.

band 8 yields a main Fermi surface centered at R, and two small hole closed Fermi surfaces exist at Γ in bands 7 and 8, as shown in Fig. 25,*a*. The solid lines in Fig. 24,*a* are the result of energy band calculation [72]. The detected dHvA branches are well explained on the basis of the Fermi surface in Fig. 25,*a*.

$CeSn_3$ at low temperatures is a so-called valence-fluctuation compound with a Kondo temperature of about 150 K where the magnetic susceptibility possesses a maximum at about 150 K, as shown in Fig. 2. It is interesting to understand the 4*f*-electron character in comparison with the antiferromagnetic Kondo compound $CeIn_3$. Figure 24,*b* shows the angular dependence of the dHvA frequency in $CeSn_3$ [67]. Some dHvA branches are similar to those of $LaSn_3$ but the other branches are considerably different from those of $LaSn_3$. The detected cyclotron masses are roughly five times larger than those of $LaSn_3$: $4.2\,m_0$ for branch *a* in $CeSn_3$ and $0.91\,m_0$ for branch γ_2 in $LaSn_3$, in agreement with γ values: 53 mJ/(K^2·mol) in $CeSn_3$ and 11 mJ/(K^2·mol)in $LaSn_3$.

The energy band calculation was carried out under the assumption that the 4*f* electron is itinerant [73]. The calculated Fermi surfaces mainly consist of a large band 8-hole Fermi surface centered at R and a large band 9-electron Fermi surface centered at Γ. The origin of the analogy in Fermi surfaces between $CeSn_3$ and $LaSn_3$ is as follows. Namely, the large distorted spherical band 8-hole Fermi surface in $LaSn_3$ is similar to the band 8-hole Fermi surface in $CeSn_3$. Small nearly spherical hole Fermi surfaces in bands 7 and 8, denoted by α and β in $LaSn_3$, are also present in $CeSn_3$, not shown in Fig. 24,*b* and Fig. 25,*b*, although their volumes of the Fermi surfaces in $CeSn_3$ are smaller than those of $LaSn_3$. The marked difference between $LaSn_3$ and $CeSn_3$ is ascribed to a large band 9-electron Fermi surface in $CeSn_3$. Note that this Fermi surface has no occupied states along ⟨111⟩.

The solid lines in Fig. 24,*b* indicate the result of the 4*f*-itinerant energy band calculation [73]. Branch *a* corresponds to the large hole-Fermi surface, while the other main branches are due to the electron Fermi surface, indicating a compensated metal. Both in the magnitude of the cross-sectional area and in the observed range of field angle, the 4*f*-itinerant band model agrees reasonably well with the experimental results. The reason for the disappearance of branch *a* at angles in the vicinity of the ⟨100⟩ direction is due to the combined effect of a curvature factor and a relatively large cyclotron mass.

We will go on to the next compound n = 15, $LaPb_3$ [63]. $LaPb_3$ should be very similar to $LaSn_3$, with n = 15,

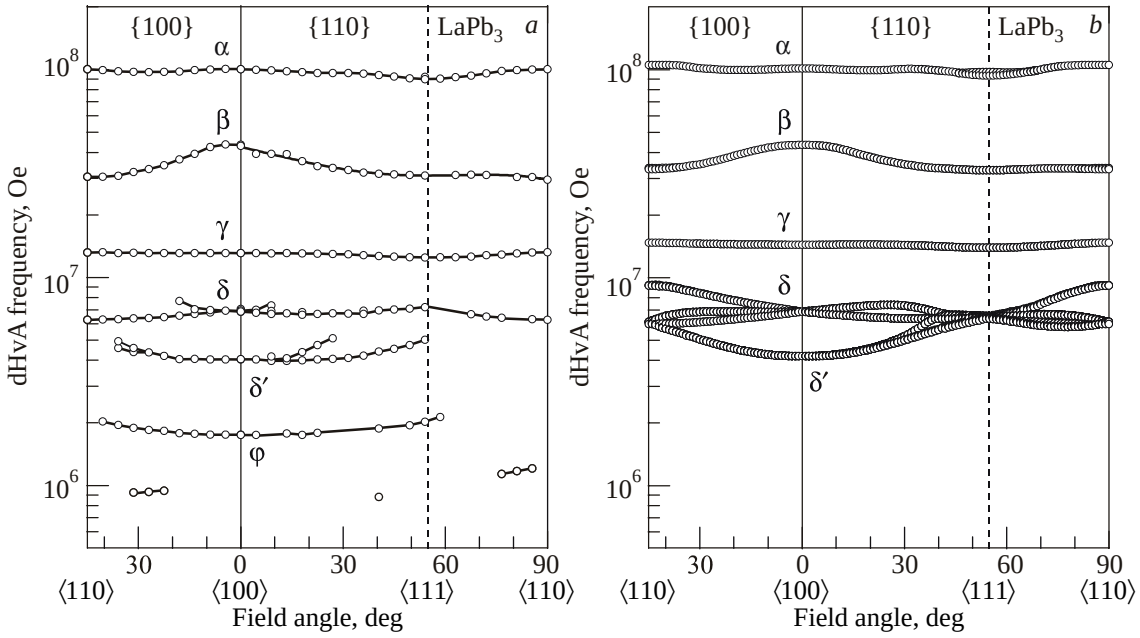

Fig. 26. Angle dependence of the dHvA frequency in $LaPb_3$ (*a*) and the theoretical one (*b*), cited from Ref. 63.

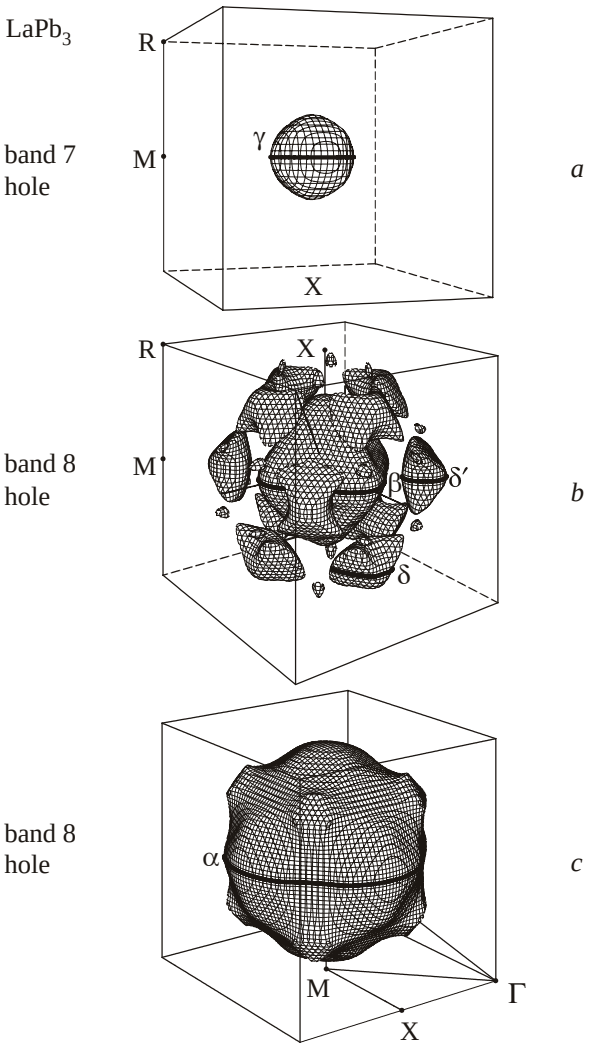

Fig. 27. Fermi surfaces in $LaPb_3$, cited from Ref. 63.

although the Fermi surface of $LaPb_3$ is slightly different and simple compared with that of $LaSn_3$. It is, however, noted that branches γ_2, δ, β, and α in $LaSn_3$, shown in Fig. 24,*a*, correspond to branches α, β, and γ in $LaPb_3$, respectively, as shown in Fig. 26,*a*. Figures 26,*a* and 26,*b* show the angular dependence of the dHvA frequency and the result of energy band calculations, respectively, in $LaPb_3$. Main three branches named α, β, and γ are closed Fermi surfaces, which are well explained by the energy band calculations of which the Fermi surfaces are shown in Fig. 27.

The angular dependence of the dHvA frequency in an antiferroquadrupolar compound $PrPb_3$ with T_Q = 0.4 K is approximately the same as that in $LaPb_3$ [63]. It is interesting that the cyclotron mass of $PrPb_3$ is strongly enhanced below 0.7 K, as shown in Fig. 28: $1.6\,m_0$ at 1.3 K and $4.0\,m_0$ at 0.18 K for branch γ. The corresponding cyclotron mass is $0.38\,m_0$ in $LaPb_3$ and $0.94\,m_0$ in an antiferromagnet $NdPb_3$. The mass enhancement in $PrPb_3$ might be ascribed to the quadrupolar ordering.

We will go on to another compounds with the number of valence electrons, n = 15, namely UAl_3, where the valence electrons are [Rn] $5f^3 6d^1 7s^2$ in the U atom and $3s^2 3p^1$ in the Al atom. The topology of the Fermi surface in UAl_3 should be similar to that in $LaPb_3$, although the 5*f* contribution to the Fermi surface in UAl_3 might change the topology of the Fermi surface and also the mass enhancement. UAl_3 does not order magnetically, and the magnetic susceptibility possesses a broad maximum around $T_{\chi\max} \simeq$ $\simeq$ 140 K, as shown in Fig. 29. At higher temperatures up to 800 K, not shown in Fig. 29, the susceptibility follows the Curie–Weiss law [74]. The obtained effective magnetic moment $\mu_{\rm eff}$ = 3.6 μ_B/U is close to 3.62 (3.58) μ_B/U in the 5*f*-localized $5f^3$ ($5f^2$) configuration. This is a reason why UAl_3 is characterized as a spin-fluctuating compound. The crossover from 5*f*-localized to 5*f*-itinerant is supposed to

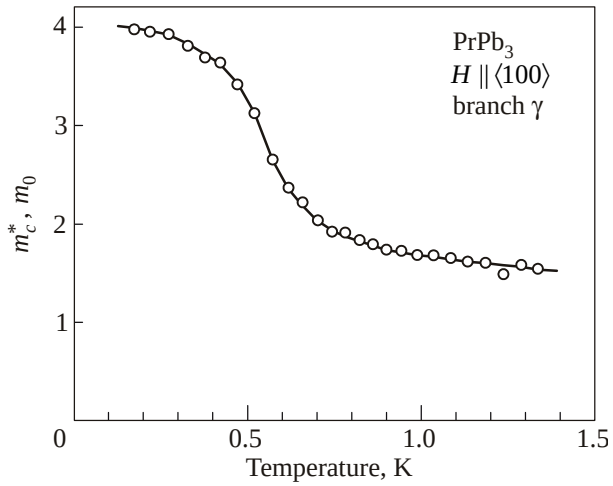

Fig. 28. Temperature dependence of the cyclotron mass in $PrPb_3$, cited from Ref. 63.

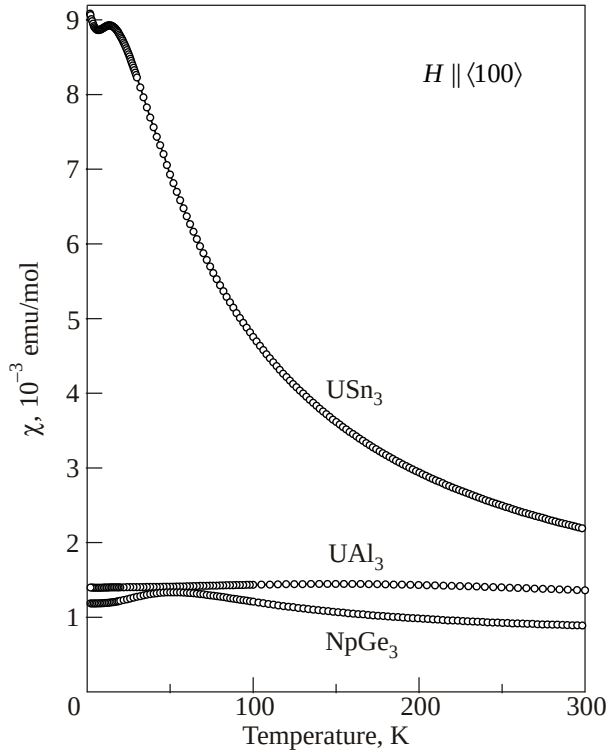

Fig. 29. Temperature dependence of the magnetic susceptibility in USn_3, UAl_3 and $NpGe_3$, cited from Ref. 74.

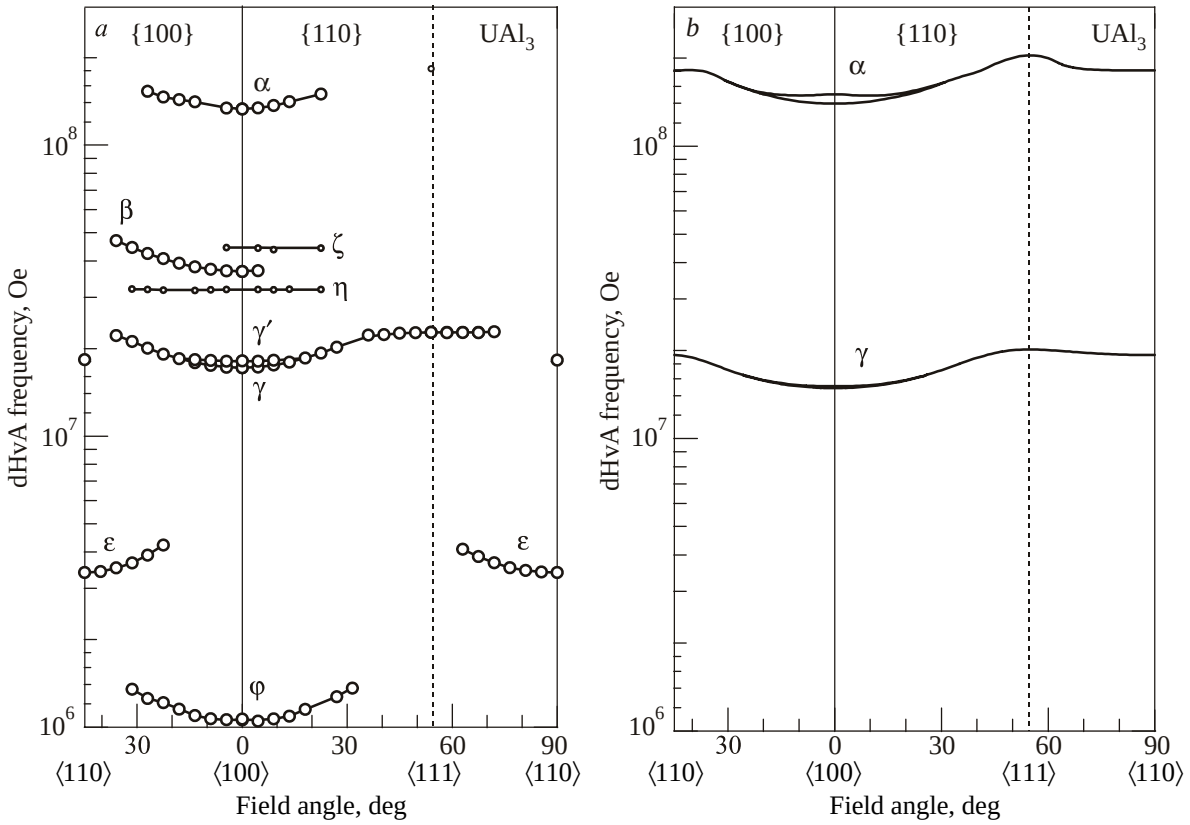

Fig. 30. Angular dependence of the dHvA frequency in a heavy fermion compound UAl_3 (*a*) and the theoretical one (*b*), cited from Ref. 64.

occur below $T_{\chi\max} \simeq 140$ K. It is thus important to clarify the 5*f*-electron character from the dHvA experiment and energy band calculation. Here it is noted that the valence-fluctuating compound mentioned for $CeSn_3$ corresponds to the spin-fluctuating compound. The former was named for Ce and Yb compounds with a relatively large T_K value, say, T_K = 50–150 K, while the latter for the similar U compounds. Both compounds become the enhanced Pauli paramagnets at low temperatures.

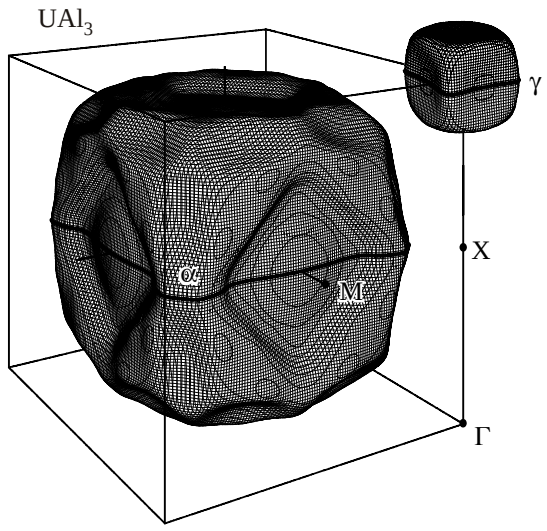

Fig. 31. Theoretical 5*f*-itinerant band 8-hole Fermi surfaces in UAl_3, cited from Ref. 64.

Figures 30,*a* and 30,*b* show the angular dependence of the dHvA frequency and the theoretical one based on the 5*f*-itinerant band model, respectively for UAl_3 [64]. Among the detected several branches, two main branches named α and γ are well explained by the theoretical closed band 8-hole Fermi surfaces, as shown in Fig. 31.

One large Fermi surface is nearly cubic, centered at Γ, and the other small Fermi surface is also nearly cubic, centered at R. The detected cyclotron mass is relatively large, ranging from 3 to 17 m_0, which is twice to three times larger than the corresponding band mass: $m_c^* = 17\,m_0$ and $m_b = 6\,m_0$ for branch α for $H \parallel \langle 100\rangle$, and $\gamma = 47$ mJ/(K^2·mol) and the theoretical value $\gamma_b = 14.8$ mJ/(K^2·mol).

UGa_3 and UIn_3 are the compounds with n = 15, similar to UAl_3. Both compounds, however, order antiferromagnetically below T_N = 67 and 90 K, respectively. UGa_3 was studied on the basis of the 5*f*-itinerant antiferromagnet [75], but the detected dHvA branches in UGa_3 are not explained by the spin-polarized 5*f*-itinerant band model, which is most likely due to the magnetic structure, not definitely determined yet in experiments. Here we show in Figs. 32 and 33 the angular dependence of the dHvA frequency in UGa_3 [65] and UIn_3 [66], respectively.

The compound with the number of electrons, n = 17, corresponds to $PuIn_3$, as shown in Table 6. It is, however, better to present the corresponding Fermi surface property as a final compound in RX_3 and AnX_3. We will go on to USi_3 with n = 18. USi_3 is a Pauli paramagnet with a small

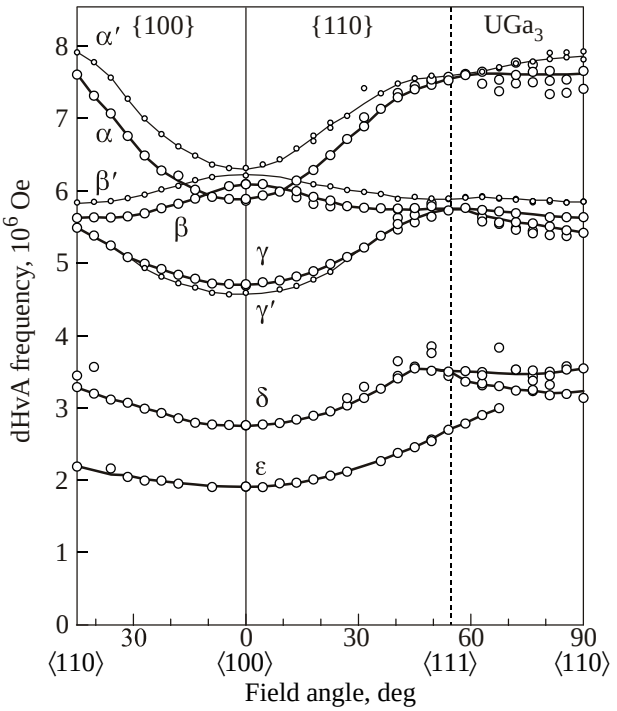

Fig. 32. Angular dependence of the dHvA frequency in an antiferromagnet UGa_3, cited from Ref. 65.

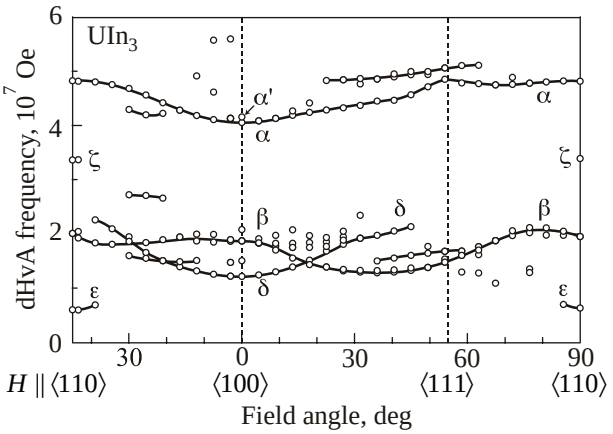

Fig. 33. Angular dependence of the dHvA frequency in an antiferromagnet UIn_3, cited from Ref. 66.

γ value of 11.9 mJ/(K^2·mol). Figures 34,*a* and 34,*b* show the angular dependence of the dHvA frequency and the corresponding theoretical one based on the 5*f*-itinerant band model, respectively [69]. Fifteen dHvA branches are observed, ranging from $7.37\cdot10^6$ to $2.33\cdot10^8$ Oe, which are in good agreement with the theoretical ones based on the 5*f*-itinerant Fermi surfaces shown in Fig. 35. Theoretically, the 5*f* electrons form wide bands across the Fermi energy, which hybridize considerably with Si-3*p* electrons. The *p*–*f* hybridization makes the dispersion of the 5*f*-bands very large. Cyclotron masses, which are in the range from 0.39 to 4.17 m_0, are thus approximately the same as the corresponding band masses, being in good agreement with a relation between the γ value of 11.9 mJ/(K^2·mol) and γ_b = = 11.7 mJ/(K^2·mol). The mass enhancement is thus extremely small in USi_3.

A small mass enhancement is observed in UGe_3 with γ = 20 mJ/(K^2·mol), with the same topology of the Fermi surface as in USi_3, from the dHvA experiment and energy

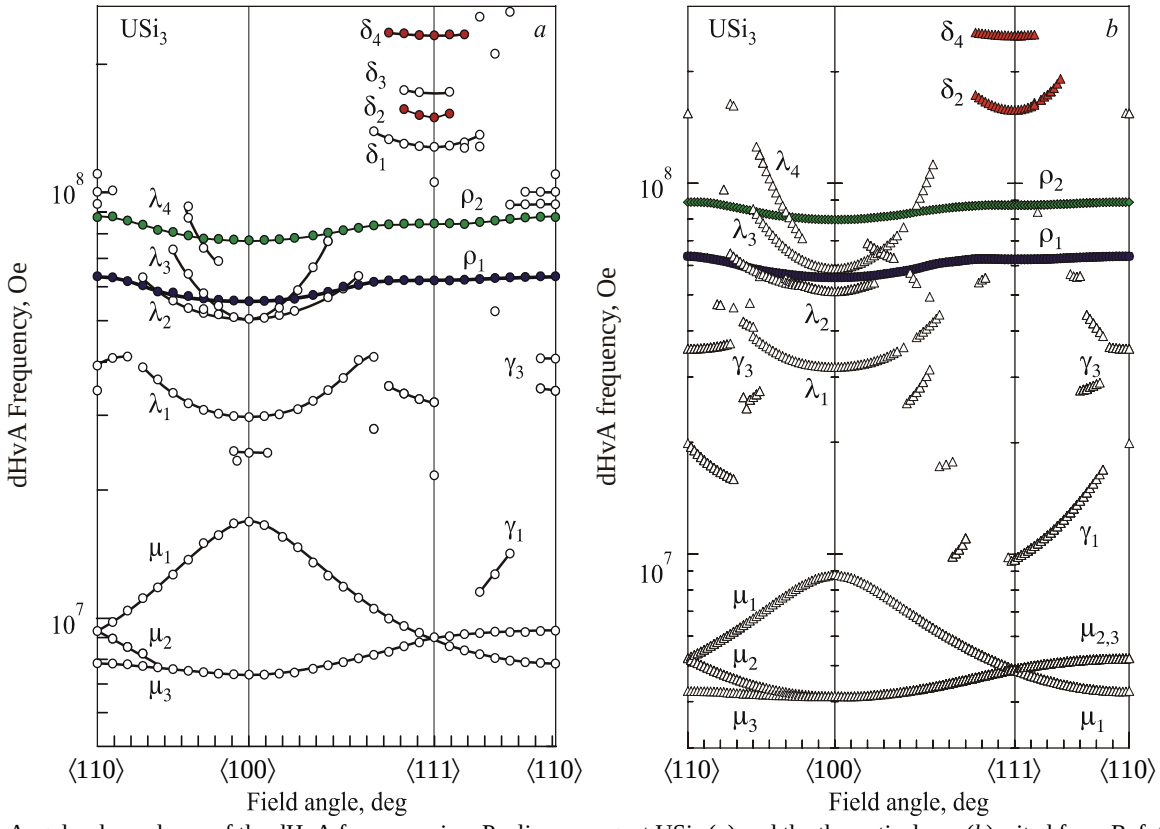

Fig. 34. Angular dependence of the dHvA frequency in a Pauli paramagnet USi_3 (*a*) and the theoretical one (*b*), cited from Ref. 69.

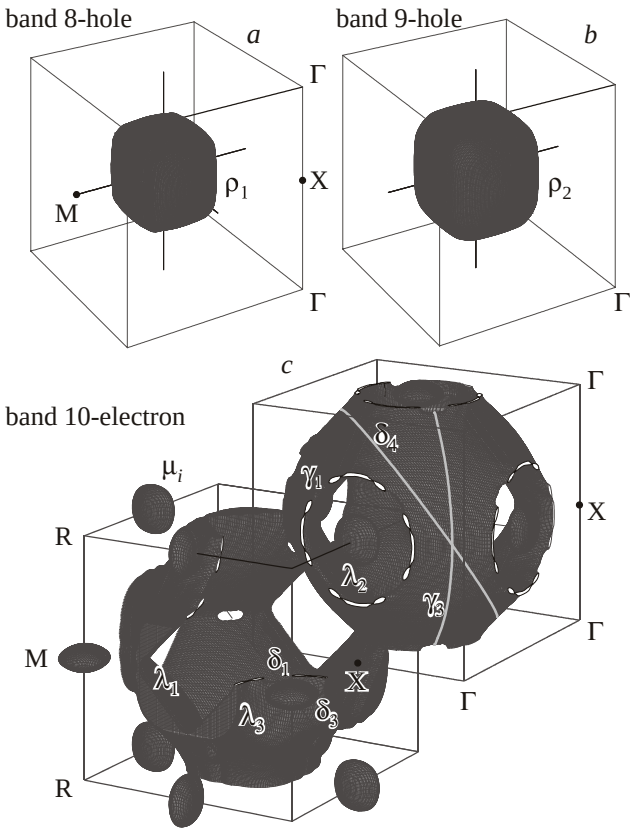

Fig. 35. Theoretical 5*f*-itinerant Fermi surfaces in USi_3, cited from Ref. 69.

band calculation [70], while a relatively large mass enhancement is expected in a spin-fluctuating compound USn_3 with $\gamma = 170$ mJ/(K^2·mol), as shown in Fig. 1,*b*. Here, the Doniach phase diagram in Fig. 1,*a* is expressed by a relation of the distance between the U atoms, a vs the γ value. Correspondingly, the low-temperature magnetic susceptibility is large, as shown in Fig. 29.

Figure 36 shows the angular dependence of the dHvA frequency in USn_3. Only branches μ_i are observed. The cyclotron mass of branches $\mu_{2,3}$ for $H \parallel \langle 100 \rangle$ is $1.5\,m_0$ in USn_3, which is large compared with $0.40\,m_0$ in USi_3 and $0.42\,m_0$ in UGe_3.

The next compound is $NpGe_3$ with $n = 19$ [71]. This is an enhanced Pauli paramagnet, similar to UAl_3. The magnetic susceptibility has a maximum around 50 K, as shown in Fig. 29. From the susceptibility data above 250 K, the estimated effective magnetic moment is $\mu_{eff} = 2.78\ \mu_B$/Np, which is close to $\mu_{eff} = 2.68\ \mu_B$/Np in Np^{3+} ($5f^4$), but is smaller than $\mu_{eff} = 3.62\ \mu_B$/Np in Np^{4+} ($5f^3$). The present result of the magnetic susceptibility suggests that the Np ion possesses a local moment at high temperatures, but the electronic state is changed into the enhanced Pauli paramagnet at temperatures lower than 50 K.

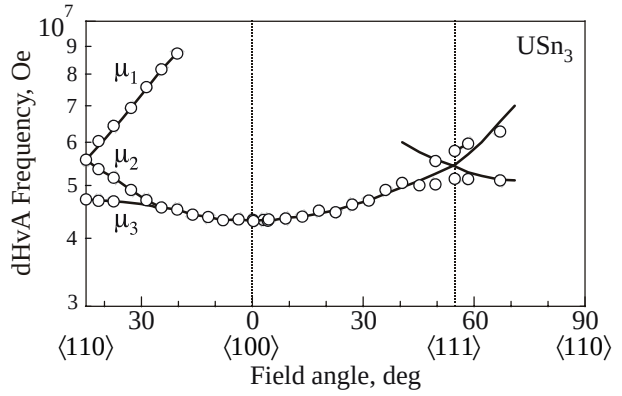

Fig. 36. Angular dependence of the dHvA frequency in a spin-fluctuation compound USn_3.

Figures 37,*a* and 37,*b* show the angular dependence of the dHvA frequency and the corresponding one based on the 5*f*-itinerant Fermi surfaces shown in Fig. 38, being in good agreement between experiment and theory [71]. The band 10-electron Fermi surface in USi_3 (UGe_3), shown in Fig. 35,*c*, is spherical, but possesses a hollow space at the center and a window for $\langle 100 \rangle$, with a flat closed Fermi surface at the M point. One more 5*f* electron becomes a valence electron in $NpGe_3$. This means that the hole bands (8 and 9) are occupied completely by the electron and also the band 10-electron Fermi surface, centered at R, is partially occupied by the remaining electron, producing a hollow ball with a "belly" orbit and a "neck", as shown in

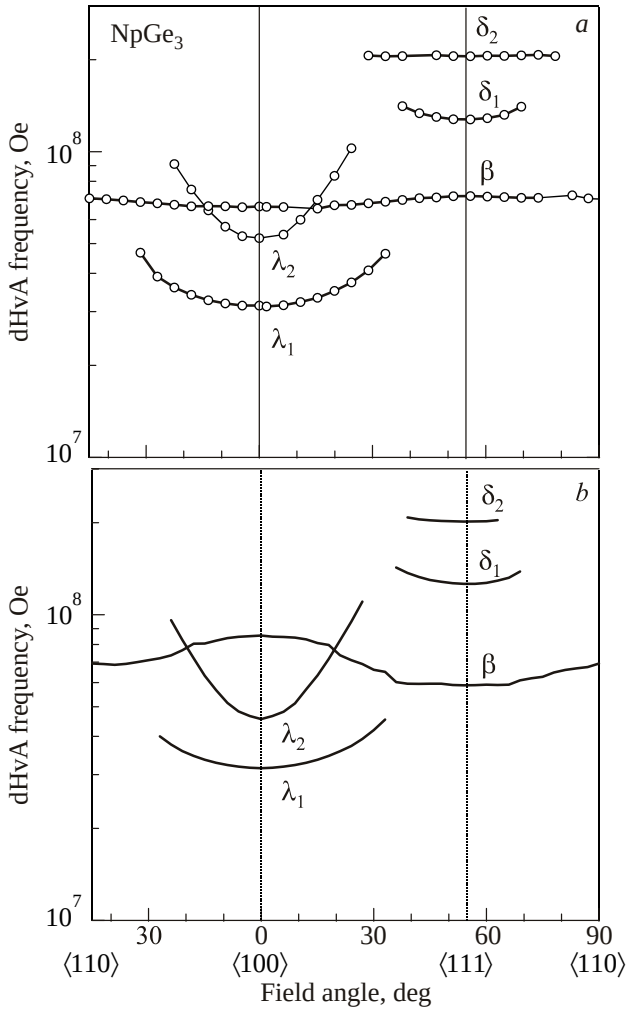

Fig. 37. Angular dependence of the dHvA frequency in a heavy fermion compound $NpGe_3$ (*a*) and the theoretical one (*b*), cited from Ref. 71.

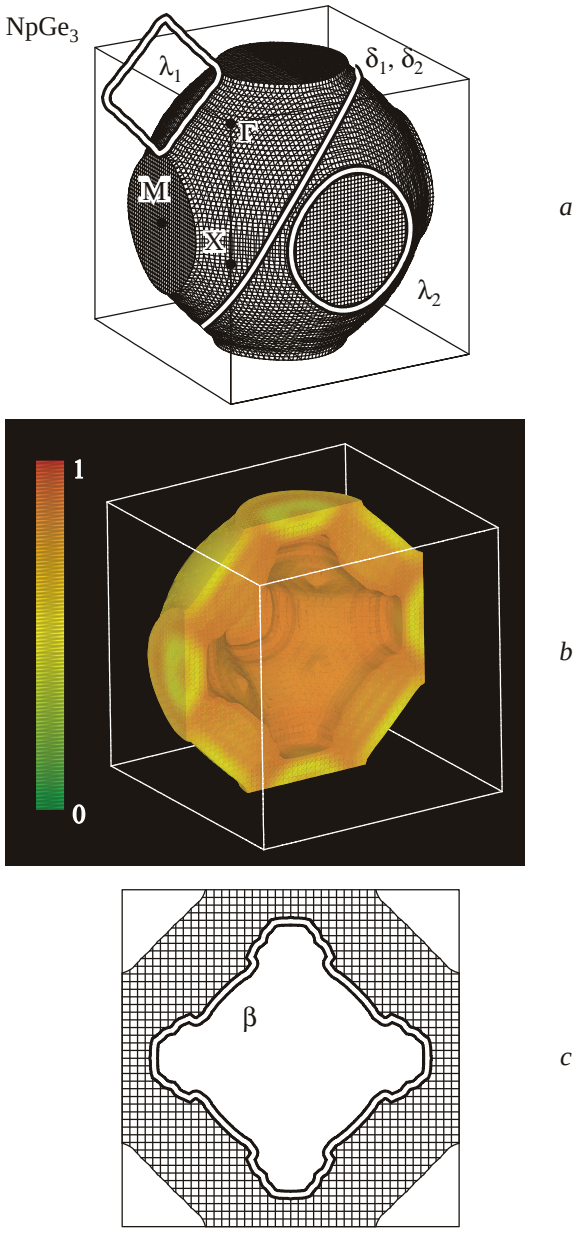

Fig. 38. (Color online) Theoretical 5*f*-itinerant Fermi surfaces and cross-sections in $NpGe_3$. The color presents the contribution of 5*f*-electrons, cited from Ref. 71.

Fig. 38. The cyclotron mass is in the range of 2.6 to 16 m_0, which is enhanced approximately 3.5 times from the corresponding band mass. This is in fairly good agreement with the ratio of $\gamma = 34$ mJ/(K^2·mol) to the theoretical one $\gamma_b = 16.8$ mJ/(K^2·mol), $\gamma/\gamma_b = 2.0$. It is noted that the cyclotron mass and the corresponding band mass for an outer "belly" orbit δ_2 are $m_c^* = 4.7\,m_0$ and $m_b = 1.35\,m_0$, respectively, which are compared with $m_c^* = 15\,m_0$ and $m_b = 4.03\,m_0$ for an inner orbit β. This is because the inner part of the band 10-electron Fermi surface is mainly due to the contribution of 5*f* electrons in Np, while the outer part is due to the 4*p* component of Ge.

Next we discuss the electronic state of a complicated magnetic compound $NpIn_3$ [58]. Ferromagnetic and antiferromagnetic orderings occur at $T_C = 14$ K and $T_N = 10$ K, respectively, together with another transition at $T^* = 8$ K. When the magnetic field is applied to the sample, the antiferromagnetic state is finally changed into a ferromagnetic state with two metamagnetic transitions at H_{c1} and H_{c2}. The antiferromagnetic ordering and two metamagnetic transitions are found to be of the first-order phase transition. We show in Fig. 39 the magnetic phase diagram for three principal directions [58]. All the dHvA signals are detected in the ferromagnetic state, namely above H_{c2}.

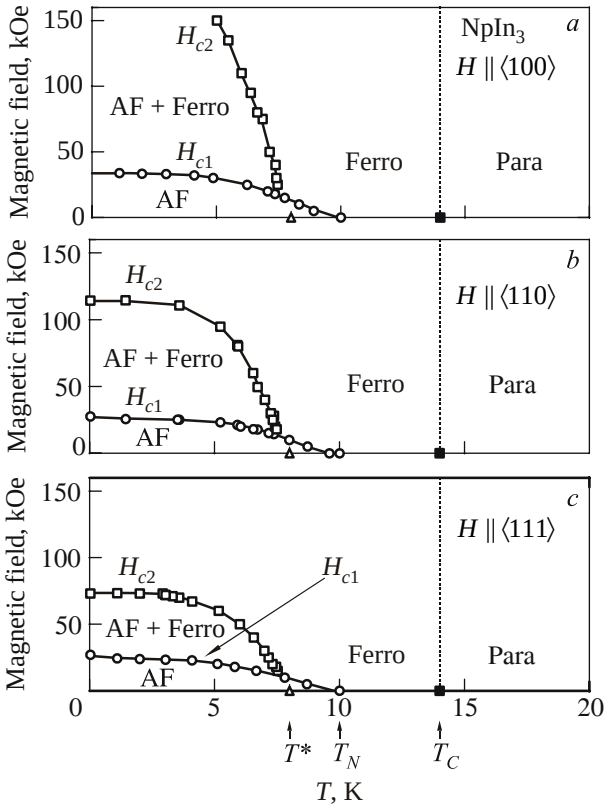

Fig. 39. Magnetic phase diagram in an antiferromagnet $NpIn_3$, cited from Ref. 58.

Figure 40 shows the angular dependence of the dHvA frequency [58]. Since the ferromagnetic state is not realized at the highest magnetic field of 150 kOe for the magnetic field around the ⟨100⟩ direction, as shown in Fig. 39, no dHvA signals are observed around ⟨100⟩. They should be observed in magnetic fields higher than $H_{c2} \simeq 200$ kOe for $H \parallel \langle 100 \rangle$. Three dHvA branches named α, β and γ are observed. Branches α and β correspond to nearly spherical Fermi surfaces. The dHvA frequency of branch γ increases with increasing the field angle from ⟨100⟩ to ⟨110⟩ or ⟨111⟩. At 31° (to ⟨110⟩ and 36° (to ⟨111⟩), branch γ abruptly disappears, suggesting the open orbit, which is most likely due to a multiply-connected Fermi surface.

From the present dHvA results, we constructed the Fermi surface of $NpIn_3$ with $n = 16$. Two cases can be considered. The one is the case based on the 5*f*-itinerant picture. Another is the case based on the 5*f*-localized picture. In the case of 5*f*-itinerant picture, the total number of va-

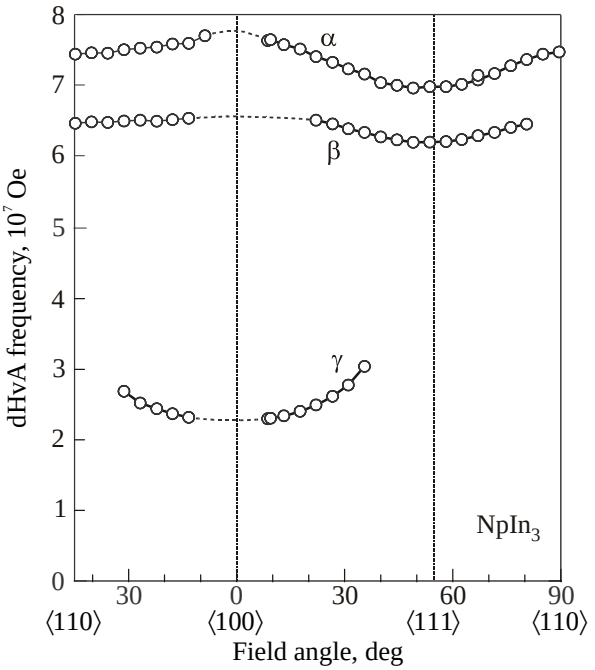

Fig. 40. Angular dependence of the dHvA frequency in an antiferromagnet $NpIn_3$, cited from Ref. 58.

lence electrons in $NpIn_3$ is even, namely 16, where the electronic configurations are Np ($5f^4 6d^1 7s^2$) and In ($5s^2 5p^1$). This means that $NpIn_3$ is a compensated metal with equal carrier numbers of electrons and holes.

In the case of 5*f*-localized picture, the Np^{3+} ($5f^4$) configuration might be applicable to $NpIn_3$, because the magnetic effective moment is close to the value for the Np^{3+} free ion. Moreover, the Mössbauer measurement indicates the Np^{3+} valence state from the isomer shift [76]. In this case, the total number of valence electrons is 12, which is also even in number, meaning that $NpIn_3$ is a compensated metal.

Both 5*f*-itinerant and localized pictures deduce $NpIn_3$ as a compensated metal. Thus we restrict ourselves to a compensated metal of $NpIn_3$ in order to construct the Fermi surface from the present dHvA results on the basis of the 5*f*-localized Np^{3+} ($5f^4$) configuration. We note that the Brillouin zone in the ferromagnetic state is the same as that in the paramagnetic state. Thus it is possible to treat $NpIn_3$ as a compensated metal in the same way as in the paramagnetic state.

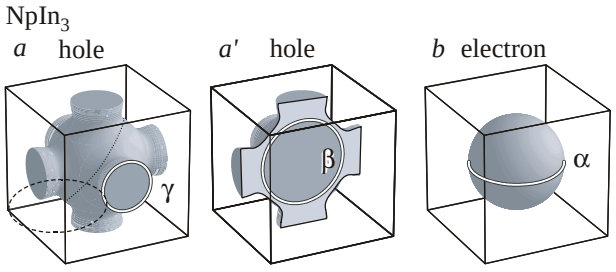

Fig. 41. Proposed Fermi surfaces in the field-induced ferromagnetic state of $NpIn_3$, cited from Ref. 58.

On the basis of the 5*f*-localized Np^{3+} ($5f^4$) configuration and the Fermi surface of $LaIn_3$, we constructed the Fermi surface in the ferromagnetic state of $NpIn_3$, as shown in Fig. 41. Characteristic features of the Fermi surface properties in $NpIn_3$ are as follows. A spherical Fermi surface with a relatively small cyclotron mass of $4m_0$ in $NpIn_3$ corresponds to a spherical electron Fermi surface in $LaIn_3$. A complicated hole-Fermi surface in $LaIn_3$ is simply modified to a multiply-connected Fermi surface with arms along ⟨100⟩ and vacant space at the center in $NpIn_3$, whose cyclotron masses are large: about $6m_0$ for the arm and 12–14 m_0 for a spherical Fermi surface (vacant space).

Finally we present the dHvA experiment for a paramagnet $PuIn_3$ with $n = 17$, where the valence electrons are $5f^5 6d^1 7s^2$ in the Pu atom and $5s^2 5p^1$ in the In atom [68]. As noted above, the Wigner–Seitz radius of Pu is an intermediate value between Np with the 5*f*-itinerant and/or 5*f*-localized nature and Am with the 5*f*-localized nature. It is thus a challenging study to clarify the electronic state of Pu compounds.

Figure 42 shows the dHvA oscillations and their FFT spectra [68]. It is noted that the dHvA amplitude of branch γ in EX 1 is extremely reduced in EX 2, where the dHvA experiment named EX 2 was done one week later than the first experiment named EX 1. An intensive reduction of the

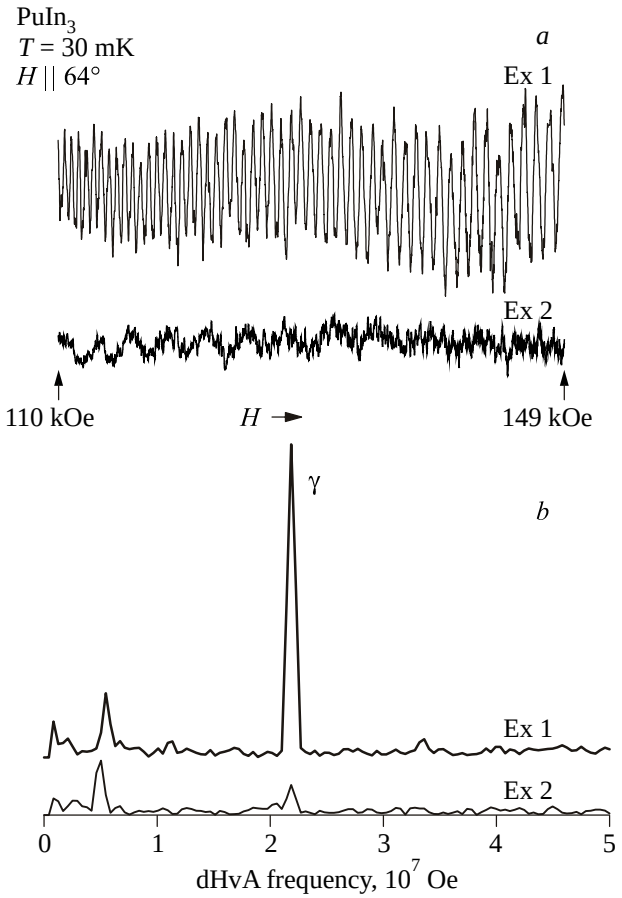

Fig. 42. dHvA oscillations (*a*) and the corresponding FFT spectra in a paramagnet $PuIn_3$ (*b*), cited from Ref. 68.

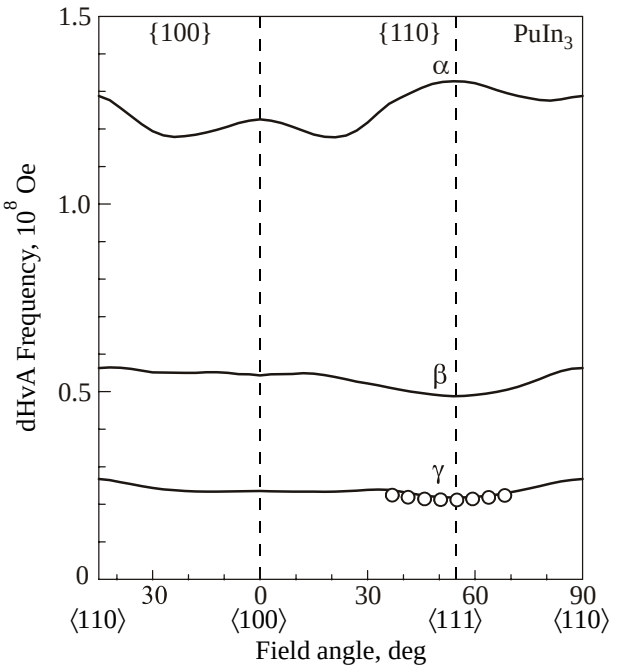

Fig. 43. Angular dependence of the dHvA frequency in a paramagnet $PuIn_3$. Solid lines are the results of 5*f*-itinerant energy band calculation, cited from Ref. 68.

dHvA amplitude is due to point defects produced by α-decay of ^{239}Pu. On the other hand, the dHvA amplitude of the dHvA frequency $F = 5.5 \cdot 10^6$ Oe is the same between EX 1 and EX 2, as shown in Fig. 42,*b*, which is not due to the dHvA branch in $PuIn_3$ but due to a dHvA signal of impurities, most likely In, which might be included in subgrain boundaries of the $PuIn_3$ single crystal sample. This is because the corresponding cyclotron mass is less than $0.5\,m_0$.

Figure 43 shows the angular dependence of the dHvA frequency, where branch γ is observed around ⟨111⟩ [68]. Solid lines in Fig. 43 are the result of 5*f*-itinerant band calculation. Branch γ corresponds to a small spherical electron Fermi surface centered at the Γ point, where two kinds of spherical Fermi surface are theoretically obtained on the basis of the 5*f*-itinerant band model, as shown in Fig. 44. The cyclotron mass of branch γ is $4.8\,m_0$, which is three times larger than the corresponding band mass of $1.56\,m_0$. A relatively large cyclotron mass of $17\,m_0$ might be expected for branch α for $H \parallel \langle 110 \rangle$. On the basis of the results of energy band calculation, the contribution of the 5*f* component to Fermi surfaces is approximately 50% for branches α and γ, while it is 70% for branch β. It is noticed that these Fermi surfaces in $PuIn_3$ are approximately the same as those of $YbIn_3$ with $n = 11$ in topology, as shown in Figs. 17 and 18, although there exists no contribution of 4*f* electrons to the Fermi surfaces in $YbIn_3$.

The Fermi surface properties such as 5*f*-itinerant characteristics and the enhanced cyclotron mass in $PuIn_3$ are very similar to those in the enhanced paramagnet $NpGe_3$, mentioned above. $PuIn_3$ is most likely an enhanced paramagnet as in $NpGe_3$, although the fundamental properties such as the magnetic susceptibility and specific heat are furthermore needed to be clarified in $PuIn_3$.

We summarize the Fermi surface properties in RX_3 compounds. The Fermi surface of $LaSn_3$ is slightly different from $LaPb_3$ in topology. Surprising is that the Fermi surface of $LaPb_3$ is roughly similar to that of UAl_3. The *f* contribution to the Fermi surface is, however, highly different between two compounds. Therefore, the cyclotron mass is large in UAl_3. The similar Fermi surface is experimentally observed between a 5*f*-localized ferromagnet $NpIn_3$ and a non-4*f* reference compound $LaIn_3$, or between an enhanced Pauli paramagnet $PuIn_3$ and an divalent compound $YbIn_3$.

It is also interesting that the topology of the Fermi surface in a divalent $YbIn_3$ is very similar to that of an enhanced Pauli paramagnet $YbAl_3$, as described in Chap. 3, although the cyclotron mass is highly different between two compounds. The topology of the Fermi surface in $ThIn_3$ is also almost the same as that of $CeIn_3$ under pressure, which will be shown later. From the present dHvA experiments and the results of energy band calculations, it is concluded that the *f*-itinerant band model is applicable to the topology of the Fermi surface in enhanced Pauli paramagnets such as $YbAl_3$, $CeSn_3$, UAl_3, UX_3 (X: Si, Ge), $NpGe_3$ and $PuIn_3$.

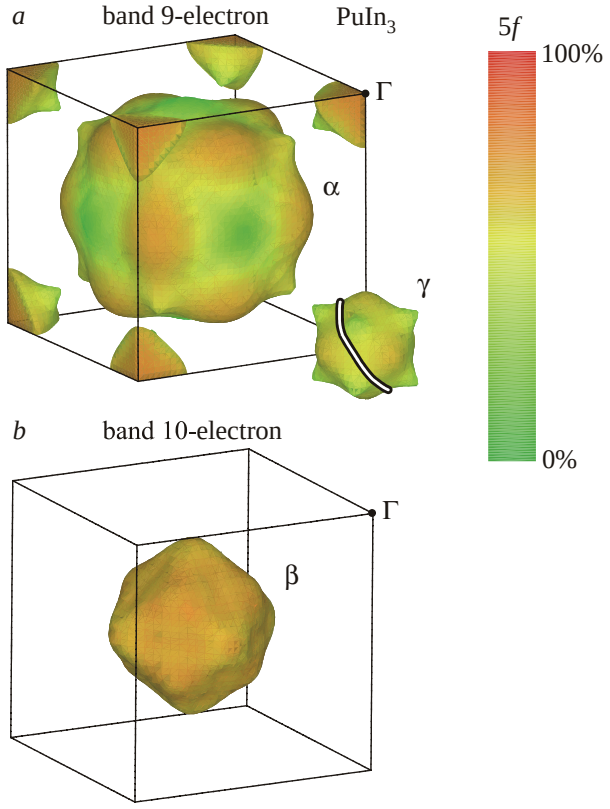

Fig. 44. (Color online) Theoretical 5*f*-itinerant Fermi surfaces in $PuIn_3$, cited from Ref. 68. The color presents the contribution of 5*f*-electrons.

5. Fermi surface properties in $RTIn_5$ and $AnTGa_5$

Next we present the Fermi surface properties of RTX_5 and $AnTX_5$ with the $HoCoGa_5$-type tetragonal structure, as shown in Fig. 45. RTX_5 and $AnTX_5$ are classified according to the number of valence electrons, as shown in Table 7 [77–85].

Table 7. Number of valence electrons and Fermi surface studies in RTX_5 and $AnTX_5$ compounds with the $HoCoGa_5$-type tetragonal structure

Number of valence electrons	Compounds	Refs.
27	$LaRhIn_5$ (P)	[77]
	$CeRhIn_5$ (AF)	[77]
28	$CeRhIn_5$ under pressure (S)	[78]
	$CeCoIn_5$ (P, S)	[79]
	$ThRhIn_5$ (P)	[80]
29	$UFeGa_5$ (P)	[81]
30	$UCoGa_5$ (P)	[82]
31	$UPtGa_5$ (AF)	[83]
	$NpRhGa_5$ (AF)	[84]
32	$PuCoGa_5$ (P, S)	[85]
	$PuRhGa_5$ (P, S)	

The electronic states in $CeTIn_5$, $ThTIn_5$ and $AnTGa_5$ indicate paramagnetism including Pauli paramagnetism, antiferromagnetism (AF), and superconductivity (S). The crystal structure in Fig. 45 is characteristic, which is closely related to the electronic state. Namely, the uniaxially distorted $AuCu_3$-type layers of RX_3 (AnX_3) and the TX_2 layers are stacked sequentially along the [001] direction (*c*-axis). For example, the 4*d* electrons of Rh in $LaRhIn_5$ hybridize with the 5*p* electrons of In, which results in a small density of states around the Fermi energy. This means that there are very few conduction electrons in the $RhIn_2$ layer and hence the $LaIn_3$ layer is conductive, producing cylindrical Fermi surfaces. This is also applicable to all the RTX_5 and $AnTX_5$ compounds, except $UTGa_5$ (T: Co, Rh and Ir), shown later.

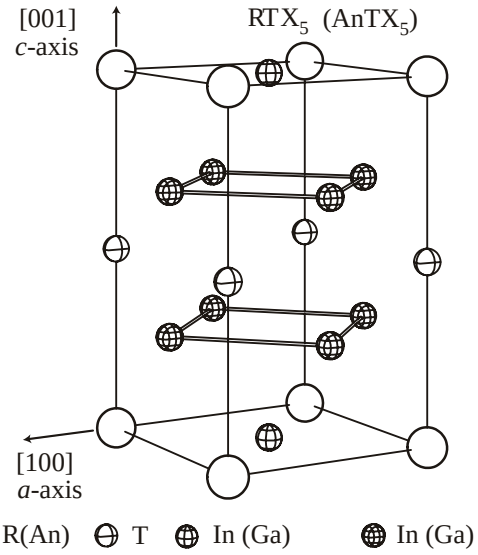

Fig. 45. The tetragonal crystal structure in RTX_5 and $AnTX_5$.

Figures 46,*a* and 46,*b* show the angular dependence of the dHvA frequency and the theoretical one in $LaRhIn_5$, respectively [77]. Main detected dHvA branches named α_i (i = 1, 2 and 3) and β_i (i = 1 and 2) are the same as the theoretical ones. These dHvA branches are well identified by

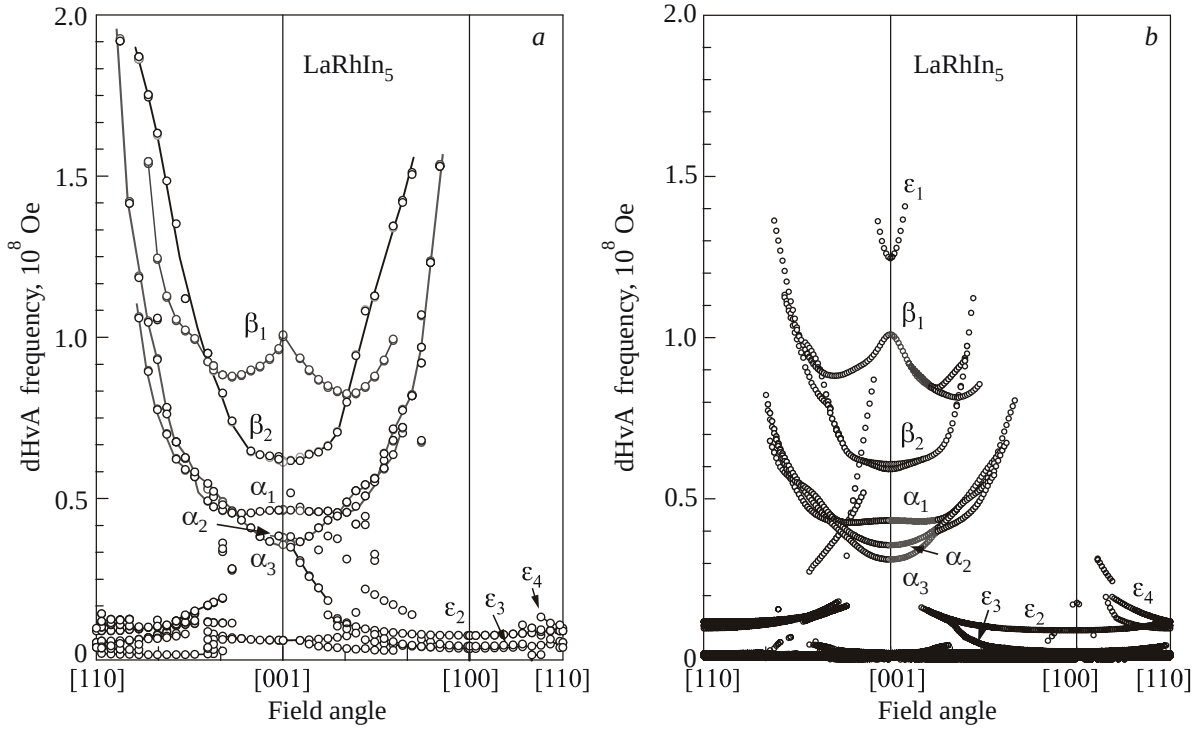

Fig. 46. Angular dependence of the dHvA frequency (*a*) and the theoretical one (*b*) in a non-4*f* reference compound $LaRhIn_5$ [77].

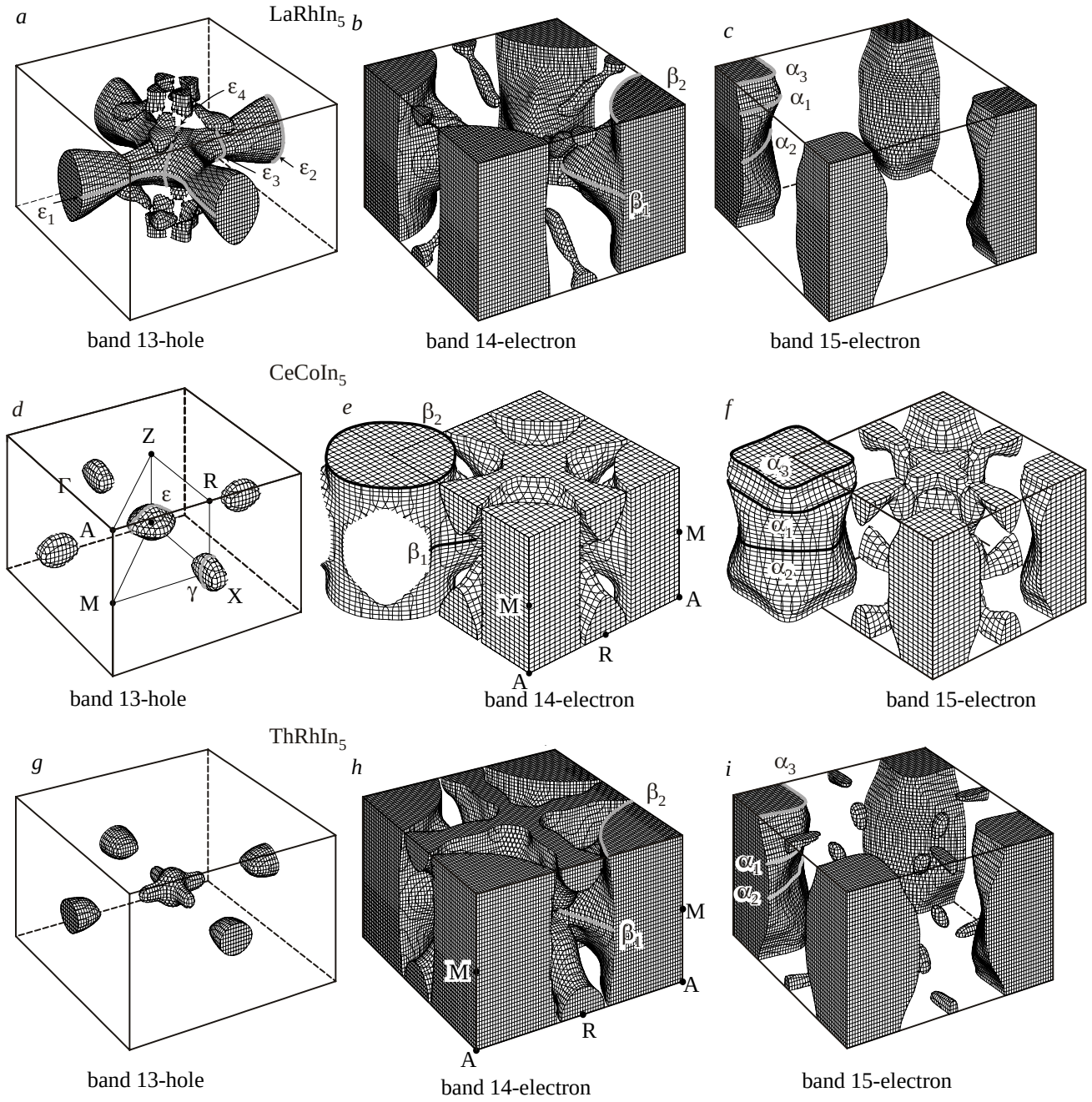

Fig. 47. Theoretical Fermi surfaces of $LaRhIn_5$ (*a*)–(*c*), $CeCoIn_5$ (*d*)–(*f*) and $ThRhIn_5$ (*g*)–(*i*), cited from Refs. 77, 80.

the theoretical Fermi surfaces in Figs. 47,*a*,*c*. The dHvA branches α_i are due to a band 15-electron Fermi surface, which is nearly cylindrical but highly corrugated, having maximum and minimum cross-sections. Branches β_i are also due to a highly-corrugated band 14-electron Fermi surface. This Fermi surface has a convex part stretching along the [110] direction. This is the main reason why the dHvA frequency of branch β_1 has a minimum at about 30°. Here, the electronic configuration in $LaRhIn_5$ is [Xe] $5d^1 6s^2$ in the La atom, [Kr] $4d^8 5s^1$ in the Rh atom and [Kr] $5s^2 5p^1$ in the In atom. The valence electrons are 27 in number, as shown in Table 7, indicating an uncompensated metal for $LaRhIn_5$.

In an antiferromagnet $CeRhIn_5$, the 4*f* electrons are considered to be localized at the Ce sites with magnetic moments of 0.8 μ_B/Ce [86], where the electronic configuration of the Ce atom is [Xe] $4f^1 5d^1 6s^2$. The detected main dHvA branches in $CeRhIn_5$ are thus approximately the same as those of $LaRhIn_5$ [77].

With increasing pressure *P* for $CeRhIn_5$, the Néel temperature T_N = 3.8 K increases, has a maximum around 1 GPa, and decreases with increasing pressure [87,88]. A smooth extrapolation indicates that $T_N \to 0$ at P_c^* = 2.4–2.5 GPa, as shown in Fig. 48. $CeCoIn_5$ is a superconductor. The superconducting transition temperature T_{sc} as a function of pressure is also shown in Fig. 48,*b* [89].

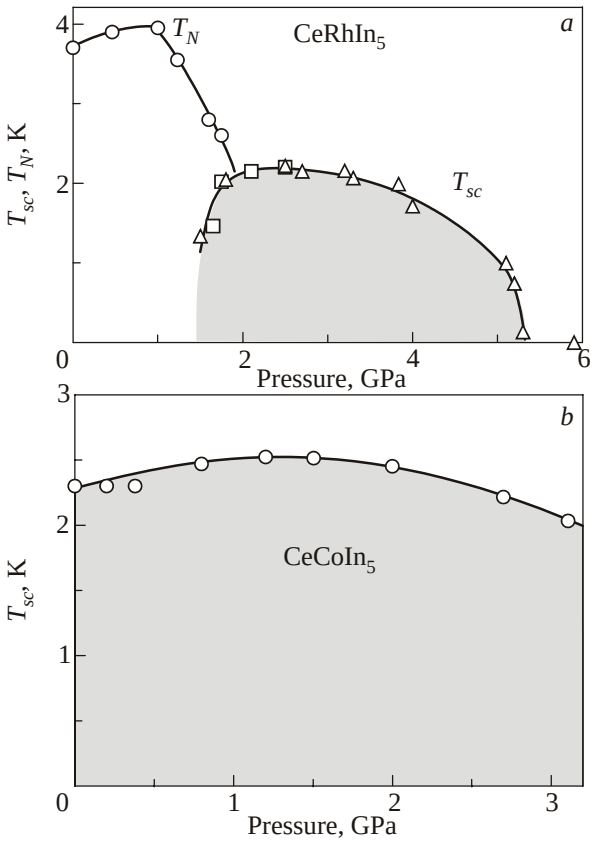

Fig. 48. Pressure phase diagram in $CeRhIn_5$ (*a*) and $CeCoIn_5$ (*b*), cited from Refs. 87–89.

Figures 49,*a* and 49,*b* show the temperature dependence of the electrical resistivity in $CeRhIn_5$ under pressure, together with the temperature dependence of electrical resistivity in $CeCoIn_5$, $NpPd_5Al_2$ and $PuCoGa_5$ [90]. At 1.60 and 1.89 GPa, superconductivity as well as antiferromagnetic ordering, shown by arrows in Fig. 49,*b*, are clearly observed in $CeRhIn_5$. Only superconductivity is observed at 2.08 GPa. Around the critical pressure region, $CeRhIn_5$ reveals superconductivity with a maximum transition temperature T_{sc} = 2.2 K [15]. From the NQR and specific heat experiments, together with the dHvA experiment shown below, the critical pressure is $P_c(H = 0) \simeq 2.0$ GPa at zero field [91], whereas $P_c^*(H \neq 0) = 2.4$–2.5 GPa in magnetic fields [78,92,93].

We studied a change of the Fermi surface properties against pressure for $CeRhIn_5$. A marked change of the dHvA frequencies occurs above $P_c^* \simeq 2.4$ GPa [78]. The detected dHvA frequencies above $P_c^* \simeq 2.4$ GPa are consistent with those of a non-magnetic heavy fermion superconductor $CeCoIn_5$ of which the dHvA branches are well explained by the 4*f*-itinerant band model [79]. A change of the 4*f*-electron nature from localized to itinerant is realized at $P_c^* \simeq 2.4$ GPa in $CeRhIn_5$, which will be described in Chap. 7. The upper critical field H_{c2} in superconductivity is also shown later in Fig. 67,*a*, together with the superconducting properties in $CeCoIn_5$, $PuRhGa_5$ and $NpPd_5Al_2$ [79,94–98].

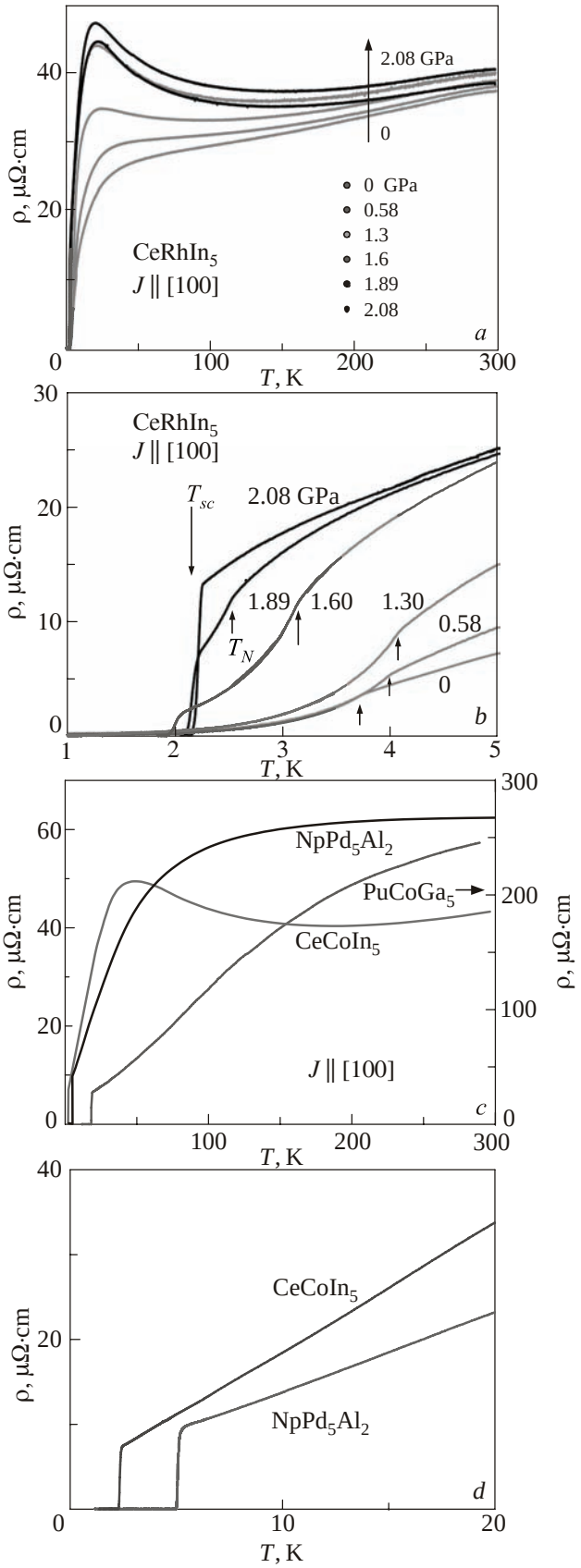

Fig. 49. Temperature dependence of the electrical resistivity in $CeRhIn_5$ under pressure (*a*), (*b*); in $CeCoIn_5$, $PuCoGa_5$, and $NpPd_5Al_2$ (*c*), (*d*). Only $PuCoGa_5$ is a polycrystal sample, and the scale is shown by the right hand in (*c*), cited from Ref. 90.

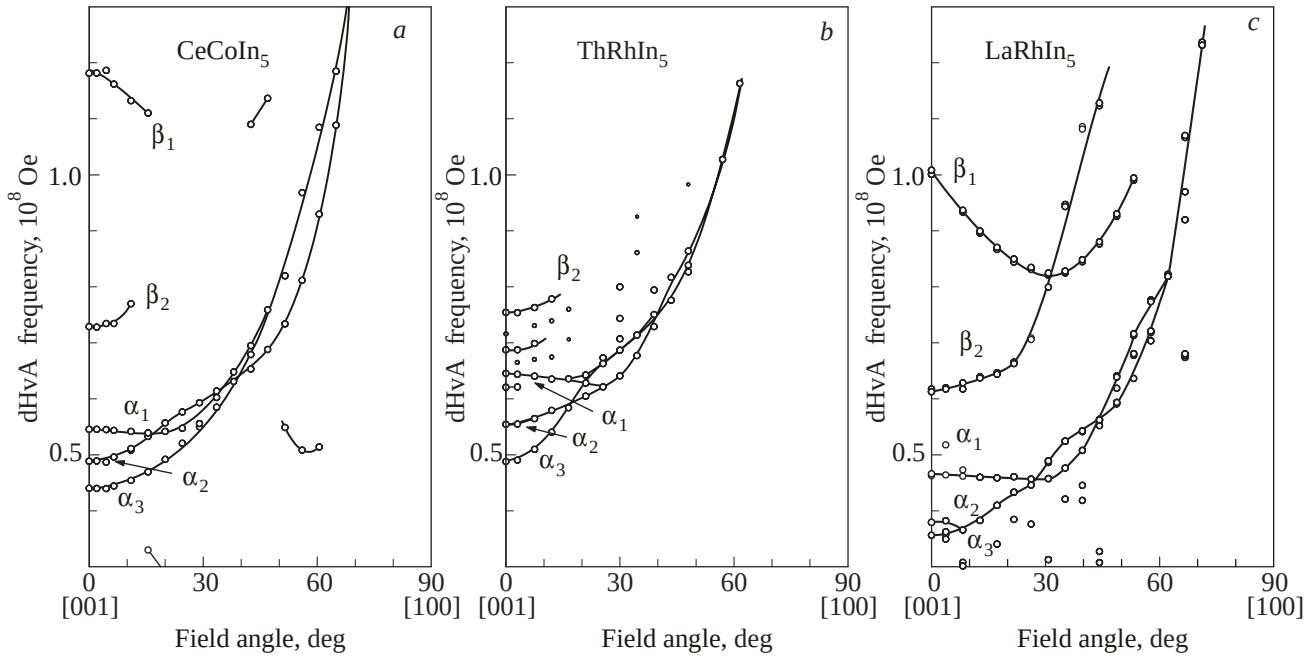

Fig. 50. Angular dependence of the dHvA frequency of a non-magnetic heavy fermion superconductor $CeCoIn_5$ (*a*), a Pauli paramagnet $ThRhIn_5$ (*b*) and a non-4*f* reference compound $LaRhIn_5$ (*c*), cited from Ref. 80.

Here, the number of valence electrons in $CeCoIn_5$ is 28, as shown in Table 7, because the 4*f* electron in the Ce atom becomes itinerant at low temperatures, as noted above. $CeCoIn_5$ thus becomes a compensated metal. Namely, the volume of the electron Fermi surface is equal to that of the hole Fermi surface. The same number of valence electrons is realized in a Pauli paramagnet $ThRhIn_5$, where the electronic configuration is [Rn] $6d^2 7s^2$ in the Th atom.

We show in Fig. 50 the angular dependence of the dHvA frequency in $CeCoIn_5$ and $ThRhIn_5$, together with $LaRhIn_5$ for comparison [79,80]. The detected dHvA branches named α_i and β_2 in $ThRhIn_5$ are approximately the same as those of $CeCoIn_5$. Note that the dHvA frequencies in both compounds are larger than those of $LaRhIn_5$ in Fig. 50,*c* [77]. The theoretical Fermi surface in $CeCoIn_5$ and $ThRhIn_5$ is shown in Figs. 47,*d–f* and 47,*g–i*, respectively. The cyclotron mass is, however, highly different between $CeCoIn_5$ and $ThRhIn_5$. The cyclotron mass in $CeCoIn_5$ at low fields is estimated as $100\,m_0$ in branch β_2 and $30\,m_0$ in branches α_i, as shown in Fig. 51,*b*. We also show in Fig. 51,*a* the magnetic field dependence of the electronic specific heat coefficient C_e/T for comparison. The large cyclotron mass in $CeCoIn_5$ is field-dependent, and decreases as a function of the magnetic field. This is characteristic in heavy fermions. These cyclotron masses in $CeCoIn_5$ are large compared with $0.87\,m_0$ in branch β_2 and $0.89–0.95\,m_0$ in branches α_i in $ThRhIn_5$. The large cyclotron mass in $CeCoIn_5$ is mainly due to the many-body Kondo effect. It is clarified from the energy band calculation that the 4*f*-electron contribution to the density of states at the Fermi energy in $CeCoIn_5$ is about 70% in magnitude. Note that the 4*f* electron does not contribute the electronic state in $ThRhIn_5$ because of no existence of 4*f* electrons, revealing a small cyclotron mass.

The characteristic features of superconductivity in $CeCoIn_5$ are as follows. Superconductivity is of the $d_{x^2-y^2}$ -type, with line nodes for the [110] direction, elongating along the [001] direction on the quasi-two dimensional Fermi surfaces, which was clarified from the angular

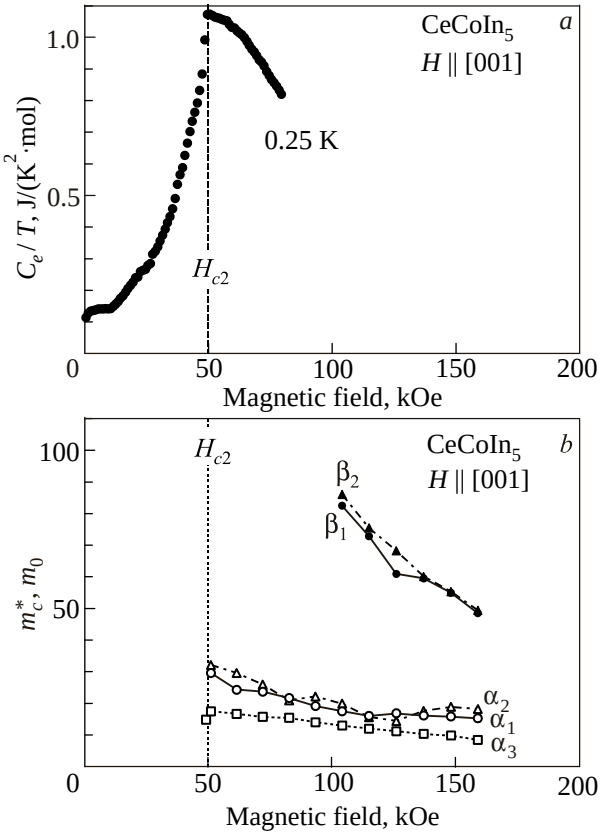

Fig. 51. Field dependence of the electronic specific heat C_e/T (*a*) and cyclotron mass in $CeCoIn_5$ (*b*), cited from Ref. 82.

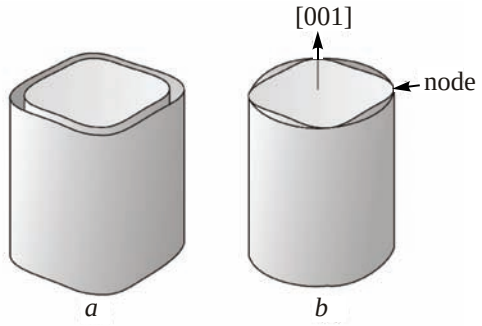

Fig. 52. Schematic pictures of the two dimensional superconducting gap with an isotropic gap (*a*) and a line node gap (*b*), cited from Ref. 21.

dependence of the thermal conductivity in magnetic fields [99]. We show schematically the gap with the line nodes in Fig. 52,*b*. The usual gap is shown in Fig. 52,*a* for comparison. The first-order phase transition from the superconducting mixed state to the normal state occurs at the upper critical field H_{c2} in $CeCoIn_5$ in the magnetization curve [100], as shown in Fig. 53,*a*, together with the similar step-like magnetization curves of $NpPd_5Al_2$ in Fig. 53,*b*, which are later discussed [96]. This persists up to about $0.3T_{sc}$ (T_{sc} = 2.3 K) for $H \parallel [001]$ and $0.4T_{sc}$ for $H \parallel [100]$ in $CeCoIn_5$. The H_{c2} value is later shown in Fig. 67,*b* as a function of temperature. The Fulde, Ferrel, Larkin, Ovchinikov (FFLO) state most likely exists in the superconducting mixed state close to H_{c2} at temperatures far lower than T_{sc} = 2.3 K [97,98]. These are closely related to the strong Pauli paramagnetic effect in the present superconductivity of $CeCoIn_5$.

Furthermore we show in Fig. 54,*a* the temperature dependence of the magnetic susceptibility in $CeCoIn_5$ [77],

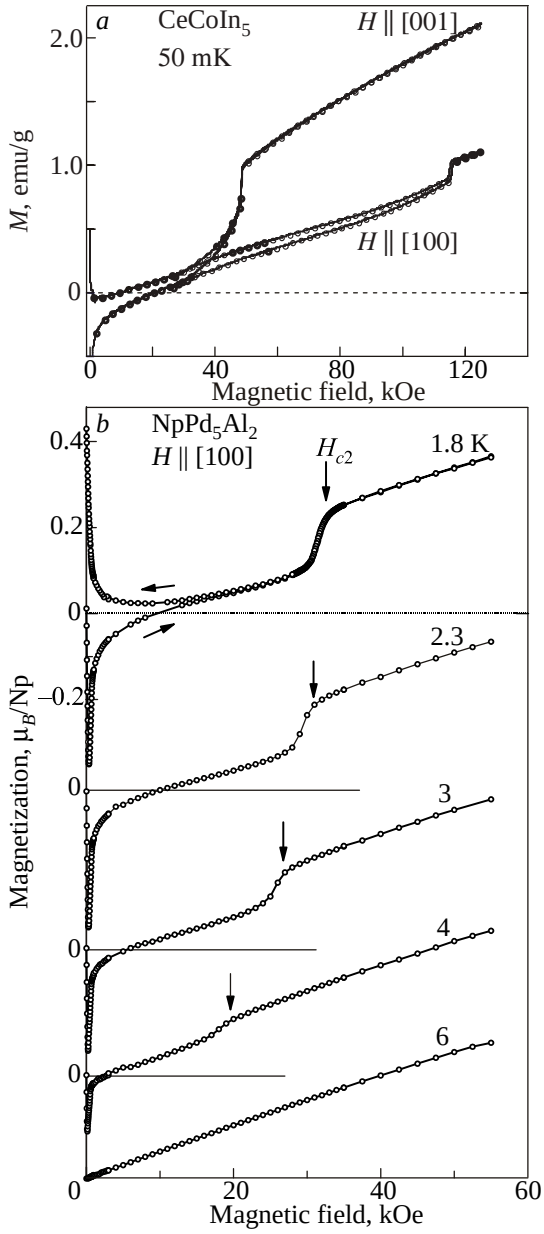

Fig. 53. Magnetization curves of $CeCoIn_5$ [100] (*a*) and $NpPd_5Al_2$ (*b*) [96], revealing a step-like increase of the magnetization at H_{c2}.

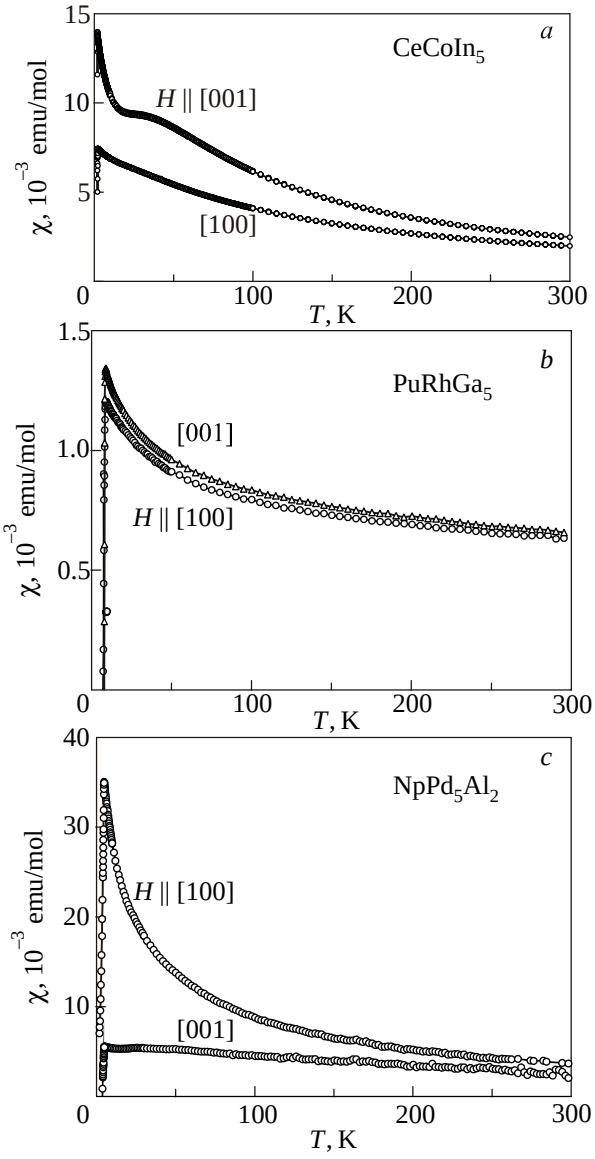

Fig. 54. Temperature dependence of the magnetic susceptibility in $CeCoIn_5$ [77] (*a*), $PuRhGa_5$ [95] (*b*) and $NpPd_5Al_2$ [96] (*c*).

together with the magnetic susceptibility in $PuRhGa_5$ and $NpPd_5Al_2$ [95,96]. The susceptibility increases steeply with decreasing temperature, but a sudden drop of the susceptibility occurs below T_{sc} = 2.3 K due to the onset of superconductivity. This is not usual. In the case of a typical heavy fermion superconductor UPt_3, for example, the magnetic susceptibility has a maximum at $T_{\chi max} \simeq 20$ K, and becomes constant at temperatures lower than $T_{\chi max}$, as shown in Fig. 2. Superconductivity occurs below T_{sc} = 0.5 K in UPt_3. This means that superconductivity is realized after the heavy fermion state is completely formed. On the other hand, the heavy fermion state is not completely formed at T_{sc} = 2.3 K in $CeCoIn_5$. Namely, superconductivity of $CeCoIn_5$ is realized in the non-Fermi liquid state. The similar behavior is observed in the other superconductors of $PrRhGa_5$ and $NpPd_5Al_2$, as shown in Figs. 54,*b* and 54,*c*, respectively, which are described later.

Superconductivity in the non-Fermi liquid state of $CeCoIn_5$ can be also seen in the specific heat data [101,102]. Figure 55 shows the temperature dependence of the specific heat in the form of C_e/T under several magnetic fields. The value of C_e/T increases with decreasing temperature under magnetic fields. The γ value is 380 mJ/(K^2·mol) at T_{sc} = = 2.3 K, but is extremely enhanced to be 1070 mJ/(K^2·mol) at 0.2 K. Note that the upper critical field H_{c2} = 49.5 kOe for $H \parallel$ [001]. The specific heat in the form of C_e/T in the normal state (under H = 60 kOe) does not saturate at low temperatures, but increases with decreasing temperature. The non-Fermi liquid state is thus observed in the specific heat, together with the magnetic susceptibility shown in

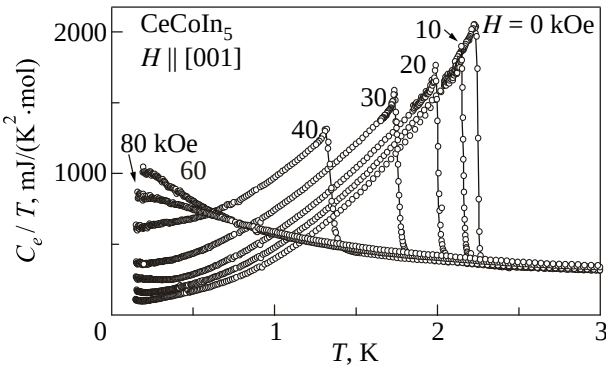

Fig. 55. Temperature dependence of the electronic specific heat in the form of C_e/T in $CeCoIn_5$, cited from Ref. 102.

Fig. 54,*a*. This is also observed in the electrical resistivity. The electrical resistivity follows a T-linear dependence below 10 K, as shown in Fig. 49,*d*. Moreover, the upper critical field $H_{c2}(0)$ and cyclotron mass m_c^* decrease monotonically with increasing pressure [89]. These results indicate that the electronic state of $CeCoIn_5$ is very close to the quantum critical point at ambient pressure.

We will go on to the next compound of a Pauli paramagnet $UFeGa_5$ with the number of valence electrons, 29, as shown in Table 7, where the electronic configuration is [Rn] $5f^3 6d^1 7s^2$ in the U atom and [Ar] $3d^6 4s^2$ in the Fe atom. Here we briefly note the electronic states in $UTGa_5$. Figure 56 shows the temperature dependence of the magnetic susceptibility [21]. $UTGa_5$ (T: Fe, Ru, Os, Co, Rh, Ir) compounds are Pauli paramagnets, while $UTGa_5$ (T: Ni, Pd, Pt) order antiferromagnetically.

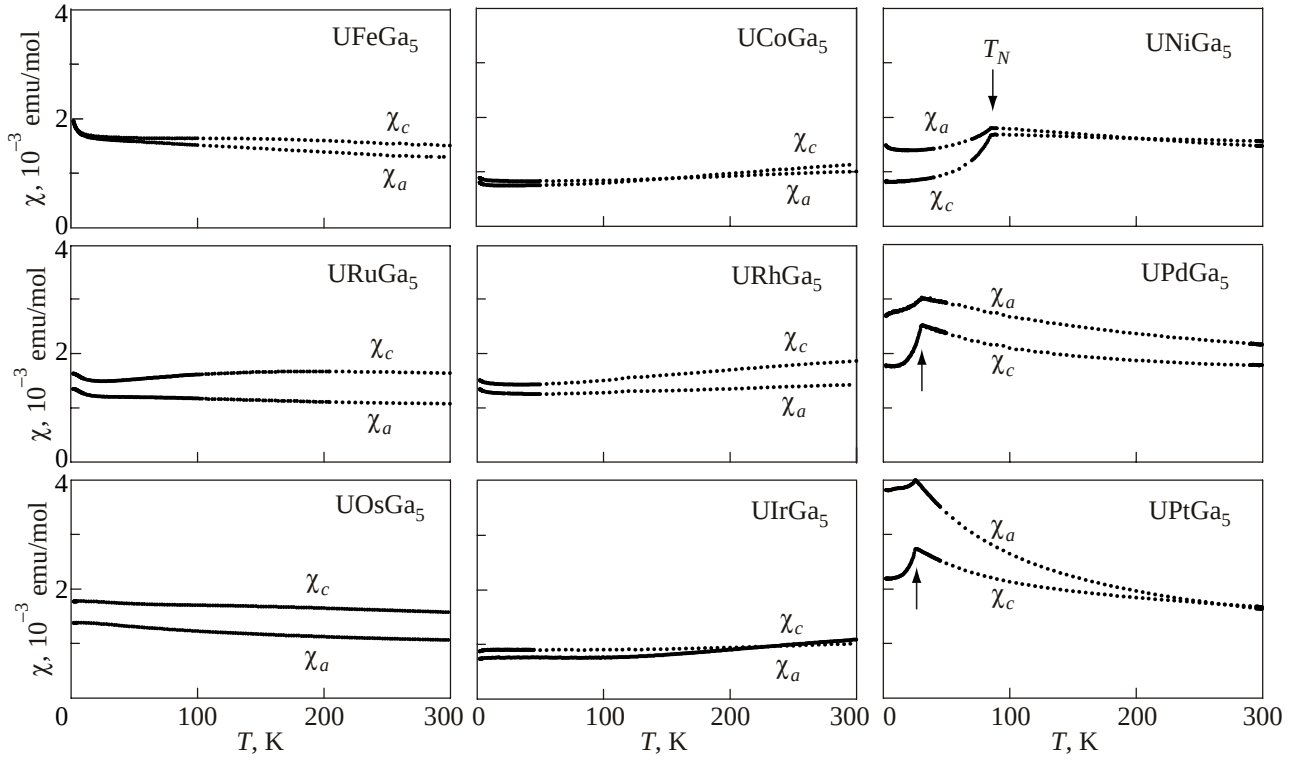

Fig. 56. Temperature dependence of the magnetic susceptibility in $UTGa_5$ (T: transition metal), cited from Ref. 21.

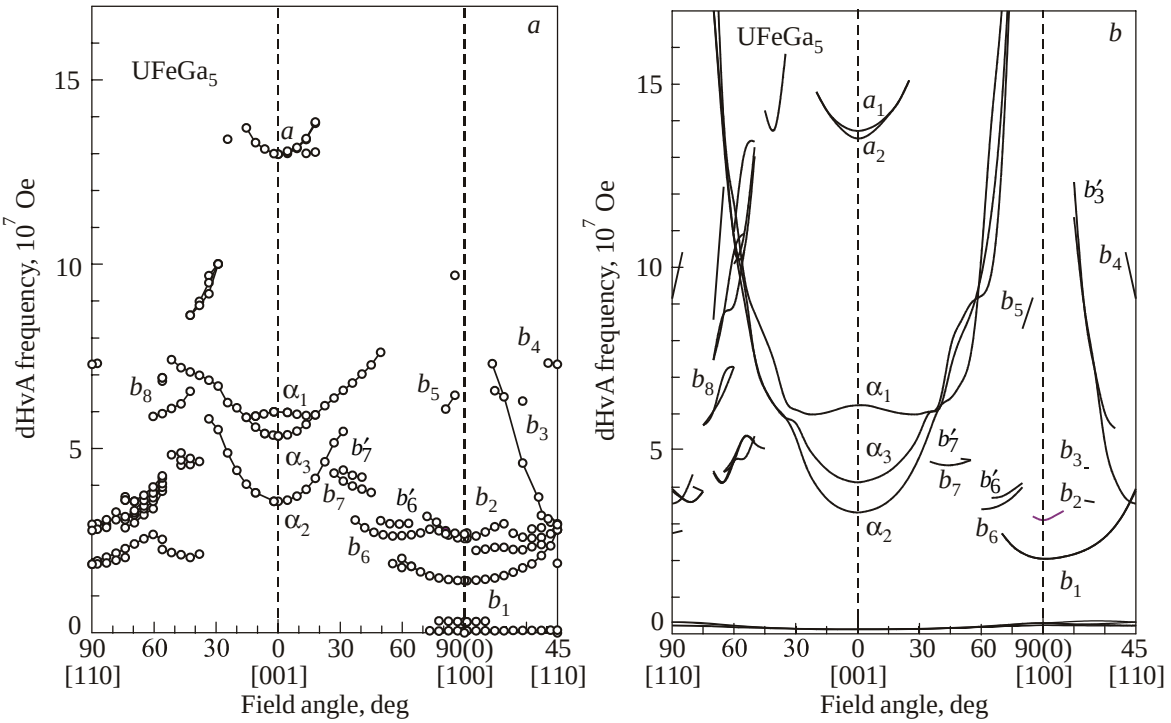

Fig. 57. Experimental angular dependence of the dHvA frequency (*a*) and the theoretical one (*b*) in a Pauli paramagnet $UFeGa_5$, cited from Ref. 81.

We show in Fig. 57 the angular dependence of the dHvA frequency and the corresponding theoretical one for $UFeGa_5$ [81]. The detected dHvA branches are consistent with the theoretical ones based on the 5*f*-itinerant band 15-electron Fermi surfaces shown in Fig. 58. The Fermi surface consists of a corrugated but cylindrical Fermi surface and a lattice-like Fermi surface. The cyclotron mass is relatively large, ranging from 2.4 to 9.9 m_0: 9.2 m_0 for branch α_1 and 9.9 m_0 for branch *a*. The theoretical band mass is about half of the experimental one, which is consistent with a relation between γ = 40 mJ/(K^2·mol) and the theoretical one γ_b = 19.6 mJ/(K^2·mol).

In a Pauli paramagnet $UCoGa_5$ with the number of valence electrons, n = 30, as shown in Table 7, we observed dHvA branches with very small dHvA frequencies, indicating a semimetal [82]. We show in Fig. 59 the angular dependence of the dHvA frequency. Three kinds of dHvA branches named *a*, *b* and *c* correspond to small ellipsoidal Fermi surfaces. We constructed the Fermi surfaces by using the present dHvA data so as to become the semimetal with equal volumes of electron and hole Fermi surfaces, as

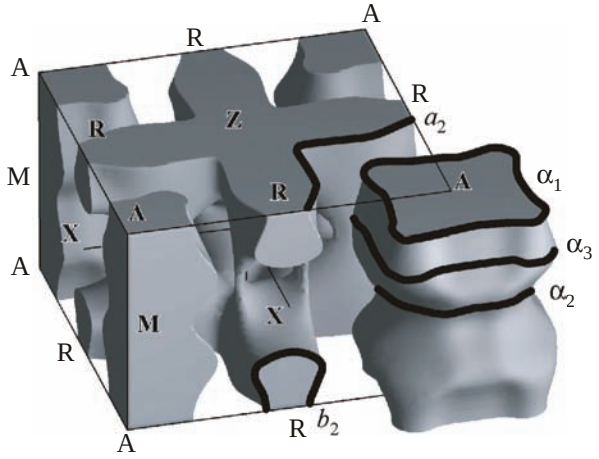

Fig. 58. Theoretical band 15-electron-Fermi surfaces based on a 4*f*-itinerant band model in a Pauli paramagnet $UFeGa_5$, cited from Ref. 81.

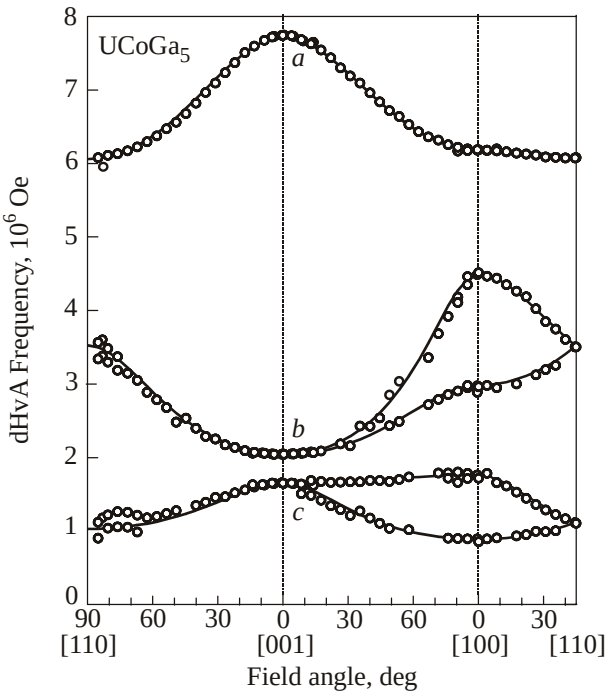

Fig. 59. Angular dependence of the dHvA frequency in a Pauli paramagnet $UCoGa_5$, cited from Ref. 82.

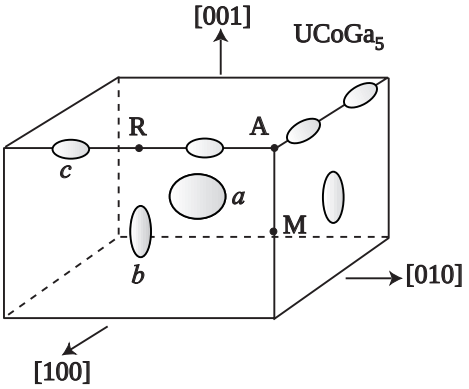

Fig. 60. Proposed Fermi surfaces in a Pauli paramagnet $UCoGa_5$, cited from Ref. 82.

shown in Fig. 60. The Fermi surface consists of small band 15-hole Fermi surfaces (branches *b* and *c*) and a small band 16-electron Fermi surface (branch *a*) because one more valence electron is added, compared with that in $UFeGa_5$, and the number of valence electrons is 30 in $UCoGa_5$, revealing a compensated metal or a semimetal. The γ value of $UCoGa_5$ is small, γ = 3.3 mJ/(K^2·mol), which corresponds to a light cyclotron mass of $m_c^* = 0.82\,m_0$ in branch *a* for $H \parallel [001]$.

The next compound is $UPtGa_5$ with the number of valence electrons, n = 31, as shown in Table 7. $UPtGa_5$ is, however, an antiferromagnet with the Néel temperature T_N = = 26 K and a small ordered moment μ_s = 0.32 μ_B/U [103]. $UPtGa_5$ is supposed to be a 5*f*-itinerant antiferromagnet, similar to UGa_3 mentioned in Chap. 4. It is however, noticed that the magnetic susceptibility follows the Curie–Weiss law

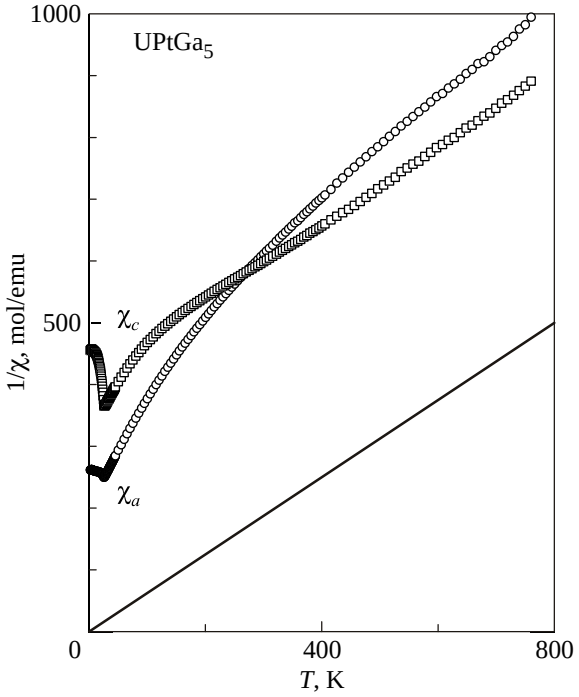

Fig. 61. Temperature dependence of the inverse magnetic susceptibility in $UPtGa_5$. A solid line corresponds to the free ion value of $5f^2$ and $5f^3$ configurations, cited from Ref. 74.

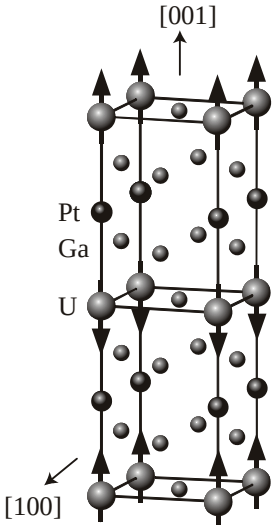

Fig. 62. Antiferromagnetic structure of $UPtGa_5$, cited from Ref. 103.

above 500 K, with effective magnetic moments of 3.5 and 3.2 μ_B/U for $H \parallel$ [001] and [100], respectively, as shown in Fig. 61 [74]. These effective moments are close to the free ion value of μ_{eff} = 3.58 μ_B/U for $5f^2$ (U^{4+}) or μ_{eff} = = 3.62 μ_B/U for $5f^3$ (U^{3+}), as shown by a solid line in Fig. 61, indicating the localized nature of 5*f* electrons at high temperatures.

A ferromagnetic coupling in the basal (001) plane was observed by the neutron scattering experiment, which is stacked along the [001] direction with an antiferromagnetic (↑ ↓) sequence, as shown in Fig. 62 [103]. Therefore, the magnetic unit cell becomes doubled, containing the 62 valence electrons. In other words, the magnetic Brillouin zone becomes flat along the [001] direction.

We show in Fig. 63 the angular dependence of the dHvA frequency in the antiferromagnetic state [83]. The detected dHvA branches named α_1, α_2, α_3 and γ, and ε roughly follow the $1/\cos\theta$ dependence (θ is the tilted angle from [001] to [100] or [110]), revealing cylindrical Fermi surfaces. These branches are well explained by the spin (orbital)-polarized 5*f*-itinerant band model, as shown in Fig. 63,*b* [83]. The Fermi surface shown in Fig. 64 consists of four kinds of corrugated but cylindrical Fermi surfaces. Branches ε, α_3, α_1, α_2 and γ correspond to orbit *a* of the band 31-hole Fermi surface, orbits c_1 and c_2 (band 32-electron), orbits d_1 and d_2 (band 33-electron) and orbits e_1 and e_2 (band 30-hole), respectively. The cyclotron effective masses are relatively large: $20\,m_0$ (branch ε), $24\,m_0$ (branch α_3), 13 and $10\,m_0$ (branches α_1, α_2, respectively) and $10\,m_0$ (branch γ). These values are consistent with γ = 57 mJ/(K^2·mol). It is stressed here that the almost localized nature of the 5*f* electrons at high temperatures is changed into the 5*f*-itinerant character, with a small ordered moment of 0.32 μ_B/U.

The similar magnetic structure is realized in an antiferromagnet $NpRhGa_5$, and the corresponding angular depen-

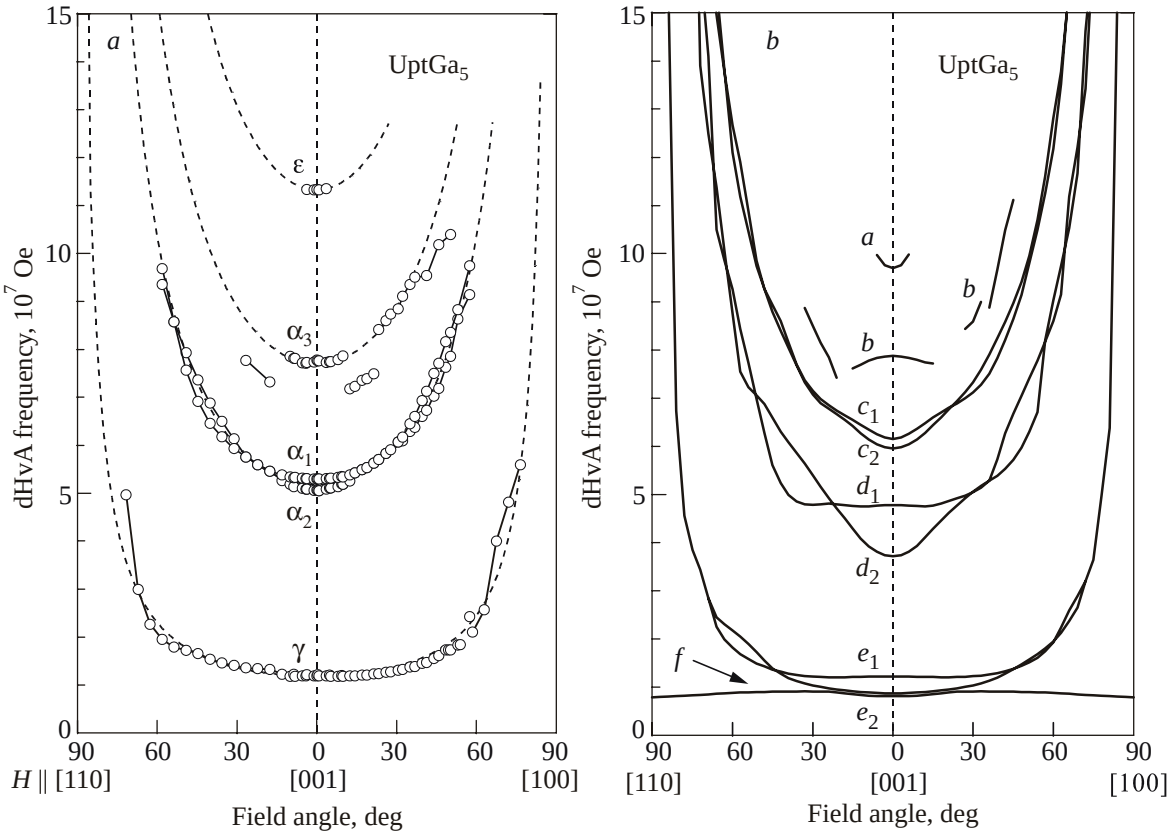

Fig. 63. Angular dependence of the dHvA frequency (*a*) and the theoretical one based on the spin (orbital)-polarized 5*f*-itinerant band model in an antiferromagnet $UPtGa_5$, cited from Ref. 83 (*b*).

dence of the dHvA frequency is similar to that of $UPtGa_5$, as shown in Fig. 65 [84]. The magnetic property of $NpRhGa_5$ is very interesting [104]. There are two successive antiferromagnetic transitions at T_{N1} = 36 K and T_{N2} = = 32 K. The magnetic structure in the temperature range from T_{N1} to T_{N2}, named AN1, is the same as that in $UPtGa_5$. We show in Fig. 66 the magnetic phase diagram for $H \parallel$ [001] [105]. Below T_{N2}, the magnetic unit cell (AN2) is the same as AN1 but the direction of the magnetic moment changes abruptly from [001] to [110]. The or-

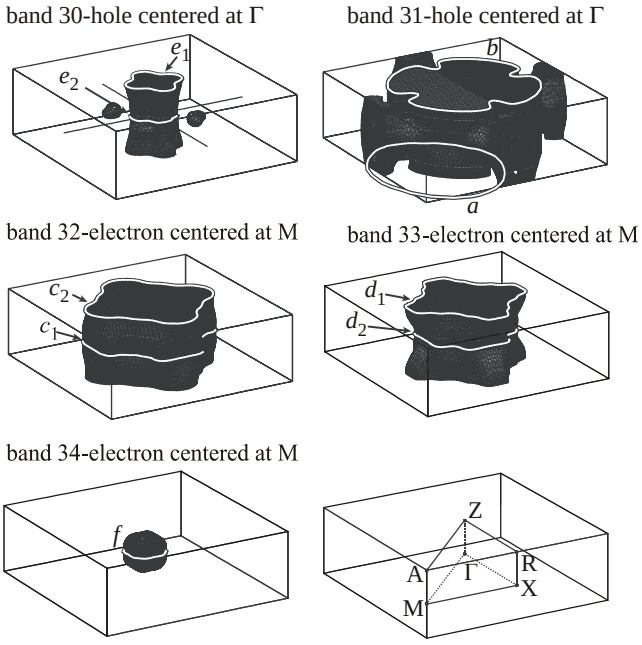

Fig. 64. Theoretical Fermi surfaces based in an antiferromagnet $UPtGa_5$, cited from Ref. 83.

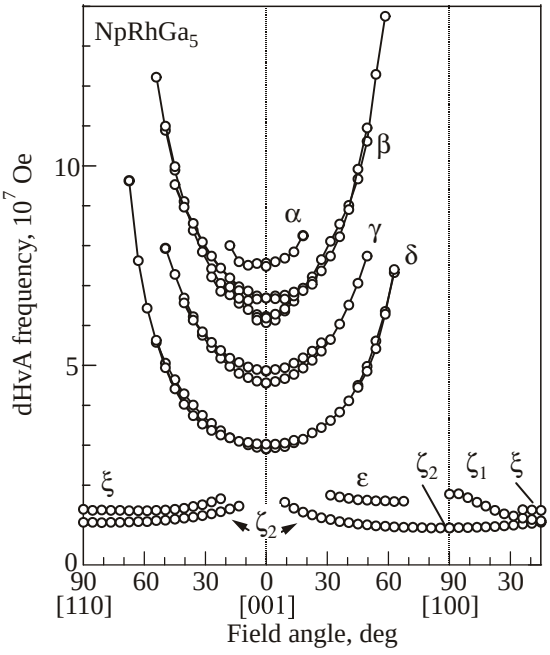

Fig. 65. Angular dependence of the dHvA frequency in an antiferromagnet $NpRhGa_5$, cited from Ref. 84.

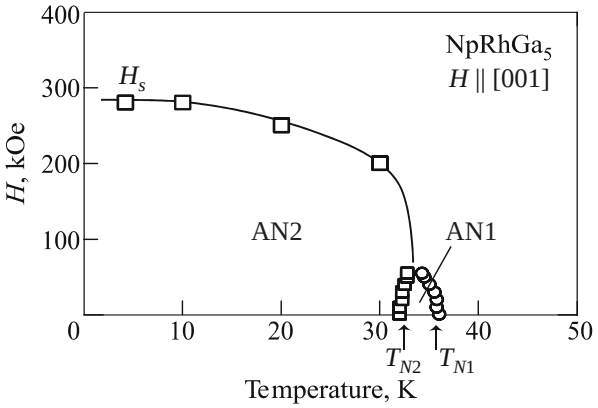

Fig. 66. Magnetic phase diagram for $H \parallel [001]$ in $NpRhGa_5$, cited from Ref. 105.

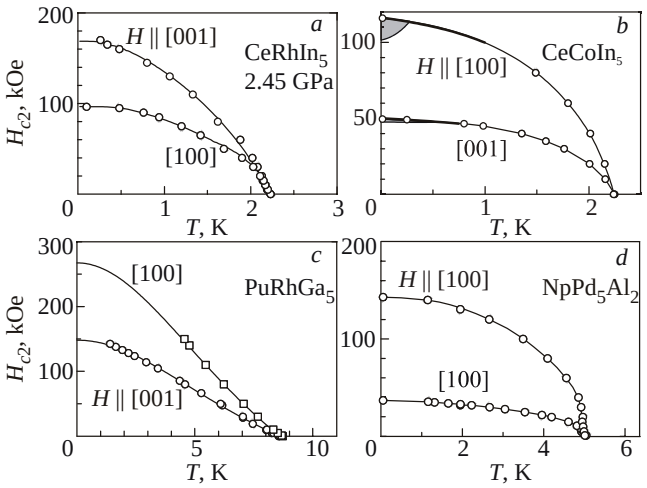

Fig. 67. Temperature dependence of the upper critical field in $CeRhIn_5$ [94] (*a*), $CeCoIn_5$ [79] (*b*), $PuRhGa_5$ [95] (*c*) and $NpPd_5Al_2$ [96] (*d*). Thick solid lines in $CeCoIn_5$ indicate the first-order phase transition at H_{c2}, and the dark-gray regions in the mixed state might be the FFLO state, cited from Refs. 97, 98.

dered moment is most likely enhanced from 0.6 μ_B/Np to 0.96 μ_B/Np. The former value is an ordered moment, estimated under the assumption that the AN1 phase persists down to 0 K without the magnetic transition at T_{N2}. The latter value of 0.96 μ_B/Np is determined experimentally at low temperatures far below T_{N2}. It is theoretically pointed out that the quadrupolar interaction plays an important role on this transition at T_{N2} [106].

Here we note that all the $NpTGa_5$ compounds order antiferromagnetically, indicating no paramagnetism, which are in contrast with the electronic states in $UTGa_5$. Moreover, the ordered moments in neptunium compounds are roughly twice larger than those in uranium compounds. This is the reason why the magnetic moment at the Np site is of the localized character. The Fermi surface properties of $NpRhGa_5$ are, however, well explained by the spin (orbital)-polarized 5*f*-itinerant band model as in $UPtGa_5$, as described above. This claims that the 5*f* electrons, as it were, possess the dual nature: the local moment at the Np site and the contribution of the 5*f* electrons to the Fermi surface.

The discovery of non-magnetic heavy fermion superconductors $PuCoGa_5$ (T_{sc} = 18.5 K) and $PuRhGa_5$ (T_{sc} = = 9 K) with the number of valence electrons, n = 32, in Table 7 has attracted attention because of its high T_{sc} and unconventional superconducting properties [90,107]. The magnetic susceptibility of $PuRhGa_5$ increases with decreasing temperature, following the Curie–Weiss law with an effective magnetic moment of the $5f^5$ (Pu^{3+}) configuration, but indicates a sudden drop of the susceptibility due to onset of superconductivity [95], as shown in Fig. 54,*b*. From the result of the upper critical field, the topology of the Fermi surface is most likely cylindrical as in $CeCoIn_5$, as shown in Fig. 67,*c* [95], although the dHvA experiment was not carried out because of the high H_{c2} value at lower temperatures. Theoretically, three kinds of cylindrical Fermi surfaces are proposed on the basis of the 5*f*-itinerant band model for $PuCoGa_5$ [85], as shown in Fig. 68,*a*, together with the cylindrical Fermi surfaces of $CeCoIn_5$ and $NpPd_5Al_2$ in Figs. 68,*b* and 68,*c*, respectively.

Finally we note superconductivity of $NpPd_5Al_2$ with the tetragonal structure [96]. The crystal structure of $NpPd_5Al_2$ is similar to the tetragonal structure of $CeCoIn_5$ and $PuCoGa_5$, as shown in Fig. 69. The $5s^25p^1$ ($4s^24p^1$) electrons of the In(Ga) atoms in $CeCoIn_5$ ($PuCoGa_5$) are, however, replaced by the 4*d* electrons of the Pd atom in $NpPd_5Al_2$. The 4*d* electrons are well hybridized with the 5*f* electrons, and produce the strongly correlated conduction electrons. $NpPd_5Al_2$ does not order magnetically. The corresponding magnetic susceptibility increases steeply with decreasing temperature, but a sudden drop of the susceptibility occurs below T_{sc} = 4.9 K due to the onset of superconductivity, as shown in Fig. 54,*c*. This is very similar to that in $CeCoIn_5$ in Fig. 54,*a*. The electronic state of $NpPd_5Al_2$ is found to be located in the vicinity of the antiferromagnetically ordered state from the results of the magnetic susceptibility and the negative value of the paramagnetic Curie temperature. In fact, the γ value is large, γ = 200 mJ/(K^2·mol) at T_{sc} = 4.9 K, and is enhanced to be 390 mJ/(K^2·mol) at 0 K from the entropy balance. Furthermore, the low-temperature electrical resistivity does not follow the Fermi liquid relation, but indicates a T-linear dependence, as shown in Fig. 49,*d*. The large paramagnetic effect is reflected in the strong suppression of the upper critical field, as shown in Fig. 67,*d* and the step-like increase of the magnetization at H_{c2}, as shown in Fig. 53,*b*. In the case of a typical *d*-wave superconductor $CeCoIn_5$, a large paramagnetic effect induces a first-order phase transition at H_{c2}, namely the step-like increase of the magnetization, below temperatures lower than $0.3T_{sc}$ or $0.4T_{sc}$ (T_{sc} = 2.3 K), as shown in Fig. 53,*a* [100]. The similar phenomenon is realized in $NpPd_5Al_2$. Surprisingly, the step-like increase of magnetization is observed up to a high temperature of 3 K (= $0.6T_{sc}$).

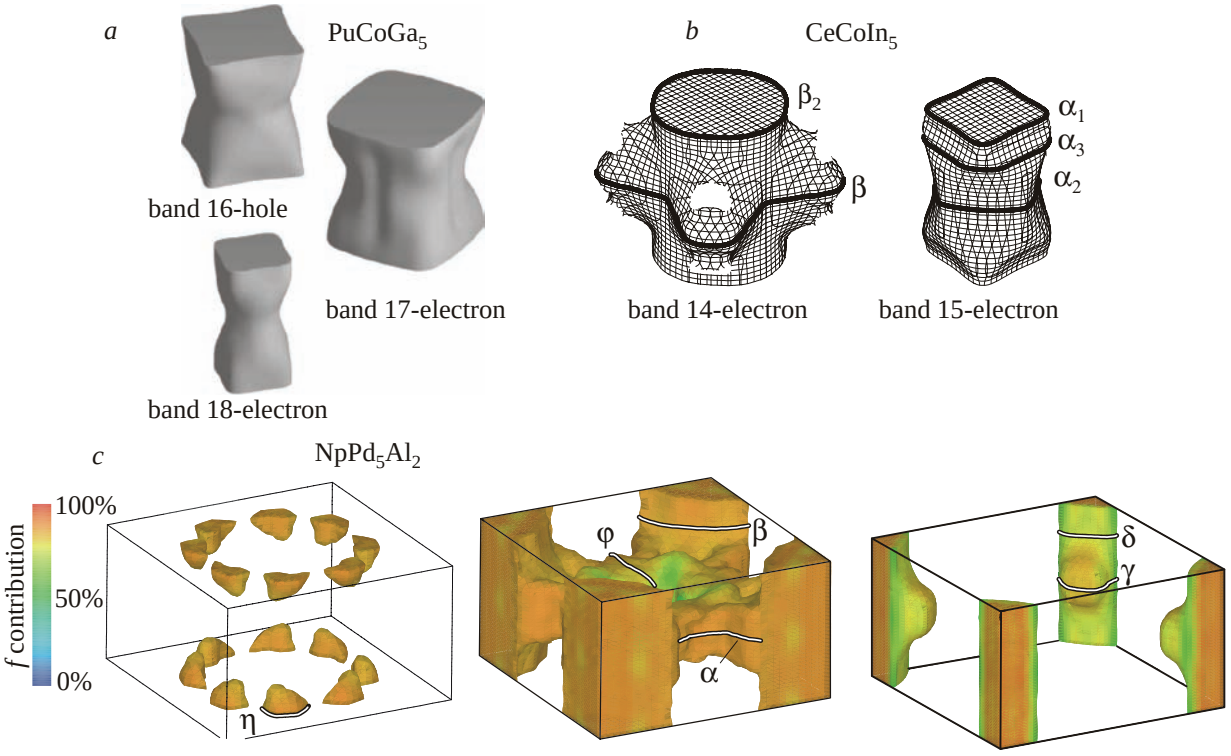

Fig. 68. Theoretical Fermi surfaces based on the *f*-itinerant band model in $PuCoGa_5$ [85] (*a*), $CeCoIn_5$ [78] (*b*) and $NpPd_5Al_2$ [108] (*c*).

It is noticed that the normal and superconducting properties of $NpPd_5Al_2$ are very similar to those of $CeCoIn_5$, but the anisotropy of the magnetic susceptibility and the upper critical field is different from each other. If we simply analyze the anisotropy of the upper critical field from the so-called effective mass model, it is deduced that the Fermi surface is of a pan-cake shape in $NpPd_5Al_2$. The corresponding Fermi surface based on the 5*f*-itinerant band model is, however, quasi-two dimensional, as shown in Fig. 68,*c* [108]. It might be necessary to consider the anisotropic spin susceptibility between $H \parallel$ [110] and [001], because the upper critical field is suppressed due to the large paramagnetic effect.

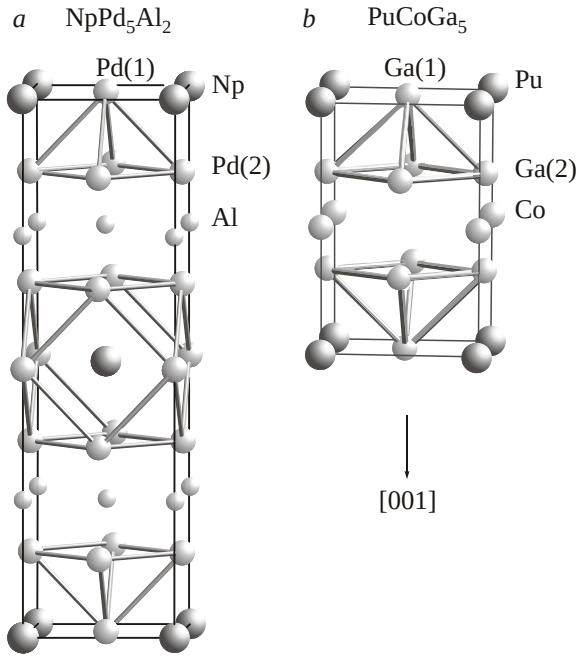

Fig. 69. Crystal structure of actinide superconductors $NpPd_5Al_2$ (*a*) and $PuCoGa_5$ (*b*), cited from Ref. 21.

We will summarize the Fermi surface properties in $RTIn_5$ and $AnTGa_5$. One of the characteristic properties in $RTIn_5$ and $AnTGa_5$ compounds is quasi-two dimensional in the electronic state, revealing nearly cylindrical Fermi surfaces along the tetragonal [001] direction. Furthermore, the quasi-two dimensional electronic state, together with the heavy fermion state, enhances heavy fermion superconductivity, as in $CeCoIn_5$, $NpPd_5Al_2$, $PuCoGa_5$ and $PuRhGa_5$. In fact, the superconducting transition temperature T_{sc} = = 0.2 K in $CeIn_3$ under 2.6 GPa is enhanced to T_{sc} = 2.3 K in $CeCoIn_5$. Interesting is a relation between the superconducting transition temperature and γ value: 2.3 K in $CeCoIn_5$, 4.9 K in $NpPd_5Al_2$, 8.6 K in $PuRhGa_5$ and 18.5 K in $PuCoGa_5$. Correspondingly, the γ value decreases from 1070 mJ/(K^2·mol) in $CeCoIn_5$ to 100 mJ/(K^2·mol) in $PuTGa_5$ (T: Co, Rh). The γ value in $CeIn_3$ under 2.6 GPa is roughly estimated as 1000 mJ/(K^2·mol) from the cyclotron mass close to 100 m_0, which is discussed later in Chap. 7. It is also stressed that heavy fermion superconductivity in these superconductors is realized in the non-Fermi liquid state. Superconducting properties of $CeRhIn_5$ at 2.45 GPa, $CeCoIn_5$, $PuRhGa_5$ and $NpPd_5Al_2$ are summarized in Table 8.

Table 8. Superconducting properties of $CeRhIn_5$ at 2.45 GPa, $CeCoIn_5$, $PuRhGa_5$ and $NpPd_5Al_2$, cited from Refs. 94, 79, 21, 96

	$CeRhIn_5$ (2.45 GPa)		$CeCoIn_5$		$PuRhGa_5$		$NpPd_5Al_2$	
	$H \parallel$ [100]	[001]	$H \parallel$ [100]	[001]	$H \parallel$ [100]	[001]	$H \parallel$ [100]	[001]
T_{sc}, K	2.22		2.3		8.6		4.9	
$-dH_{c2}/dT$, kOe/K	184	193	240	110	35	20	64	310
$H_{c2}(0)$, kOe	97	169	116	50	270	150	37	143

6. Metamagnetism

Metamagnetism or the metamagnetic behavior is a phenomenon showing an abrupt nonlinear increase of magnetization at the magnetic field H_c or H_m. The magnetization curve of an antiferromagnet is a typical example, which was shown in Chaps. 3–5, see Fig. 11, for example. In this Chapter we will introduce two different kinds of metamagnetic behavior.

As mentioned in Introduction, some Ce, Yb or U compounds such as $CeCu_6$, $CeRu_2Si_2$, $YbCu_2Si_2$, and UPt_3 exhibit no long-range magnetic ordering. The magnetic susceptibility of these compounds increases with decreasing temperature, following the Curie–Weiss law at high temperatures, and shows a maximum at a characteristic temperature $T_{\chi max}$. Below $T_{\chi max}$, the susceptibility becomes almost temperature-independent, and the *f*-electron system is changed into a new electronic state, called the heavy fermion state, as shown in Fig. 2. The almost localized *f*-electrons at high temperatures become itinerant at temperatures lower than $T_{\chi max}$ via the many-body Kondo effect. The crossover from "localized" to "itinerant" occurs at a characteristic temperature $T_{\chi max}$, which approximately corresponds to the Kondo temperature T_K. Below $T_{\chi max}$, the magnetization indicates a metamagnetic behavior or an abrupt nonlinear increase in magnitude at the magnetic field H_m. We will present the Fermi surface properties below and above H_m, together with a relation between $T_{\chi max}$ and H_m, for $CeRu_2Si_2$, UPt_3 and YbT_2Zn_{20} (T: Co, Rh, Ir).

Moreover, we will show another metamagnetic behavior based on the field-induced ferroquadrupolar ordering in $PrCu_2$ in the last section.

6.1. Metamagnetic behavior of a heavy fermion compound $CeRu_2Si_2$

Here we discuss a metamagnetic behavior in $CeRu_2Si_2$, which crystallizes in the tetragonal structure with one molecule per primitive cell, as shown in Fig. 70. The metamagnetic behavior occurs at a critical field H_m = 77 kOe for the magnetic field along the [001] direction, as shown in Fig. 71. The magnetization curve is reversible at the metamagnetic behavior, showing no hysteresis [109,110].

An important point is as follows. We define a field differential magnetization $\chi = dM/dH$. The magnitude of $\Delta\chi = \chi - \chi_0$ at $H = H_m$, where χ_0 is a field-independent susceptibility, namely, χ at low fields ($H \ll H_m$), is found to become finite at low temperatures. This is shown in inset of Fig. 71, indicating a finite value of $\Delta\chi^{-1}$ as $T \to 0$. This result clearly indicates that the present metamagnetic be-

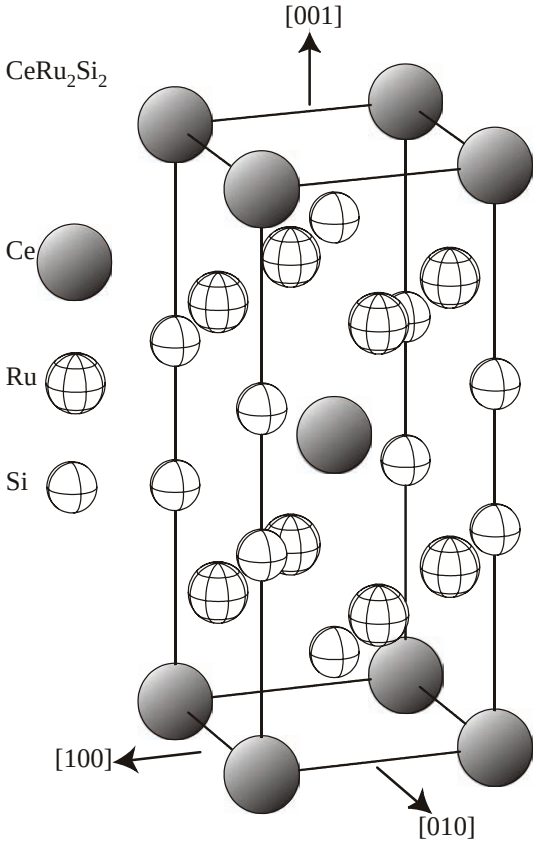

Fig. 70. Crystal structure of $CeRu_2Si_2$.

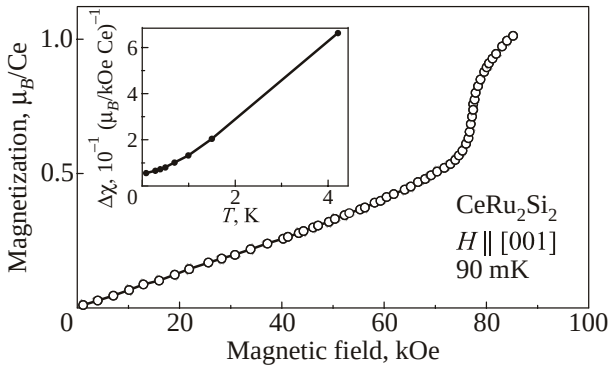

Fig. 71. Magnetization curve of $CeRu_2Si_2$, cited from Refs. 109, 110. The insert shows the temperature dependence of $\Delta\chi^{-1}$ defined in the text.

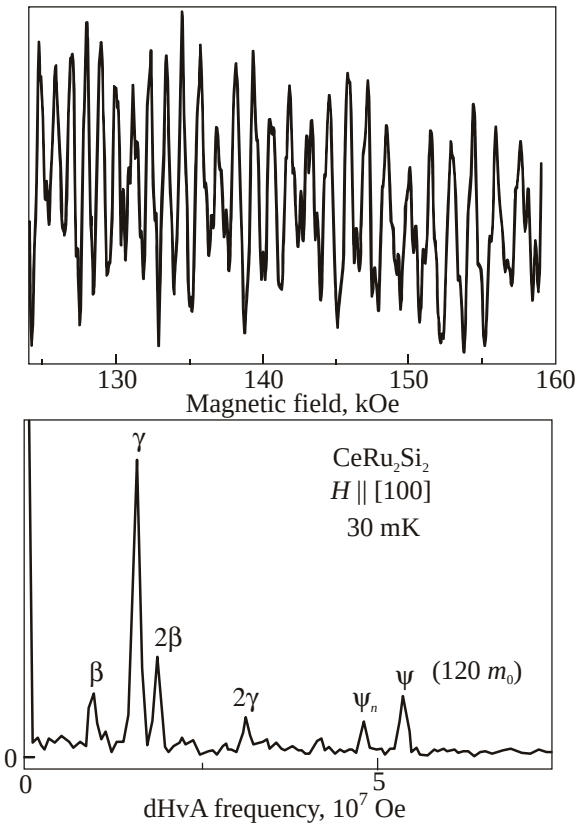

Fig. 72. dHvA oscillation (*a*) and the corresponding FFT spectrum of $CeRu_2Si_2$ for the field along [100] (*b*).

havior is not of the first-order. We may expect that the heavy fermion state at $H < H_m$ is continuously connected to the high-field spin-polarized state where the magnetic moment at each cerium site is polarized along the field direction of [001]. Note that the magnetic moment of the doublet in the 4*f*-CEF scheme is about 1 μ_B/Ce. When the magnetic moment is tilted from [001], the metamagnetic field increases as a function of 1/ cos θ, where θ is a field-tiled angle. The present metamagnetism is of an Ising-type.

The Fermi surface was observed by the dHvA experiment in magnetic fields up to 190 kOe at low temperatures down to 20 mK [111–113]. Figure 72 shows the dHvA oscillation for $H \parallel [100]$ and the corresponding FFT spectrum. Figure 73 shows the angular dependence of the dHvA frequency, which was obtained below H_m, and the result of the energy band calculations under the assumption that the 4*f*-electrons in the Ce ions are itinerant. All the dHvA branches are identified as follows:

branches ψ and ψ_n : band 14-hole.
branches κ, ε and α : band 15-electron.
branch γ : band 13-hole.
branch β : band 12-hole.

The theoretical Fermi surface is shown in Fig. 74 [114]. The experimental dHvA result is in good agreement with the 4*f*-itinerant band model, although the calculated Fermi surfaces have a slightly larger volume than the experimental surfaces. The branches ψ and ψ_n have an extremely large cyclotron mass of $120\,m_0$. The cyclotron mass is about 60 times larger than the corresponding band mass because the many-body Kondo effect is not included in the usual band calculations.

The metamagnetic behavior occurs at 77 kOe for $H \parallel [001]$, as mentioned above. Figure 75 shows the magnetic field dependence of dHvA frequency and cyclotron

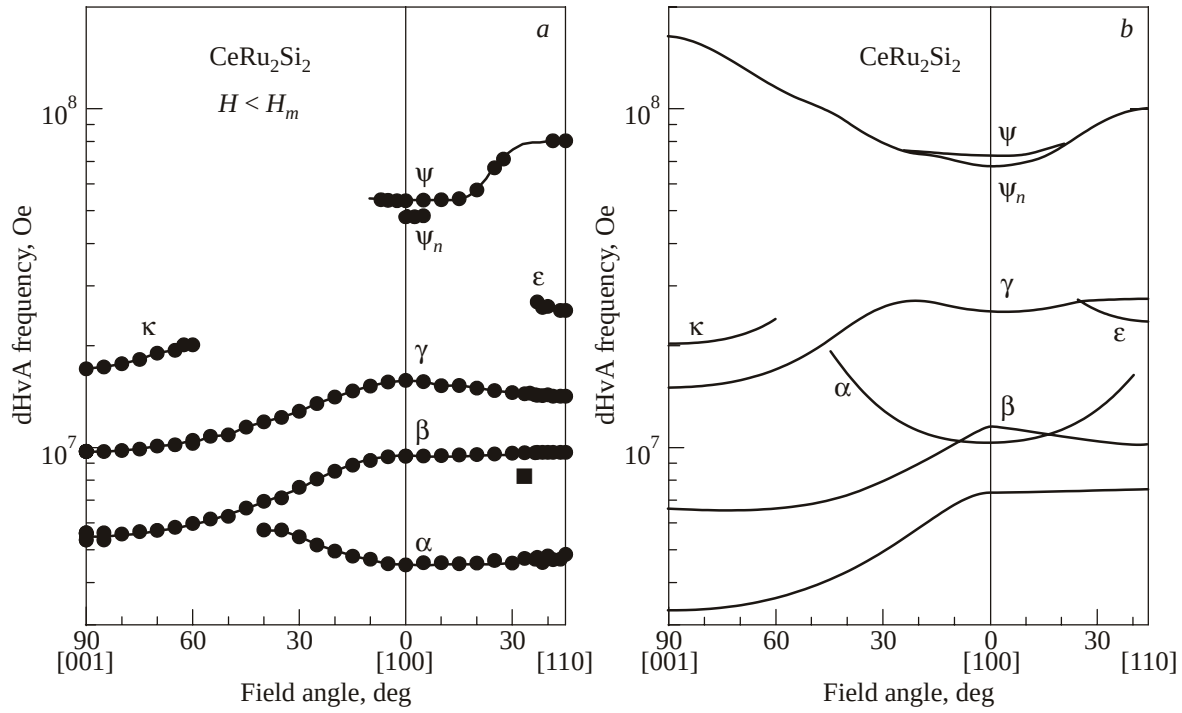

Fig. 73. Angular dependence of the dHvA frequency below H_c (*a*) and the result of the 4*f*-itinerant band calculations of $CeRu_2Si_2$ (*b*), cited from Refs. 113, 114.

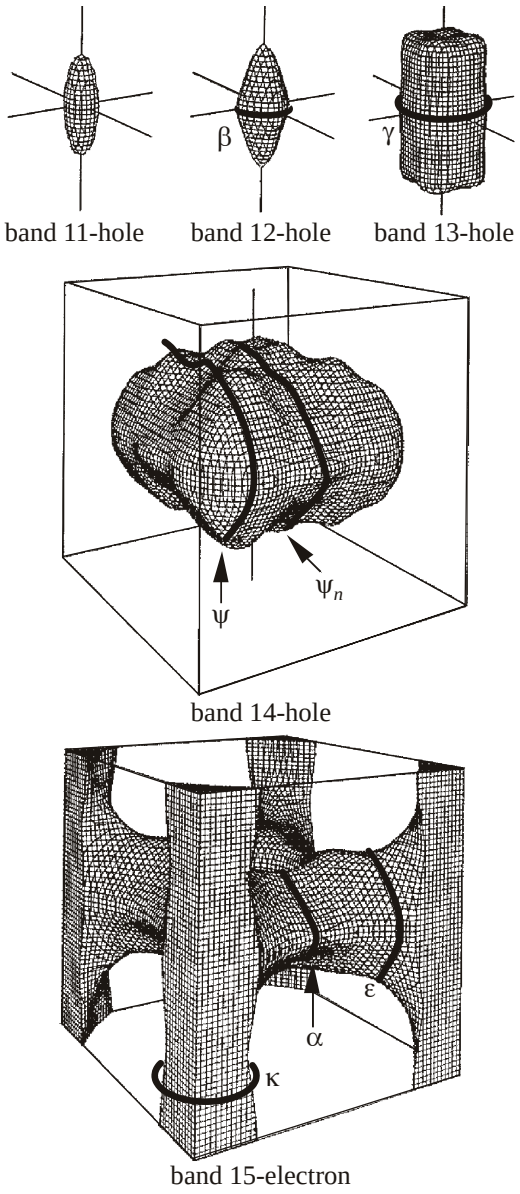

Fig. 74. Theoretical Fermi surface of $CeRu_2Si_2$ below H_c, cited from Ref. 114.

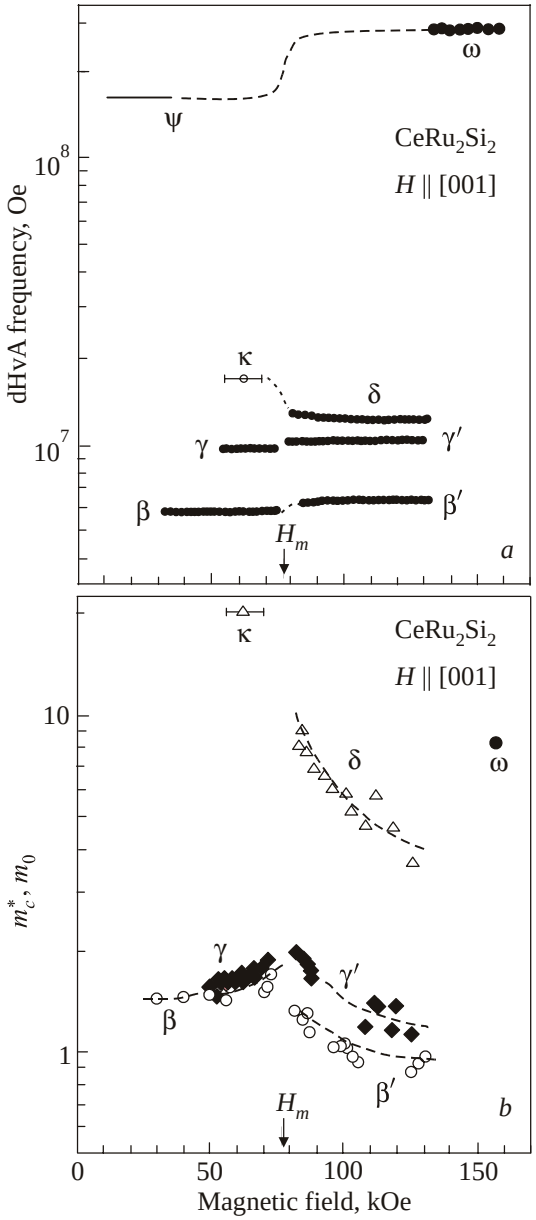

Fig. 75. Field dependence of the dHvA frequency (*a*) and cyclotron mass (*b*) for $H \parallel [001]$ in $CeRu_2Si_2$, cited from Ref. 113.

mass for $H \parallel [001]$ [111–113]. A step-like change of dHvA frequency, together with a change of the cyclotron mass, is observed at H_m. After the metamagnetic behavior, i.e. at $H > 77$ kOe, a larger Fermi surface is observed for $H \parallel [001]$ [111–113]. This dHvA frequency is the same as that of the main band 14-hole Fermi surface in $LaRu_2Si_2$, as shown in Fig. 76. Note that the experimental dHvA result of $LaRu_2Si_2$ is consistent with the theoretical calculation [115]. This result claims that the nature of the 4*f*-electrons in $CeRu_2Si_2$ is changed from itinerant to localized. The Fermi surface of $LaRu_2Si_2$ is shown in Fig. 77.

These results of dHvA experiments are not consistent with those of the magnetization experiments mentioned above. The dHvA results reveal that the spin-polarized state in $H > H_m$ is equal to the localized 4*f*-electron state from the viewpoint of the topology of the Fermi surface,

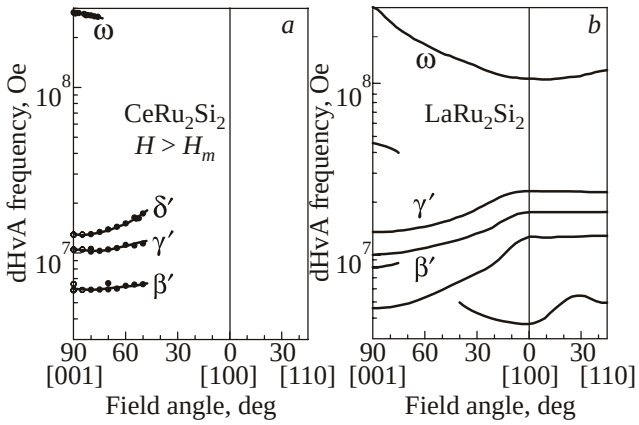

Fig. 76. Angular dependence of experimental dHvA results above H_c for $CeRu_2Si_2$ (*a*) and the band calculation results of $LaRu_2Si_2$ (*b*), cited from Refs. 113, 115.

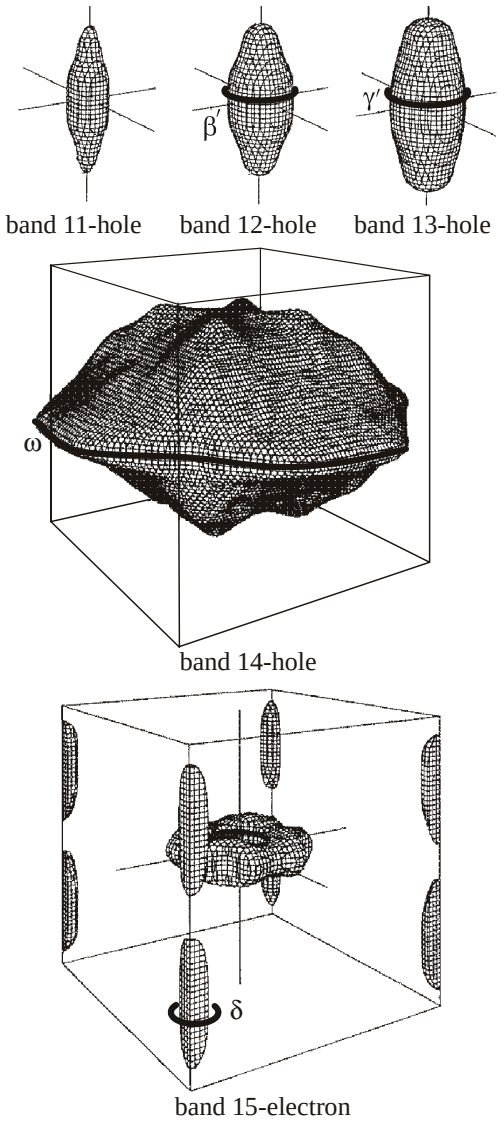

Fig. 77. Theoretical Fermi surface of $LaRu_2Si_2$, cited from Ref. 115.

indicating a change of 4*f*-electron nature from itinerant to localized at H_m, while the magnetization results indicate that the heavy fermion state in $H < H_m$ is continuously connected to the high-field spin-polarized state in $H > H_m$.

The metamagnetic behavior in $CeRu_2Si_2$ was considered to be an abrupt non-linear increase of the magnetization of which the magnetic field H_m is plotted as a function of temperature, as shown in Fig. 78,*a* [109,110]. Direct and clear evidence was obtained by the specific heat experiment [116]. Two peaks were observed in the field dependence of the specific heat above 0.5 K, as shown in Fig. 79. The phase diagram thus corresponds to that shown in Fig. 78,*b* [116,117]. These results were explained by the Zeeman effect of the conduction electrons with the characteristic density of states.

A change of the 4*f*-electronic state, which occurs below $T_{\chi max}$, is not of the first order because the many-body Kondo effect is not of a first order transition. Therefore, a change of the Fermi surface which occurs at $H > H_m$

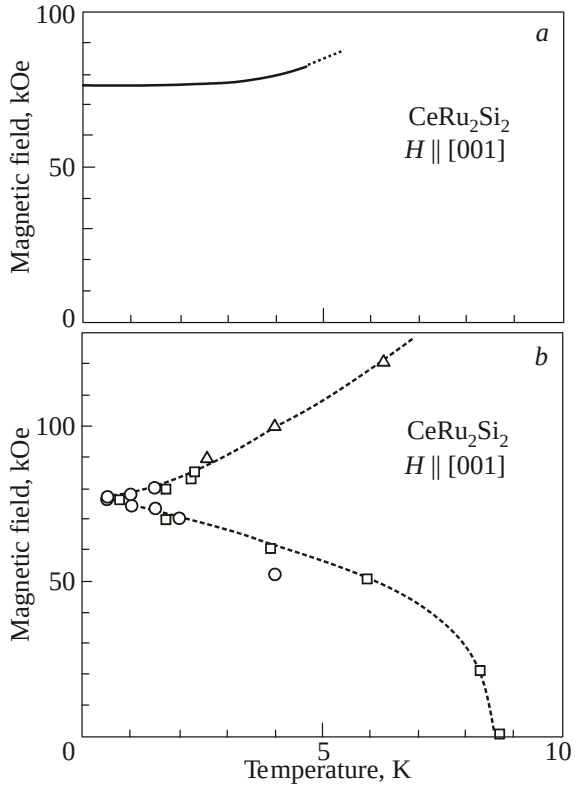

Fig. 78. Temperature dependence of metamagnetic field (*a*) and phase diagram of $CeRu_2Si_2$, which was determined from the specific heat (shown by circles) and from the thermal expansion coefficient (shown by squares and triangles) (*b*), cited from Refs. 109, 110, 116, 117.

should not be of the first order, although the present change of the Fermi surface at H_m reveals the first-order phase transition. It is not easy to understand the present metamagnetic behavior because it occurs in a small field region around H_m with $T \to 0$, as shown in Fig. 78,*b*.

Several theories were presented to explain the metamagnetic behavior in $CeRu_2Si_2$, but this is still an open question [118–120].

A similar metamagnetic behavior occurs in $CeFe_2Ge_2$ [121] and $CeCu_6$ [122]. The relation between $T_{\chi max}$ and H_m for these compounds is later shown in Fig. 90 [123].

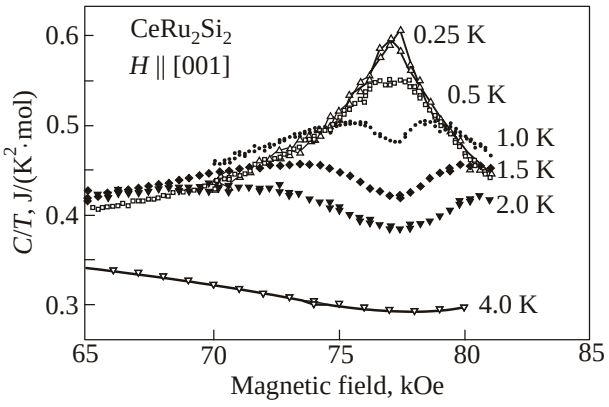

Fig. 79. Magnetic field dependence of the specific heat in $CeRu_2Si_2$, cited from Ref. 116.

6.2. 5f-itinerant heavy fermion compound: UPt_3

UPt_3 with the hexagonal structure is a well-known heavy superconductor in which unconventional pairing state is realized [11]. To understand the 5*f*-electron nature, it is essentially important to clarify the Fermi surface property [124,125].

Figure 80 shows the angular dependence of the dHvA frequency. The origin of the detected dHvA branches is identified on the basis of the 5*f*-itinerant band model. Figure 81 shows the theoretical Fermi surfaces. The branches are as follows:

branch ω: band 37-electron

branch τ , σ, ρ, λ, ε and α: band 36-hole

branch *δ*: band 35-hole.

The dHvA frequencies, shown by circles in Fig. 80, are in good agreement with theoretical results (solid lines) based on the 5*f*-itinerant band model. The dHvA branch ω possesses the largest cross-sectional area and cyclotron mass. The mass is determined as $80\,m_0$ in the field range of 150 to 175 kOe for the field along [0001], $105\,m_0$ in the field range of 182 to 196 kOe for $[10\bar{1}0]$ and $90\,m_0$ in the field range of 170 to 196 kOe for $[11\bar{2}0]$. The corresponding band masses are 5.09, 6.84 and $5.79\,m_0$, respectively. The cyclotron masses are about 15 times larger than the corresponding band masses. It should be noted that all the conduction bands contain a 5*f*-electron component of about 70% at the Fermi energy.

UPt_3 exhibits the metamagnetic behavior at about 200 kOe as in $CeRu_2Si_2$. Figure 82 shows the high-field magnetization curve. This metamagnetic behavior persists up to $T_{\chi max}$ ($\simeq$ 20 K) where the magnetic susceptibility has

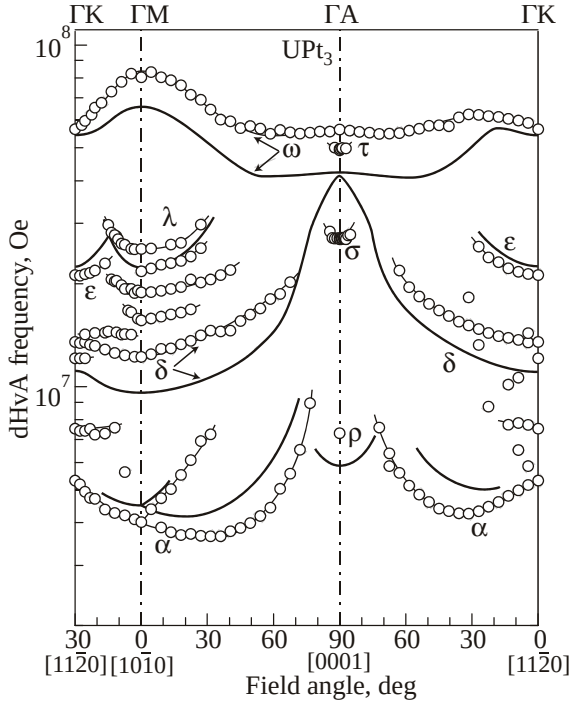

Fig. 80. Angular dependence of the dHvA frequency in UPt_3, cited from Ref. 125. Theoretical results are shown by solid lines.

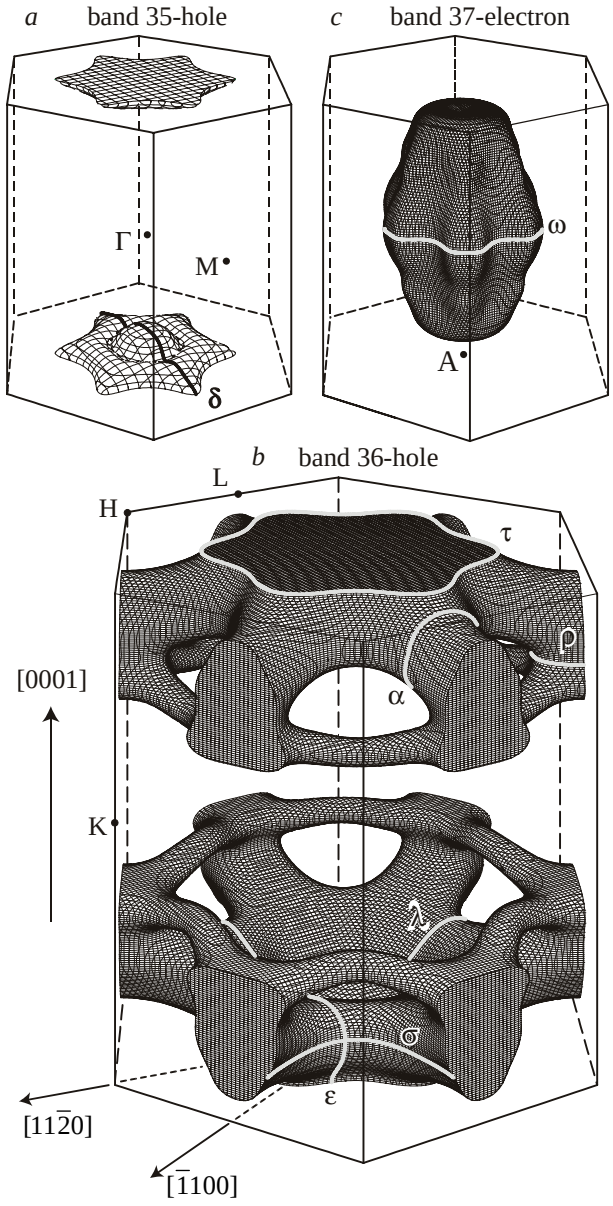

Fig. 81. Fermi surfaces in UPt_3, cited from Ref. 125.

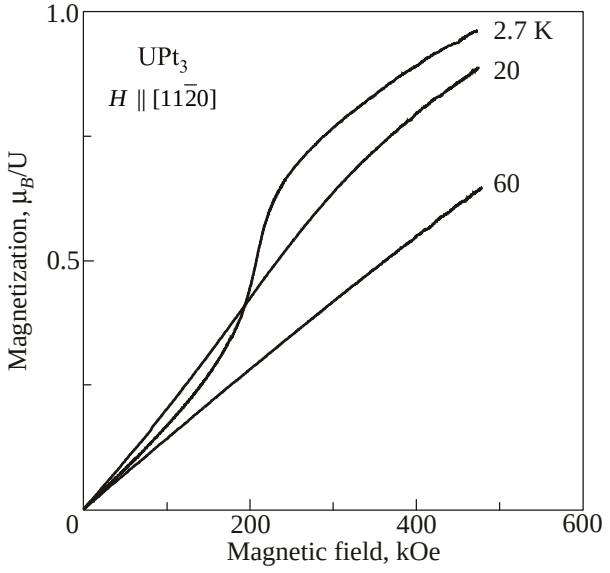

Fig. 82. High-field magnetization in UPt_3, cited from Ref. 126.

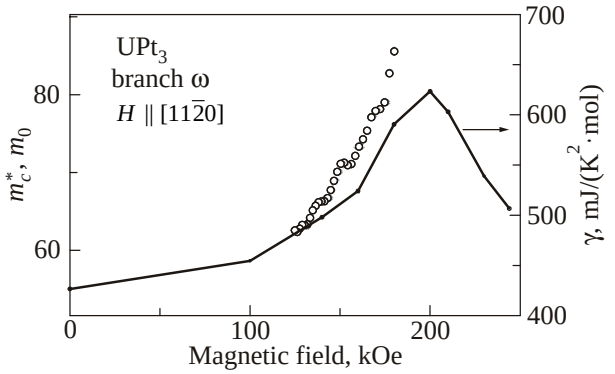

Fig. 83. Field dependence of the cyclotron mass and the γ value in UPt_3 [126]. The result of the γ value was cited from Ref. 127.

a maximum in the temperature dependence, as shown in Fig. 2. Here we note the growth of the cyclotron effective mass at this metamagnetic field $H_m \simeq 200$ kOe, as shown in Fig. 83. The mass in the main band 37-electron Fermi surface, named branch ω, is strongly enhanced with increasing the field from $63\,m_0$ at 125 kOe to $86\,m_0$ at 180 kOe [126]. This is roughly consistent with the field dependence of the γ value shown in Fig. 83 [127].

It can be thus concluded that the 5*f*-electrons in UPt_3 are of itinerant nature. Namely, the dHvA results are well explained by the 5*f*-itinerant band model. All the branches are heavy, with cyclotron masses of 15–$105\,m_0$, i.e. ten to twenty times larger than the corresponding band masses. The mass enhancement is caused by magnetic fluctuations, where the freedom of charge transfer of the 5*f* electrons appears in the form of the 5*f*-itinerant band but the freedom of spin fluctuations of the same 5*f* electrons enhances the effective mass as in the many-body Kondo effect. These heavy conduction electrons or quasiparticles condense into Cooper pairs. To avoid a large overlap of the wave functions of the paired particles, the heavy fermion state would rather choose an anisotropic channel, like a *p*-wave spin triplet to form Cooper pairs in UPt_3.

6.3. Heavy fermion state in YbT_2Zn_{20} (T: Co, Rh, Ir)

In the usual Ce compounds, the magnetic ordering occurs on the basis of the RKKY interaction, as in an antiferromagnet $CeCu_2Ge_2$ with $T_N = 4.2$ K [128]. This is because the ground state is the Kramers doublet in the 4*f*-CEF scheme. On the other hand, the Néel temperature is close to zero in a heavy fermion superconductor $CeCu_2Si_2$, via the many-body Kondo effect [129]. This is because the ionic radius of Ge is larger than that of Si. In fact, the antiferromagnetic state of $CeCu_2Ge_2$ is changed into a superconducting state by applying pressure: $T_N \to 0$ for $P \to P_c = 8$ GPa in $CeCu_2Ge_2$ [130]. The electronic states of two compounds are schematically presented in the well-known Doniach phase diagram, as shown in Fig. 84 [4].

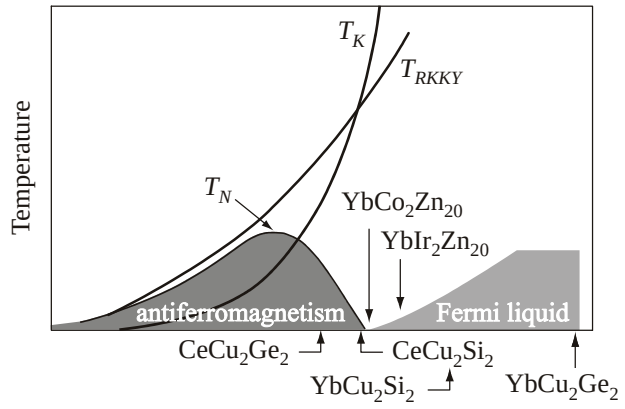

Fig. 84. Doniach phase diagram.

Yb compounds possess the similar Kramers doublet in the 4*f*-CEF scheme and are expected to order magnetically at low temperatures. $YbCu_2Si_2$ with the tetragonal crystal structure and $YbIr_2Zn_{20}$ with the cubic crystal structure compounds, however, do not order magnetically. The temperature dependence of the linear thermal expansion is characteristic [57,131], as shown in Fig. 85. The linear thermal expansion of a Pauli paramagnet $YbCu_2Ge_2$ shrinks monotonically with decreasing temperature, and becomes approximately zero at low temperatures. This is a usual behavior, indicating an unchange of the electronic state as a function of temperature. On the other hand, there

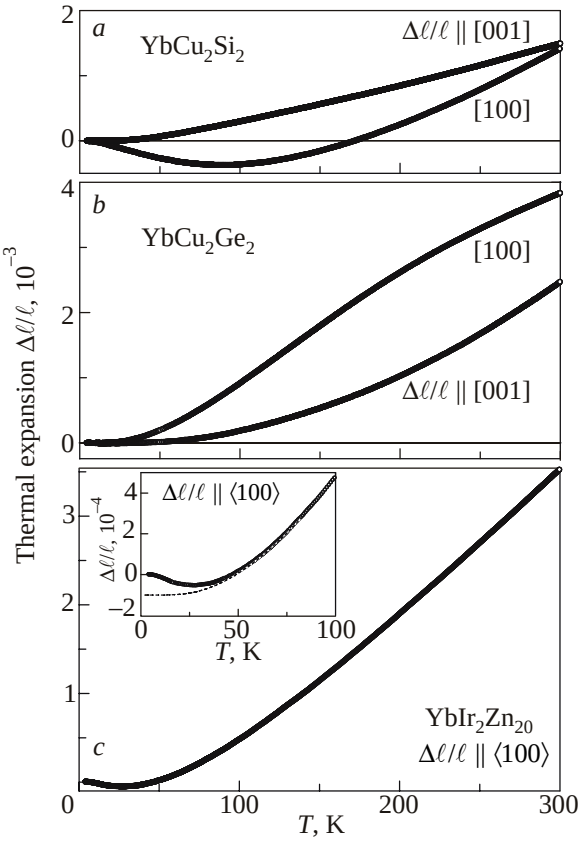

Fig. 85. Linear thermal expansions $\Delta\ell/\ell$ along [001] and [100] in $YbCu_2Si_2$ (*a*) and $YbCu_2Ge_2$ (*b*), cited from Ref. 57, and along ⟨100⟩ of $YbIr_2Zn_{20}$ (*c*), cited from Ref. 131. The inset in shows enlarged scales of the experimental data of $YbIr_2Zn_{20}$ at low temperatures (*c*). The broken line in the inset is the lattice contribution calculated on the basis of the Grüneisen relation using the specific heat data of YIr_2Zn_{20}.

appears a negative thermal expansion in $YbCu_2Si_2$ and $YbIr_2Zn_{20}$ below 90 K and 30 K, respectively, revealing that the electronic state changes from the trivalent state of the Yb ion to the 4*f*-itinerant state with decreasing temperature. In other words, $YbCu_2Si_2$ and $YbIr_2Zn_{20}$ should order antiferromagnetically if the 4*f* electrons are localized even at low temperatures. Following the Doniach phase diagram, a change of the 4*f*-localized state to a non-magnetic 4*f*-itinerant state corresponds to expansion of the volume in $YbCu_2Si_2$ and $YbIr_2Zn_{20}$. These results suggest that the non-magnetic 4*f*-itinerant state of $YbIr_2Zn_{20}$ can be tuned to the magnetically ordered state, crossing the quantum critical point, with increasing pressure. It is also noted that the electronic state of $YbCo_2Zn_{20}$ is very close to the quantum critical point even at ambient pressure, which is also shown below.

Here, YbT_2Zn_{20} (T: Co, Rh, Ir) crystallizes in the cubic $CeCr_2Al_{20}$ ($Fd\bar{3}m$) crystal structure, as shown in Fig. 86. It is remarkable that the lattice constant a = 14.187 Å in $YbIr_2Zn_{20}$ is very large, and thus the distance between Yb–Yb atoms is considerably large, 6.14 Å, compared with a = 4.20 Å in $YbAl_3$ with the $AuCu_3$-type cubic structure. Note that the Yb atom, which forms the diamond structure, as shown in Fig. 86,*a*, is coordinated by 16 zinc atoms, while the Ir atom has an icosahedral zinc coordination, forming caged structures, as shown in Fig. 86,*b*.

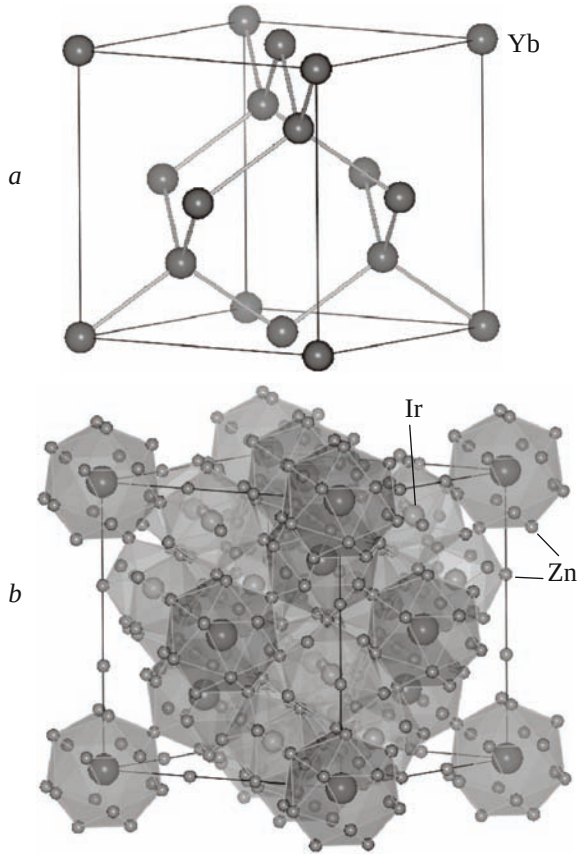

Fig. 86. Crystal strucutre of $YbIr_2Zn_{20}$, where Yb atoms form the diamond structure (*a*). Caged structure in $YbIr_2Zn_{20}$ (*b*).

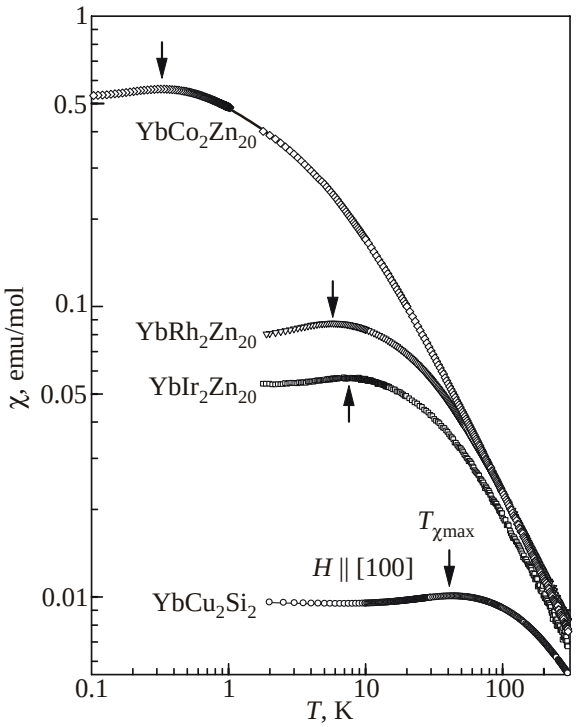

Fig. 87. Temperature dependence of the magnetic susceptibility in $YbCo_2Zn_{20}$, $YbRh_2Zn_{20}$, and $YbIr_2Zn_{20}$ for $H \parallel \langle 100 \rangle$, and in $YbCu_2Si_2$ for $H \parallel [100]$. The data above 2 K were measured by SQUID magnetometer, and the data below 1 K for $YbCo_2Zn_{20}$ were obtained by the ac-susceptibility measurement, cited from Ref. 123.

One of the characteristic properties in the heavy fermion compounds is the metamagnetic behavior or an abrupt nonlinear increase of magnetization at the magnetic field H_m below $T_{\chi max}$, as noted above. Figure 87 shows the logarithmic scale of temperature dependence of the magnetic susceptibility in $YbCu_2Si_2$, $YbIr_2Zn_{20}$, $YbRh_2Zn_{20}$ and $YbCo_2Zn_{20}$ [123,131–135]. The $T_{\chi max}$ values in these compounds, as shown by arrows in Fig. 87, are 40, 7.4, 5.8, and 0.32 K, respectively, where a low-temperature value of $T_{\chi max}$ = 0.32 K in $YbCo_2Zn_{20}$ is remarkable, revealing that the electronic state of $YbCo_2Zn_{20}$ is very close to the quantum critical point.

We measured the magnetization at 1.3 K for these compounds [123,131,133,134], as shown in Fig. 88. The metamagnetic behavior was observed at H_m = 97 kOe in $YbIr_2Zn_{20}$, 63 kOe in $YbRh_2Zn_{20}$, and 6 kOe in $YbCo_2Zn_{20}$, shown by arrows, where the magnetization at 1.3 K does not reveal the metamagnetic behavior, but the ac-susceptibility at 60 mK indicates a peak at H_m = 6 kOe in $YbCo_2Zn_{20}$. Here, it is noted that the metamagnetic field is almost temperature-independent below $T_{\chi max}$: H_m = 97 kOe at 1.3 K and 100 kOe at 4 K in $YbIr_2Zn_{20}$, for example. In $YbCo_2Zn_{20}$, we also observed the metamagnetic behavior below $T_{\chi max}$ = 0.32 K, as shown in Fig. 89,*a*. Interesting is a magnetic phase diagram in Fig. 89,*b*, which is very similar to the phase diagram of $CeRu_2Si_2$ shown in Fig. 78. Namely, the specific heat coefficient C/T of $YbCo_2Zn_{20}$ has a

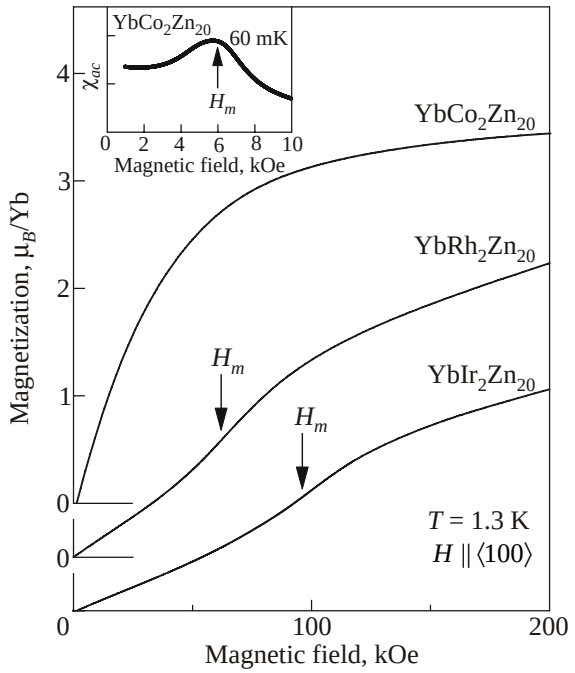

Fig. 88. Magnetization curves at 1.3 K in YbT_2Zn_{20} (T: Co, Rh, Ir). Inset shows the field dependence of the ac-susceptibility at 60 mK in $YbCo_2Zn_{20}$, cited from Ref. 123.

two-peak structure in the field dependence, as shown in Fig. 79 for $CeRu_2Si_2$. Such two-peak structure in *C/T* is not observed in $YbIr_2Zn_{20}$ and $YbRh_2Zn_{20}$.

The metamagnetic behavior thus appears at H_m below $T_{\chi max}$. The present results are summarized in Fig. 90, representing a relation between $T_{\chi max}$ and H_m in several Ce, Yb, and U compounds: H_m (kOe) = $15T_{\chi max}$ (K). This relation corresponds to $\mu_B H_m = k_B T_{\chi max}$ [123,136].

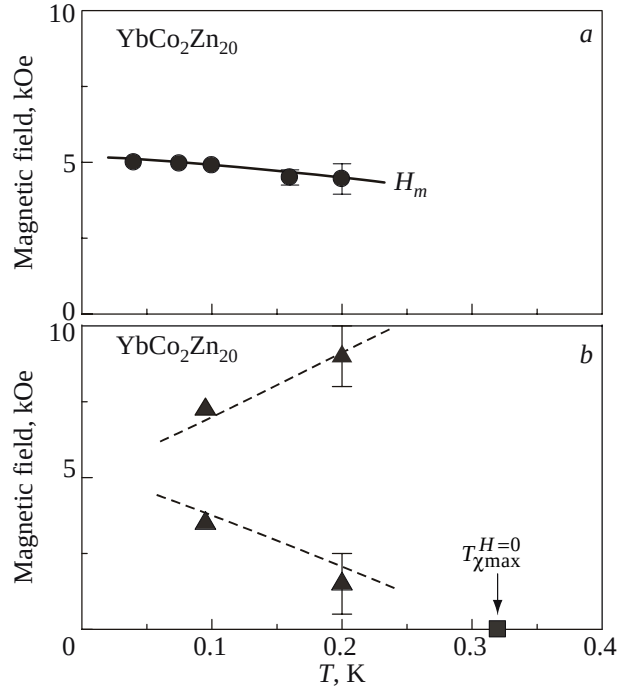

Fig. 89. Temperature dependence of the metamagnetic field (*a*) and phase diagram of $YbCo_2Zn_{20}$ which was determined from the specific heat (shown by triangles) (*b*), cited from Ref. 134.

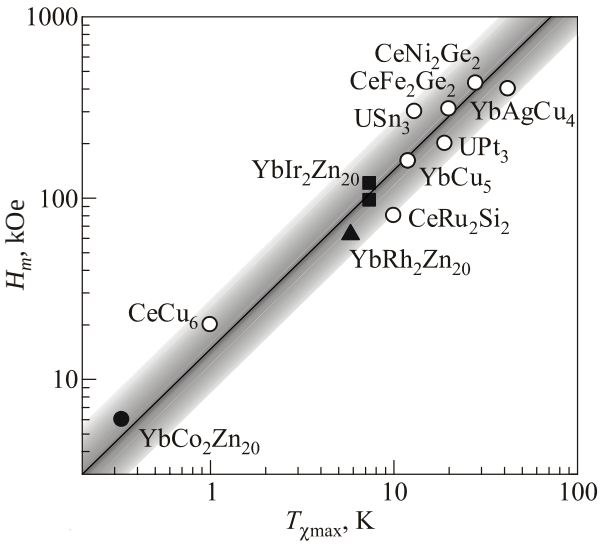

Fig. 90. Relation between $T_{\chi max}$ and H_m in several Ce, Yb, and *U* compounds. The solid line represent the relation of H_m (kOe) = $=15T_{\chi max}$ (K), cited from Ref. 123.

We studied the metamagnetic behavior of $YbIr_2Zn_{20}$ via the dHvA experiment. Figure 91 shows the magnetic field dependence of dHvA frequency named branch β and cyclotron mass, together with the $\sqrt{A}$ value in the electrical

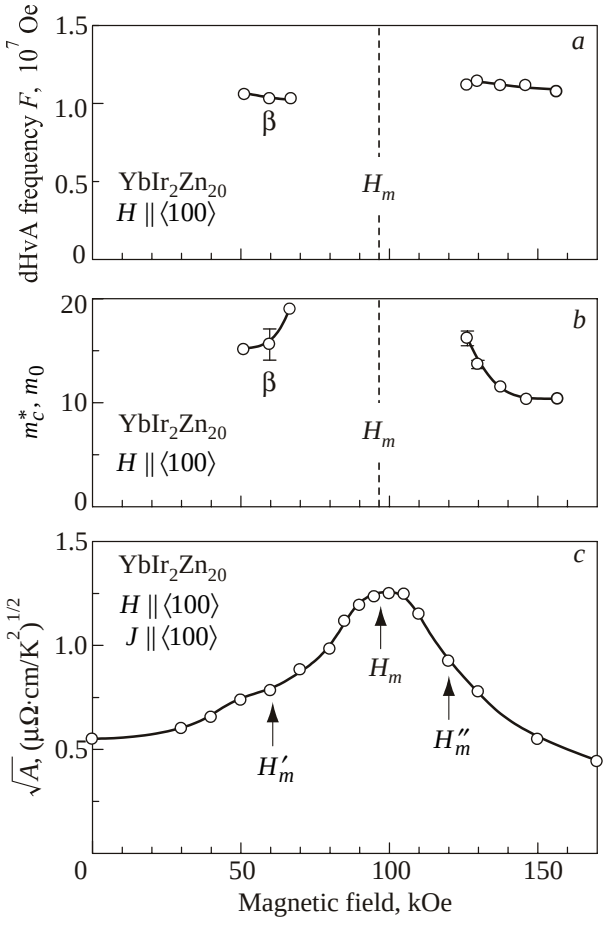

Fig. 91. Magnetic field dependences of the dHvA frequency of branch β (*a*), the corresponding cyclotron mass m_c^* (*b*), and $\sqrt{A}$ for $H \parallel \langle 100 \rangle$ in $YbIr_2Zn_{20}$ (*c*), cited from Ref. 131.

resistivity $\rho = \rho_0 + AT^2$ under magnetic field, for $H \parallel \langle 100 \rangle$. The dHvA frequency is approximately unchanged above and below H_m = 97 kOe, which is highly different from the result of $CeRu_2Si_2$ shown in Fig. 75. The cyclotron mass of branch β ($F = 1.1 \cdot 10^7$ Oe), however, has a maximum around H_m, following a field dependence of $\sqrt{A}$, which is the same result of $CeRu_2Si_2$ shown in Fig. 75.

We measured the magnetoresistance at 0.1 K under several pressures for $YbIr_2Zn_{20}$. With increasing pressure, the metamagnetic field H_m = 97 kOe at ambient pressure, shown by an arrow, shifts to lower magnetic fields and becomes zero at $P_c \simeq 5.2$,GPa [135], as shown in Fig. 92. It is remarkable that a shoulder-like feature of metamagnetic behavior at 0 and 1.2 GPa is changed into a sharp peak at higher pressures. The present peak, associated with the metamagnetic behavior, is a guiding parameter to reach the quantum critical point: $P \to P_c$ for $H_m \to 0$, as shown in Fig. 93,*a*. Here, the *A* value is extremely enhanced with increasing pressure and has a maximum at $P_c \simeq 5.2$ GPa, with A = 380 μΩ·cm/K^2 at 5.0 GPa, as shown in Fig. 93,*b*.

The relation between *A* and γ is known as the Kadowaki–Woods plot [137]. The *A* and γ values in YbT_2Zn_{20} (T: Co, Rh, Ir) is found to belong to the generalized Kadowaki–Woods relation for N = 4, as shown in Fig. 94 [132, 138,139]. The value of A = 380 μΩ·cm/K^2 at 0 kOe under 5.0 GPa exceeds γ = 10 J/(K^2·mol) if we follow this relation. An extremely heavy fermion state is realized in $YbIr_2Zn_{20}$

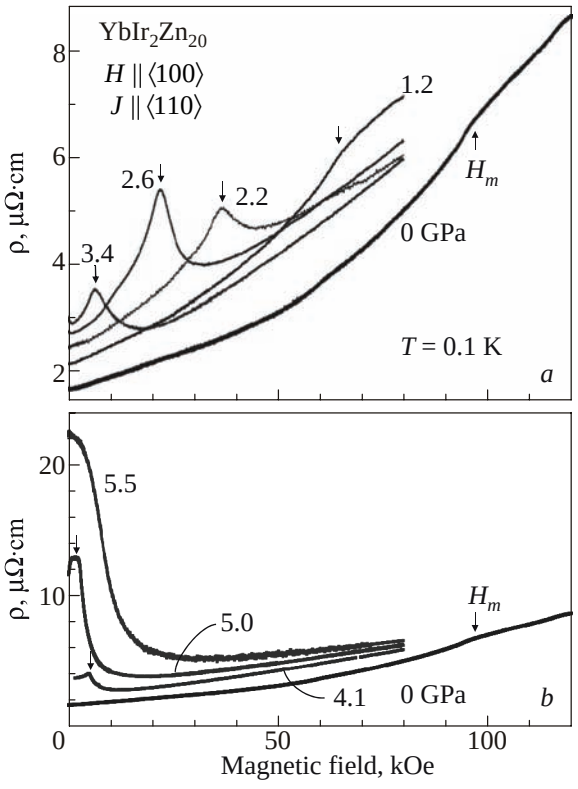

Fig. 92. Transverse magnetoresistance in the pressure region from ambient pressure to 3.4 GPa (*a*) and from 4.1 to 5.5 GPa in $YbIr_2Zn_{20}$ (*b*), cited from Ref. 135. Arrows indicate the metamagnetic transition.

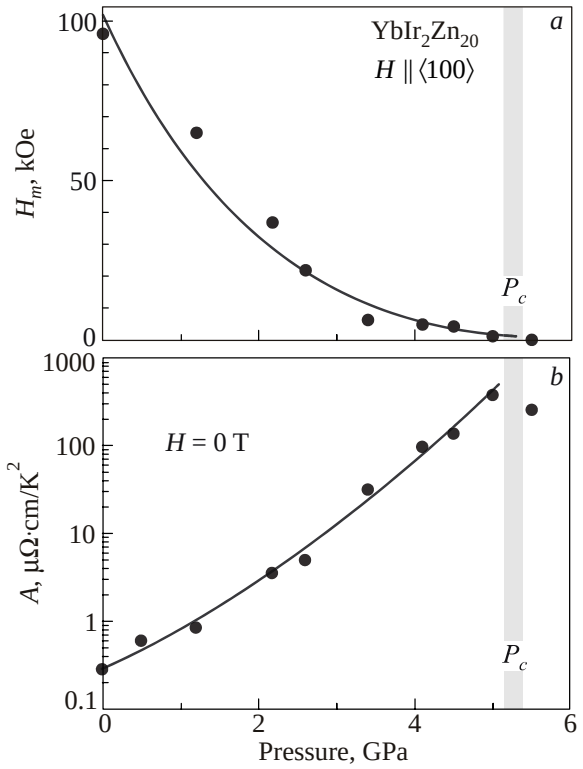

Fig. 93. Pressure dependence of H_m (*a*) and *A* values (*b*) in $YbIr_2Zn_{20}$, cited from Ref. 135. Solid lines connecting the data are guides for the eyes.

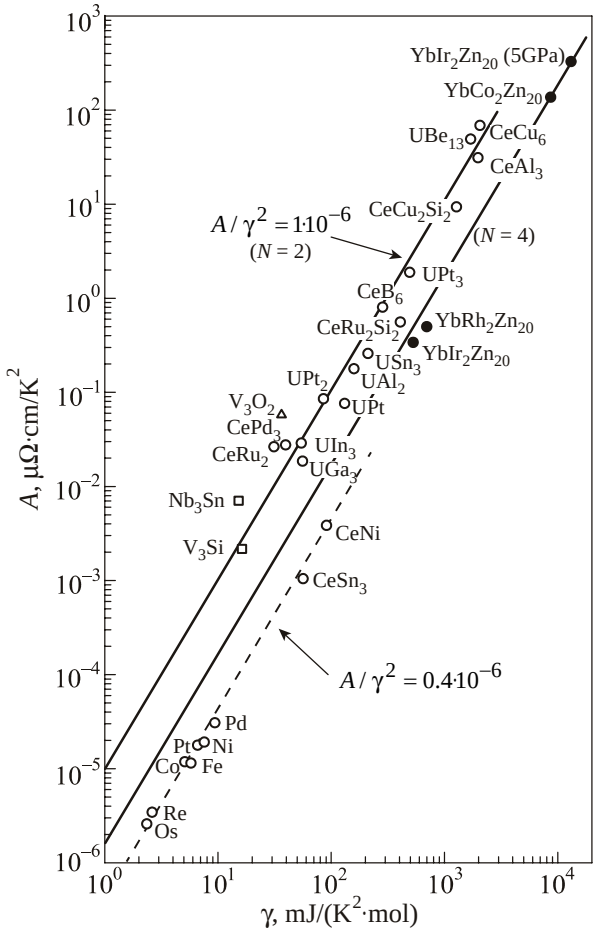

Fig. 94. Generalized Kadowaki–Woods relation in Ce, Yb, U and the other compounds.

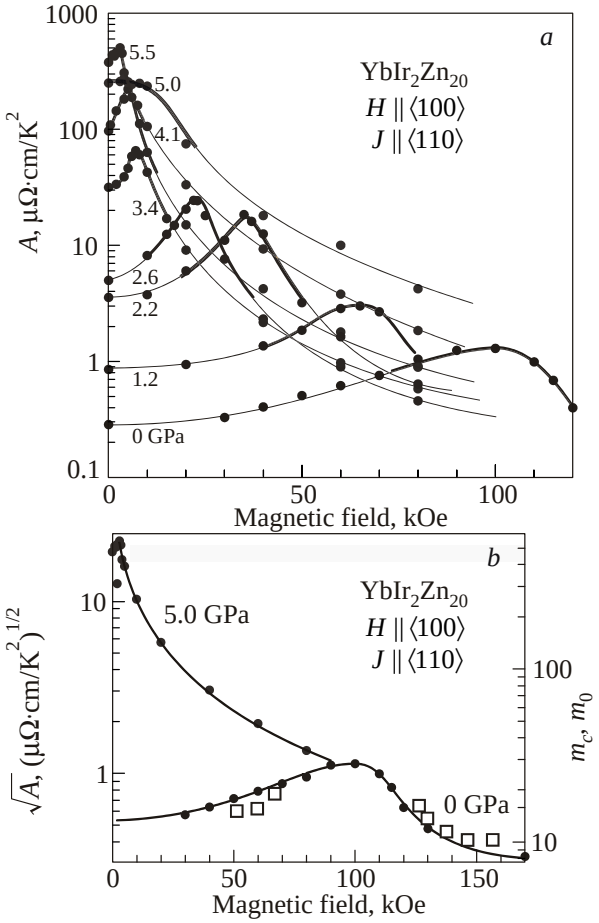

Fig. 95. Field dependence of the A value under several pressures (0–5.5 GPa) (*a*), and the $\sqrt{A}$ values under 0 and 5.0 GPa (*b*), shown by circles, and cyclotron effective mass m_c^* at 0 GPa, shown by open squares in $YbIr_2Zn_{20}$, cited from Ref. 135.

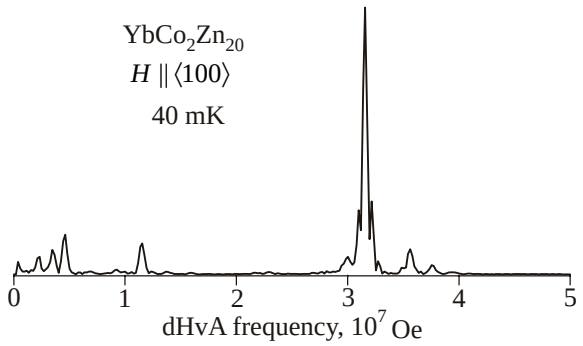

Fig. 96. FFT spectrum for $H \parallel \langle 100 \rangle$ in $YbCo_2Zn_{20}$, cited from Ref. 134.

under pressure. Surprisingly $YbCo_2Zn_{20}$ is very close to this state: $A = 160$ μΩ·cm/K^2 and $\gamma = 8 \cdot 10^3$ mJ/(K^2·mol).

We also measured the temperature dependence of the electrical resistivity below 0.8 K under magnetic fields and pressures. The Fermi liquid relation of $\rho = \rho_0 + AT^2$ is satisfied in these experimental conditions, and the obtained A value is shown in Fig. 95,*a* as a function of magnetic field. A broad peak at $H_m = 97$ kOe at ambient pressure in the A value is changed into a distinct peak at 2.2 and 3.4 GPa, together with an anomalous enhancement of A value at higher pressures: $A = 380$ μΩ·cm/K^2 at 0 kOe under 5.0 GPa, as mentioned above, which is strongly reduced with increasing magnetic field: $A = 1.45$ μΩ·cm/K^2 at 80 kOe under 5.0 GPa.

We studied the relation between $\sqrt{A}$ and the cyclotron effective mass m_c^* obtained from the dHvA experiment for $YbIr_2Zn_{20}$ [135]. Figure 95,*b* shows the field dependence of the cyclotron mass for the dHvA frequency $F = 1.1 \cdot 10^7$ Oe in the magnetic field $H \parallel \langle 100 \rangle$ at ambient pressure, as shown by open squares, revealing from $10\,m_0$ to $20\,m_0$. The cyclotron mass increases slightly with increasing magnetic fields up to H_m, but decreases gradually in much higher fields. The cyclotron mass well correlates with the $\sqrt{A}$ value at 0 GPa against the magnetic field, shown by solid circles. From the experimental results of $\sqrt{A}$ at 0 and 5.0 GPa in Fig. 95,*b*, we can estimate the cyclotron mass at 0 kOe to be about $450\,m_0$ at 5.0 GPa, revealing an extremely large cyclotron mass. In other words, a strong field quenching of the cyclotron mass is expected to occur at high magnetic fields in $YbIr_2Zn_{20}$ at 5.0 GPa.

The similar results are obtained in $YbCo_2Zn_{20}$ at ambient pressure. Figure 96 shows the FFT spectrum for $H \parallel \langle 100 \rangle$ in $YbCo_2Zn_{20}$. The dHvA frequency is in the range $1 \cdot 10^6$–$4 \cdot 10^7$ Oe. From the size of the small Brillouin zone, these dHvA branches correspond to main Fermi surfaces [131]. The cyclotron effective mass is found to be highly field-dependent, decreasing steeply with increasing

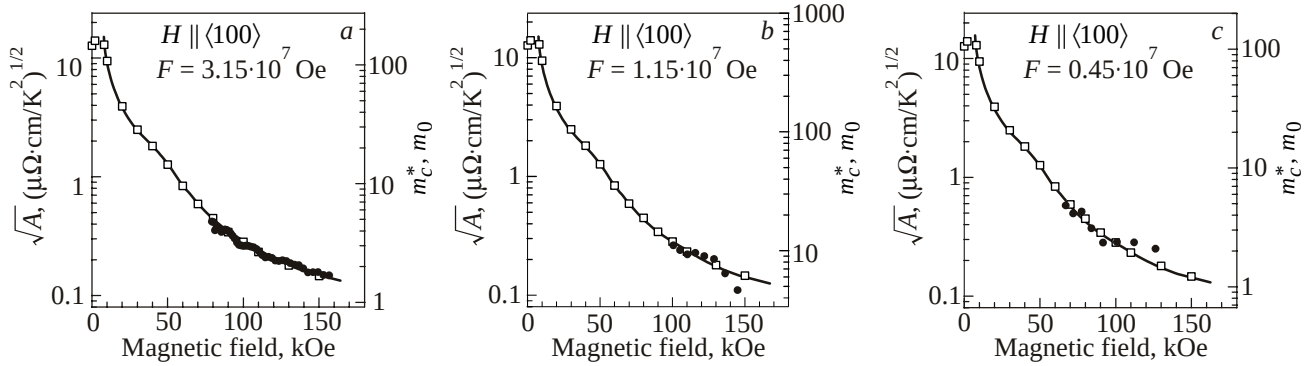

Fig. 97. Magnetic field dependence of the $\sqrt{A}$ value for $J \parallel H \parallel \langle 100 \rangle$, shown by squares, together with the field dependence of the cyclotron effective mass m_c^*, shown by closed circles for $H \parallel \langle 100 \rangle$ in $YbCo_2Zn_{20}$, for F, Oe: $3.15 \cdot 10^7$ (*a*), $1.15 \cdot 10^7$ (*b*), and $0.45 \cdot 10^7$ (*c*), cited from Ref. 123. Solid lines connecting the data are guide lines.

magnetic field. Figures 97,*a*,*b*,*c* show the field dependence of the cyclotron mass for the dHvA frequency F = $= 3.15 \cdot 10^7$, $1.15 \cdot 10^7$, and $0.45 \cdot 10^7$ Oe, respectively, together with the $\sqrt{A}$ value obtained from the electrical resistivity under magnetic field.

Following the Fermi liquid relation, the $\sqrt{A}$ value well correlates with the cyclotron effective mass. The cyclotron mass at 0 kOe is thus estimated to be 150, 500, and $110\,m_0$, respectively. The present experimental results indicate, however, that the super-heavy effective masses at 0 kOe are quenched, or strongly reduced in high magnetic fields.

6.4. Field-induced ferroquadrupolar ordering in $PrCu_2$

The quadrupolar interaction is of basic importance in the *f*-electron magnetism as well as the magnetic interactions such as the RKKY interaction and the many-body Kondo effect. The quadrupole moment is obtained from the electrostatic energy:

$$\mathcal{H} = \int \rho(r) V(r)\, d^3r =$$

$$= ZeV(0) + \sum_j P_j \left(\frac{\partial V}{\partial x_j} \right)_0 + \frac{1}{2} \sum_{j,k} Q_{jk} \left(\frac{\partial^2 V}{\partial x_j \partial x_k} \right) + \ldots, \quad (16)$$

$$Ze = \int \rho(r)\, d^3r\,, \quad (17)$$

$$P_j = \int \rho(r) x_j\, d^3r\,, \quad (18)$$

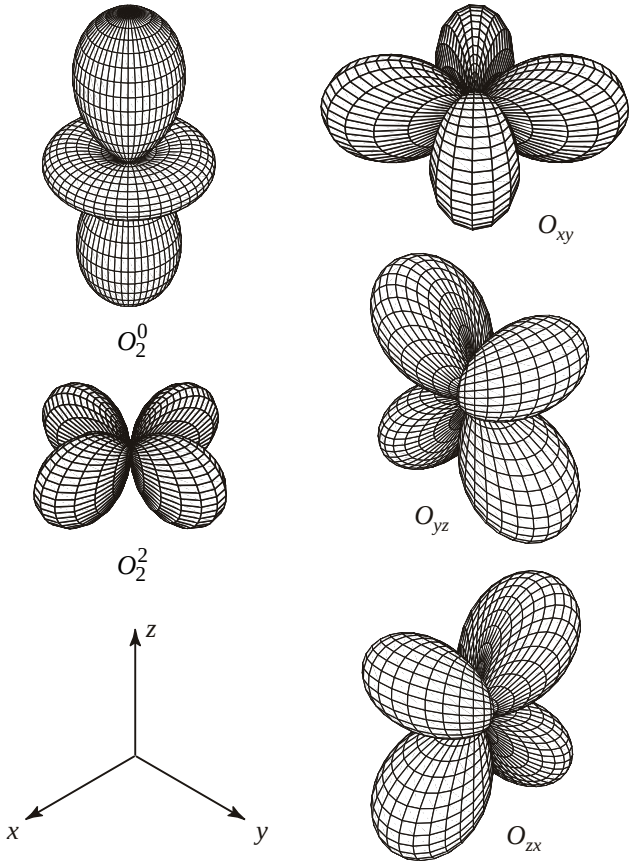

Fig. 98. Schematic view of the quadrupole moments.

$$Q_{jk} = \int \rho(r) x_j x_k\, d^3r\,, \quad (19)$$

where $\rho(r)$ is the charge distribution of the *f*-electrons in the rare earth and uranium compounds, $V(r)$ is the electrostatic potential, Ze is the charge of the *f*-electrons, P_j is a dipole term and Q_{jk} is a quadrupole term. The independent terms in $x_j x_k$ of Eq. (19) are the following five: $2z^2 - x^2 - y^2$, $x^2 - y^2$, xy, yz and zx. These are converted into the quadrupole moments $(2J_z^2 - J_x^2 - J_y^2)/\sqrt{3} = O_2^0$, $J_x^2 - J_y^2 = O_2^2$, $J_x J_y + J_y J_x = O_{xy}$, $J_y J_z + J_z J_y = O_{yz}$ and $J_z J_x + J_x J_z = O_{zx}$, respectively, as shown in Fig. 98.

The quadrupole moment $O_{\Gamma\gamma}$ couples to the strain $\varepsilon_{\Gamma\gamma}$ and distorts the crystal. For example, the cubic structure in CeAg is changed into a tetragonal structure when O_2^0 becomes the order parameter below 16 K [140]. This is because O_2^0 couples to the strain ε_u, which brings about expansion along the *z*-axis and shrinkage along the *x*-and *y*-axes.

In the following we discuss the metamagnetic transition based on the quadrupolar interaction $\langle O_2^0 \rangle$ in $PrCu_2$ [141–143]. The crystal structure of $PrCu_2$ is orthorhombic. This can be viewed as a distorted hexagonal AlB_2 type structure, as shown in Fig. 99,*a*. $PrCu_2$ is a van Vleck paramagnetic compound in which the quadrupolar interaction plays an important role in the magnetic behavior.

Figure 100 shows the magnetization curves at 15 K for three principal axes. The *c*-axis magnetization M_c is the hard-axis magnetization, while M_a corresponds to the easy-axis magnetization. Both magnetizations should show almost the same curves if $PrCu_2$ forms the hexagonal structure, but they indicate highly different behavior. This is due to the CEF effect based on the orthorhombic symmetry.

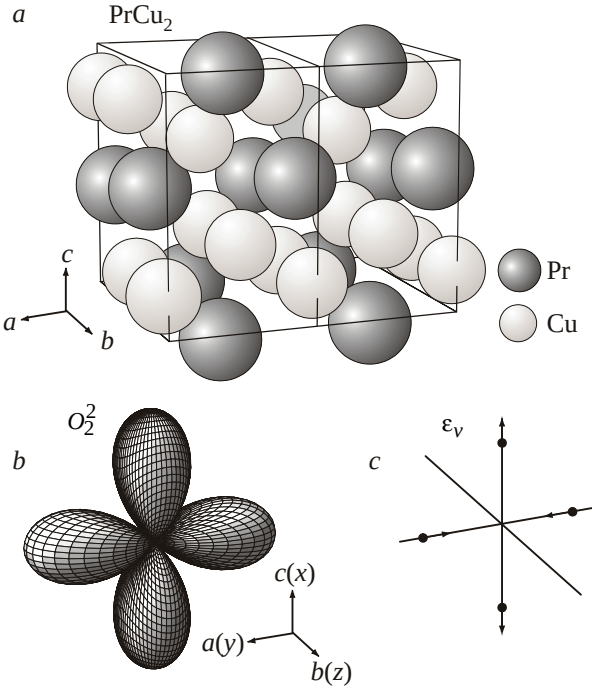

Fig. 99. Crystal structure with two unit cells (*a*), quadrupole moment O_2^2 (*b*) and local distortion ε_v of $PrCu_2$ (*c*).

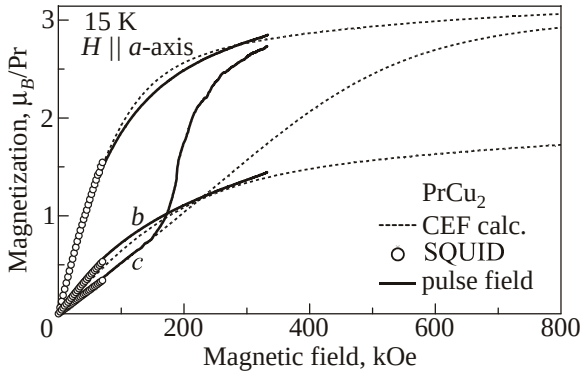

Fig. 100. Magnetization curves of $PrCu_2$. Thick lines, open circles and dotted lines show the pulse-field experimental curves, SQUID magnetometer data and CEF calculated curves, respectively, cited from Ref. 143.

M_c shows a metamagnetic transition at H_c = 200 kOe and reaches the *a*-axis magnetization M_a at higher fields. In fact it shows the M_a-curve with decreasing magnetic field, showing a large hysteresis. On increasing the field again, M_c is changed into M_a. This metamagnetic transition thus brings about the conversion between the hard *c*-and easy *a*-axis magnetizations. To elucidate this metamagnetic transition, we show in Fig. 100 the calculated magnetizations (broken lines) based on the CEF effect. We also note

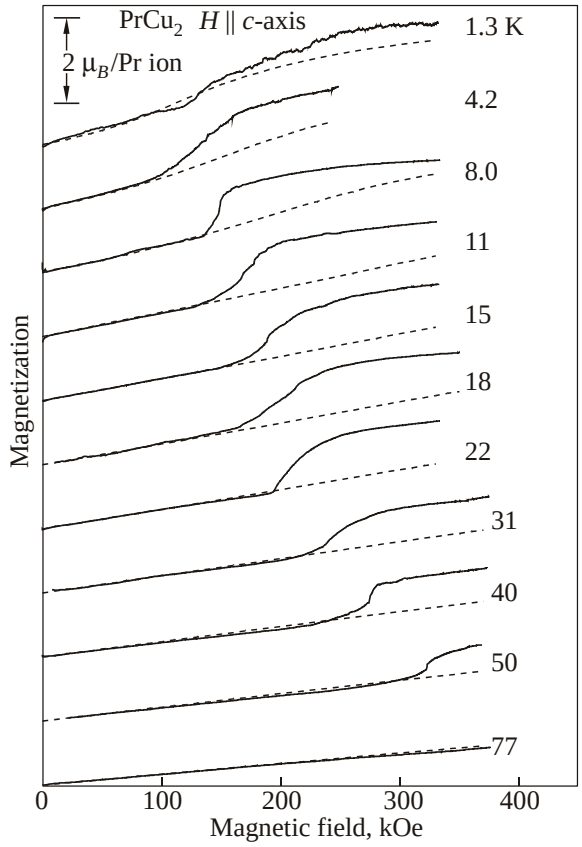

Fig. 101. Magnetization curves of $PrCu_2$. Thick lines and dotted lines show the experimental and CEF calculated curves, respectively, cited from Ref. 143.

that the critical field for this metamagnetic transition increases with increasing temperature, from 80–90 kOe at 1.3–4.2 K to 320 kOe at 50 K, as shown in Fig. 101.

The present metamagnetic transition is also observed in the electrical resistivity, magnetostriction and dHvA experiments [141,142]. Figure 102 shows the corresponding magnetostriction curves. First, the magnetic field was applied along the *c*-axis, as shown by open circles in Fig. 102,*a*. The magnetostriction ε_c along the *c*-axis steeply increases at 90 kOe by about 0.5% and then increases smoothly up to 140 kOe; see the processes (*1*) and (*2*) in Fig. 102,*a*. On decreasing the field, the magnetostriction decreases slightly, showing a large hysteresis. A large residual strain of 0.5% remains in the sample.

Next we rotated the sample by 90° and applied the field along the *a*-axis. The magnetostriction initially decreases monotonically and shows a step-like decrease at 90 kOe, as shown by the processes (*2*) and (*1′*). The strain in the sample, which is brought about by the metamagnetic transition in the field along the *c*-axis, is released by applying the field along the *a*-axis. We note that there is no such a metamagnetic transition if we first apply the field along the *a*-axis.

A similar metamagnetic transition was obtained for the magnetostriction ε_a, as shown in Fig. 102,*b*. The magnetostriction in the field along the *c*-axis steeply decreases at 60 kOe, as shown by the processes (*1*) and (*2*) in Fig. 102,*b*. The strain reaches up to 2.7% at 140 kOe. The residual strain at 0 kOe is −1.5%. The strain is released by applying the field along the *a*-axis, as shown by the processes (*2*) and (*1′*) in Fig 102,*b*, although the residual

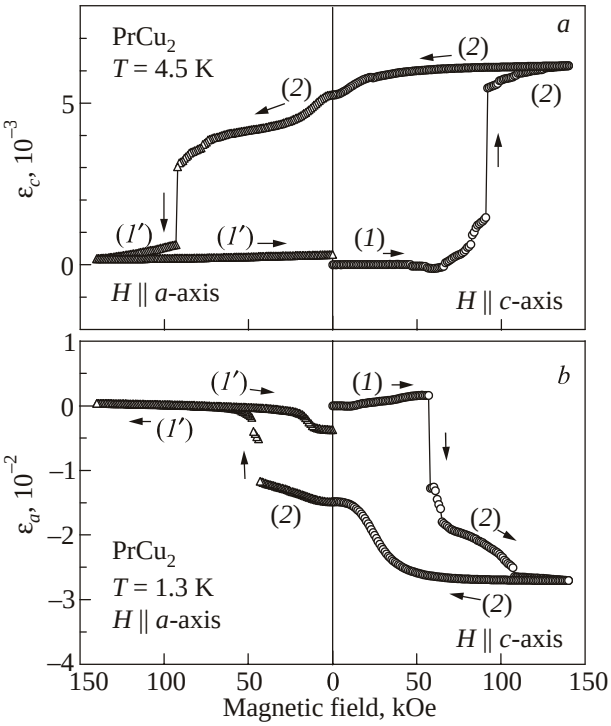

Fig. 102. Magnetostriction along the *a* (*a*) and *c* (*b*) axes of $PrCu_2$, cited from Ref. 141.

strain does not recover completely at 0 kOe, retaining a residual value of −0.4%.

The present metamagnetic transition is closely related to the distortion in the *ac*-plane. Namely, the magnetostriction along the *c*-axis, ε_c, is increased and the corresponding ε_a is decreased in magnitude. The strain relation of expansion along the *c*-axis and shrinkage along the *a*-axis corresponds to ε_v in Fig. 99,*c*. Therefore, the quadrupolar operator in this system is O_2^0, as shown in Fig. 99,*b*.

The dHvA effect is a powerful method to detect the metamagnetic transition via the electron scattering [142]. Figure 103 shows the dHvA oscillations for the field along the *a*-axis. When we first apply the magnetic field along the *a*-axis, there is no appreciable change in oscillation, showing a reversible oscillation, as shown in Fig. 103,*a*. On the other hand, the dHvA oscillation is extremely reduced in amplitude after the metamagnetic transition, as shown in Fig. 103,*b*, corresponding to the process (2) in the left-side figure of Fig. 102,*a*. As shown in Fig. 103,*b*, the dHvA oscillation is completely recovered after the metamagnetic transition, i.e. at fields higher than 74 kOe. The corresponding dHvA oscillation is again reversible against the magnetic field, as shown in Fig. 103,*c*.

We explain the present metamagnetic transition on the basis of the quadrupolar interaction $\langle O_2^0 \rangle$. First, we calculated the magnetic susceptibility in the temperature range from about 8 K to room temperature, and determined the CEF parameters and the coupling constant K_M in order to reproduce the susceptibility data and the metamagnetic field transition field on the basis of the following Hamiltonian:

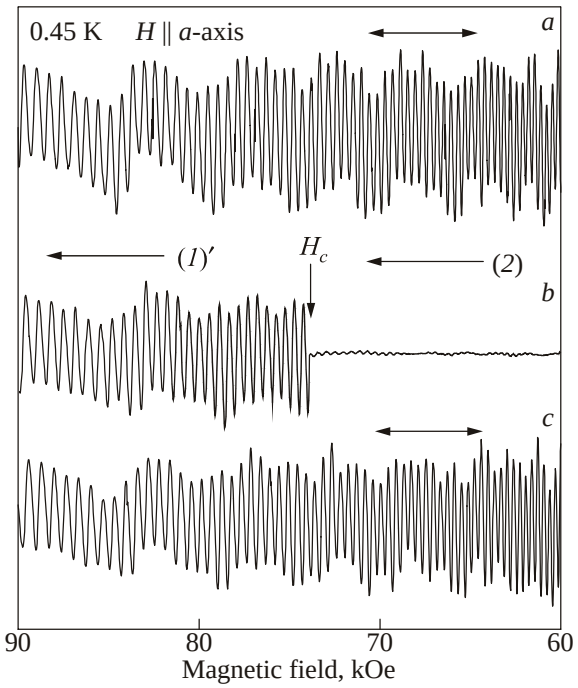

Fig. 103. dHvA oscillations of $PrCu_2$, cited from Ref. 142. Note that the magnetic field in the left-hand side is larger than that in the right-hand side.

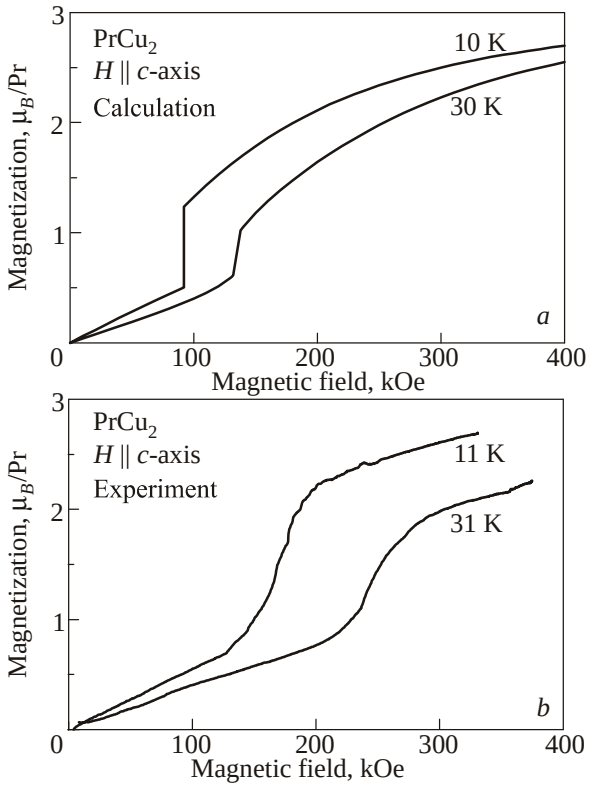

Fig. 104. Calculated (*a*) and experimental (*b*) magnetization curves of $PrCu_2$, cited from Ref. 141.

$$\mathcal{H} = \mathcal{H}_{CEF} + \mathcal{H}_{\text{Zeeman}} - K_M \langle O_2^2 \rangle O_2^2 . \qquad (20)$$

Figure 104,*a* shows the calculated magnetization curves at 10 and 30 K, where K_M is obtained as 0.3. Here, the magnetization M_α ($\alpha = x, y, z$) can be calculated by the following formula:

$$M_\alpha = g_J \mu_B \sum_n |\langle n | J_\alpha | n \rangle| \frac{e^{-\beta E_n}}{\sum_n e^{-\beta E_n}}, \qquad (21)$$

where the eigenvalue E_n and the eigenfunction $|n\rangle$ are determined by diagonalizing the total Hamiltonian in Eq. (20). We note that the *x*-, *y*- and *z*-axes correspond to the *c*-, *a*- and *b*-axes, as shown in Fig. 99,*b*. These calculated results are approximately consistent with the experimental data given in Fig. 104,*b*.

Here we note that the metamagnetic transition occurs when the sign of $\langle O_2^2 \rangle$ changes from negative to positive, as shown in Fig. 105. There are three solutions at zero field for $\langle O_2^2 \rangle$. The ground state possesses the lowest value as indicated by (*1*) in Fig. 105. The present metamagnetic transition corresponds to the process from (*1*) to (*2*). We can say that the present metamagnetic transition corresponds to field-induced ferroquadrupolar ordering.

The metamagnetic transition based on the same quadrupolar interaction is observed in the other compounds: $CeCu_2$, $DyCu_2$ and $TbCu_2$ [144–146].

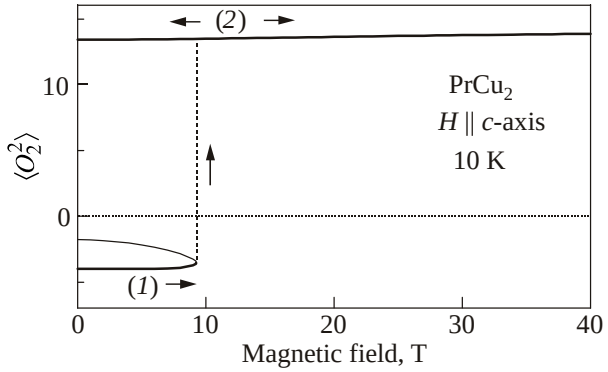

Fig. 105. Field dependence of the calculated quadrupole moment $\langle O_2^0 \rangle$ in $PrCu_2$, cited from Ref. 141.

7. Change of Fermi surface properties in quantum critical point

The electronic states in Ce, Yb and U compounds can be tuned by applying pressure P and/or magnetic field H. The Néel temperature in the Ce compounds becomes a guiding parameter to tune the electronic state under pressure. The quantum critical point is therefore defined as the electronic state at which the Néel temperature becomes zero at the critical pressure P_c: $T_N \to 0$ at $P \to P_c$. We will present the Fermi surface properties as a function of pressure, especially at P_c, for three typical antiferromagnets of $CeRh_2Si_2$, $CeIn_3$ and $CeRhIn_5$.

7.1. Pressure-induced superconductivity in $CeRh_2Si_2$ *based on conduction electrons with the relatively large cyclotron mass*

$CeRh_2Si_2$ crystallizes in a tetragonal $ThCr_2Si_2$-type structure and orders antiferromagnetically below the Néel temperature T_N = 36 K at ambient pressure. The magnetic structure was investigated by neutron diffraction measurements [147], as shown in Fig. 106. Below T_N, the propagation vector is $\mathbf{q}_1$ = (1/2, 1/2, 0), and the magnetic moment is oriented along the [001] direction. Furthermore, the magnetic structure changes to the 4**q** structure with two propagation vectors $\mathbf{q}_1$ and $\mathbf{q}_2$ = (1/2, 1/2, 1/2) below T_N' = = 25 K. The magnitude of the ordered moment μ_s is 1.42 μ_B at the corner Ce site of the tetragonal structure and 1.34 μ_B at the body-centered Ce site. The present magnetic structure is clearly reflected in the temperature dependence of the magnetic susceptibility, indicating an easy-axis of magnetization along [001], as shown in Fig. 107,*a*. The magnetic phase diagram for $H \parallel$ [001] is also shown in Fig. 107,*b* [148].

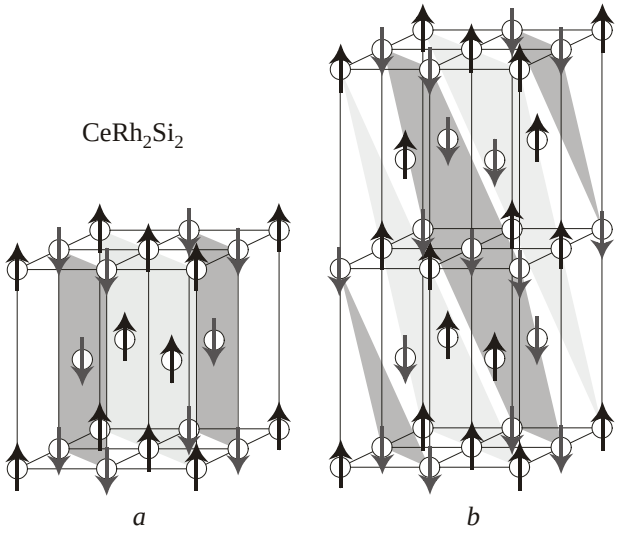

Fig. 106. Magnetic structures of the $\mathbf{q}_1$ -structure in the temperature range from T_N = 36 K to T_N' = 25 K (*a*) and the 4**q**-structure below T_N' (*b*) in $CeRh_2Si_2$, cited from Ref. 147.

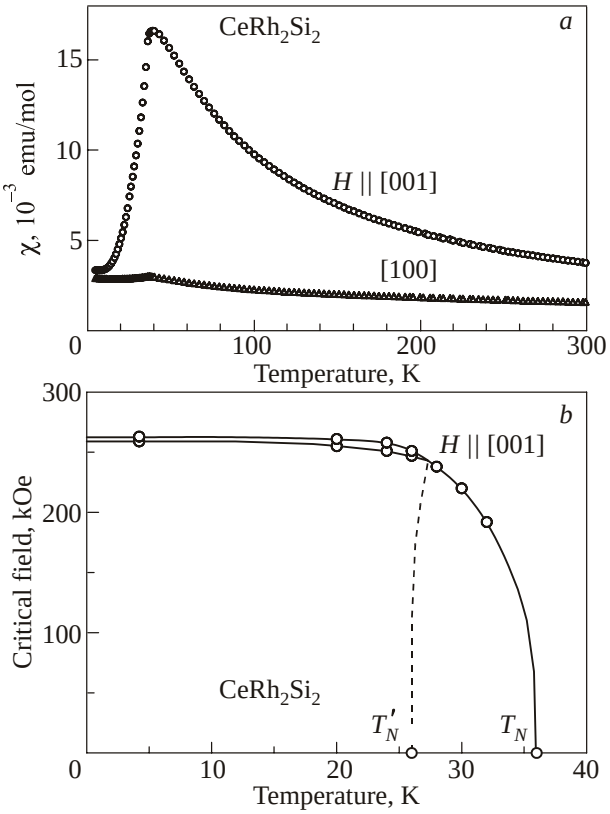

Fig. 107. Temperature dependence of the magnetic susceptibility (*a*) and the magnetic phase diagram (*b*) in $CeRh_2Si_2$, cited from Ref. 148.

When pressure is applied to $CeRh_2Si_2$, the Néel temperature T_N = 36 K and the magnetic transition temperature T_N' are reduced to 0 K at $P_c \simeq 1.06$ GPa and $P_c' \simeq$ $\simeq 0.6$ GPa, respectively, as shown in Fig. 108. Note that the ordered moment is also reduced with increasing pressure [147], as shown by triangles in Fig. 108. The value of the superconducting transition temperature T_{sc}, which is shown in Fig. 108 as a function of pressure, is enlarged by a factor of ten compared with those of T_N and T_N'. Superconductivity is observed around $P_c \simeq 1.06$ GPa.

The low-temperature resistivity under pressure follows the Fermi liquid form of $\rho = \rho_0 + AT^2$ [149]. Figure 109 shows the T^2 dependence of the electrical resistivity under several constant pressures. Note that the T^2 dependence is satisfied even at around P_c [150,151].

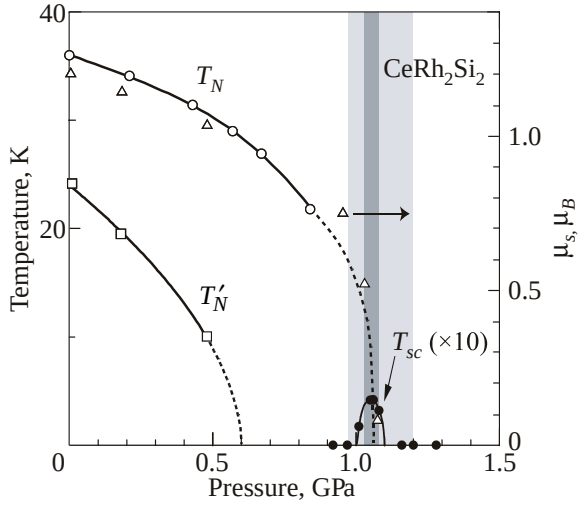

Fig. 108. Pressure dependence of T_N, T_N', and T_{sc}, shown by open circles, open squares and closed circles, respectively, in $CeRh_2Si_2$. T_{sc} is enlarged by ten times compared with T_N and T_N'. The ordered moment μ_s is shown by triangles. The data on T_N' and μ_s are cited from Ref. 147.

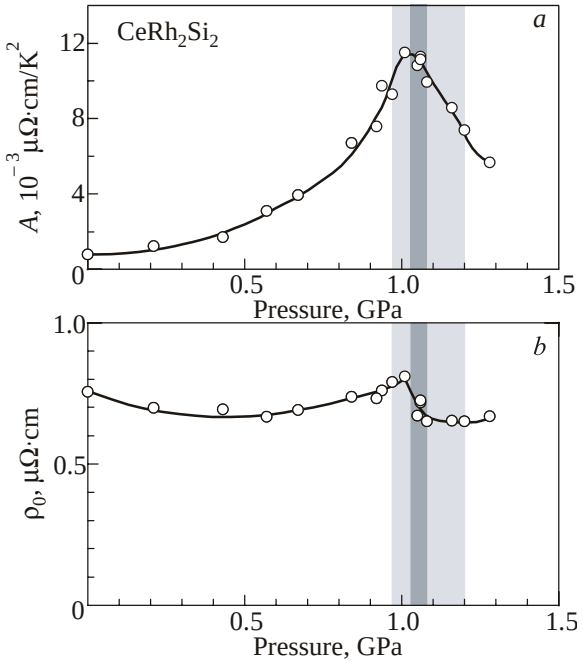

Fig. 110. Pressure dependence of A (*a*) and ρ_0 (*b*) in $CeRh_2Si_2$, cited from Ref. 149.

Figure 110 shows the pressure dependence of A and ρ_0. The A value has a maximum at 1.0 GPa, very close to P_c. The residual resistivity ρ_0 also has a small anomaly around P_c.

The specific heat measurement under pressure indicated that the electronic specific heat coefficient γ increases almost linearly with increasing pressure from 23 mJ/(K^2·mol) at ambient pressure to about 80 mJ/(K^2·mol) at P_c [152]. Above P_c, the γ value decreases slightly with increasing pressure. The γ value is found to correlate well with $\sqrt{A}$.

Superconductivity in $CeRh_2Si_2$ was first discovered by Movshovich *et al.* for a polycrystal sample [153]. The transition temperature, determined from the onset of the resistivity drop, was T_{sc} = 0.35 K, at which superconductivity appeared in the pressure range from 0.6 to 1.6 GPa. Figure 111 shows the low-temperature resistivity for a high-quality single crystal sample with ρ_0 = 0.75 μΩ·cm and ρ_{RT}/ρ_0 = 100 [149]. An indication of superconductivity appears in the pressure region from 0.97 to 1.20 GPa, which is shown in Fig. 108 as a gray region. As shown in Fig. 111, the resistivity at P = 1.01 and 1.16 GPa decreases rapidly with decreasing temperature below 0.5 K. Zero

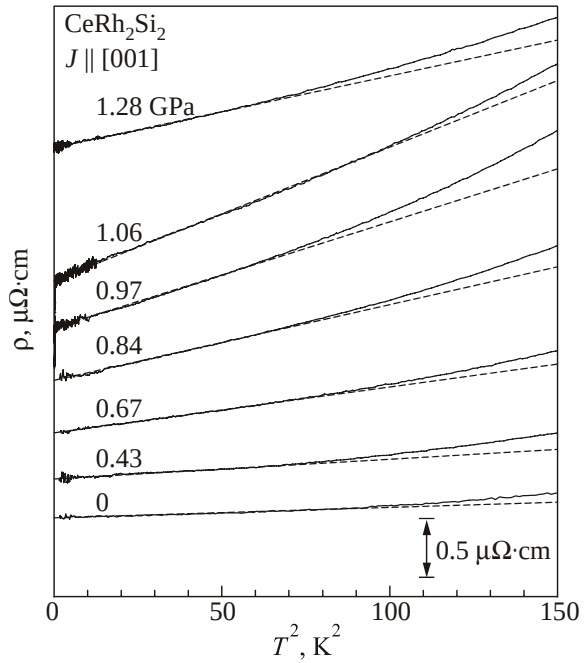

Fig. 109. Quadratic temperature dependence of the electrical resistivity in $CeRh_2Si_2$ under various pressures, cited from Ref. 149.

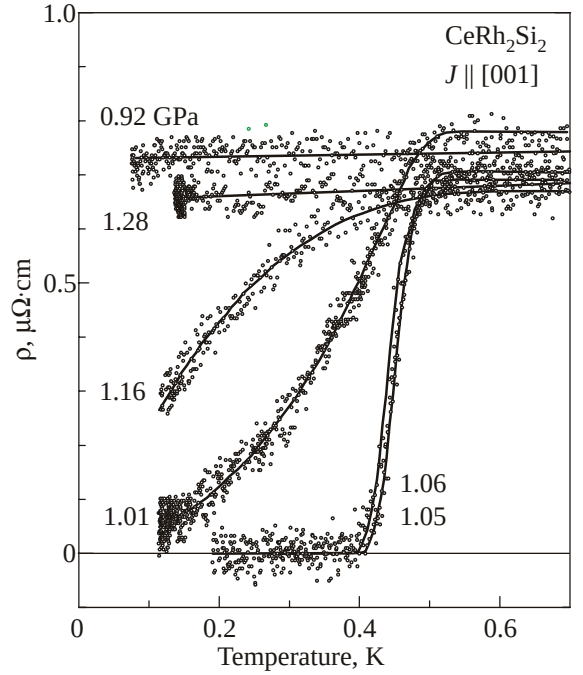

Fig. 111. Low-temperature resistivity under pressure in $CeRh_2Si_2$, cited from Ref. 149.

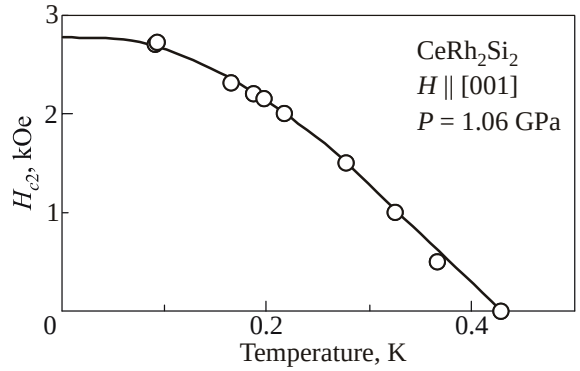

Fig. 112. Temperature dependence of H_{c2} at 1.06 GPa in $CeRh_2Si_2$, cited from Ref. 149.

resistivity, however, is not attained. The zero resistivity is observed in an extremely narrow pressure region around P_c, which is shown in Fig. 108 as a dark-gray region. Namely, the resistivity at P = 1.05 and 1.06 GPa decreases steeply below 0.5 K and reaches zero at 0.42 K. Note that the onset temperature of superconductivity is 0.4–0.5 K in the pressure region from 0.97 to 1.20 GPa, but the zero resistivity is attained in the pressure region from 1.03 to 1.08 GPa. This implies that homogeneous bulk-superconductivity is realized in an extremely narrow pressure region around $P_c \simeq 1.06$ GPa.

Figure 112 shows the temperature dependence of the upper critical field H_{c2}. The solid line connecting the data in Fig. 112 is a visual guide. The coherence length ξ is simply estimated as 340 Å from a relation of $H_{c2} = \phi_0/2\pi\xi^2$: $H_{c2}(0) = 2.8$ kOe, where ϕ_0 is a quantum fluxoid. Note that the mean free path for the present sample is estimated from the dHvA experiment as about 1000 Å around $P_c \simeq 1.06$ GPa. This indicates that the present sample is close to the clean limit.

The dHvA experiment was carried out under pressure [154,155]. Figures 113,*a* and 113,*b* show the dHvA oscillation and its FFT spectrum at ambient pressure and 1.29 GPa, respectively.

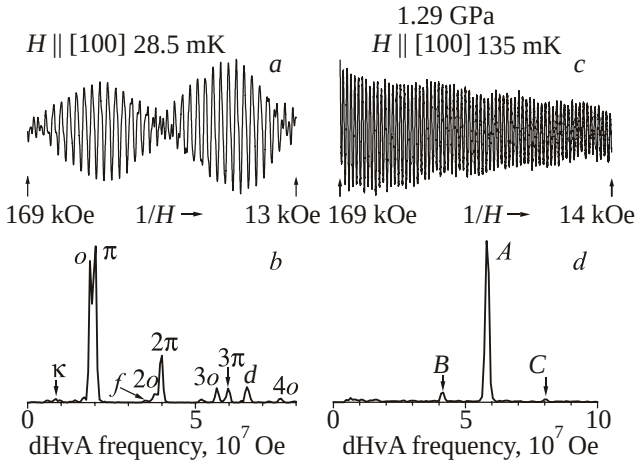

Fig. 113. dHvA oscillation (*a*) and its FFT spectrum at ambient pressure (*b*), dHvA oscillation (*c*) and its FFT spectrum at 1.29 GPa (*d*) in $CeRh_2Si_2$, cited from Refs. 154, 155.

The angular dependence of the dHvA branches at ambient pressure in $CeRh_2Si_2$ is approximately explained by the Fermi surfaces of a non-4*f* reference compound $LaRh_2Si_2$, as shown in Fig. 114,*a*. This is because the 4*f* electron in $CeRh_2Si_2$ is localized, as mentioned above; thus, the 4*f* electron does not significantly contribute to the Fermi surface. These detected dHvA branches are formed by the conduction electrons which break through the antiferromagnetic Brillouin zone boundary and circulate around the original paramagnetic Fermi surface and/or correspond to Fermi surfaces, which are not affected by antiferromagnetic ordering. Antiferromagnetic ordering, however, changes the topology of the Fermi surface. This might be approximated by a band-folding procedure, where the paramagnetic Fermi surface is folded into a small Brillouin zone based on a large magnetic unit cell. The magnetic structure in the ground state is the 4*q* structure shown in Fig. 106. The magnetic unit cell is eight times larger than the chemical unit cell. Correspondingly, the Brillouin zone of $CeRh_2Si_2$ in the antiferromagnetic state is reduced to one-eighth of the size of that in the paramagnetic state. It is supposed that dHvA branches such as κ, which are relatively small in dHvA frequency, are thus formed by magnetic ordering. Because the dHvA data are usually obtained over a wide field range from a low field of 25 kOe to a high field of 170 kOe to construct the angular dependence of the dHvA frequency, the experimentally obtained Fermi surfaces consist of the Fermi surfaces in the paramagnetic state and many kinds of small Fermi surfaces produced in the antiferromagnetic state. These are also applicable to the dHvA data in the antiferromagnets of $CeIn_3$ and $CeRhIn_5$ shown later.

Figures 113,*c* and 113,*d* indicate the dHvA oscillation and its FFT spectrum at 1.29 GPa, namely, in the paramagnetic state. New branches named *A*, *B*, and *C* appear, which are convincingly explained by the 4*f*-itinerant Fermi surfaces shown in Fig. 114,*b*.

The pressure dependence of the dHvA frequency up to 1.54 GPa is plotted in Fig. 115,*a*. The dHvA branches at ambient pressure, which are identified from the 4*f*-localized band model, namely, the Fermi surfaces of $LaRh_2Si_2$, are slightly changed at $P_c' \simeq 0.6$ GPa. Branches *o*, κ, and ζ disappear completely and new branches named *p*, *q*, and *r* appear above $P_c' \simeq 0.6$ GPa. This is because the magnetic structure changes from the 4*q* structure to the q_1 structure at $P_c' \simeq 0.6$ GPa, as mentioned above. Branches *d* and π are, however, unchanged for pressure up to P_c. Note that branches *d* and π are found at 1.03 GPa, while at 1.08 GPa they disappear completely and a new branch named *A* appears. With further increasing pressure, two branches named *B* and *C* are also detected. These three branches named *A*, *B* and *C* are clearly identified by the 4*f*-itinerant band model, as shown in Fig. 114,*b*, the detected dHvA frequency is $8.03 \cdot 10^7$ Oe (the corresponding theore-

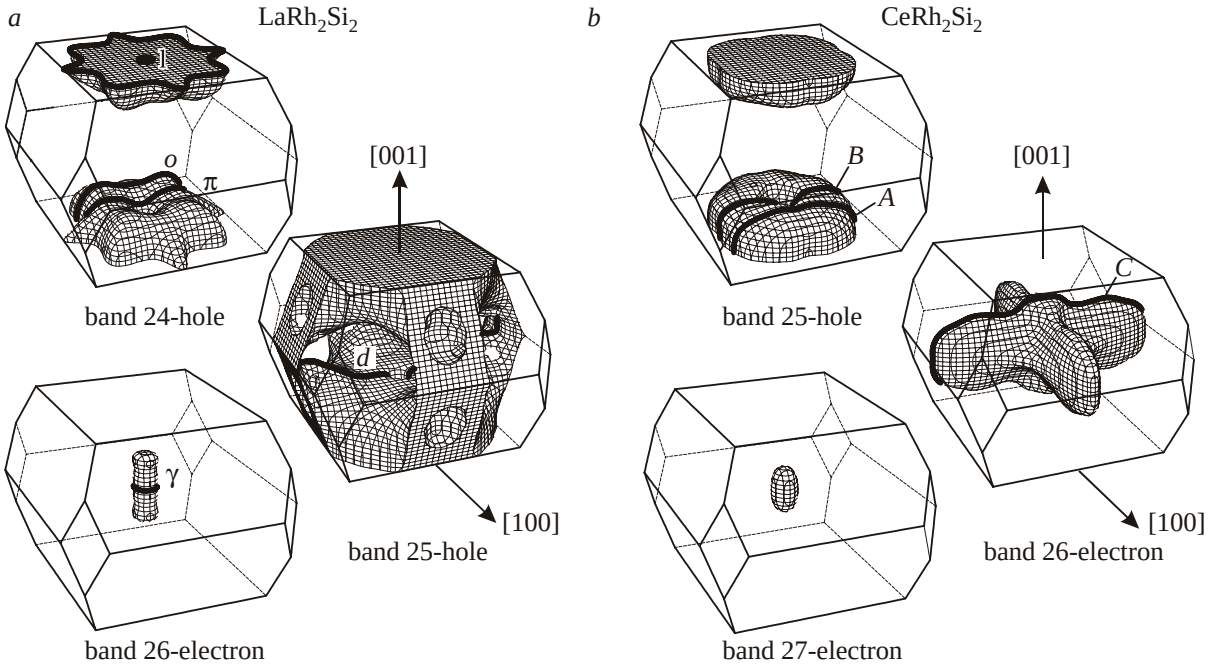

Fig. 114. Theoretical Fermi surfaces in $LaRh_2Si_2$ (*a*) and 4*f*-itinerant $CeRh_2Si_2$ (*b*), cited from Refs. 154, 155.

tical dHvA frequency is $9.21 \cdot 10^7$ Oe) for branch *C*, $5.80 \cdot 10^7$ Oe ($4.65 \cdot 10^7$ Oe) for branch *A*, and $4.10 \cdot 10^7$ Oe ($3.43 \cdot 10^7$ Oe) for branch *B*. The Fermi surface of $CeRh_2Si_2$ in Fig. 114,*b* has one more electron per primitive cell compared with the Fermi surface in $LaRh_2Si_2$ in Fig. 114,*a*, based on the itinerant electron model for the 4*f* electron. The 4*f* electronic state above P_c in $CeRh_2Si_2$ is similar to those of $CeSn_3$, and $CeRu_2Si_2$ mentioned above.

The cyclotron mass shown in Fig. 115,*b* increases with increasing pressure, reaching $28\,m_0$ at 1.03 GPa for branch *d*, which is four to five times larger than that at ambient pressure. Above P_c, the cyclotron masses of branches *A*, *B*, and *C* are large, ranging from 24 to $34\,m_0$. The cyclotron masses are about four times larger than the corresponding band masses. The mass enhancement $m_c^*/m_b \simeq 4$ is consistent with the enhancement of the electronic specific heat coefficient $\gamma/\gamma_b = 4.4$, where $\gamma = 80$ mJ/(K^2·mol) at 1.3 GPa [152] and $\gamma_b = 18$ mJ/(K^2·mol).

From these experimental results, it is thus concluded that the detected dHvA frequencies clearly change at $P_c \simeq$ $\simeq 1.06$ GPa, implying a first-order phase transition. This indicates a discontinuous change in the Fermi surface from 4*f*-localized to itinerant at P_c, although the Fermi liquid nature holds even at P_c.

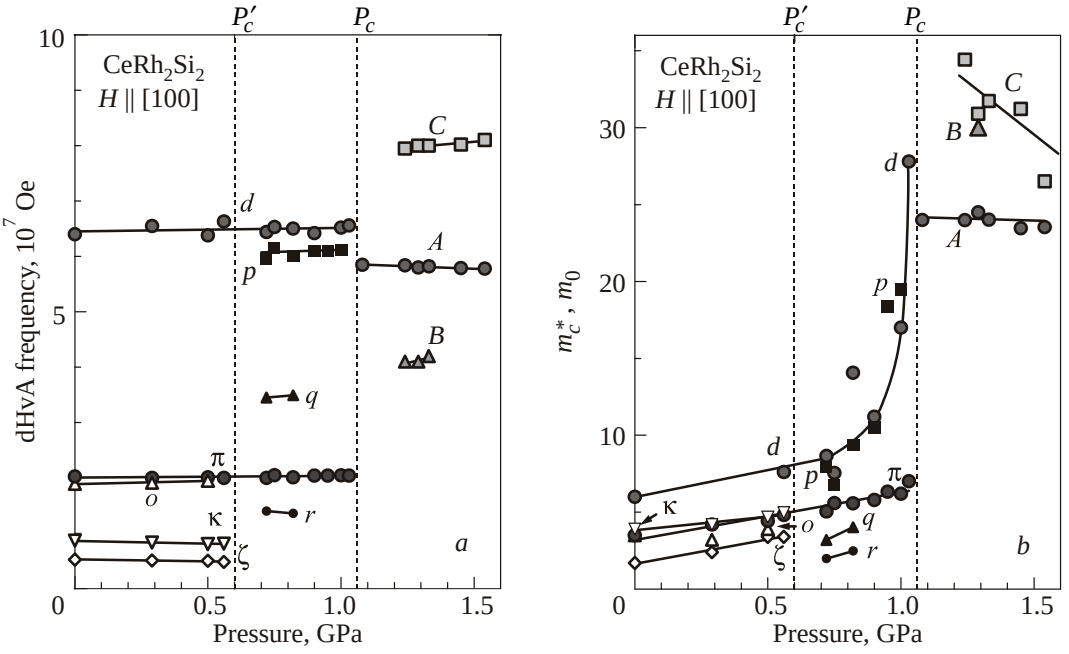

Fig. 115. Pressure dependence of the dHvA frequency (*a*) and the cyclotron effective mass (*b*) in $CeRh_2Si_2$, cited from Refs. 154, 155.

7.2. Pressure-induced heavy fermion superconductivity in $CeIn_3$

Superconductivity in $CeIn_3$, which was mentioned in Chap. 3, was also realized under pressure [14]. With increasing pressure, the Néel temperature decreases and reaches zero at a critical pressure of around $P_c \simeq 2.6$ GPa, in which the narrow pressure region superconductivity appears below $T_{sc} = 0.21$ K [14,38], as shown in Fig. 116.

The Fermi surface of the antiferromagnet $CeIn_3$ is similar to that of $LaIn_3$, although the Fermi surface is modified by the antiferromagnetic Brillouin zone boundaries [45]. The antiferromagnetic Brillouin zone in $CeIn_3$ is the same as that for the face-centered cubic structure. The R point is reduced to the Γ point in this Brillouin zone. The Fermi surface of $LaIn_3$ consists of two sheets of bands 6 and 7, as shown again in Figs. 117,*a* and 117,*b*, respectively [38,39]. The band 7-electron Fermi surface named *a* is essentially a sphere centered at the R point. The band 6-hole Fermi surface looks complex and possesses the same volume as the band 7-electron Fermi surface, indicating that $LaIn_3$ is a compensated metal. An inner orbit circulating along the hole Fermi surface, denoted by *d*, is electron in dispersion and is spherical in topology but possesses slender arms along the ⟨111⟩ direction, as in the Fermi surface of copper. The present small electron Fermi surface denoted by *d* becomes a closed Fermi surface in a similar non-4*f* reference compound

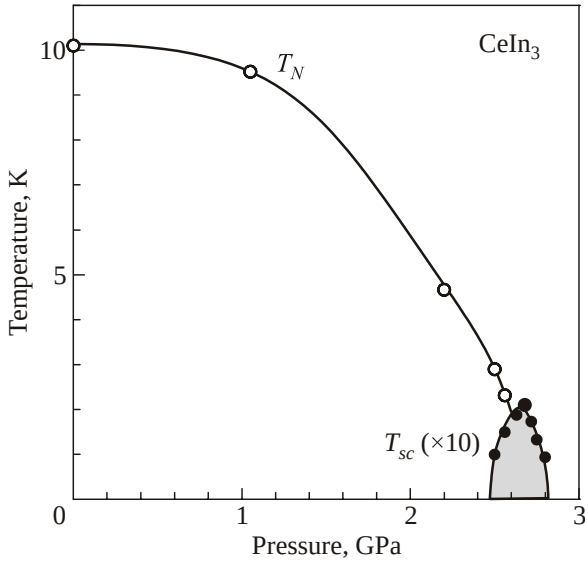

Fig. 116. Phase diagram for the Néel temperature T_N and the superconducting transition temperature T_{sc} in $CeIn_3$, cited from Ref. 38.

$LuIn_3$ [49], as shown in Fig. 117,*c*′, where the main Fermi surfaces in $LuIn_3$ are shown in Figs. 117,*c*,*d*.

In $CeIn_3$, the detected dHvA branch named *d* is very close to that of $LaIn_3$ or $LuIn_3$. The dHvA branch *d* in $CeIn_3$ is, however, observed in the whole angle region, as shown in Fig. 21, and possesses no arms, indicating that

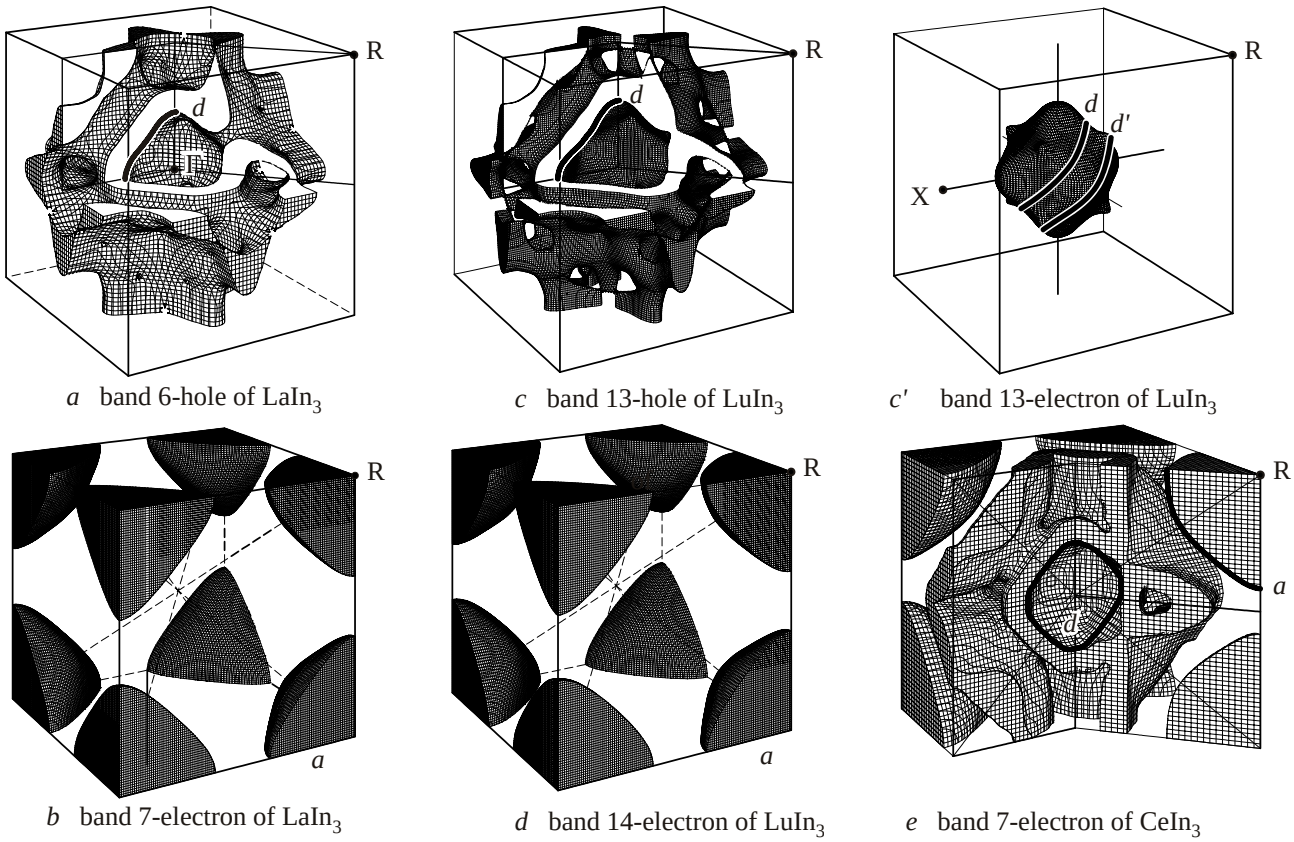

a band 6-hole of $LaIn_3$ *c* band 13-hole of $LuIn_3$ *c′* band 13-electron of $LuIn_3$

b band 7-electron of $LaIn_3$ *d* band 14-electron of $LuIn_3$ *e* band 7-electron of $CeIn_3$

Fig. 117. Fermi surfaces of $LaIn_3$, $LuIn_3$, and 4*f*-itinerant $CeIn_3$, cited from Ref. 38. The vacant space centered at Γ in the band 13-hole Fermi surface of $LuIn_3$, shown in (*c*), corresponds to the closed band 13-electron Fermi surface shown in (*c*′).

the Fermi surface is a closed spherical Fermi surface as in $LuIn_3$. The cyclotron mass m_c^* of branch *d* is highly anisotropic regarding the magnetic field direction: $m_c^* = 2-3\,m_0$ for the ⟨100⟩ direction and $12-16\,m_0$ for ⟨110⟩, as mentioned in Chap. 3 [45,51]. Moreover, two kinds of branches named *d* and *d*′ are observed only for $H \parallel \langle 111\rangle$: $m_c^* = 3\,m_0$ for branch *d* and $m_c^* = 13\,m_0$ for branch *d*′, compared with $m_c^* = 0.37\,m_0$ for branch *d* in $LaIn_3$. The large spherical Fermi surface centered at the R point, which is observed in $LaIn_3$, is not observed in $CeIn_3$. This is due to the influence of the band folding based on the antiferromagnetic ordering, as discussed by Biasini *et al*. [156], whereas branch *d* is not significantly influenced by the antiferromagnetic Brillouin zone except for the disappearance of the arms, because this Fermi surface is small in volume and centered at Γ. The cyclotron mass is strongly enhanced in $CeIn_3$. This is reflected in the electronic specific heat coefficient γ: γ = 150 mJ/(K^2·mol) in $CeIn_3$ and 7.2 mJ/(K^2·mol) in $LaIn_3$ [38].

The dHvA experiment was performed at ambient pressure and also under pressures up to 3GPa [38,157]. Figure 118 shows the pressure dependence of the dHvA frequency *F* and its cyclotron effective mass m_c^* for the magnetic field along the principal axes $H \parallel \langle 100\rangle$, ⟨110⟩, and ⟨111⟩. The dHvA frequency and the cyclotron mass for branch *d* increase slightly with increasing pressure: $F = 3.22\cdot10^7$ Oe ($m_c^* = 2.9\,m_0$) at ambient pressure and $3.56\cdot10^7$ Oe ($4.4\,m_0$) at 2.4 GPa for $H \parallel \langle 100\rangle$, as shown in Figs. 118,*a* and 118,*a*′. Similar pressure dependences of the dHvA frequency and the cyclotron mass are also observed for $H \parallel \langle 110\rangle$: $F = 3.60\cdot10^7$ Oe ($m_c^* = 17\,m_0$) at ambient pressure and $F = 4.0\cdot10^7$ Oe ($21\,m_0$) at 2.4 GPa, as shown in Figs. 118,*b* and 118,*b*′. Here, note that the cyclotron mass of branch *d* is strongly enhanced for $H \parallel \langle 110\rangle$ compared with $H \parallel \langle 100\rangle$, although the dHvA frequency is almost the same as that for $H \parallel \langle 100\rangle$. Branch *d* splits into two branches *d* and *d*′ for $H \parallel \langle 111\rangle$, as shown in Fig. 118,*c*. Branch *d*′, which is observed for $H \parallel \langle 111\rangle$, is considered to be due to the shape of the spherical Fermi surface with humps along the ⟨111⟩ direction as in $LuIn_3$, as mentioned above. The cyclotron mass of branch *d* for $H \parallel \langle 111\rangle$ is $3.0\,m_0$ at ambient pressure and $7\,m_0$ at 2.4 GPa. On the other hand, branch *d*′ for $H \parallel \langle 111\rangle$ possesses a relatively large cyclotron mass: $10\,m_0$ at ambient pressure and $14\,m_0$ at 2.4 GPa. A new branch shown by reverse triangles appears near branch *d* at 2.86 and 2.90 GPa for $H \parallel \langle 100\rangle$ and at 2.60 GPa for $H \parallel \langle 110\rangle$.

Interestingly, branch *a* appears abruptly above 2.7 GPa, where the Néel temperature reaches zero and the antiferromagnetic state disappears completely. The appearance of branch *a* indicates that $CeIn_3$ is paramagnetic above 2.7 GPa. It is very important to elucidate the origin of branch *a* in order to clarify the 4*f* electron character above P_c. Also note that the cyclotron mass of branch *a* is extremely large: $m_c^* \simeq 60\,m_0$ for $H \parallel \langle 100\rangle$. Considering the cyclotron effective mass $m_c^* = 0.57\,m_0$ of branch *a* [39] and the electronic specific heat coefficient γ = 7.2 mJ/(K^2·mol) in $LaIn_3$, an extremely large value γ ≃ 1000 mJ/(K^2·mol) is realized in $CeIn_3$ around P_c, where the γ value in $CeIn_3$ at ambient pressure is 150 mJ/(K^2·mol), as mentioned above.

The strongly enhanced cyclotron mass of branch *a* decreases with increasing pressure, as shown in Fig. 118,*a*′.

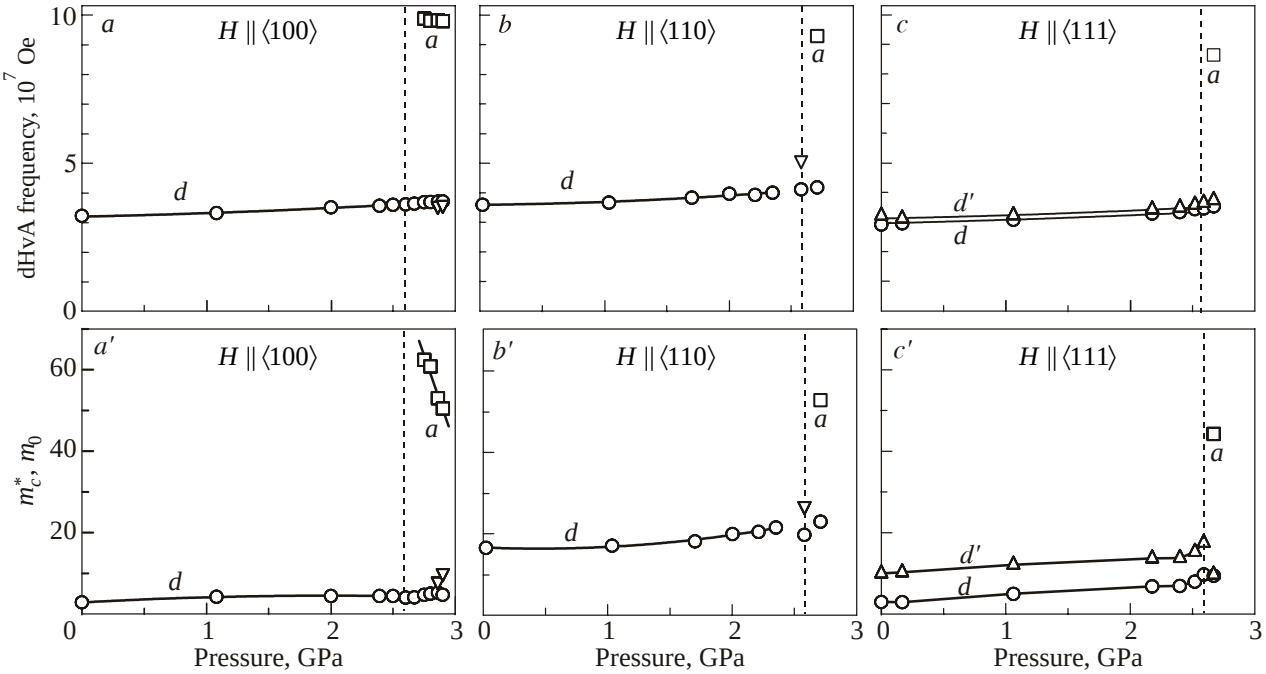

Fig. 118. Pressure dependence of the dHvA frequency and its cyclotron effective mass in $CeIn_3$ for the magnetic field along the principal axes $H \parallel \langle 100\rangle$, ⟨110⟩, and ⟨111⟩, cited from Ref. 38. Open circles, triangles, and squares indicate branches *d*, *d*′, and *a*, respectively. A new branch indicated by reverse triangles appears at 2.86 and 2.90 GPa for $H \parallel \langle 100\rangle$ and at 2.60 GPa for $H \parallel \langle 110\rangle$.

The reduction of the cyclotron mass with increasing pressure is a characteristic feature of the heavy fermion state.

A new dHvA branch named *a* was observed above 2.7 GPa, which corresponds to a main Fermi surface, judging from the large value of dHvA frequency. The abrupt appearance of branch *a* implies that the electronic state in $CeIn_3$ is changed at high pressures and correspondingly the antiferromagnetic state is changed into the paramagnetic state. The paramagnetic state under the magnetic field might be realized not only by a change in the character of the 4*f* electronic state by applying pressure, but also by a metamagnetic transition from the antiferromagnetic state to the field-induced ferromagnetic (or paramagnetic) state. At ambient pressure, no metamagnetic transition was observed for the magnetic fields of up to 400 kOe. In order to consider a possibility of the metamagnetic transition under pressure, a magnetic phase diagram under pressure was constructed from the temperature dependence of the ac susceptibility. The ac susceptibility was measured using the same experimental setup as that for the dHvA experiment. The antiferromagnetic ordering reflected in the ac susceptibility was observed up to 2.56 GPa, but was not seen above 2.63 GPa. Therefore, the critical pressure P_c of $CeIn_3$ is between 2.56 and 2.63 GPa, namely, $P_c \simeq$ $\simeq$ 2.6 GPa. From these experiments, the phase diagram for the Néel temperature was constructed, as shown in Fig. 119, at 2.20 and 2.56 GPa. The antiferromagnetic state is robust to the magnetic field even slightly below the critical pressure, namely, 2.56 GPa. Note that no metamagnetic transition was observed in the present dHvA measurements. From these experimental results, it is concluded that the present experiments below $P_c \simeq 2.6$ GPa under magnetic fields were performed in the antiferromagnetic state, and the appearance of branch *a* is not due to the change from the antiferromagnetic state to the field-induced ferromagnetic (or paramagnetic) state but due to the change in the 4*f* electronic state.

A large spherical Fermi surface named *a* also exists in 4*f*-itinerant $CeIn_3$. Figure 117,*e* shows the band 7-electron Fermi surface based on the 4*f*-itinerant band model [158]. The theoretical dHvA frequency of branch *a* in $CeIn_3$ is $8.82 \cdot 10^7$ Oe for the 4*f*-itinerant band model for $H \parallel \langle 100 \rangle$, while it is $F = 6.84 \cdot 10^7$ Oe for $LaIn_3$. The Fermi surface of branch *a* in $CeIn_3$ on the basis of the 4*f*-itinerant model is larger than that in $LaIn_3$ or the 4*f*-localized model, because the 4*f* electron considerably contribute to a conduction electron. Namely, the band 6-hole Fermi surface in $LaIn_3$ is completely occupied by the electron, and the band 7-electron Fermi surface in $LaIn_3$ is changed into an enlarged spherical Fermi surface centered at R in the 4*f*-itinerant $CeIn_3$, although a complicated multiply connected electron Fermi surface centered at Γ appears in the band 7-electron Fermi surface of the 4*f*-itinerant $CeIn_3$. Branches *a* and *d* are similar in shape for $LaIn_3$ and the 4*f*-itinerant $CeIn_3$. Therefore, the volume of the main Fermi surface *a* is very important for determining the character of the 4*f* electron in $CeIn_3$. The experimentally obtained dHvA frequency of $9.39 \cdot 10^7$ Oe for $H \parallel \langle 100 \rangle$ at 2.7 GPa in $CeIn_3$ is close to $F = 8.82 \cdot 10^7$ Oe in the 4*f*-itinerant model, although the experimental result is larger than the theoretical value. It is important that the volume of the spherical Fermi surface of branch *a* in $CeIn_3$ above $P_c \simeq 2.6$ GPa is larger than that in $LaIn_3$, as shown in Fig. 120. This enlarged spherical Fermi surface in $CeIn_3$ indicates that the 4*f* electron is itinerant and contributes to the Fermi surface.

It is interesting to compare the dHvA data of $CeIn_3$ under $P = 2.7$ GPa with those of $ThIn_3$ because the number of valence electrons is the same between two compounds [59]. $ThIn_3$, with the tetravalent electrons ($6d^2 7s^2$) of thorium, is a good candidate for investigating the topology of the 4*f*-itinerant Fermi surface in $CeIn_3$, which has tetravalent electrons ($4f^1 5d^1 6s^2$) of cerium. The dHvA frequency of the main Fermi surface a in $ThIn_3$ is very close to that of $CeIn_3$ at 2.7 GPa, as shown in Fig. 120,*b*. This result also

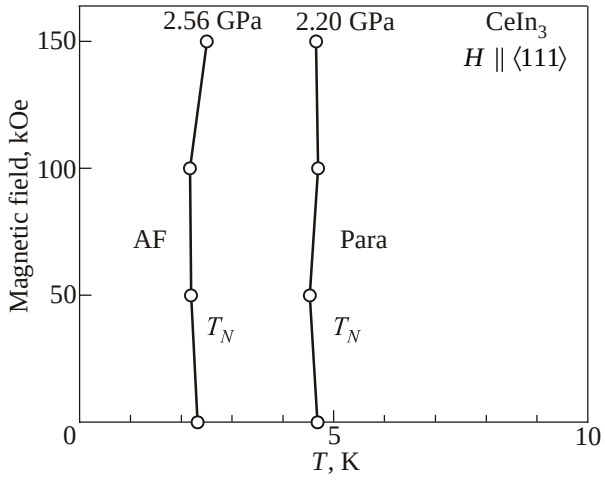

Fig. 119. Magnetic phase diagram for the paramagnetic (Para) and antiferromagnetic (AF) phases at 2.20 and 2.56 GPa for $H \parallel \langle 111 \rangle$ in $CeIn_3$, cited from Ref. 38.

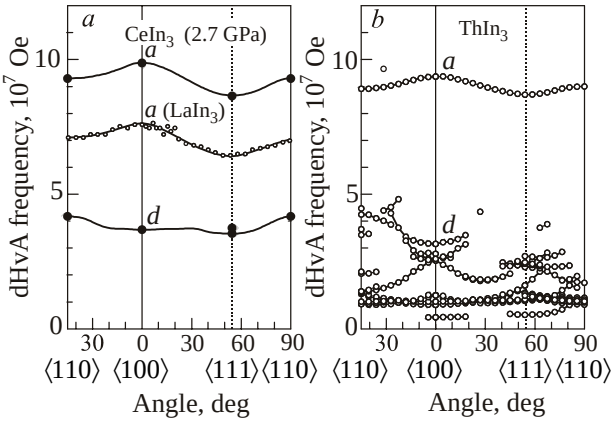

Fig. 120. Angular dependence of the dHvA frequency in $CeIn_3$ at 2.7 GPa (closed circles), together with those of branch a in $LaIn_3$ (open circles) [38] (*a*) and $ThIn_3$ [59] (*b*). Solid lines connecting the data are visual guides.

supports the existence of a 4*f*-itinerant Fermi surface in $CeIn_3$ above P_c. These dHvA experiments under pressure indicate that a change of electronic states at P_c is of the first-order.

Superconductivity was observed in the pressure range from 2.50 to 2.81 GPa. Note that the change in the ac susceptibility at the superconducting transition in $CeIn_3$ is almost the same magnitude as that at the superconducting transition of aluminum with the same volume, indicating that bulk superconductivity is realized in the narrow pressure region from 2.50 to 2.81 GPa. The pressure dependence of the superconducting transition temperature T_{sc} is shown by closed circles in Fig. 116, where the superconducting transition temperature is enlarged by a factor of ten because of a low T_{sc} of about 0.2 K.

Next, the temperature dependence of upper critical field H_{c2} was determined from the ac susceptibility measurement. The superconducting transition temperature under a magnetic field was defined as the temperature corresponding to the onset of the susceptibility drop. Figure 121 shows the temperature dependence of H_{c2} at 2.68 GPa. A solid curve is a visual guide based on Werthamer–Helfand–Hohenberg (WHH) theory [159]. H_{c2} (0) at 2.68 GPa is estimated as 4.4 kOe, indicating a coherence length ξ = = 270 Å. Heavy fermion superconductivity is realized in the quantum critical region of of $CeIn_3$.

In an ^{115}In-NQR experiment, no coherence peak is observed at T_{sc}, and the nuclear spin lattice relaxation rate $1/T_1$ at P = 2.50 GPa has a T^3 dependence below T_{sc} = = 0.19 K, indicating a line-node gap [160]. In the quantum critical region, the electrical resistivity does not follow the Fermi liquid relation $\rho = \rho_0 + AT^n$ (n = 2), which indicates that $n \simeq 1.6-1.7$ [161] or 1.6±0.2 [14]. The *d*-wave pairing state is theoretically proposed on the basis of the three-dimensional spin fluctuations near the propagation vector **q** = (1/2, 1/2, 1/2) [162].

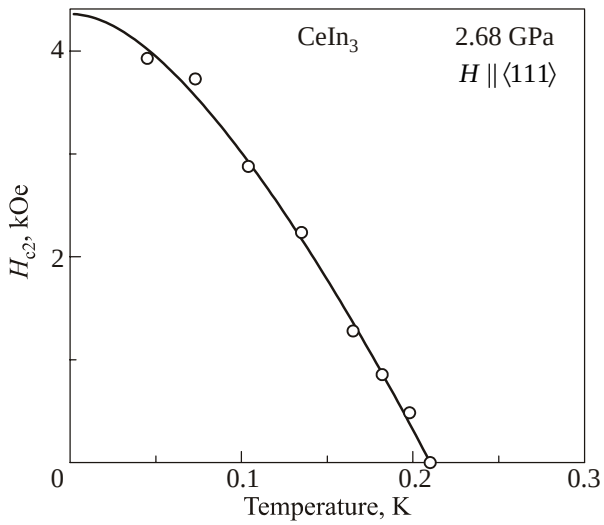

Fig. 121. Temperature dependence of the upper critical field H_{c2} in $CeIn_3$ at 2.68 GPa, cited from Ref. 38.

7.3. Pressure-induced heavy fermion superconductivity in $CeRhIn_5$ with the quasi-two dimensional electronic state

The detected dHvA branches of $CeRhIn_5$ are convincingly explained by the result of energy band calculations for $LaRhIn_5$, as described in Chap. 5. The corresponding topologies of the main Fermi surfaces in $CeRhIn_5$ are nearly cylindrical, and are found to be approximately the same as those in $LaRhIn_5$, as shown in Fig. 122,*a*, indicating that the 4*f*-electron in $CeRhIn_5$ is localized and does not contribute to the Fermi surfaces [77,163,164].

The dHvA experiment was also carried out for $CeCoIn_5$ [79,165–167], as described in Chap. 5. The detected dHvA branches are consistent with the 4*f*-itinerant band model. The main Fermi surfaces in $CeCoIn_5$ are also nearly cylindrical, as shown in Fig. 122,*b*. The topologies of the two kinds of cylindrical electron Fermi surfaces in $CeCoIn_5$ are similar to those in $LaRhIn_5$ ($CeRhIn_5$), but the Fermi surfaces of $CeCoIn_5$ are larger than those of $LaRhIn_5$ in volume. Moreover, the band 13-hole Fermi surface in $LaRhIn_5$, not shown in Fig. 122, is considerably reduced in volume for $CeCoIn_5$. This is because one 4*f*-electron in each Ce site becomes a valence electron in $CeCoIn_5$ and contributes to the Fermi surface. The contribution of the 4*f* electron to the density of states at the Fermi energy is about 60%. The corresponding cyclotron masses of 5–87 m_0 in $CeCoIn_5$ are extremely large, reflecting a large γ value of 1070 mJ/(K^2·mol) [101,102].

Keeping in mind that the 4*f* electron is localized in the antiferromagnet $CeRhIn_5$ but becomes itinerant at low temperatures in $CeCoIn_5$, the dHvA experiment in $CeRhIn_5$ was carried out under pressure [78]. Figures 123,*a* and 123,*b* show the dHvA oscillation in the field range from 30 to 169 kOe and its FFT spectrum, respec-

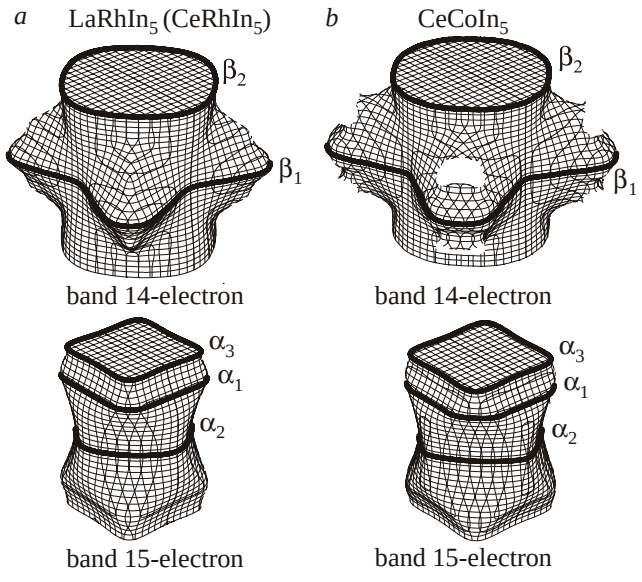

Fig. 122. Theoretical Fermi surfaces in $LaRhIn_5$ ($CeRhIn_5$) (*a*) and $CeCoIn_5$ (*b*), cited from Ref. 78. Small Fermi surfaces are not shown.

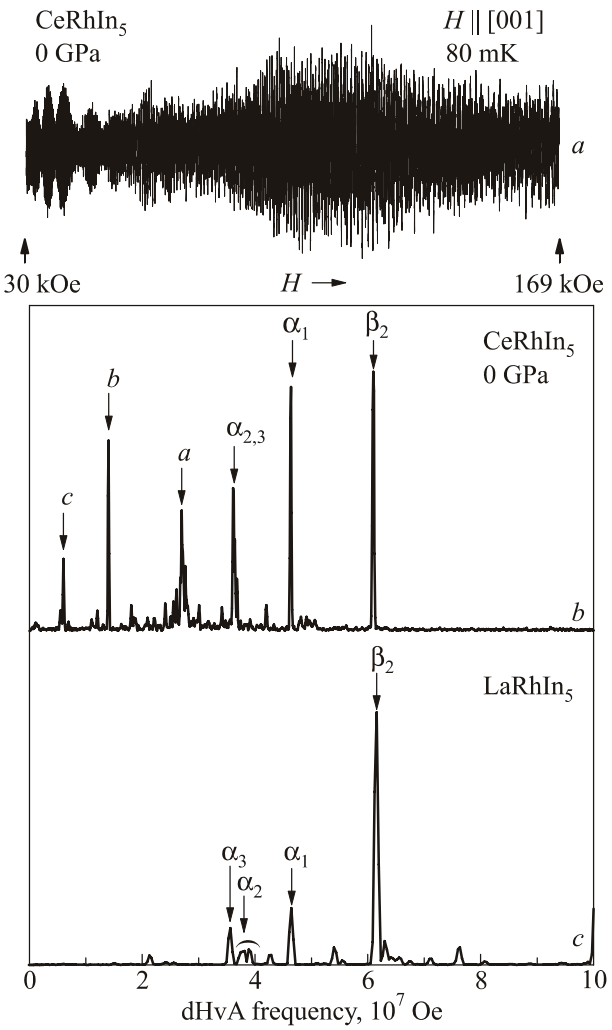

Fig. 123. dHvA oscillation at 0 GPa in $CeRhIn_5$ (*a*) and its FFT spectrum (*b*), together with the FFT spectrum in a non-4*f* reference compound $LaRhIn_5$ (*c*), cited from Ref. 78.

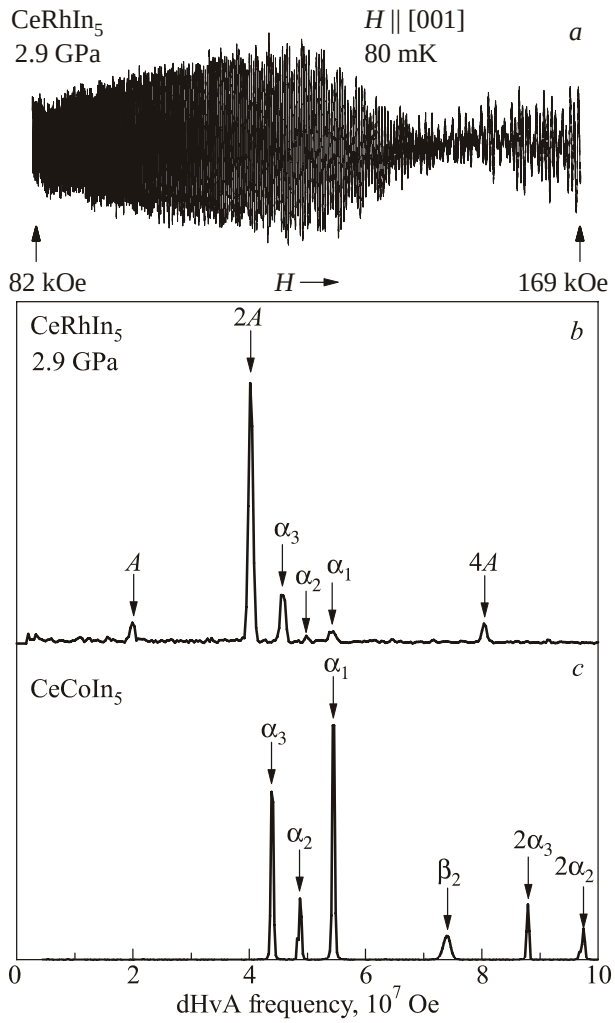

Fig. 124. dHvA oscillation at 2.9 GPa in $CeRhIn_5$ (*a*) and its FFT spectrum (*b*), together with the FFT spectrum in $CeCoIn_5$ at ambient pressure (*c*), cited from Ref. 78.

tively, at ambient pressure. Two kinds of main cylindrical Fermi surfaces named α_i (i = 1, 2, 3) and β_2 are detected. The dHvA frequencies F and the cyclotron effective masses m_c^* are $F = 6.13\cdot10^7$ Oe ($m_c^* = 5.5\,m_0$) in β_2, $4.67\cdot10^7$ Oe ($6.0\,m_0$) in α_1, and $3.67\cdot10^7$ Oe ($3.5\,m_0$) in $\alpha_{2,3}$. These dHvA frequencies are in good agreement with those of $LaRhIn_5$, shown in Fig. 123,*c*: $F = 6.13\cdot10^7$ Oe ($0.73\,m_0$) in β_2, $4.62\cdot10^7$ Oe ($0.69\,m_0$) in α_1, $3.76\cdot10^7$ Oe ($0.51\,m_0$) in α_2, and $3.56\cdot10^7$ Oe ($0.64\,m_0$) in α_3 [77]. The mass enhancement observed in $CeRhIn_5$ is also consistent with the γ value: γ = 50–60 mJ/(K^2·mol) in $CeRhIn_5$ and 5.7 mJ/(K^2·mol) in $LaRhIn_5$ [77,168].

Next, the dHvA oscillation in the field range from 82 to 169 kOe and its FFT spectrum at pressure P = 2.9 GPa are shown in Figs. 124,*a* and 124,*b*, respectively. Four kinds of dHvA branches are observed: $F = 5.43\cdot10^7$ Oe ($m_c^* = 23\,m_0$) in α_1, $4.96\cdot10^7$ Oe ($30\,m_0$) in α_2, $4.58\cdot10^7$ Oe ($24\,m_0$) in c α_3, and $1.98\cdot10^7$ Oe ($9\,m_0$) in branch *A*. The dHvA frequencies of these branches are larger than those at ambient pressure, but are approximately the same as those of $CeCoIn_5$ at ambient pressure: $F = 5.56\cdot10^7$ Oe ($15\,m_0$) in α_1, $4.53\cdot10^7$ Oe ($18\,m_0$) in α_2, and $4.24\cdot10^7$ Oe ($8.4\,m_0$) in α_3, as shown in Fig. 124,*c* [79]. The origin of branch *A* is not clear, but it is close to branch ε with $F = 0.79\cdot10^7$ Oe in $CeCoIn_5$, which was, however, not observed experimentally along $H \parallel [001]$ in $CeCoIn_5$ [79]. Here, branch ε in $CeCoIn_5$ is identified as a band 13-hole nearly spherical Fermi surface, not shown in Fig. 122,*b*.

To elucidate a change in the Fermi surface properties under pressure, the pressure dependences of the dHvA frequency and the cyclotron mass were measured, as shown in Figs. 125,*a*,*b*, respectively. The dHvA frequencies for the main dHvA branches named β_2, α_1 and $\alpha_{2,3}$, together with those for branches named *a*, *b*, and *c* in Fig. 125,*a*, are approximately unchanged up to about 2.3 GPa [78]. These branches, however, disappear completely at 2.35 GPa, and another two branches with $F = 4.23\cdot10^7$ Oe ($m_c^* \simeq 30\,m_0$) and $4.03\cdot10^7$ Oe ($20\,m_0$) appear. Furthermore, new branches α_3 and *A* appear abruptly at 2.4 GPa, which are connected with the branches at 2.9 GPa.

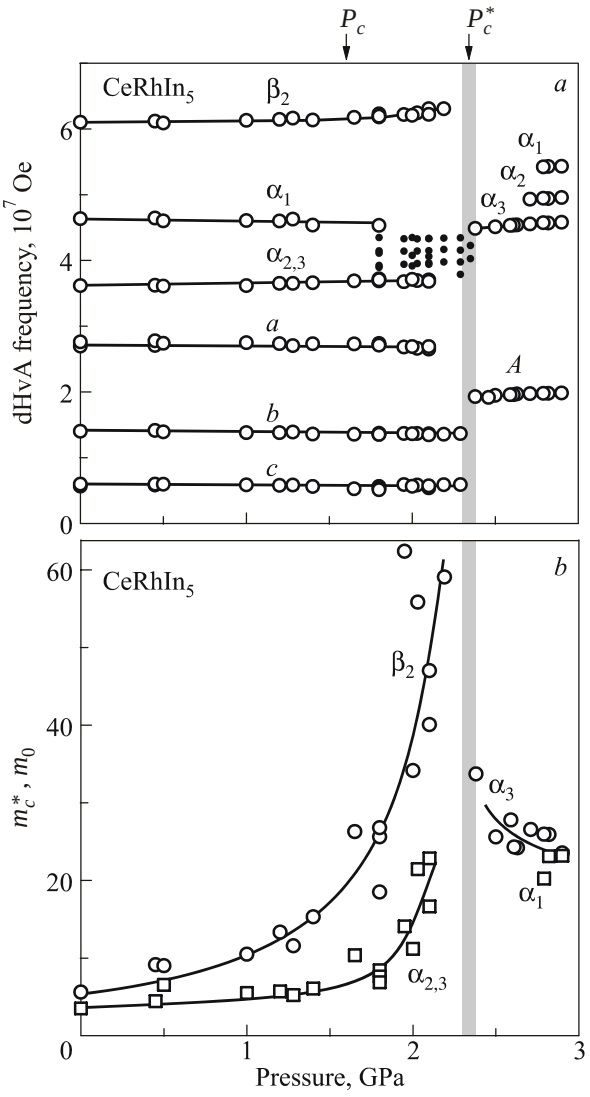

Fig. 125. Pressure dependence of dHvA frequency (*a*) and cyclotron mass (*b*) in $CeRhIn_5$, cited from Ref. 78.

Note that the branches at 2.35 GPa appear from 1.80 to 2.35 GPa, which are shown by small closed circles in Fig. 125. The origin of these branches is unknown, but they might be related to the magnetic and/or electronic state, because at a zero field the antiferromagnetic ordering disappears above $P_c \simeq 2.0$ GPa but persists up to $P_c^* \simeq$ $\simeq 2.4$ GPa in magnetic fields, as mentioned above. It is observed from the neutron-scattering experiment that the helical magnetic structure and the ordered moment remain up to 1.63 GPa [86]. Furthermore, the present dHvA experiment was carried out in high magnetic fields up to 169 kOe. Even in these high fields, $CeRhIn_5$ is in the antiferromagnetic state at ambient pressure, because the magnetization for $H \parallel [001]$ indicated neither a metamagnetic transition nor a saturated feature in magnetic fields of up to 500 kOe [169]. The dHvA branches *a*, *b*, etc., which are not observed in $LaRhIn_5$, are characteristic in the antiferromagnet $CeRhIn_5$. These branches are observed continuously in the present measured field range even under pressures up to approximately P_c^*, indicating that an antiferromagnetic state persists up to $P_c^* \simeq 2.4$ GPa in the present dHvA experiment.

As shown in Fig. 125,*b*, the cyclotron masses of the main branches β_2 and $\alpha_{2,3}$ increase rapidly above 1.6 GPa, where superconductivity occurs: $5.5\,m_0$ at ambient pressure, $20\,m_0$ at 1.6 GPa, and $60\,m_0$ at 2.2 GPa for branch β_2, where the cyclotron mass was determined in the field range from 100 to 169 kOe, namely, at an effective field $H_{\text{eff}} =$ $= 126$ kOe. This is approximately consistent with the pressure dependence of the γ value: 50−60 mJ/(K^2·mol) at ambient pressure and 380 mJ/(K^2·mol) at 2.1 GPa [168]. On the other hand, the cyclotron mass of the new branch α_3, which was observed above 2.4 GPa, decreases slightly with increasing pressure: about $30\,m_0$ at 2.4 GPa and $24\,m_0$ at 2.9 GPa. Branch β_2 was, however, not detected above 2.4 GPa. This is mainly due to the existence of a large cyclotron effective mass close to $100\,m_0$. Anyway, it is remarkable that the pressure dependence of the cyclotron mass indicates a divergent tendency at $P_c^* \simeq 2.4$ GPa.

It has also been reported from other experiments that the residual resistivity ρ_0 [87], and the $\sqrt{A}$ value become maximum at P_c^* [170].

It is concluded from the present dHvA experiment that the Fermi surface in $CeRhIn_5$ under pressure is changed from a 4*f*-localized Fermi surface to a 4*f*-itinerant Fermi surface. A notable change in the Fermi surface occurs $P_c^* \simeq 2.4$ GPa, revealing a first-order phase transition. Pressure-induced superconductivity is not related to the topology of the Fermi surface, but to the heavy fermion state, although the Fermi surface is very similar between $P < P_c^*$ and $P > P_c^*$.

8. Split Fermi surfaces in the non-centrosymmetric crystal structure

Recently superconductivity in the non-centrosymmetric crystal structure has been reported in $CePt_3Si$ [171,172] with the tetragonal structure ($P4mm$), UIr [18,173] with the monoclinic structure ($P2_1$), $CeRhSi_3$ [174–176], $CeIrSi_3$ [23,29,177], $CeCoGe_3$ [178,179] and $CeIrGe_3$ [180] with the tetragonal $BaNiSn_3$ type structure ($I4mm$). We show in Fig. 126 the crystal structure of $CePt_3Si$ and $CeIrSi_3$, which lack inversion symmetry along the tetragonal [001] direction (*c*-axis). In $CeIrSi_3$, the Ce atoms occupy the four corners and the body center of the tetragonal structure, similar to the well-known tetragonal $CeCu_2Si_2$ ($ThCr_2Si_2$-type), but the Ir and Si atoms lack inversion symmetry along the [001] direction.

Inversion is an essential symmetry for the formation of Cooper pairs. In non-centrosymmetric metals, a splitting of Fermi surfaces with different spins occurs, restricting the possible Cooper pair states which can be formed keeping the total momentum zero. In the case of $CePt_3Si$, $CeRhSi_3$, $CeIrSi_3$, $CeCoGe_3$ and $CeIrGe_3$, split Fermi surfaces,

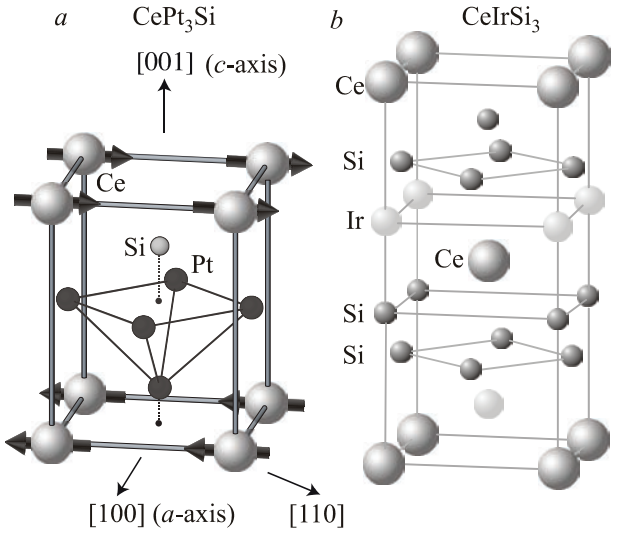

Fig. 126. Crystal and magnetic structure of $CePt_3Si$ (*a*), and the crystal structure of $CeIrSi_3$ (*b*), which also lack inversion symmetry along the [001] direction.

which are very similar to each other in topology but different in volume, are formed due to the presence of a Rashba-type antisymmetric spin-orbit interaction:

$$\mathcal{H}_{so} = -\frac{\hbar}{4m^{*2}c_2}(\nabla V(\mathbf{r})\times\mathbf{p})\cdot\boldsymbol{\sigma} = \alpha(\mathbf{n}\times\mathbf{p})\cdot\boldsymbol{\sigma} = \alpha\mathbf{p}_{\perp}\cdot\boldsymbol{\sigma} \quad (22)$$

where α denotes the strength of the spin-orbit coupling, $\mathbf{n}$ is a unit vector derived from $\nabla V(\mathbf{r})$, which lies along the [001] direction (*c*-axis) for these compounds, and $\boldsymbol{\sigma}$ is the Pauli matrix [181,182]. This additional term in the electron Hamiltonian separates the spin degenerate bands into two given by [181,183,184],

$$\varepsilon_{p\pm} = \frac{\mathbf{p}^2}{2m^*} \mp |\alpha\mathbf{p}_{\perp}|, \quad (23)$$

where $\mathbf{p}_{\perp} = (p_y, -p_x, 0)$. This splitting appears in the absence of a magnetic field and introduces a characteristic momentum-dependent spin structure to the electronic states, as shown in Fig. 127,*c*, which is compared with a spherical Fermi surface with degenerated up and down spin states in Fig. 127,*a*. Note that the spins of the conduction electrons are rotated for the direction of the effective magnetic field, $\mathbf{n}\times\mathbf{p}$, clockwise or anti-clockwise, depending on the up and down spin states. For comparison, in Fig. 127,*b*, we show the well-known Zeeman splitting, where the degenerated Fermi surface is split into two Fermi surfaces corresponding to a

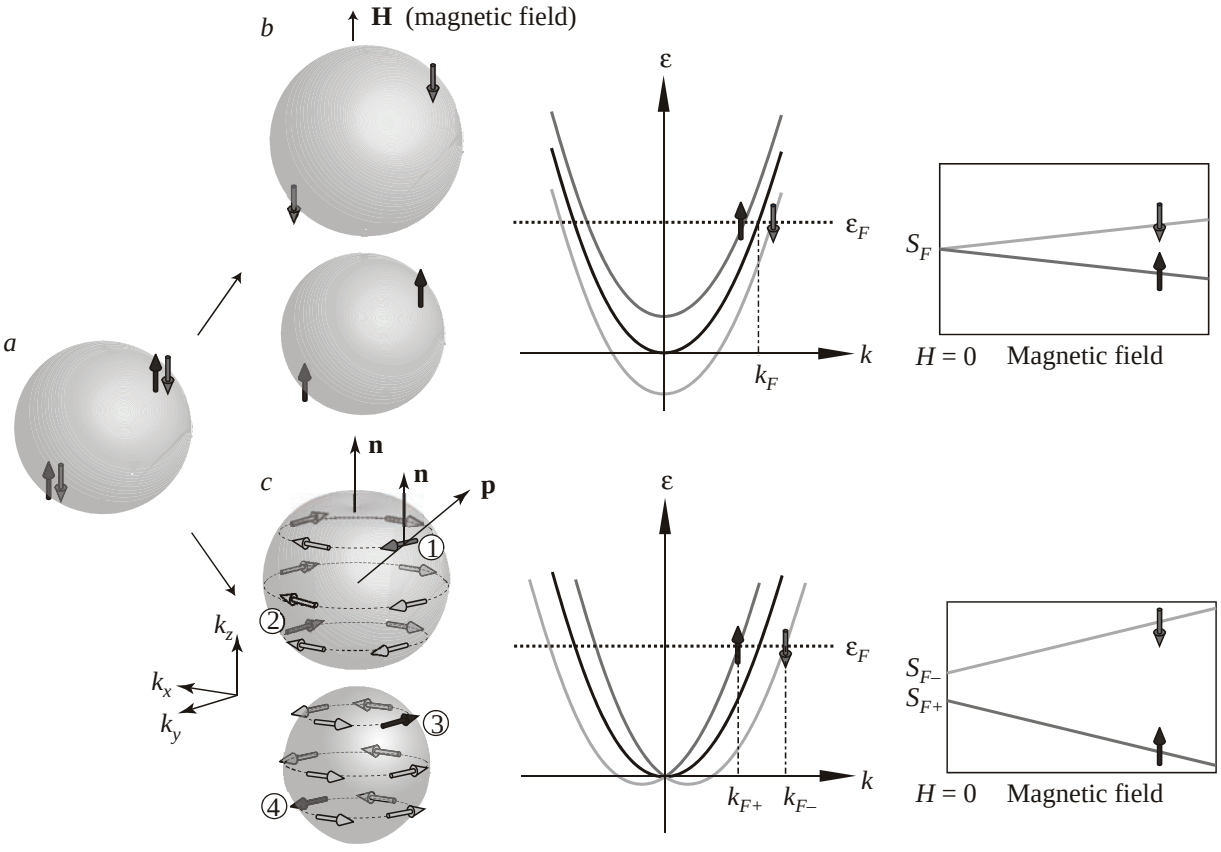

Fig. 127. Spherical Fermi surface with degenerated up (↑) and down (↓) spin states (*a*), and the Fermi surface and the corresponding energy bands are split into two components depending on the up and down spin states when the magnetic field *H* is applied to the material. The maximum cross-sectional areas S_F are also split into two components as a function of the magnetic field, well known as Zeeman splitting (*b*). The Fermi surface and the corresponding energy band are split into two components depending on the up and down spin states due to the antisymmetric spin-orbit interaction even when $H = 0$. The field dependence of the maximum cross-sectional areas S_{F-} and S_{F+} are also shown in the non-centrosymmetric structure (*c*).

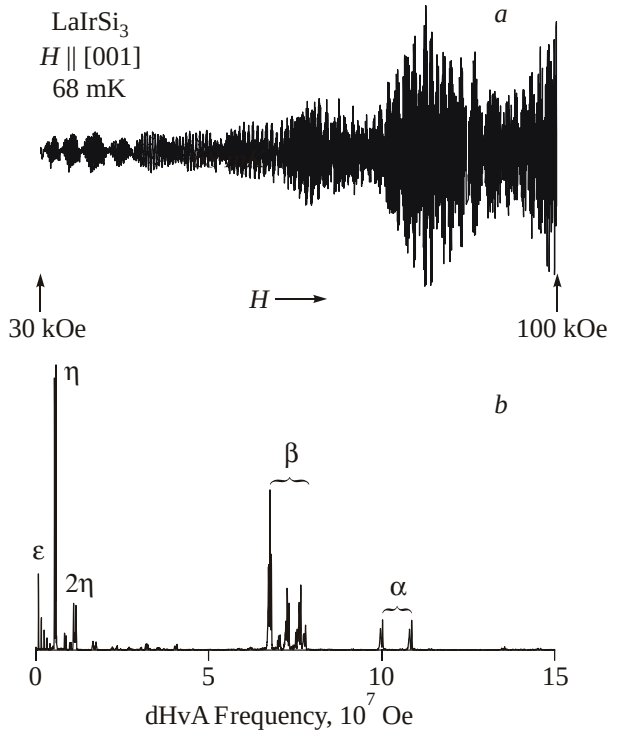

Fig. 128. Typical dHvA oscillation for $H \parallel [001]$ (*a*) and its FFT spectrum (*b*) in $LaIrSi_3$, cited from [23].

majority and minority spin, respectively, for a given quantization axis parallel to an applied magnetic field.

Due to the Fermi surface splitting in Fig. 127,*c*, the dHvA frequency F is split into two dHvA frequencies, F_+ and F_-. Using the relations of $\varepsilon_F = \hbar^2 k_F^2 / 2m_c^*$, $S_F = \pi k_F^2$, and $S_F = (2\pi e/c\hbar)F$, we obtain from Eq. (21)

$$|F_+ - F_-| = \frac{2c}{\hbar e} |\alpha\, p_\perp|\, m_c^*. \qquad (24)$$

We can thus determine the magnitude of the antisymmetric spin-orbit interaction $2|\alpha p_\perp|$ via the dHvA experiment.

As noted above, the existence of inversion symmetry in the crystal structure is believed to be an important factor for the formation of Cooper pairs, particular for the spin-triplet configuration. For example, parallel spin pairing is prohibited in the non-centrosymmetric structure because one conduction electron with a momentum **p** and an up-spin state, named ①, and the other conduction electron with a momentum $-\mathbf{p}$ and an up-spin state, named ④, belong to two different Fermi surfaces, as shown in Fig. 127,*c*. The possible existence of a spin-triplet pairing state in the non-centrosymmetric tetragonal crystal structure was, however, proposed theoretically [185,186].

First, we show the Fermi surface properties of $LaTX_3$ (T = Co, Rh, Ir and X = Si, Ge). In Fig. 128,*a* we show the typical dHvA oscillations of $LaIrSi_3$ for the magnetic field H along the [001] direction (*c*-axis) and its FFT spectrum [23]. The observed dHvA branches, α, β, ε, and η, are depicted in Fig. 128,*b*. The signal α with the largest dHvA frequency is clearly split into two branches, each of which separates once more into two branches. The former splitting is due to antisymmetric spin-orbit coupling, while the latter one is mainly due to the slight corrugation of each Fermi surface, possessing two extremal (maximum and minimum) cross-sections.

Figures 129,*a* and 129,*b* show the angular dependence of the dHvA frequency in $LaIrSi_3$, together with the theoretical one [23]. The detected dHvA branches are well explained by the result of the energy band calculation. The corresponding theoretical Fermi surfaces are shown in Fig. 130. The dHvA branches are identified as follows:

— branches α and η correspond to outer and inner orbits of the electron-Fermi surfaces belonging to band 41 and 42, respectively. These Fermi surfaces have a void around the center of the Brillouin zone (Γ point). Also the branches α′ and α″ are due to these Fermi surfaces;

— branch β is due to the hole-Fermi surfaces corresponding to band 39 and 40;

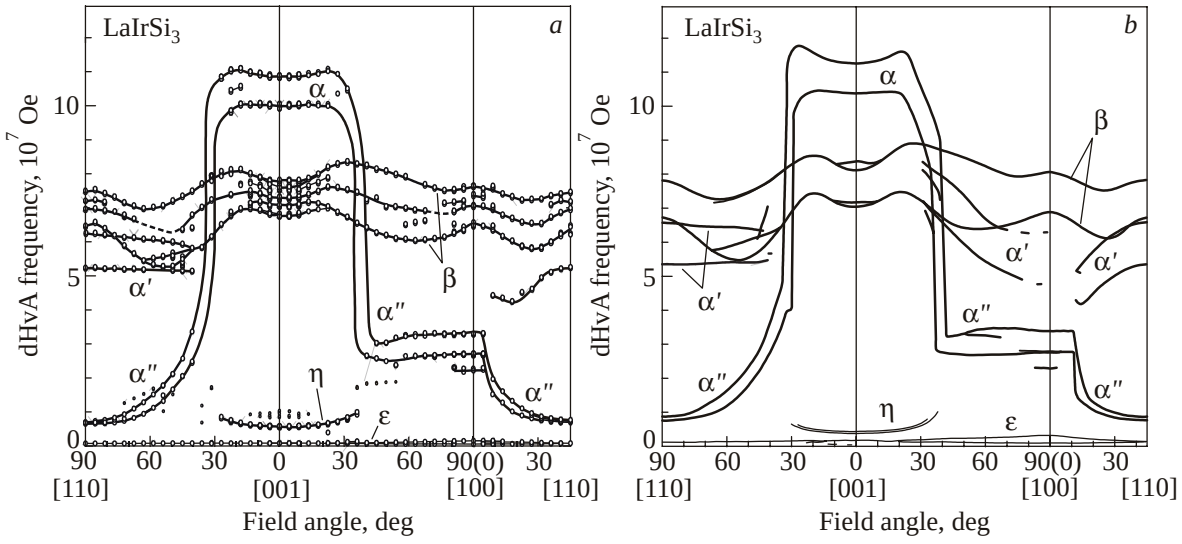

Fig. 129. Angular dependence of the dHvA frequency (*a*) and theoretical angular dependence (*b*) in $LaIrSi_3$, cited from Ref. 23.

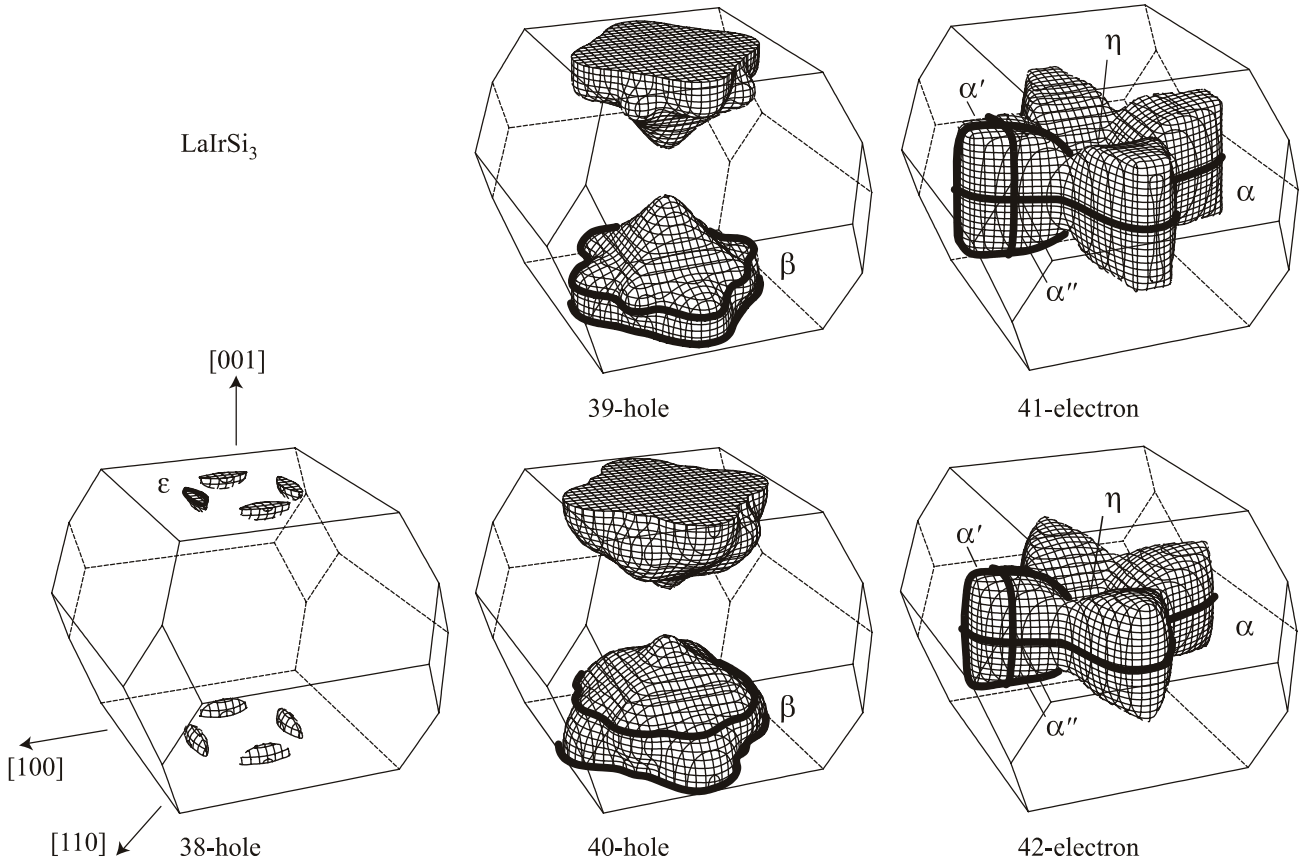

Fig. 130. Theoretical Fermi surfaces in $LaIrSi_3$, cited from Ref. 23.

— branch ε originates from the hole-Fermi surface of band 38.

We determine the cyclotron effective mass m_c^* from the temperature dependence of the dHvA amplitude and find, for example, $1.03\,m_0$ for branch α in the magnetic field along the [001] direction. Fermi surface properties are summarized in Table 9, where the dHvA data for $LaTGe_3$ (T: Co, Rh, Ir) and a paramagnet $PrCoGe_3$ with the singlet CEF scheme are also presented.

The dHvA results of $LaIrSi_3$ are also compared with that of $LaIrGe_3$, as shown in Fig. 131 [26]. The valence electrons are $3s^2 3p^2$ in Si and $4s^2 4p^2$ in Ge. The dHvA frequency of $LaIrGe_3$ is slightly smaller than that of $LaIrSi_3$, because the lattice constants of a = 4.4343 Å and c = 10.0638 Å in $LaIrGe_3$ are larger than a = 4.2820 Å and c = 9.8391 Å in $LaIrSi_3$ and the corresponding Brillouin zone of $LaIrGe_3$ has a smaller volume than that of $LaIrSi_3$. However, the $2|\alpha p_\perp|$ value is almost the same for the two compounds as listed in Table 9.

We now discuss the Fermi surface properties and the magnitude of the antisymmetric spin-orbit coupling in $LaTGe_3$ (T: Co, Rh, Ir) [26]. Figure 132 shows the angular dependence of the dHvA frequency. The topologies of the Fermi surfaces are essentially the same in $LaTGe_3$(T = Co,

Table 9. Experimental dHvA frequency F, the cyclotron mass m_c^*, and the antisymmetric spin-orbit interaction $2|\alpha p_\perp|$ for $H \parallel [001]$ in $LaTX_3$ (T = Co, Rh, Ir and X = Si, Ge) and $PrCoGe_3$, cited from Ref. 26

	branch α			branch β		
	F, 10^7 Oe	m_c^*, m_0	$2\|\alpha p_\perp\|$, K	F, 10^7 Oe	m_c^*, m_0	$2\|\alpha p_\perp\|$, K
$LaCoGe_3$	9.15 8.74	1.19 1.20	461	7.09 6.72	1.28 1.11	416
$LaRhGe_3$	10.4 10.0	1.04 1.04	511	6.98 6.67	0.83 0.85	505
$LaIrGe_3$	10.4 9.29	1.13 1.51	1090	7.25 6.22	1.32 1.29	1066
$LaIrSi_3$	10.9 10.0	0.97 1.03	1100	7.64 6.76	0.97 0.92	1250
$PrCoGe_3$	9.04 8.64	1.80 1.97	284	7.13 6.71	2.04 1.70	302

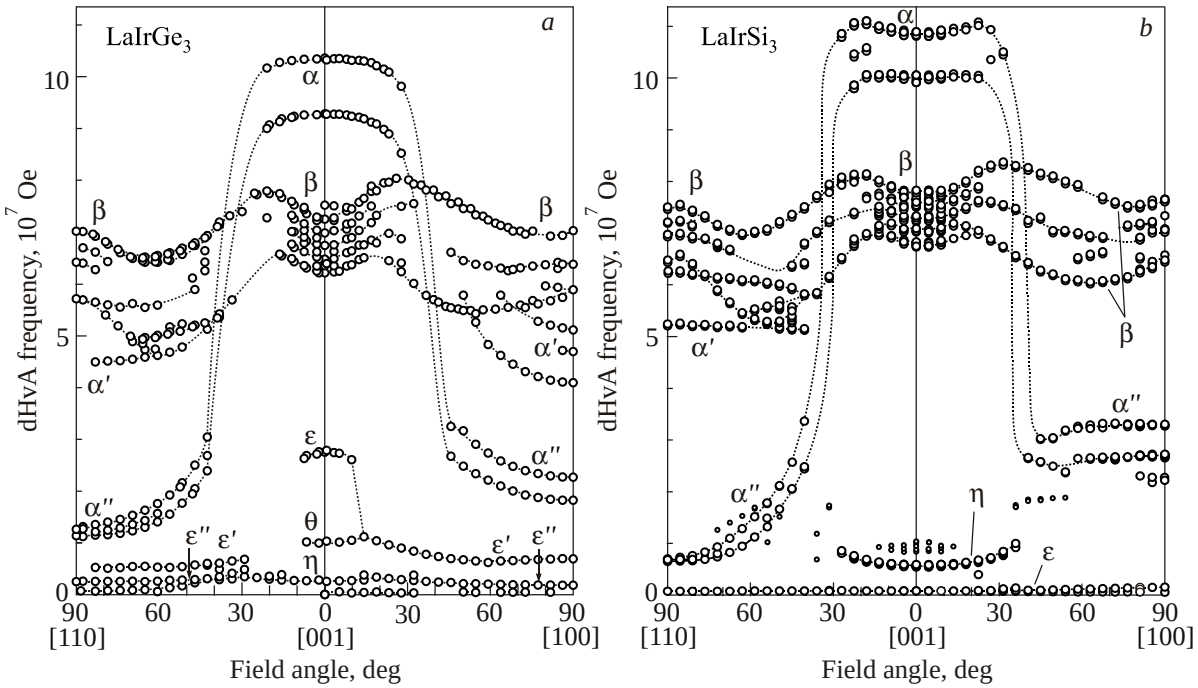

Fig. 131. Angular dependence of the dHvA frequency in $LaIrGe_3$ (*a*) and $LaIrSi_3$ (*b*), cited from Ref. 26.

Rh, Ir). This is plausible in view of the fact that the valence electron configurations do not differ in $LaTGe_3$: $3d^7 4s^2$ in Co, $4d^8 5s^1$ in Rh and $5d^9$ in Ir. Note, however, that the dHvA frequency of branch α in $LaCoGe_3$ is smaller than those in both $LaRhGe_3$ and $LaIrGe_3$, and the width of the split dHvA frequencies, $|F_+ - F_-|$, for branch α in $LaIrGe_3$ is larger than those in $LaCoGe_3$ and $LaRhGe_3$. Hence the Fermi surface in $LaCoGe_3$ is slightly smaller in volume than those in $LaRhGe_3$ and $LaIrGe_3$. Moreover, we may conclude that the antisymmetric spin-orbit coupling $2|\alpha p_\perp|$ in $LaIrGe_3$ is larger than in $LaCoGe_3$ and $LaRhGe_3$: $2|\alpha p_\perp| = 460$ K in $LaCoGe_3$, 510 K in $LaRhGe_3$ and 1090 K in $LaIrGe_3$ for branch α. Precise values for branches α and β are given in Table 9.

In this series of dHvA experiments, the potentials can be varied by changing the transition metal ions T = Co, Rh and Ir in $LaTGe_3$. This may explain the reason why the antisymmetric spin-orbit coupling in $LaIrGe_3$ is relatively large compared with those in $LaCoGe_3$ and $LaRhGe_3$. The difference is connected with both the characteristic radial wave function $\phi(r)$ of Ir-5*d* electrons and the relatively large effective atomic number Z_{eff} in Ir close to the nuclear center. Here we simply calculate the spin-orbit interaction for the *d* electrons, not in the lattice but in the isolated atom, following the method presented by Koelling and Harmon [187].

Figure 133 shows the *r*-dependence of the radial wave function $r\phi(r)$ for Ir-5*d*, Rh-4*d* and Co-3*d* electrons. We

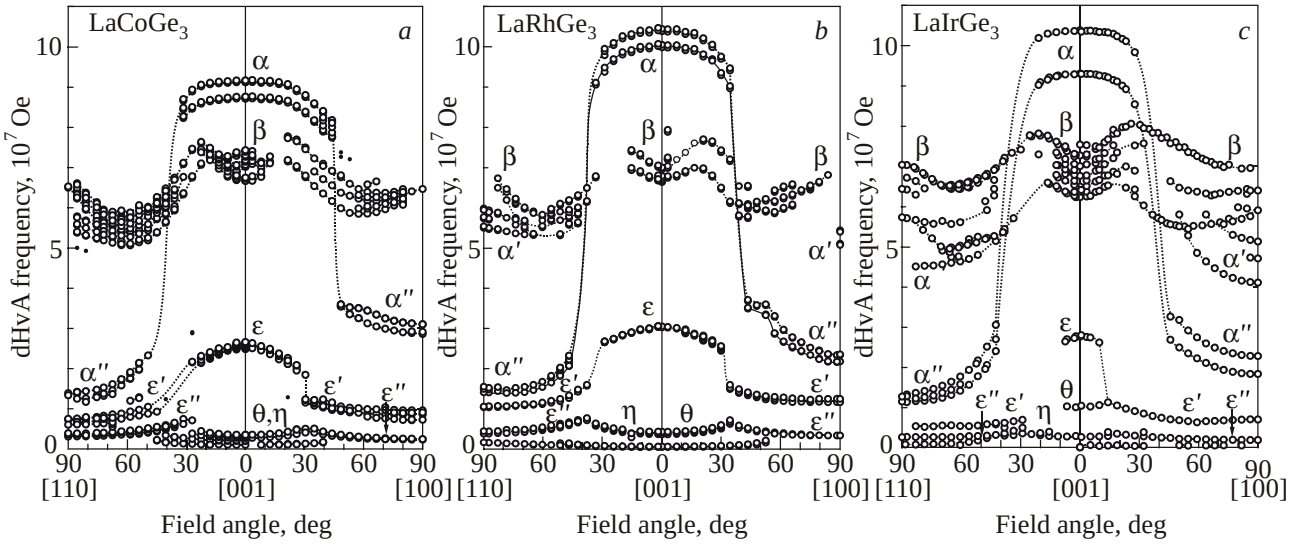

Fig. 132. Angular dependence of the dHvA frequency in $LaCoGe_3$ (*a*), $LaRhGe_3$ (*b*) and $LaIrGe_3$ (*c*), cited from Ref. 26.

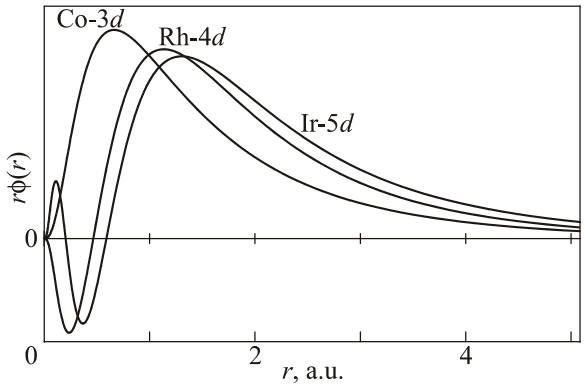

Fig. 133. Radial wave function $r\phi(r)$ as a function of the distance r for Ir-5*d*, Rh-4*d* and Co-3*d* electrons in the isolated atoms, cited from Ref. 26.

assumed the valence electrons to be $3d^7 4s^2$ in Co, $4d^7 5s^2$ in Rh and $5d^7 6s^2$ in Ir. The $r\phi(r)$ function of Ir-5*d* electrons possesses a maximum at $r = 0.11$ a.u. (atomic units), very close to the atomic center, while the corresponding distance r is 0.37 a.u. in Rh-4d and 0.66 a.u. in Co-3*d*, farther from the atomic center.

Next we will consider the potential $V(r)$, which corresponds to the sum of the nuclear potential, and the classical Coulomb and exchange-correlation potentials derived from electrons. Figure 134,*a* shows the coupling constant of the spin-orbit interaction, $r^2 dV(r)/dr$. Simply thinking, this value corresponds to the effective atomic number Z_{eff} in the potential $V(r) = -Z_{\text{eff}}/r$. Z_{eff} at $r = 0$ is very close to the atomic number Z in the nuclear potential $V(r) = -Z/r$, where Z is 77, 45 and 27 for Ir, Rh and Co, respectively. As seen in Fig. 134,*a*, the coupling constant of the spin-orbit interaction is reduced strongly as a function of the distance r, because of screening of the nuclear charge by the electron cloud, reaching $Z_{\text{eff}} \to 1$ for $r \to \infty$.

Finally we calculate the spin-orbit interaction, I_{so}:

$$I_{so}(r) = \frac{\hbar^2}{2m^2c^2} \int_0^r \frac{1}{r'} \frac{dV(r')}{dr'} |\, r'\phi(r')\,|^2 \, dr' , \qquad (25)$$

which is shown in Fig. 134,*b* as a function of the distance r. I_{so} becomes constant at about 1.0 a.u., but approximately reaches this constant value at $r = 0.11$ a.u. for Ir-5*d*, 0.37 a.u. for Rh-4*d* and 0.66 a.u. for Co-3*d*, where the corresponding radial wave functions possess the extremal values, as mentioned above. The spin-orbit coupling is, thus, obtained to be 38.0 mRy (6000 K) for Ir-5*d*, 12.8 mRy (2020 K) for Rh-4*d* and 5.72 mRy (900 K) for Co-3*d*. These calculations suggest that the radial wave function of Ir-5*d* electrons have a larger weight at distances close to the center, compared with those of Rh-4*d* and Co-3*d*, and develops a relatively strong spin-orbit coupling in Ir, closely connected with the relatively large effective atomic number Z_{eff} for Ir at the distance r close to the atomic center.

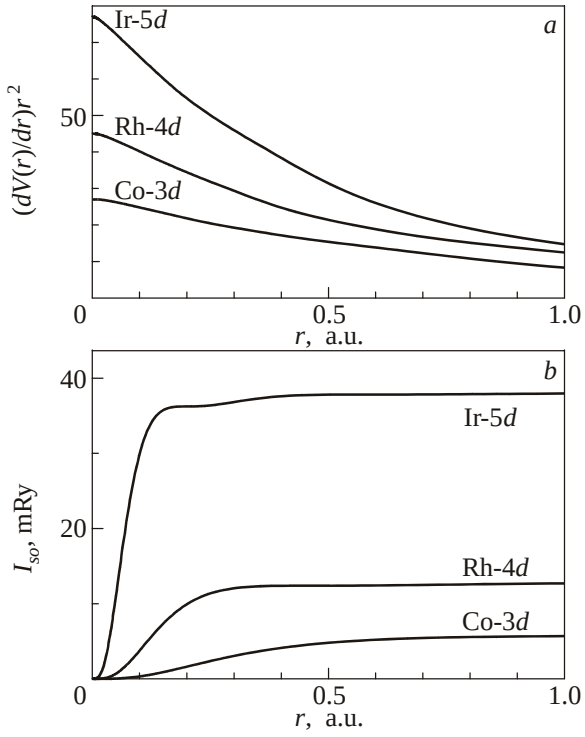

Fig. 134. Coupling constant of the spin-orbit interaction $(dV(r)/dr)r^2$ (*a*) and the spin-orbit interaction I_{so} as a function of the distance r (*b*) for Ir-5*d*, Rh-4*d* and Co-3*d* electrons in the isolated atoms, cited from Ref. 26.

This result of the spin-orbit interaction for an isolated atom is applied to the non-centrosymmetric crystal lattice. In this case, the degenerate Fermi surface is split into two Fermi surfaces of which the magnitude of the antisymmetric spin-orbit interaction is approximately proportional to the spin-orbit coupling of Eq. (25), because the same potential is in principle used in the band structure calculation. The *d* electrons in the transition atom as well as the 5*d* electrons in the La atom and the other electrons contribute to the conduction electrons in $LaTGe_3$. This is the main reason why the antisymmetric spin-orbit interaction $2|\alpha p_\perp|$ in $LaIrGe_3$ and $LaIrSi_3$ is larger than in $LaCoGe_3$ and $LaRhGe_3$. These results may also be applied to Li_2Pt_3B and Li_2Pd_3B [188], where the spin-orbit coupling in Li_2Pt_3B, which originates mainly form Pt-5*d* electrons, is expected to be larger than the contribution from Pd-4*d* orbitals in Li_2Pd_3B. The magnitude of the antisymmetric spin-orbit coupling of $CeIrSi_3$ cannot be determined from the result of the present dHvA experiments, but can be roughly estimated from the γ value: we estimate $2|\alpha p_\perp| \simeq$ $\simeq 40$ K from $\gamma = 120$ mJ/(K^2·mol) in $CeIrSi_3$ based on $2|\alpha p_\perp| \simeq 1000$ K and $\gamma = 4.5$ mJ/(K^2·mol) for $LaIrSi_3$ [23]. This value is much larger than the superconducting transition temperature $T_{sc} = 1.6$ K at 2.65 GPa in $CeIrSi_3$, as shown below.

To understand the electronic properties of $CeTX_3$, we plot the Néel temperature and the electronic specific heat coefficient γ as a function of the average lattice constant $\sqrt[3]{a^2 c}$ for $CeTX_3$, in Figs. 135,*a* and 135,*b*, respectively. It

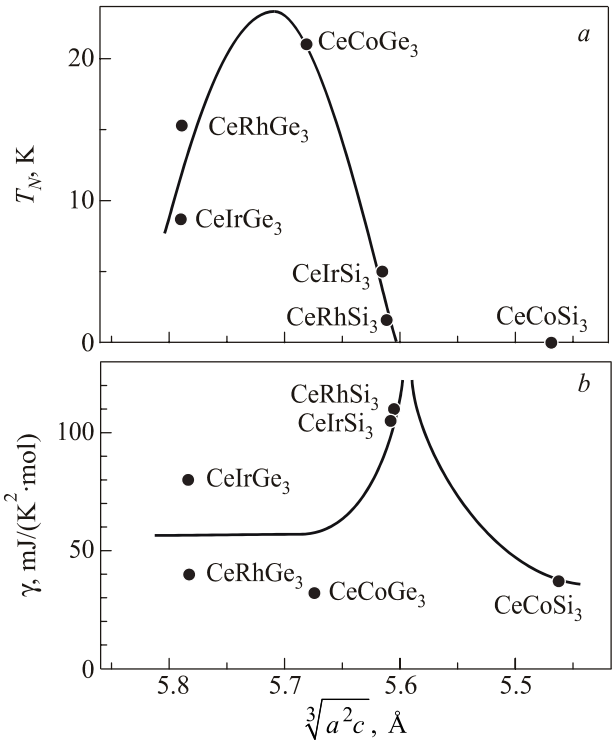

Fig. 135. $\sqrt[3]{a^2c}$ -dependence of the Néel temperature (*a*) and the γ value (*b*) in $CeTSi_3$ and $CeTGe_3$ (T: Co, Rh, Ir), cited from Refs. 23, 176, 189, 190.

is noted that the lattice constant on the left hand side is larger than that in the right hand side (data from Refs. 23, 176, 189, 190). The observed relation of T_N vs $\sqrt[3]{a^2c}$ in Fig. 135,*a* roughly corresponds to the Doniach phase diagram [4], which indicates a competition between the RKKY interaction and the Kondo screening effect, as mentioned in Chap. 1. $CeRhSi_3$ and $CeIrSi_3$ are close to the quantum critical point in the electronic state, with a relatively large γ value, as shown in Fig. 135,*b*. In fact, the Néel temperatures in $CeRhSi_3$ and $CeIrSi_3$ become zero at a relatively small value of pressure, $P_c \simeq 2$ GPa.

Figure 136 shows the pressure dependence of the Néel temperature T_N, the superconducting transition temperature T_{sc}, the specific heat jump at T_{sc}, $\Delta C_{ac}/C_{ac}(T_{sc})$, and the upper critical field at 0 K, $H_{c2}(0)$ for $H \parallel [001]$ [191,192]. The critical pressure, where the Néel temperature becomes zero, is estimated to be $P_c = 2.25$ GPa. The superconducting transition temperature becomes maximum at about 2.6 GPa, as shown in Fig. 136,*a*. Simultaneously, the jump of the specific heat at T_{sc} becomes extremely large at 2.58 GPa: $\Delta C_{ac}/C_{ac}(T_{sc}) = 5.8$ as shown in Fig. 136,*b*, indicating a strong-coupling superconductivity for $CeIrSi_3$. The upper critical field $H_{c2}(0)$ for $H \parallel [001]$ becomes maximum at $P_{c2}^* = 2.63$ GPa, as shown in Fig. 136,*c*.

As shown in Fig. 137, the upper critical field deviates substantially between $H \parallel [001]$ and [110] [191]. The superconducting properties become highly anisotropic: $-dH_{c2}/dT = 170$ kOe/K at $T_{sc} = 1.56$ K, and $H_{c2}(0) \simeq 450$ kOe for

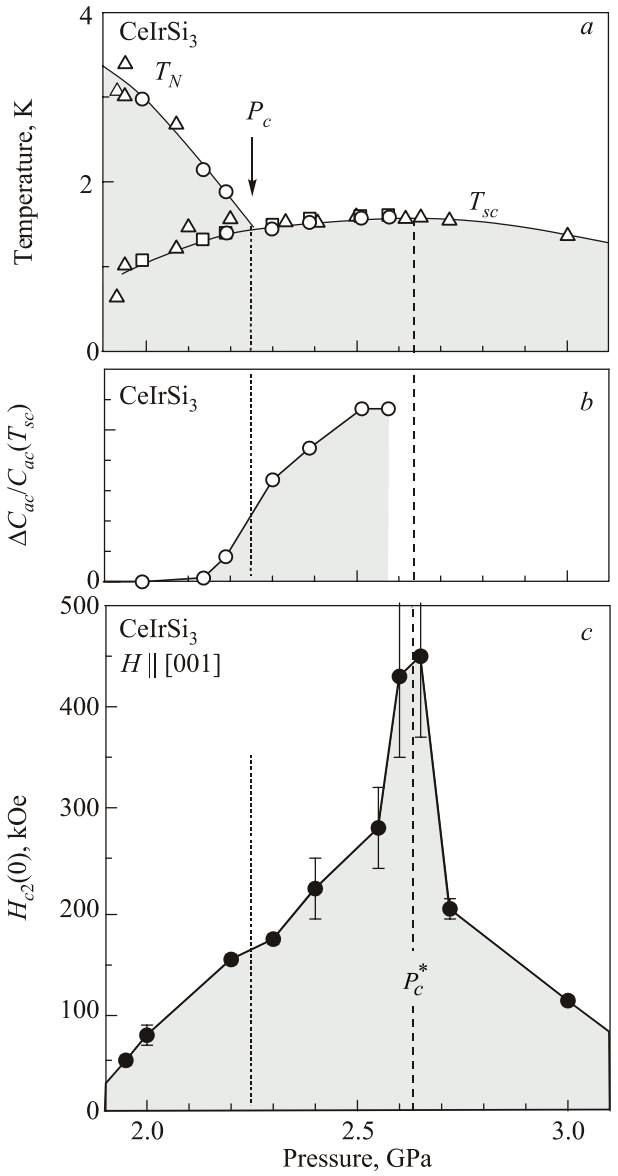

Fig. 136. Pressure dependences of the Néel temperature T_N and superconducting transition temperature T_{sc} (*a*), specific heat jump $\Delta C_{ac}/C_{ac}(T_{sc})$ (*b*), cited from Ref. 192, and the upper critical field $H_{c2}(0)$ for $H \parallel [001]$ (*c*) in $CeIrSi_3$, cited from Ref. 191.

$H \parallel [001]$, and $-dH_{c2}/dT = 145$ kOe/K at $T_{sc} = 1.59$ K, and $H_{c2}(0) = 95$ kOe for $H \parallel [110]$ at 2.65 GPa. The upper critical field H_{c2} for $H \parallel [110]$ shows strong signs of Pauli paramagnetic suppression with decreasing temperature because the orbital limiting field $H_{orb} = -0.73(dH_{c2}/dT)T_{sc}$ is estimated to be 170 kOe [159], which is larger than $H_{c2}(0) = 95$ kOe for $H \parallel [110]$. On the other hand, the upper critical field $H \parallel [001]$ is not destroyed by spin polarization based on Zeeman coupling but possesses an upturn curvature below 1 K, reflecting a strong-coupling nature of superconductivity. This is because all the spins of conduction electrons are perpendicular to the magnetic field direction of $H \parallel [001]$, as shown in Fig. 127,*c*, revealing that the spin susceptibility for $H \parallel [001]$ is unchanged below T_{sc} in this non-centro-

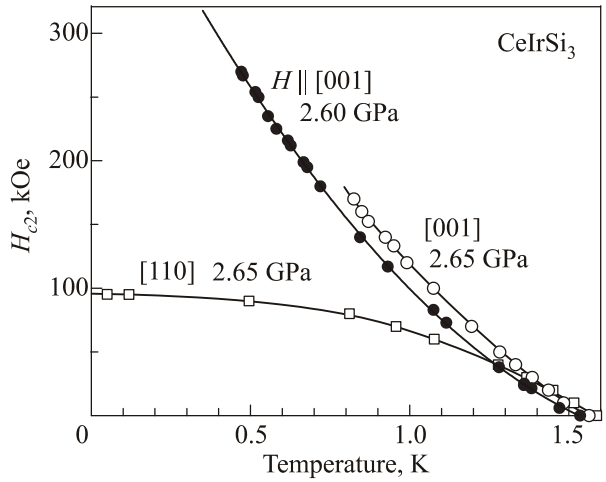

Fig. 137. Temperature dependence of upper critical field H_{c2} for the magnetic field along [001] at 2.60 GPa, together with those at 2.65 GPa in $CeIrSi_3$, cited from Ref. 191.

symmetric crystal structure and then the Pauli paramagnetic suppression of H_{c2} is not realized for $H \parallel [001]$. Moreover, the electronic state at P_c^* is found to correspond to an antiferromagnetic quantum critical point from the result of the ^{29}Si-NMR experiment [193].

The magnetic quantum phase transition thus occurs in $CeIrSi_3$ at $P_c^* \simeq 2.6$ GPa, coinciding with a huge H_{c2} value of $H_{c2}(0) \simeq 450$ kOe for $H \parallel [001]$ for a low $T_{sc} = 1.6$ K value. A similar result is also obtained for $CeRhSi_3$ [174,175].

9. de Haas–van Alphen oscillation in the superconducting mixed state

To our surprise, the dHvA oscillation was observed even in the superconducting mixed state of type II-superconductors [194]. Here we show the dHvA oscillation in *f*-electron superconductors $CeRu_2$ [195], $CeCoIn_5$ [79], URu_2Si_2 [196] and UPd_2Al_3 [197] in both the normal and superconducting mixed states, as shown in Fig. 138. The main Fermi surface named α_i in $CeCoIn_5$ was detected in magnetic fields very close to H_{c2} [79]. Surprisingly, a small Fermi surface in $CeRu_2$, URu_2Si_2 and UPd_2Al_3 was detected in low fields down to $H/H_{c2} = 0.3$–0.5, for example down to a low field of 15 kOe or $0.3H_{c2}$ in $CeRu_2$. It is questionable whether the small Fermi surface has a superconducting energy gap in magnetic fields far below H_{c2}. This might indicate the growth of a pair-breaking effect far below H_{c2} for the small Fermi surface. More importantly, there is a possibility that the superconducting state for the small Fermi surface is changed into a normal state far below H_{c2}.

Till now, the dHvA oscillation in the mixed state has been observed for several compounds such as $NbSe_2$ [198], V_3Si [199], Nb_3Sn [200], YNi_2B_2C [201,202] as well as *f*-electron system of $CeRu_2$, $CeCoIn_5$, URu_2Si_2 and UPd_2Al_2.

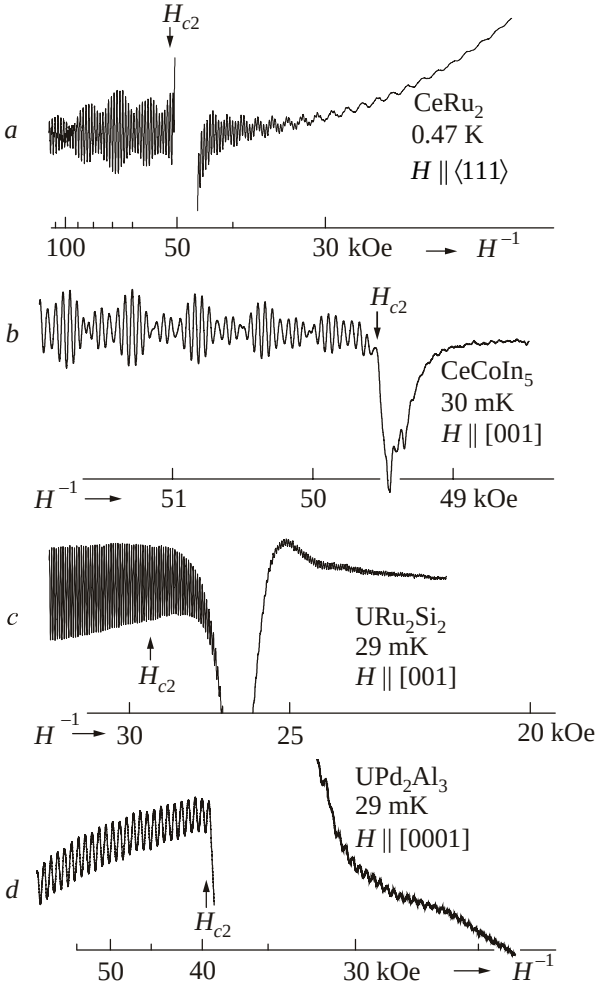

Fig. 138. dHvA oscillations in the superconducting mixed states of $CeRu_2$ [195], $CeCoIn_5$ [79], URu_2Si_2 [196] and UPd_2Al_3 [197].

10. Conclusion

We summarize the present Fermi surface studies in the *f*-electron systems of rare earth and actinide compounds.

1. Fermi surface studies are very important to know the ground-state properties of these various *f*-electron compounds. Even in the 4*f*-electron localized system, the presence of 4*f*-electron alter the Fermi surface through the 4*f*-electron contribution to the crystal potential and through the introduction of new Brillouin zone boundaries and magnetic energy gaps which occur when 4*f*-electron moments order. The latter effect may be approximated by a band-folding procedure where the paramagnetic Fermi surface, which is similar to the Fermi surface of the corresponding La compound, is folded into a smaller Brillouin zone based on the magnetic unit cell, which is larger than the chemical unit cell. If the magnetic energy gaps associated with the magnetic structure are small enough, conduction electrons undergoing the cyclotron motion in the presence of a magnetic field can tunnel through these gaps and circulate the orbits on the paramagnetic Fermi surface. If

this magnetic breakthrough occurs, the paramagnetic Fermi surface is observed in the dHvA effect even in the presence of magnetic order. The typical example was an antiferromagnet $NdIn_3$ in RIn_3 (R: rare earth). A nearly spherical Fermi surface in the paramagnetic state, which corresponds to branch *a* of the band 7-electron Fermi surface of $LaIn_3$, is changed into a multiply-connected Fermi surface based on the magnetic Brillouin zone in the antiferromagnetic state. Even in the antiferromagnetic state, the dHvA oscillation for branch *a* was observed, with an extremely small dHvA amplitude based on the breakthrough effect.

2. Mass enhancement due to the electron–magnon interaction in the 4*f* localized compounds RIn_3 is large compared with the one due to the electron–phonon interaction. The cyclotron mass is enhanced by twice or three times in RIn_3 compared with the cyclotron mass in $LaIn_3$. An antiferroquadrupolar ordering in $PrPb_3$ is also found to enhance the cyclotron mass. An exceptionally large mass enhancement is observed in a Kondo-lattice compound with magnetic ordering such as $CeIn_3$ in RIn_3. The Fermi surface of $CeIn_3$ is similar to a non-4*f* reference compound $LuIn_3$ or $LaIn_3$ in topology, especially for branch *d*, but is altered by the magnetic Brillouin zone boundaries for branch *a*. Nevertheless, the cyclotron mass is extremely large compared with the corresponding one of $LuIn_3$. In this system, a small amount of 4*f* electron most likely contributes to make a sharp density of states at the Fermi energy. Thus the energy band becomes flat around the Fermi energy, which brings about the large effective mass. It is stressed that the heavy electronic state exists locally in the Fermi surface. The Fermi surface named branch *d* is a nearly spherical Fermi surface with humps. The hump region on the Fermi surface is extremely heavy.

3. The *f*-itinerant band model is well applicable to the topology of the Fermi surface in enhanced Pauli paramagnets such as $CeSn_3$, $YbAl_3$, UAl_3, UX_3 (X: Si, Ge), $NpGe_3$ and $PuIn_3$ in RX_3 and AnX_3 compounds. These compounds are called a valence fluctuating compound or a spin fluctuating compound. The magnetic susceptibility in these compounds increases with decreasing temperature, roughly following the Curie–Weiss law at high temperatures, with an *f*-localized magnetic moment, has a maximum at $T_{\chi max}$ and reaches an enhanced Pauli paramagnetic susceptibility $\chi(0)$ for $T \to 0$ K. A characteristic feature is that $T_{\chi max}$ is in the range from 50 to 200 K. $T_{\chi max}$ roughly corresponds to a Kondo temperature. The *f* electrons in a Kondo lattice compound with a relatively large value of T_K are itinerant. It is, however, stressed that the cyclotron mass is larger than the corresponding band mass because the many-body Kondo effect is not included in the conventional energy band calculations.

4. It is interesting that the topology of Fermi surface is very similar between two compounds: $LaPb_3$ vs UAl_3, $LaIn_3$ vs $NpIn_3$, and $YbIn_3$ vs $PuIn_3$, although the cyclotron mass is extremely different between two compounds. It is also noticed that the topology of a divalent compound $YbIn_3$ is very similar to a 4*f*-itinerant compound $YbAl_3$. It is also noted that $YbCu_2Ge_2$ is similar to $YbCu_2Si_2$ in topology of the Fermi surface. Furthermore, 4*f*-itinerant Ce compounds are similar to the corresponding non-5*f* Th compounds in the topology of the Fermi surface: $CeIn_3$ under pressure vs $ThIn_3$, and $CeRhIn_5$ under pressure and $CeCoIn_5$ vs $ThRhIn_5$.

5. 5*f* electrons in magnetically ordered U and Np compounds reveal dual nature: localized and itinerant. Namely, the 5*f* electrons contribute to the magnetic moment and also to the Fermi surface. The topology of the Fermi surface of antiferromagnets $UPtGa_5$ and $NpRhGa_5$ is approximately explained by the spin-and orbital-polarized 5*f*-itinerant band model.

6. $RTIn_5$ (T: Co, Rh, Ir) and $AnTGa_5$ (T: transition metal) with the tetragonal structure possess the quasi-two dimensional electronic state. Simply thinking, a conductive RIn_3 ($AnGa_3$) layer and an insulating TIn_2 ($AnGa_2$) layer stack along the tetragonal *c*-axis. The quasi-two dimensional electronic state, together with the heavy fermion state, enhances heavy fermion superconductivity, as in $CeRhIn_5$ under pressure, $CeCoIn_5$, $PuRhGa_5$, $PuCoGa_5$ and also $NpPd_5Al_2$. Interesting is the relation between the superconducting transition temperature T_{sc} and the γ value: T_{sc} = 2.3 K (γ = 1070 mJ/(K^2·mol)) in $CeCoIn_5$, 4.9 K (400 mJ/(K^2·mol)) in $NpRh_5Al_2$, 8.6 K (70 mJ/(K^2·mol)) in $PuRhGa_5$ and 18.5 K (77 mJ/(K^2·mol)) in $PuCoGa_5$. It is also stressed that T_{sc} = 0.2K (γ = 1000 mJ/(K^2·mol)) in a three dimensional electronic state of $CeIn_3$ under pressure is enhanced by one order, T_{sc} = 2.3 K in a two dimensional electronic state of $CeCoIn_5$. It is also noted that heavy fermion superconductivity of $CeCoIn_5$ and $NpPd_5Al_2$ is realized in the non-Fermi liquid state

7. Heavy fermion compounds with a small $T_{\chi max}$ value, less than 50 K, indicate a metamagnetic behavior or an abrupt nonlinear increase of magnetization at H_m. We obtained a simple relation for $CeRu_2Si_2$, UPt_3 and YbT_2Zn_20 (T: Co, Rh, Ir): H_m (kOe) = 15$T_{\chi max}$, K or, $k_BT_{\chi max}$ = = μ_BH_m. A superheavy fermion state is realized in $YbCo_2Zn_{20}$: γ = 8000 mJ/(K^2·mol)), $T_{\chi max}$ = 0.32 K and H_m = 6 kOe, and also under pressure for $YbIr_2Zn_{20}$, exceeding γ = 10 J/(K^2·mol) at 5.0 GPa. The present superheavy fermion state is, however, drastically reduced in magnetic fields. It is also noted that the metamagnetic field H_m is a good guiding parameter to reach the quantum critical point in heavy fermion Yb compounds without magnetic ordering: $P \to P_c$ for $H_m \to 0$. The topology of the Fermi surface is changed at H_m in $CeRu_2Si_2$, but not in $YbIr_2Si_{20}$, although the cyclotron mass in both compounds possesses a maximum at H_m and reduces extremely in magnetic fields larger than H_m. The metamagnetic transition based on the field-induced ferroquadrupolar ordering was also studied in $PrCu_2$.

8. From the dHvA experiments under pressure for antiferromagnets $CeRh_2Si_2$, $CeIn_3$ and $CeRhIn_5$, it was clarified that a drastic change in the 4*f* electronic state from a 4*f*-localized Fermi surface to a 4*f*-itinerant Fermi surface occurs when pressure P crosses a critical pressure P_c or P_c^*. The Fermi surface instability occurs at P_c (P_c^*), indicating a first-order phase transition. The cyclotron mass is enhanced around P_c (P_c^*), especially indicating a divergent tendency at P_c^* in $CeRhIn_5$. Superconductivity in these compounds is observed in the heavy fermion state around P_c (P_c^*).

9. The split Fermi surface properties based on the non-centrosymmetric tetragonal crystal structure in $LaTX_3$ (T: Co, Rh, Ir; X: Si, Ge) were studied by the dHvA experiments, together with the energy band calculations. The magnitude of the antisymmetric spin-orbit interaction $2|\alpha p_\perp|$ is found to vary when $LaTGe_3$ is changed from T = Co, Rh, to Ir, but remains unchanged in $LaIrX_3$ from X = Si to Ge: $2|\alpha p_\perp|$ = 460 K in $LaCoGe_3$, 510 K in $LaRhGe_3$, 1090 K in $LaIrGe_3$, and 1100 K in $LaIrSi_3$ for the main orbit named α of bands 69 and 70 electron-Fermi surfaces, for example. The corresponding superconducting properties were also studied in $CeTX_3$ compounds under pressure. One of the characteristic superconducting properties in $CeIrSi_3$ is the upper critical field H_{c2} at pressure of about 2.6 GPa. A huge value of $H_{c2}(0) \simeq 450$ kOe was found for the magnetic field along the non-centrosymmetric tetragonal [001] direction, with a very small T_{sc} = = 1.6 K, while $H_{c2}(0)$ = 95 kOe for $H \parallel [110]$. The present superconductivity is realized in the electronic instability at $P_c^* \simeq 2.6$ GPa, strong-coupling nature and non-centrosymmetric electronic state.

10. The dHvA oscillation was observed clearly in both the normal and superconducting mixed states in $CeRu_2$, $CeCoIn_5$, URu_2Si_2 and UPd_2Al_3.

Acknowledgments

We are very grateful to K. Miyake and K. Ueda for helpful discussions, and to F. Honda, K. Sugiyama, T. Takeuchi, Y. Haga, E. Yamamoto, T. D. Matsuda, N. Tateiwa, K. Shimizu, D. Aoki, H. Aoki, H. Harima, H. Yamagami, A. Hasegawa, and Y. Kitaoka for collaborations.

1. Y. Ōnuki, T. Goto, and T. Kasuya, *Materials Science and Technology*, K.H.J. Buschow (ed.), VCH, Weinheim (1991), Vol. 3A, Part I, Ch. **7**, p. 545.
2. Y. Ōnuki and A. Hasegawa, *Handbook on the Physics and Chemistry of Rare Earths*, K.A. Gschneidner, Jr., and L. Eyring (eds.), Elsevier Science, Amsterdam (1995), Vol. 20, p. 1.
3. Y. Ōnuki, R. Settai, K. Sugiyama, T. Takeuchi, T.C. Kobayashi, Y. Haga, and E. Yamamoto, *J. Phys. Soc. Jpn.* **73**, 769 (2004).
4. S. Doniach, *Valence Instabilities and Related Narrow Band Phenomena*, R.D. Parks (ed.), Plenum, New York (1977), p. 169.
5. Y. Ōnuki, Y. Inada, H. Ohkuni, R. Settai, N. Kimura, H. Aoki, Y. Haga, and E. Yamamoto, *Physica* **B280**, 276 (2000).
6. M. Sigrist and K. Ueda, *Rev. Mod. Phys.* **63**, 239 (1991).
7. N. Metoki, Y. Haga, Y. Koike, and Y. Ōnuki, *Phys. Rev. Lett.* **80**, 5417 (1998).
8. N. Bernhoeft, N. Sato, B. Roessli, N. Aso, A. Heiss, G.H. Lander, Y. Endoh, and T. Komatsubara, *Phys. Rev. Lett.* **81**, 4244 (1998).
9. N.K. Sato, N. Aso, K. Miyake, R. Siina, P. Thalmeier, G. Varelogiannis, C. Geibel, F. Steglich, P. Fulde, and T. Komatsubara, *Nature* **410**, 340 (2001).
10. M. Kyogaku, Y. Kitaoka, K. Asayama, C. Geibel, C. Schank, and F. Steglich, *J. Phys. Soc. Jpn.* **62**, 4016 (1993).
11. H. Tou, Y. Kitaoka, K. Ishida, K. Asayama, N. Kimura, Y. Ōnuki, E. Yamamoto, Y. Haga, and K. Maezawa, *Phys. Rev. Lett.* **80**, 3129 (1998).
12. K. Tenya, M. Ikeda, T. Sakakibara, E. Yamamoto, K. Maezawa, N. Kimura, R. Settai, and Y. Ōnuki, *Phys. Rev. Lett.* **77**, 3193 (1996).
13. D. Jaccard, H. Wilhelm, K. Alami-Yadri, and E. Vargoz, *Physica* **B259–261**, 1 (1999).
14. N.D. Mathur, F.M. Grosche, S.R. Julian, I.R. Walker, D.M. Freye, R.K.W. Haselwimmer, and G.G. Lonzarich, *Nature* **394**, 39 (1998).
15. H. Hegger, C. Petrovic, E.G. Moshopoulou, M.F. Hundley, J.L. Sarrao, Z. Fisk, and J.D. Thompson, *Phys. Rev. Lett.* **84**, 4986 (2000).
16. S.S. Saxena, P. Agarwal, K. Ahilan, F.M. Grosche, R.K.W. Haselwimmer, M.J. Steiner, E. Pugh, I.R. Walker, S.R. Julian, P. Monthoux, G.G. Lonzarich, A. Huxley, I. Sheikin, D. Braithwaite, and J. Flouquet, *Nature* **406**, 587 (2000).
17. D. Aoki, A. Huxley, E. Ressouche, D. Braithwaite, J. Flouquet, J.P. Brison, E. Lhotel, and C. Paulsen, *Nature* **413**, 613 (2001).
18. T. Akazawa, H. Hidaka, T. Fujiwara, T.C. Kobayashi, E. Yamamoto, Y. Haga, R. Settai, and Y. Ōnuki, *J. Phys.: Condens. Matter* **16**, L29 (2004).
19. N.T. Huy, A. Gasparini, D.E. de Nijs, Y. Huang, J.C.P. Klaasse, T. Gortenmulder, A. de Visser, A. Hamann, T. Görlach, and H. v. Lühneysen, *Phys. Rev. Lett.* **99**, 067006 (2007).
20. H.R. Ott and Z. Fisk, in: *Handbook on the Physics and Chemistry of the Actinides*, A.J. Freeman and G.H. Lander (eds.), Elsevier Science, Amsterdam (1987), Vol. 5, Ch. 2, p. 85.
21. Y. Haga, H. Sakai, and S. Kambe, *J. Phys. Soc. Jpn.* **76**, 051012 (2007).
22. Y. Ōnuki, R. Settai, K. Sugiyama, Y. Inada, T. Takeuchi, Y. Haga, E. Yamamoto, H. Harima, and H. Yamagami, *J. Phys.: Condens. Matter* **19**, 125203 (2007).
23. Y. Okuda, Y. Miyauchi, Y. Ida, T. Yamada, Y. Ooduchi, T.D. Matsuda, Y. Haga, T. Takeuchi, K. Kindo, M. Hagiwara, H. Harima, K. Sugiyama, R. Settai, and Y. Ōnuki, *J. Phys. Soc. Jpn.* **76**, 044708 (2007).
24. Y. Haga, T. Honma, E. Yamamoto, H. Ohkuni, Y. Ōnuki, M. Ito, and N. Kimura, *Jpn. J. Appl. Phys.* **37**, 3604 (1998).
25. R. Settai, T. Kawai, T. Endo, H. Muranaka, Y. Doi, Y. Ōnuki, and H. Harima, *J. Phys. Soc. Jpn.* **A77**, 339 (2008).

26. T. Kawai, H. Muranaka, T. Endo, N.D. Dung, Y. Doi, S. Ikeda, T.D. Matsuda, Y. Haga, H. Harima, R. Settai, and Y. Ōnuki, *J. Phys. Soc. Jpn.* **77**, 064717 (2008).
27. H. Sugawara, R. Settai, Y. Doi, H. Muranaka, K. Katayama, H. Yamagami, and Y. Ōnuki, *J. Phys. Soc. Jpn.* **77**, 113711 (2008).
28. D. Shoenberg, *Magnetic Oscillations in Metals*, Cambridge University Press, Cambridge (1984).
29. R. Settai, T. Takeuchi, and Y. Ōnuki, *J. Phys. Soc. Jpn.* **76**, 051003 (2007).
30. Y. Ōnuki, R. Settai, K. Sugiyama, T. Takeuchi, T.C. Kobayashi, Y. Haga, and E. Yamamoto, *Physica* **B300**, 61 (2001).
31. Y. Haga, E. Yamamoto, Y. Tokiwa, D. Aoki, Y. Inada, R. Settai, T. Maehira, H. Yamagami, H. Harima, and Y. Ōnuki, *J. Nucl. Sci. Technol. Suppl.* **3**, 56 (2002).
32. I. Harris and G. Raynor, *J. Less-Common Met.* **9**, 7 (1965).
33. R.M. Galera and P. Morin, *J. Magn. Magn. Mater.* **116**, 159 (1992).
34. K.H.J. Buschow, H.W. de Wijn, and A.M. van Diepen, *J. Chem. Phys.* **50**, 137 (1969).
35. J.M. Lawrence and S.M. Shapiro, *Phys. Rev.* **B22**, 4379 (1980).
36. A. Benoit, J.X. Boucherle, P. Convert, J. Flouquet, J. Pellau, and J. Schweizer, *Solid State Commun.* **34**, 293 (1980).
37. Y. Kohori, T. Kohara, Y. Yamato, G. Tomka, and P.C. Riedi, *Physica* **B281–282**, 12 (2000).
38. R. Settai, T. Kubo, T. Shiromoto, D. Honda, H. Shishido, K. Sugiyama, Y. Haga, T.D. Matsuda, K. Betsuyaku, H. Harima, T.C. Kobayashi, and Y. Ōnuki, *J. Phys. Soc. Jpn.* **74**, 3016 (2005).
39. I. Umehara, N. Nagai, and Y. Ōnuki, *J. Phys. Soc. Jpn.* **60**, 591 (1991).
40. A. Hasegawa, in: *Crystalline Electric Field Effects in f-Electron Magnetism*, R.P. Guetin, W. Suski, and Z. Zolnierek (eds.), Plenum, New York (1982), p. 201.
41. I. Umehara, T. Ebihara, N. Nagai, K. Satoh, Y. Fujimaki, and Y. Ōnuki, *J. Phys. Soc. Jpn.* **61**, 1633 (1992).
42. R. Settai, T. Ebihara, H. Sugawara, N. Kimura, M. Takashita, H. Ikezawa, K. Ichihashi, and Y. Ōnuki, *Physica* **B201**, 102 (1994).
43. P. Lethuillier, J. Pierre, G. Fillion, and B. Barbara, *Phys. Status Solidi* **A15**, 613 (1973).
44. A. Czopnik, N. Iliev, B. Stalihski, C. Bazan, H. Madge, and R. Pott, *Physica* **B130**, 259 (1985).
45. T. Ebihara, I. Umehara, A.K. Albessard, K. Satoh, and Y. Ōnuki, *Physica* **B186–188**, 123 (1993).
46. I. Umehara, N. Nagai, and Y. Ōnuki, *J. Phys. Soc. Jpn.* **60**, 3150 (1991).
47. T. Ebihara, I. Umehara, A.K. Albessard, Y. Fujimaki, K. Satoh, Y. Ōnuki, B. Liu, and M. Kasaya, *J. Phys. Soc. Jpn.* **61**, 2104 (1992).
48. I. Umehara, T. Ebihara, N. Nagai, Y. Fujimaki, K. Satoh, and Y. Ōnuki, *J. Phys. Soc. Jpn.* **61**, 19 (1992).
49. S. Nojiri, Y. Katayama, D. Aoki, N. Suzuki, K. Sugiyama, R. Settai, Y. Inada, Y. Ōnuki, and H. Harima, *Physica* **B28–282**, 747 (2000).
50. N. Nagai, I. Umehara, T. Ebihara, A.K. Albessard, H. Sugawara, T. Yamazaki, K. Satoh, and Y. Ōnuki, *Physica* **B186–188**, 139 (1993).
51. R. Settai, T. Ebihara, M. Takashita, H. Sugawara, N. Kimura, K. Metoki, Y. Ōnuki, S. Uji, and H. Aoki, *J. Magn. Magn. Mater.* **140**–**144**, 1153 (1995).
52. T. Ebihara, N. Harrison, M. Jaime, S. Uji, and J.C. Lashley, *Phys. Rev. Lett.* **93**, 246401 (2004).
53. T. Ebihara, I. Umehara, A.K. Albessard, K. Satoh, and Y. Ōnuki, *J. Phys. Soc. Jpn.* **61**, 1472 (1992).
54. N. Harrison, S.E. Sebastian, C.H. Mielke, A. Paris, M.J. Gordon, C.A. Swenson, D.G. Rickel, M.D. Pacheco, P.F. Ruminer. J.B. Schillig, J.R. Sims, A.H. Lacerda, M.-T. Suzuki, H. Harima, and T. Ebihara, *Phys. Rev. Lett.* **99**, 056401 (2007).
55. V.B. Pluzhnikov, A. Czopnik, and I.V. Svechkarev, *Physica* **B212**, 375 (1995).
56. T. Ebihara, Y. Inada, M. Murakawa, S. Uji, C. Terakura, T. Terashima, E. Yamamoto, Y. Haga, Y. Ōnuki, and H. Harima, *J. Phys. Soc. Jpn.* **69**, 895 (2000).
57. N.D. Dung, T.D. Matsuda, Y. Haga, S. Ikeda, E. Yamamoto, T. Ishikura, T. Endo, S. Tatsuoka, Y. Aoki, H. Sato, T. Takeuchi, R. Settai, H. Harima, and Y. Ōnuki, *J. Phys. Soc. Jpn.* **78**, 084711 (2009).
58. D. Aoki, Y. Homma, H. Sakai, S. Ikeda, Y. Shiokawa, E. Yamamoto, A. Nakamura, Y. Haga, R. Settai, and Y. Ōnuki, *J. Phys. Soc. Jpn.* **75**, 084710 (2006).
59. T.D. Matsuda, Y. Haga, E. Yamamoto, S. Ikeda, H. Shishido, R. Settai, H. Harima, and Y. Ōnuki, *J. Phys. Soc. Jpn.* **74**, 3276 (2005).
60. I. Sakamoto, S. Ohara, I. Oguro, E. Yamamoto, Y. Haga, Y. Ōnuki, and S. Maruno, *J. Alloys Comp.* **275**–**277**, 505 (1998).
61. D. Aoki, Y. Katayama, R. Settai, N. Suzuki, K. Sugiyama, K. Kindo, H. Harima, and Y. Ōnuki, *J. Phys. Soc. Jpn.* **67**, 4251 (1998).
62. I. Umehara, N. Nagai, and Y. Ōnuki, *J. Phys. Soc. Jpn.* **60**, 1294 (1991).
63. D. Aoki, Y. Katayama, R. Settai, Y. Inada, Y. Ōnuki, H. Harima, and Z. Kletowski, *J. Phys. Soc. Jpn.* **66**, 3988 (1997).
64. D. Aoki, N. Watanabe, Y. Inada, R. Settai, K. Sugiyama, H. Harima, T. Inoue, K. Kindo, E. Yamamoto, Y. Haga, and Y. Ōnuki, *J. Phys. Soc. Jpn.* **69**, 2609 (2000).
65. D. Aoki, N. Suzuki, K. Miyake, Y. Inada, R. Settai, K. Sugiyama, E. Yamamoto, Y. Haga, Y. Ōnuki, T. Inoue, K. Kindo, H. Sugawara, H. Sato, and H. Yamagami, *J. Phys. Soc. Jpn.* **70**, 538 (2001).
66. Y. Tokiwa, D. Aoki, Y. Haga, E. Yamamoto, S. Ikeda, R. Settai, A. Nakamura, and Y. Ōnuki, *J. Phys. Soc. Jpn.* **70**, 3326 (2001).
67. I. Umehara, Y. Kurosawa, N. Nagai, M. Kikuchi, K. Satoh, and Y. Ōnuki, *J. Phys. Soc. Jpn.* **59**, 2848 (1990).
68. Y. Haga, D. Aoki, H. Yamagami, T.D. Matsuda, K. Nakajima, Y. Arai, E. Yamamoto, A. Nakamura, Y. Homma, Y. Shiokawa, and Y. Ōnuki, *J. Phys. Soc. Jpn.* **74**, 2889 (2005).

69. Y. Tokiwa, H. Harima, D. Aoki, S. Nojiri, M. Murakawa, K. Miyake, N. Watanabe, R. Settai, Y. Inada, H. Sugawara, H. Sato, Y. Haga, E. Yamamoto, and Y. Ōnuki, *J. Phys. Soc. Jpn.* **69**, 1105 (2000).
70. J. Arko and D.D. Koelling, *Phys. Rev.* **B17**, 3104 (1978).
71. D. Aoki, H. Yamagami, Y. Homma, Y. Shiokawa, E. Yamamoto, A. Nakamura, Y. Haga, R. Settai, and Y. Ōnuki, *J. Phys. Soc. Jpn.* **74**, 2149 (2005).
72. A. Hasegawa and H. Yamagami, *J. Phys. Soc. Jpn.* **60**, 1654 (1991).
73. A. Hasegawa, H. Yamagami, and H. Johbettoh, *J. Phys. Soc. Jpn.* **59**, 2457 (1990).
74. A. Galatanu, Y. Haga, T.D. Matsuda, S. Ikeda, E. Yamamoto, D. Aoki, T. Takeuchi, and Y. Ōnuki, *J. Phys. Soc. Jpn.* **74**, 1582 (2005).
75. P. Dervenagas, D. Kaczorowski, F. Bourdarot, P. Burlet, A. Czopnik, and G.H. Lander, *Physica* **B269**, 368 (1999).
76. J.P. Sanchez, E. Colineau, P. Vulliet, and K. Tomala, *J. Alloys Comp.* **275–277**, 195 (1998).
77. H. Shishido, R. Settai, D. Aoki, S. Ikeda, H. Nakawaki, T. Iizuka, Y. Inada, K. Sugiyama, T. Takeuchi, K. Kindo, T.C. Kobayashi, Y. Haga, H. Harima, Y. Aoki, T. Namiki, H. Sato, and Y. Ōnuki, *J. Phys. Soc. Jpn.* **71**, 162 (2002).
78. H. Shishido, R. Settai, H. Harima, and Y. Ōnuki, *J. Phys. Soc. Jpn.* **74**, 1103 (2005).
79. R. Settai, H. Shishido, S. Ikeda, Y. Murakawa, M. Nakashima, D. Aoki, Y. Haga, H. Harima, and Y. Ōnuki, *J. Phys.: Condens. Matter* **13**, L627 (2001).
80. T.D. Matsuda, Y. Haga, E. Yamamoto, S. Ikeda, H. Shishido, R. Settai, H. Harima, and Y. Ōnuki, *J. Phys. Soc. Jpn.* **76**, 064712 (2007).
81. Y. Tokiwa, T. Maehira, S. Ikeda, Y. Haga, E. Yamamoto, A. Nakamura, Y. Ōnuki, M. Higuchi, and A. Hasegawa, *J. Phys. Soc. Jpn.* **70**, 2982 (2001).
82. S. Ikeda, Y. Tokiwa, T. Okubo, Y. Haga, E. Yamamoto, Y. Inada, R. Settai, and Y. Ōnuki, *J. Nucl. Sci. Technol. Suppl.* **3**, 206 (2002).
83. S. Ikeda, Y. Tokiwa, Y. Haga, E. Yamamoto, T. Okubo, M. Yamada, N. Nakamura, K. Sugiyama, K. Kindo, Y. Inada, H. Yamagami, and Y. Ōnuki, *J. Phys. Soc. Jpn.* **72**, 576 (2003).
84. D. Aoki, H. Yamagami, Y. Homma, Y. Shiokawa, E. Yamamoto, A. Nakamura, Y. Haga, R. Settai, and Y. Ōnuki, *J. Phys.: Condens. Matter* **17**, L169 (2005).
85. T. Maehira, T. Hotta, K. Ueda, and A. Hasegawa, *Phys. Rev. Lett.* **90**, 207007 (2003).
86. A. Llobet, J.S. Gardner, E.G. Moshopoulou, J.-M. Mignot, M. Nicklas, W. Bao, N.O. Moreno, P.G. Pagliuso, I.N. Goncharenko, J.L. Sarrao, and J.D. Thompson, *Phys. Rev.* **B69**, 024403 (2004).
87. T. Muramatsu, N. Tateiwa, T.C. Kobayashi, K. Shimizu, K. Amaya, D. Aoki, H. Shishido, Y. Haga, and Y. Ōnuki, *J. Phys. Soc. Jpn.* **70**, 3362 (2001).
88. S. Kawasaki, T. Mito, G.-Q. Zheng, C. Thessiu, Y. Kawasaki, K. Ishida, Y. Kitaoka, T. Muramatsu, T.C. Kobayashi, D. Aoki, S. Araki, Y. Haga, R. Settai, and Y. Ōnuki, *Phys. Rev.* **B65**, 020504 (2002).
89. H. Shishido, T. Ueda, S. Hashimoto, T. Kubo, R. Settai, H. Harima, and Y. Ōnuki, *J. Phys.: Condens. Matter* **15**, L499 (2003).
90. J.L. Sarrao, L.A. Morales, J.D. Thompson, B.L. Scott, G.R. Stewart, F. Wastin, J. Rebizant, P. Boulet, E. Colineau, and G.H. Lander, *Nature (London)* **420**, 297 (2002).
91. Y. Kitaoka, H. Mukuda, M. Yashima, and A. Harada, *J. Phys. Soc. Jpn.* **76**, 051001 (2007).
92. T. Park, F. Ronning, H.Q. Yuan, M.B. Salamon, R. Movshovich, J.L. Sarrao, and J.D. Thompson, *Nature* **440**, 65 (2006).
93. G. Knebel, D. Aoki, D. Braithwaite, B. Salce, and J. Flouquet, *Phys. Rev.* **B74**, 020501 (2006).
94. Y. Ida, R. Settai, Y. Ota, F. Honda, and Y. Ōnuki, *J. Phys. Soc. Jpn.* **77**, 084708 (2008).
95. Y. Haga, D. Aoki, T.D. Matsuda, K. Nakajima, Y. Arai, E. Yamamoto, A. Nakamura, Y. Homma, Y. Shiokawa, and Y. Ōnuki, *J. Phys. Soc. Jpn.* **74**, 1698 (2005).
96. D. Aoki, Y. Haga, T.D. Matsuda, N. Tateiwa, S. Ikeda, Y. Homma, H. Sakai, Y. Shiokawa, E. Yamamoto, A. Nakamura, R. Settai, and Y. Ōnuki, *J. Phys. Soc. Jpn.* **76**, 063701 (2007).
97. A. Bianchi, R. Movshovich, C. Capan, P.G. Pagliuso, and J.L. Sarrao, *Phys. Rev. Lett.* **91**, 187004 (2003).
98. K. Kakuyanagi, M. Saitoh, K. Kumagai, S. Takashima, M. Nohara, H. Takagi, and Y. Matsuda, *Phys. Rev. Lett.* **94**, 0476202 (2005).
99. K. Izawa, H. Yamaguchi, Y. Matsuda, H. Shishido, R. Settai, and Y. Ōnuki, *Phys. Rev. Lett.* **87**, 057002 (2001).
100. T. Tayama, A. Harita, T. Sakakibara, Y. Haga, H. Shishido, R. Settai, and Y. Ōnuki, *Phys. Rev.* **B65**, 180504(R) (2002).
101. C. Petrovic, P.G. Pagliuso, M.F. Hundley, R. Movshovich, J.L. Sarrao, J.D. Thompson, Z. Fisk, and P. Monthoux, *J. Phys.: Condens. Matter* **13**, L337 (2001).
102. S. Ikeda, H. Shishido, M. Nakashima, R. Settai, D. Aoki, Y. Haga, H. Harima, Y. Aoki, T. Namiki, H. Sato, and Y. Ōnuki, *J. Phys. Soc. Jpn.* **70**, 2248 (2001) [*Errata*; **70**, 3187 (2001)].
103. K. Kaneko, N. Metoki, N. Bernhoeft, G.H. Lander, Y. Ishii, S. Ikeda, Y. Tokiwa, Y. Haga, and Y. Ōnuki, *Phys. Rev.* **B68**, 214419 (2003).
104. S. Jonen, N. Metoki, F. Honda, K. Kaneko, E. Yamamoto, Y. Haga, D. Aoki, Y. Homma, Y. Shiokawa, and Y. Ōnuki, *Phys. Rev.* **B74**, 144412 (2006).
105. K. Sugiyama, H. Nakashima, D. Aoki, Y. Haga, E. Yamamoto, A. Nakamura, Y. Homma, Y. Shiokawa, K. Kindo, M. Hagiwara, and Y. Ōnuki, *J. Phys. Soc. Jpn.* **75**, 094707 (2006).
106. A. Kiss and Y. Kuramoto, *J. Phys. Soc. Jpn.* **75**, 034709 (2006).
107. F. Wastin, P. Boulet, J. Rebizant, E. Colineau, and G.H. Lander, *J. Phys.: Condens. Matter* **15**, S2279 (2003).
108. H. Yamagami, D. Aoki, Y. Haga, and Y. Ōnuki, *J. Phys. Soc. Jpn.* **76**, 083708 (2007).

109. T. Sakakibara, T. Tayama, K. Matsuhira, H. Mitamura, H. Amitsuka, K. Maezawa, and Y. Ōnuki, *Phys. Rev.* **B51**, 12030 (1995).
110. T. Sakakibara, T. Tayama, K. matsuhira, A. Nomachi, S. Honma, T. Tayama, H. Amitsuka, K. Maezawa, and Y. Ōnuki, *Jpn. J. Appl. Phys.*, Ser. **11**, 6 (1999).
111. H. Aoki, S. Uji, A.K. Albessard, and Y. Ōnuki, *Phys. Rev. Lett.* **71**, 2110 (1993).
112. H. Aoki, S. Uji, A.K. Albessard, and Y. Ōnuki, *J. Phys. Soc. Jpn.* **62**, 3157 (1993).
113. M. Takashita, H. Aoki, T. Terashima, S. Uji, K. Maezawa, R. Settai, and Y. Ōnuki, *J. Phys. Soc. Jpn.* **65**, 515 (1996).
114. H. Yamagami and A. Hasegawa, *J. Phys. Soc. Jpn.* **65**, 592 (1993).
115. H. Yamagami and A. Hasegawa, *J. Phys. Soc. Jpn.* **61**, 2388 (1992).
116. Y. Aoki, T.D. Matsuda, H. Sugawara, H. Sato, H. Ohkuni, R. Settai, Y. Ōnuki, E. Yamamoto, Y. Haga, A.V. Andreev, V. Sechovsky, L. Havela, H. Ikeda, and K. Miyake, *J. Magn. Magn. Mater.* **177–181**, 271 (1998).
117. S. Holtmeier, P. Haen, A. Lacerda, P. Lejay, J.L. Tholence, J. Voiron, and J. Flouquet, *Physica* **B204**, 250 (1995).
118. T. Kasuya, *J. Phys. Soc. Jpn.* **67**, 2372 (1998).
119. K. Hanzawa, K. Ohara, and K. Yosida, *J. Phys. Soc. Jpn.* **66**, 3001 (1997). .
120. Y. Ono, *J. Phys. Soc. Jpn.* **65**, 19 (1996).
121. K. Sugawara, Y. Aoki, H. Sato, N. Mushnikov, and T. Goto, *J. Phys. Soc. Jpn.* **68**, 1094 (1999).
122. H. von Löhneysen, H.G. Schlager, and A. Schröder, *Physica* **B186–188**, 590 (1993).
123. Y. Ōnuki, S. Yasui, M. Matsushita, S. Yoshiuchi, M. Ohya, Y. Hirose, N.D. Dung, F. Honda, T. Takeuchi, R. Settai, K. Sugiyama, E. Yamamoto, T.D. Matsuda, Y. Haga, T. Tanaka, Y. Kubo, and H. Harima, *J. Phys. Soc. Jpn.* **80**, SA003 (2011).
124. N. Kimura, T. Komatsubara, D. Aoki, Y. Ōnuki, Y. Haga, E. Yamamoto, H. Aoki, and H. Harima, *J. Phys. Soc. Jpn.* **67**, 2185 (1998).
125. N. Kimura, T. Tani, H. Aoki, T. Komatsubara, S. Uji, D. Aoki, Y. Inada, Y. Ōnuki, Y. Haga, E. Yamamoto, and H. Harima, *Physica* **B281–282**, 710 (2000).
126. K. Sugiyama, M. Nakashima, D. Aoki, K. Kindo, N. Kimura, H. Aoki, T. Komatsubara, S. Uji, Y. Haga, E. Yamamoto, H. Harima, and Y. Ōnuki, *Phys. Rev.* **B60**, 9248 (1999).
127. H.P. van der Meulen, Z. Tarnawski, A. de Visser, J.J.M. Franse J., A.A.J. Perenboom, D. Althof, and H. van Kempen, *Phys. Rev.* **B41**, 9352 (1990).
128. G. Knopp, A. Loidl, K. Knorr, L. Pawlak, M. Duczmal, R. Caspary, U. Gottwick, H. Spille, F. Steglich, and A.P. Murani, *Z. Phys.* **B77**, 95 (1989).
129. F. Steglich, J. Aarts, C.D. Bredl, W. Lieke, D. Meschede, W. Franz, and J. Schäfer, *Phys. Rev. Lett.* **43**, 1892 (1979).
130. D. Jaccard, K. Behnia, and J. Sierro, *Phys. Lett.* **A163**, 475 (1992).
131. T. Takeuchi, S. Yasui, M. Toda, M. Matsushita, S. Yoshiuchi, M. Ohya, K. Katayama, Y. Hirose, N. Yoshitani, F. Honda, K. Sugiyama, M. Hagiwara, K. Kindo, E. Yamamoto, Y. Haga, T. Tanaka, Y. Kubo, R. Settai, and Y. Ōnuki, *J. Phys. Soc. Jpn.* **79**, 064609 (2010).
132. M.S. Torikachvili, S. Jia, E.D. Mun, S.T. Hannahs, R.C. Black, W.K. Neils, Dinesh Martien, S.L. Bud'ko, and P.C. Canfield, *Proc. Natl. Acad. Sci. U.S.A.* **104**, 9960 (2007).
133. S. Yoshiuchi, M. Toda, M. Matsushita, S. Yasui, Y. Hirose, M. Ohya, K. Katayama, F. Honda, K. Sugiyama, M. Hagiwara, K. Kindo, T. Takeuchi, E. Yamamoto, Y. Haga, R. Settai, T. Tanaka, Y. Kubo, and Y. Ōnuki, *J. Phys. Soc. Jpn.* **78**, 123711 (2009).
134. M. Ohya, M. Matsushita, S. Yoshiuchi, T. Takeuchi, F. Honda, R. Settai, T. Tanaka, Y. Kubo, and Y. Ōnuki, *J. Phys. Soc. Jpn.* **79**, 083601 (2010). .
135. F. Honda, S. Yasui, S. Yoshiuchi, T. Takeuchi, R. Settai, and Y. Ōnuki, *J. Phys. Soc. Jpn.* **79**, 083709 (2010).
136. K. Sugimaya and Y. Ōnuki, *High Magnetic Fields*, F. Herlach and N. Miura (eds.), World Scientific, Singapore (2003), p. 139.
137. K. Kadowaki and S.B. Woods, *Solid State Commun.* **58**, 507 (1986).
138. K. Miyake, T. Maatsuura, and C.M. Varma, *Solid State Commun.* **71**, 1149 (1989).
139. N. Tsujii, H. Kontani, and K. Yoshimura, *Phys. Rev. Lett.* **94**, 057201 (2005).
140. P. Morin, *J. Magn. Magn. Mater.* **71**, 151 (1988).
141. R. Settai, S. Araki, P. Ahmet, M. Abliz, K. Sugiyama, Y. Ōnuki, T. Goto, H. Mitamura, T. Goto, and S. Takayanagi, *J. Phys. Soc. Jpn.* **67**, 636 (1998).
142. M. Abliz, R. Settai, P. Ahmet, D. Aoki, K. Sugiyama, and Y. Ōnuki, *Philos. Mag.* **B75**, 443 (1997).
143. P. Ahmet, M. Abliz, R. Settai, K. Sugiyama, Y. Ōnuki, T. Takeuchi, K. Kindo, and S. Takayanagi, *J. Phys. Soc. Jpn.* **65**, 1077 (1996).
144. K. Sugiyama, M. Nakashima, Y. Yoshida, R. Settai, T. Takeuchi, K. Kindo, and Y. Ōnuki, *Physica* **B256–261**, 896 (1999).
145. K. Sugiyama, M. Nakashima, Y. Yoshida, Y. Kimura, K. Kindo, T. Takeuchi, R. Settai, and Y. Ōnuki, *J. Phys. Soc. Jpn.* **67**, 3244 (1998).
146. Y. Yoshida, K. Sugiyama, T. Takeuchi, Y. Kimura, D. Aoki, M. Kozaki, R. Settai, K. Kindo, and Y. Ōnuki, *J. Phys. Soc. Jpn.* **67**, 1421 (1998).
147. S. Kawarazaki, M. Sato, Y. Miyako, N. Chigusa, K. Watanabe, N. Metoki, Y. Koike, and M. Nishi, *Phys. Rev.* **B61**, 4167 (2000).
148. R. Settai, A. Misawa, S. Araki, M. Kosaki, K. Sugiyama, T. Takeuchi, K. Kindo, Y. Haga, E. Yamamoto, and Y. Ōnuki, *J. Phys. Soc. Jpn.* **66**, 2260 (1997). .
149. S. Araki, M. Nakashima, R. Settai, T.C. Kobayashi, and Y. Ōnuki, *J. Phys.*: *Condens. Matter* **14**, L377 (2002).
150. F.M. Grosche, S.R. Julian, N.D. Mathur, F.V. Carter, and G.G. Lonzarich, *Physica* **B237–238**, 197 (1997).
151. M. Ohashi, F. Honda, T. Eto, S. Kaji, I. Minamidake, G. Oomi, S. Koiwai, and Y. Uwatoko, *Physica* **B312–313**, 443 (2002).

152. T. Graf, J.D. Thompson, M.F. Hundley, R. Movshovich, Z. Fisk, D. Mandrus, R.A. Fisher, and N.E. Phillips, *Phys. Rev. Lett.* **78**, 3769 (1997).
153. R. Movshovich, T. Graf, D. Mandrus, J.D. Thompson, J.L. Smith, and Z. Fisk, *Phys. Rev.* **B53**, 8241 (1996).
154. S. Araki, R. Settai, T.C. Kobayashi, H. Harima, and Y. Ōnuki, *Phys. Rev.* **B64**, 224417 (2001).
155. S. Araki, R. Settai, M. Nakashima, H. Shishido, S. Ikeda, H. Nakawaki, Y. Haga, N. Tateiwa, T.C. Kobayashi, H. Harima, H. Yamagami, Y. Aoki, T. Namiki, H. Sato, and Y. Ōnuki, *J. Phys. Chem. Solids* **63**, 1133 (2002).
156. M. Biasini, G. Ferro, and A. Czopnik, *Phys. Rev.* **B68**, 094513 (2003).
157. M. Endo, N. Kimura, H. Aoki, T. Terashima, S. Uji, T. Matsumoto, and T. Ebihara, *Phys. Rev. Lett.* **93**, 247003 (2004).
158. K. Betsuyaku and H. Harima, *J. Magn. Magn. Mater.* **272–276**, 187 (2004).
159. N.R. Werthamer, E. Helfand, and P.C. Hohenberg, *Phys. Rev.* **147**, 295 (1966).
160. S. Kawasaki, T. Mito, Y. Kawasaki, H. Kotegawa, G.-Q. Zheng, Y. Kitaoka, H. Shishido, S. Araki, R. Settai, and Y. Ōnuki, *J. Phys. Soc. Jpn.* **73**, 1647 (2004).
161. G. Knebel , D. Braithwaite, P.C. Canfield, G. Lapertot, and J. Flouquet, *Phys. Rev.* **B65**, 024425 (2001).
162. H. Fukazawa and K. Yamada, *J. Phys.*: *Condens. Matter* **15**, S2259 (2003).
163. D. Hall, E.C. Palm, T.P. Murphy, S.W. Tozer, C. Petrovic, E. Miller-Ricci, L. Peabody, C.Q. H. Li, U. Alver, R.G. Goodrich, J.L. Sarrao, P.G. Pagliuso, J.M. Wills, and Z. Fisk, *Phys. Rev.* **B64**, 064506 (2001).
164. S. Elgazzar, I. Opahle, R. Hayn, and P.M. Oppeneer, *Phys. Rev.* **B69**, 214510 (2004).
165. D. Hall, E.C. Palm, T.P. Murphys, S.W. Tozer, Z. Fisk, U. Alver, R.G. Goodrich, J.L. Sarrao, P.G. Pagliuso, and T. Ebihara, *Phys. Rev.* **B64**, 212508 (2001).
166. A. McCollam, S.R. Julian, P.M. C. Rourke, D. Aoki, and J. Flouquet, *Phys. Rev. Lett.* **94**, 186401 (2005).
167. I. Sheikin, H. Jin, R. Bel, K. Behnia, C. Proust, J. Flouquet, Y. Matsuda, D. Aoki, and Y. Ōnuki, *Phys. Rev. Lett.* **96**, 077207 (2006).
168. N.F. Phillips, R.A. Fisher, F. Bouquet, M.F. Hundley, P.G. Pagliuso, J.L. Sarrao, Z. Fisk, and J.D. Thompson, *J. Phys.: Condens. Matter* **15**, S2095 (2003).
169. T. Takeuchi, T. Inoue, K. Sugiyama, D. Aoki, Y. Tokiwa, Y. Haga, K. Kindo, and Y. Ōnuki, *J. Phys. Soc. Jpn.* **70**, 877 (2001).
170. G. Knebel, D. Aoki, J.-P. Brison, and J. Flouquet, *J. Phys. Soc. Jpn.* **77**, 114704 (2008).
171. E. Bauer, G. Hilscher, H. Michor, C. Paul, E.W. Scheidt, A. Gribanov, Y. Seropegin, H. Noel, M. Sigrist, and P. Rogl, *Phys. Rev. Lett.* **92**, 027003 (2004).
172. E. Bauer, H. Kaldarar, A. Prokofiev, E. Royanian, A. Amato, J. Sereni, W. Brämer-Escamilla, and I. Bonalde, *J. Phys. Soc. Jpn.* **76**, 051009 (2007).
173. T.C. Kobayashi, A. Hori, S. Fukushima, H. Hidaka, H. Kotegawa, T. Akazawa, K. Takeda, Y. Ohishi, and E. Yamamoto, *J. Phys. Soc. Jpn.* **76**, 051007 (2007).
174. N. Kimura, K. Ito, K. Saitoh, Y. Umeda, H. Aoki, and T. Terashima, *Phys. Rev. Lett.* **95**, 247004 (2005).
175. N. Kimura, K. Ito, H. Aoki, S. Uji, and T. Terashima, *Phys. Rev. Lett.* **98**, 197001 (2007).
176. N. Kimura, Y. Muro, and H. Aoki, *J. Phys. Soc. Jpn.* **76**, 051010 (2007).
177. I. Sugitani, T.D. Matsuda, Y. Haga, T. Takeuchi, R. Settai, and Y. Ōnuki, *J. Phys. Soc. Jpn.* **76**, 043703 (2006).
178. R. Settai, Y. Okuda, I. Sugitani, Y. Ōnuki, T.D. Matsuda, Y. Haga, and H. Harima, *Int. J. Mod. Phys.* **B21**, 3238 (2007).
179. T. Kawai, H. Muranaka, M.-A. Measson, T. Shimoda, Y. Doi, T.D. Matsuda, Y. Haga, G. Knebel, G. Lapertot, D. Aoki, J. Flouquet, T. Takeuchi, R. Settai, and Y. Ōnuki, *J. Phys. Soc. Jpn.* **77**, 064716 (2008).
180. F. Honda, I. Bonalde, K. Shimizu, S. Yoshiuchi, Y. Hirose, T. Nakamura, R. Settai, and Y. Ōnuki, *Phys. Rev.* **B81**, 140507(R) (2010).
181. E.I. Rashba, *Sov. Phys. Solid State* **2**, 1109 (1960).
182. P.A. Frigeri, D.F. Agterberg, A. Koga, and M. Sigrist, *Phys. Rev. Lett.* **92**, 097001 (2004) [*Errata*; **93**, 099903 (2004)].
183. K.V. Samokhin, E.S. Zijlstra, and S.K. Bose, *Phys. Rev.* **B69**, 094514 (2004).
184. V.P. Mineev and K.V. Samokhin, *Phys. Rev.* **B72**, 212504 (2005).
185. P.A. Frigeri, D.F. Agterberg, and M. Sigrist, *New J. Phys.* **6**, 115 (2004).
186. S. Fujimoto, *J. Phys. Soc. Jpn.* **76**, 051008 (2007).
187. D.D. Koelling and B.N. Harmon, *J. Phys. C: Solid State Phys.* **10**, 3107 (1977).
188. M. Nishiyama, Y. Inada, and G.-Q. Zheng, *Phys. Rev. Lett.* **98**, (2007) 047002.
189. Y. Muro, D.H. Eom, N. Takeda, and M. Ishikawa, *J. Phys. Soc. Jpn.* **67**, 3601 (1998).
190. A. Thamizhavel, T. Takeuchi, T.D. Matsuda, Y. Haga, K. Sugiyama, R. Settai, and Y. Ōnuki, *J. Phys. Soc. Jpn.* **74**, 1858 (2005).
191. R. Settai, Y. Miyauchi, T. Takeuchi, I. Sheikin, F. Lévy, and Y. Ōnuki, *J. Phys. Soc. Jpn.* **77**, 073705 (2008).
192. N. Tateiwa, Y. Haga, T.D. Matsuda, S. Ikeda, E. Yamamoto, Y. Okuda, Y. Miyauchi, R. Settai, and Y. Ōnuki, *J. Phys. Soc. Jpn.* **76**, 083706 (2007).
193. H. Mukuda, T. Fujii, T. Ohara, A. Harada, M. Yashima, Y. Kitaoka, Y. Okuda, R. Settai, and Y. Ōnuki, *Phys. Rev. Lett.* **100**, 107003 (2008).
194. Y. Inada and Y. Ōnuki, *Fiz. Nizk. Temp.* **25**, 775 (1999) [*Low Temp. Phys.* **25**, 573 (1999)].
195. M. Hedo, Y. Inada, K. Sakurai, E. Yamamoto, Y. Haga, Y. Ōnuki, S. Takahashi, M. Higuchi, T. Maehira, and A. Hasegawa, *Philos. Mag.* **B77**, 975 (1998).
196. H. Ohkuni, Y. Inada, Y. Tokiwa, K. Sakurai, R. Settai, T. Honma, Y. Haga, E. Yamamoto, Y. Ōnuki, H. Yamagami, S. Takahashi, and T. Yanagisawa, *Philos. Mag.* **B79**, 1045 (1999).

197. Y. Inada, H. Yamagami, Y. Haga, K. Sakurai, Y. Tokiwa, T. Honma, E. Yamamoto, Y. Ōnuki, and T. Yanagisawa, *J. Phys. Soc. Jpn.* **68**, 3643 (1999).
198. Y. Ōnuki, I. Umehara, T. Ebihara, A.K. Albessard, K. Satoh, K. Takita, H. Aoki, S. Uji, and T. Shimizu, *Physica* **B186–188**, 1050 (1993).
199. R. Corcoran, N. Harrison, S.M. Hayden, P. Meeson, M. Springford, and P.J. van der Wel, *Phys. Rev. Lett.* **72**, 701 (1994).
200. H. Harrison, S.M. Hayden, P. Meeson, M. Springford, P.J. van der Wel, and A.A. Menovsky, *Phys. Rev.* **B50**, 4208 (1994).
201. T. Terashima, H. Takeya, S. Uji, K. Kadowaki, and H. Aoki, *Solid State Commun.* **96**, 459 (1995).
202. G. Goll, M. Heinecke, A.G.M. Jansen, W. Joss, L. Nguyen, E. Steep, K. Winzer, and P. Wyder, *Phys. Rev.* **B53**, 8871 (1996).